Investigation of the Effect of Surgical Factors on the Transition from Primary to Secondary Stability of Press-Fit Components in the Proximal Medial Tibia



A DISSERTATION SUBMITTED TO THE UNIVERSITY OF OXFORD
IN PARTIAL FULFILMENT OF THE REQUIREMENTS FOR THE DEGREE OF

Doctor of Philosophy

Xiaoyi Min
Kellogg College
Trinity Term 2024

Abstract

Primary stability of the cementless Oxford Unicompartmental Knee Replacement (OUKR) is achieved through press-fit. It is a prerequisite for successful secondary stability and is crucial for successful long-term implant survival. The aetiology of tibial periprosthetic fracture (PPF) and tibial component subsidence which are two complications after OUKR associated with tibial component fixation were unknown.

As primary stability of cementless components is related to the mechanical response of bone after press-fit at an interference, an explicit finite element (FE) model that required only two sets of input was developed to simulate the physical process of cementless peg implantation. A plastic strain-based element deletion mechanism was applied to account for material deformation in press-fit insertion. The results from these FE simulations agreed well with experimental results. To improve the accuracy of the FE models in this thesis, an experiment was designed and conducted to find the coefficient of friction between bone and implant to eliminate the number of unknown model input parameters.

The risk of tibial PPF is higher in patients with tibia vara, small tibias, and/or overhanging tibial plateaus. An FE study on two high-risk patients who experienced tibial PPF in one of their tibias after receiving bilateral OUKR revealed that damage to the peripheral cortical bone due to surgical errors was the main cause of their fractures. The results of an FE parameter study on the effects of implant positioning on the risk of fracture discovered that the risk of experiencing PPF increased as the keel slot moved closer to either the anterior or posterior cortex. Therefore, the surgical guidance should be followed strictly when deciding the mediolateral and proximal-distal position of the tibial component. Extreme internal or external rotation in the transverse plane which leads to a short distance between the keel slot and the cortex should be avoided. Good coverage beneath the tibial tray should be achieved while making component size choices to secure an appropriate slot-cortex distance. Placing the component in varus relative to the tibial mechanical axis reduces the risk of fracture in these high-risk patients with tibia varus, while this may increase the risk of lateral progression of osteoarthritis due to medial subluxation of the femur. Therefore, decisions about the varus placement should be made with care. An FE study on five new small keel designs suggested that the introduction of a small keel design could greatly reduce the risk of tibial PPF, and the keel should be placed in the centre in the anteroposterior direction to lower the chance of damaging either the anterior or posterior cortex during tibial preparation.

The incidence of tibial component subsidence after cementless OUKR ranged from 0.3-5% and most components subsided posteriorly and/or into valgus. Conservative treatment with close monitoring of progression in component movement was recommended. The cause of subsidence is likely to be multifactorial rather than solely mechanical and may involve the biological response of bone. Further interdisciplinary studies are therefore suggested.

This thesis concludes that the risk of tibial PPF rises as the minimum distance between the keel slot and cortex decreases. Damage to the cortex would further increase the risk. Therefore, surgical technique guidance should be closely followed to avoid unsatisfactory component positioning. The use of a small keel has the potential to notably reduce the risk of tibial PPF while maintaining the same level of fixation as the current design. Further clinical studies are required to verify if adequate primary stability is preserved. If this design change is implemented, the risk of tibial PPF after cementless OUKR will greatly decrease in patients with tibia vara, small tibias and/or overhanging tibial plateaus, which are common in the Asian populations where the incidence of PPF can be as high as 8%.

Acknowledgement

I am deeply indebted to my DPhil supervisors: Professor David Murray, Associate Professor Stephen Mellon, and Laurence Marks. Words cannot express my gratitude for their invaluable assistance, guidance, and feedback at every stage and in every aspect of my research project, and for their advice and help on my career path. It has been my privilege to learn and grow under their supervision.

I am thankful to Barbara Marks and Jo Brown for all their care and support throughout my DPhil, and for making this journey as smooth as possible. I would also like to express my gratitude to all past and present members of OOEC: Lachlan Arthur, Nisrina Widari, Jack Tu, Azmi Rahman, Sandy MacAulay, David Heath, Irene Yang, and Thomas Hamilton. I am honoured to have worked with and learned from these incredible people for three years. Thank you all for making my whole time at OOEC joyful.

I am also grateful to Associate Professor Philippa Hulley, Associate Professor Laurence Brassart and Associate Professor Alison Jones for being my viva examiners. I truly appreciate all your feedback and found our discussions to be a great source of inspiration.

I would like to acknowledge Professor Yihui Tu, his team, and Dr Zhidao Xia for offering me the precious opportunity to be involved in the publication of the first Unicompartmental Knee Replacement book in China. Thank you for all your help and guidance.

I would like to express my gratitude to all my amazing Imperial MechEng friends and those I met in Oxford. Thank you for accompanying me through my time here. I will treasure all our moments and laughs. A big thank-you to my long-distance best friend, 潘栩悦 (Pan Xuyue), who though far away, provided me the most irreplaceable support and cherished memories, and my cousins, my lifelong best friends, 闵东赫 (Min Donghe), 鲁昱儿 (Lu Yuer), and 闵智懿 (Min Zhiyi), who have always been my support and source of happiness. I am thrilled to see how we have all entered new stages of life over the past three years.

My greatest thanks go to my family, especially my mother, 鲁潇 (Lu Xiao), and my father, 闵声赞 (Min Shengzan), without whom this journey could not have been possible. Thank you for guiding me onto this path, for always being the most supportive parents, for always having faith in me, and for respecting every single decision I have made. I am more than blessed to have grown up in this family filled with love, encouragement, and positivity. Last but not least, I would like to thank our dog, Coco, for being the sweetest, most adorable creature in this world, and for keeping good company with my parents while I am far away. I am grateful for having you in my life, and I will always be.

Table of Contents

Abstract ..... **ii**

Acknowledgement ..... **iii**

Table of Contents ..... **iv**

Abbreviations ..... **x**

List of Figures ..... **xii**

List of Tables ..... **xxiii**

Chapter 1. Introduction and Literature Review **1**

1.1 The Knee 1

1.2 Knee Osteoarthritis and Knee Replacement 3

1.3 Cemented vs Cementless Fixation 7

1.4 Primary and Secondary Stability of Implants 9

1.5 Medial Oxford Unicompartmental Knee Replacement 12

1.5.1 Complications of Cementless Medial Oxford Unicompartmental Knee Replacement 15

1.5.1.1 Tibial Component Subsidence 16

1.5.1.2 Periprosthetic Tibial Fracture 19

1.6 Application of Finite Element Analysis in Orthopaedics 21

1.7 Thesis Overview 22

1.7.1 Thesis Aim 22

1.7.2 Thesis Structure 23

Chapter 2. Finite Element Analysis and Experimental Verification of Press-fit Component Primary Fixation **25**

2.1 Introduction and Aim 25
2.2 Method 28
2.2.1 Model Geometry and Boundary Conditions 28
2.2.2 Material 30
2.2.3 Mesh 32
2.2.4 Contact 32
2.2.5 Experimental Validation 33
2.3 Results 35
2.4 Discussion 40
2.5 Chapter Summary 43

Chapter 3. Experimental Characterisation of Coefficient of Friction at Bone-implant Interface 45

3.1 Introduction and Aim 45
3.2 Method 46
3.3 Results 53
3.4 Discussion 54
3.5 Chapter Summary 57

Chapter 4. Finite Element Analysis of Periprosthetic Tibial Fractures after Cementless Oxford Unicompartmental Knee Replacement 58

4.1 Introduction and Aim 58
4.2 Methods 70
4.2.1 Patient 1 70
4.2.1.1 Finite Element Modelling 76

4.2.1.2 Finite Element Modelling of Fractured Tibial Resection in the Unfractured Tibia 82
4.2.2 Patient 2 82
4.2.3 Validation of Finite Element Model against Experiment 83
4.3 Results 87
4.3.1 Patient 1 87
4.3.2 Patient 2 96
4.3.3 Validation of Finite Element Model against Experiment 103
4.4 Discussion 106
4.5 Chapter Summary 112

Chapter 5. Effects of Tibial Component Positioning and Design on Risk of Periprosthetic Tibial Fracture after Cementless Oxford Unicompartmental Knee Replacement 113

5.1 Introduction and Aim 113
5.2 Methods 117
5.2.1 Effects of Component Positioning on Risk of Fracture 117
5.2.2 Testing of Smaller Keel Designs 122
5.3 Results 124
5.3.1 Effects of Component Positioning on Risk of Fracture 124
5.3.1.1 Medial-lateral Movements 124
5.3.1.2 Proximal-Distal Movements 125
5.3.1.3 Internal-External Rotations 126
5.3.1.4 Varus-Valgus Rotations 128
5.3.2 Testing of Smaller Keel Designs 129
5.4 Discussion 133

5.5 Chapter Summary 140

Chapter 6. Risk of Lateral Progression of Osteoarthritis after Varus Placement of Tibial Component 142

6.1 Introduction 142

6.2 Methods 145

6.2.1 Finite Element Analysis of Standard Placement of Tibial Component 145

6.2.1.1 Model Setup 145

6.2.1.2 Boundary Conditions and Loads 146

6.2.1.3 Material Properties 149

6.2.1.4 Mesh 150

6.2.1.5 Contact 150

6.2.2 Finite Element Analysis of Varus and Valgus Placements of Tibial Component 151

6.2.2.1 Model Setup 151

6.2.2.2 Boundary Conditions 152

6.3 Results 153

6.4 Discussion 153

6.5 Chapter Summary 155

Chapter 7. Risk Factors of Cementless Oxford Unicompartmental Knee Replacement Tibial Component Subsidence 156

7.1 Introduction and Aim 156

7.1.1 Symptoms of Cementless Tibial Component Subsidence after OUKR 156

7.2 Part A: Systematic Review on Tibial Component Subsidence after Cementless OUKR 157

7.2.1 Methods 157
7.2.1.1 Search Strategy 158
7.2.1.2 Eligibility Criteria and Study Selection 160
7.2.1.3 Data Collection and Extraction 160
7.2.2 Results 161
7.2.2.1 Literature Search Results 161
7.2.2.2 Proposed Aetiology of Subsidence 167
7.2.2.3 Revisions 168
7.2.3 Discussion 168
7.3 Part B: Computational Analysis of Hypothesised Causes of Subsidence 171
7.3.1 Introduction and Aim 171
7.3.2 Methods 174
7.3.2.1 Forced Subsidence Model 174
7.3.2.2 Bearing Impingement Model 177
7.3.2.3 Posterior Cortex Damage Model 181
7.3.3 Results 182
7.3.3.1 Forced Subsidence Model 182
7.3.3.2 Bearing Impingement Model 183
7.3.3.3 Posterior Cortex Damage Model 188
7.3.4 Discussion 190
7.3.5 Conclusions 193
7.4 Chapter Summary 194
Chapter 8. Discussion 195
8.1 Summary of Findings 195
8.2 Limitations and Future Works 199

8.3 Thesis Conclusions 202

Chapter 9. References 204

Appendices 222

Appendix A: Python Script for Generating Model of Patient 1 Left Tibia 222

Appendix B: Python Script for Generating Models of Patient 1 Left Tibia with Modified Vertical and Horizontal Cuts 242

Appendix C: Change in Loading Position when Tibial Component was Rotated Internally/Externally 266

Appendix D: Search Strings Used in Systematic Review 267

Appendix E: Excluded Studies in Systematic Review with Reasons 268

Appendix F: Radiographs of Cementless OUKR Tibial Component Subsidence Cases and Supplementary Details 270

Appendix G: Modifications to the py_bonemat_abaqus Python Package to Apply Elastic-plastic Material Properties 288

Appendix G – 1: Update to code run.py 288

Appendix G – 2: Update to code data_output.py (edits in bold) 290

Appendix H: Radiographic Study of Difference in Bone Density in Subsidence and Non-Subsidence Patients 293

Appendix I: Study of Unilateral Subsidence in Bilateral OUKR Patients 298

Abbreviations

2D	2-Dimensional
3D	3-Dimensional
AA	Anatomical Axis
ACL	Anterior Cruciate Ligament
AM	Anteromedial
AMOA	Anteromedial Osteoarthritis
AP	Anteroposterior
ASIS	Anterior Superior Iliac Spine
BMI	Body Mass Index
CI	Confidence Interval
COF	Coefficient of Friction
CT	Computed Tomography
DICOM	Digital Imaging and Communications in Medicine
FE	Finite Element
FEA	Finite Element Analysis
HA	Hydroxyapatite
HU	Hounsfield Unit
KCD	Keel-cortex Distance
LCC	Lateral Condyle Centre
LCL	Lateral Collateral Ligament
MA	Mechanical Axis
MCC	Medial Condyle Centre
MCL	Medial Collateral Ligament
MEL	Medial Eminence Line
MPTA	Medial Proximal Tibial Angle

MTPM	Maximal Total Point Motion
N/A	Not Applicable
OA	Osteoarthritis
OKS	Oxford Knee Score
OUKR	Oxford Unicompartmental Knee Replacement
PCF	Pounds per Cubic Foot
PCL	Posterior Cruciate Ligament
PIPO	Push-in-pull-out
PLA	Polylactic Acid
PMMA	Polymethylmethacrylate
Post-op	Post-operative
PPF	Periprosthetic Fracture
Pre-op	Pre-operative
PROM	Patient-Reported Outcome Measures
PU	Polyurethane
ROI	Region of Interest
RSA	Radiostereometric Analysis
SCD	Slot-cortex Distance
SD	Standard Deviation
SONK	Spontaneous Osteonecrosis of the Knee
TKR	Total Knee Replacement
UK	United Kingdom
UKR	Unicompartmental Knee Replacement
X-small	Extra-small

List of Figures

Figure 1.1: Anatomy of the knee joint [14]. 2

Figure 1.2: Weight-bearing radiograph of an anteromedial osteoarthritic knee. Subchondral sclerosis, formation of osteophytes and narrowing of joint space are shown. 5

Figure 1.3: Post-operative anteroposterior (AP) radiographs of a Total Knee Replacement (TKR) (left, adapted from [42]) and a medial Unicompartmental Knee Replacement (UKR) (right). 6

Figure 1.4: Cemented (left) and cementless (right) version of Oxford Unicompartmental Knee Replacement. Figure adapted from [44]. 7

Figure 1.5: Onset of action of primary stability and secondary stability of implants. The dominating stability transits from the primary stability to the secondary stability at around 2-4 weeks post-operation [64]. 10

Figure 1.6: Varus-stressed (left) and valgus-stressed (right) anteroposterior radiographs of an osteoarthritic knee with anteromedial osteoarthritis. When a varus stress was applied to the knee, bone-on-bone contact was shown in the medial compartment. When valgus stress was applied, a normal joint space was shown in the lateral compartment. 13

Figure 1.7: Radiograph showing a physiological radiolucent line beneath the tibial component. Figure adapted from [83]. 15

Figure 1.8: Anteroposterior and lateral radiographs of a subsidence case. The component subsided into valgus and fixated at the subsided position. Figure adapted from [87]. 17

Figure 1.9: Proposed mechanism of tibial component valgus subsidence: lateral placement of the femoral component relative to the tibial component caused bearing impingement on the lateral wall of the tibial tray. This subsequently caused the bearing to tip and created a concentrated compressive load beneath the lateral side of the tibial tray. After the tibial component subsides into valgus, congruency between the bearing and the tibial component is regained. Figure adapted from [87]. 18

Figure 1.10: Vertical overcut potentially weakening the load-bearing ability of the bony support. 19

Figure 1.11: Anteroposterior radiograph of tibial periprosthetic fracture after a cementless medial Oxford Unicompartmental Knee Replacement [93]. 20

Figure 2.1: Axisymmetric finite element model setup..... 29

Figure 2.2: True stress-true plastic strain curve of the Sawbones foam [120]. The upturn value is 0.31 at which the gradient of the curve greatly increases. PCF: pounds per cubic foot. 31

Figure 2.3: PIPO test experimental setup. 34

Figure 2.4: Pegs of smooth (left) and porous (right) surface finish. 34

Figure 2.5: Force-displacement curves from experiments (grey) and finite element analysis (FEA) (red) of the PIPO of the smooth 5.7 mm peg at 0.70 mm interference with the fracture strain of 0.31 (red). 36

Figure 2.6: Force-displacement curve from experiments (grey) and finite element analysis (FEA) (red) of the PIPO of the smooth 5.7 mm peg at 0.684 mm interference with the fracture strain of 0.31. 37

Figure 2.7: Force-displacement curves from experiments (grey) and finite element analysis (FEA) (red) of the PIPO of the smooth 5.7 mm peg at 0.92 mm interference with the fracture strain of 0.31. 37

Figure 2.8: Force-displacement curve at 0.6 mm interference for the smooth 4.7 mm peg. 38

Figure 2.9: Push-in and pull-out forces from the experiment with a 95% confidence interval (left) and from finite element analysis (FEA) (right) of the smooth and porous pegs of 4.7 mm diameter. The porous peg was modelled with mean diameter (4.7 mm) and maximum diameter (4.8 mm). 39

Figure 2.10: Force-displacement curve for the porous 4.7 mm peg. FEA simulation was conducted with both the mean diameter (at 0.60 mm interference) and the maximum diameter (at 0.70 mm interference) of the peg. 40

Figure 3.1: Schematic of the experimental setup. W: weight of the suspended mass, f: friction force, FN: normal force. 47

Figure 3.2: 3D-printed smooth keel (left), 3D-printed porous keel (middle), cementless Oxford Unicompartmental Knee Replacement (OUKR) tibial component (right) 48

Figure 3.3: Surface microstructure of the 3D-printed porous keel (left) and the cementless Oxford Unicompartmental Knee Replacement (OUKR) tibial component (right). 49

Figure 3.4: Schematic of the bone sample holder. Figure adapted from [134]. 49

Figure 3.5: Equipment setup. The tested fixation component was clamped between two pieces of samples through the load applied by the vertical load cell. The 3D-printed component was held by the holder which was connected to the weight via a piece of string and a pulley (left). The string was directly connected to the keel of the Oxford Unicompartmental Knee Replacement tibial component (right). 50

Figure 3.6: CAD model of the keel holder. 51

Figure 3.7: Schematic of bone sample collection. The samples were resected from the proximal tibial plateau along the axial direction of the tibia. 53

Figure 3.8: Examples of porcine samples (top) and bovine samples (bottom) tested in the experiment. 53

Figure 4.1: Oxford Unicompartmental Knee Replacement tibial components of Size AA, Size C, and Size F. When the components are scaled to have the same length, the smallest component (Size AA) has the largest depth, implying the depths of smaller components are relatively larger. Figure adapted from [117]. 59

Figure 4.2: Post-fracture anteroposterior (a, b) and lateral (c, d) radiographs of Patient 1, showing periprosthetic fracture in the right tibia (a). Medial and anterior overhang was shown in the right leg (a, c). 61

Figure 4.3: Post-fracture anteroposterior (a, b) and lateral (c, d) radiographs of Patient 2, showing periprosthetic fracture in the left tibia (b). Medial overhang of the tibial component is shown in the left tibia (b). 63

Figure 4.4: The medial eminence line (MEL) is defined as the line that starts from the medial tibial spine and extends parallel to the tibial anatomical axis. In the intramedullary-type tibia, MEL does not pass through the medial cortex. In the extramedullary-type tibia, MEL passes through the medial cortex [95]. 65

Figure 4.5: Medial proximal tibial angle (MPTA) is the acute angle between the tangent to the tibial plateau and the tibial mechanical axis (MA). 66

Figure 4.6: The vertical tibial saw cut should be immediately medial to the medial tibial spine and should point towards the anterior superior iliac spine (ASIS). Figure adapted from [32]. 67

Figure 4.7: Criteria for the positioning and sizing of the Oxford Unicompartmental Knee Replacement tibial component. 68

Figure 4.8: Measurements of keel-cortex distances (KCDs) made in different regions: a) anterior, b) anteromedial, c) posterior, and d) posteromedial [96]. 69

Figure 4.9: Anatomical directions on tibias resected for medial Oxford Unicompartmental Knee Replacement. 71

Figure 4.10: Alignments of the tibial and femoral components. Figure adapted from [152]. 71

Figure 4.11: Definition of (a) lateral condyle centre (LCC), (b) medial condyle centre (MCC), (c) Cobb axis (Red) is the perpendicular bisector of the line connecting LCC and MCC. 73

Figure 4.12: Measurement of the mediolateral position of the tibial cuts. The mediolateral distance (Red) is defined as the distance between the midpoint of the AP cut and the Cobb axis's projection on the horizontal cut plane (Blue). 74

Figure 4.13: Measurement of the proximal-distal position of the tibial cuts. The proximal-distal distance (Red) is defined as the distance from the proximal tibial centre to the horizontal cut plane. 74

Figure 4.14: Measurement of the varus-valgus orientation of the tibial cuts. The varus-valgus angle is defined as the angle between the vertical cut plane and the tibial long axis (Blue). 75

Figure 4.15: Measurement of the internal-external rotation of the tibial cuts. The internal-external angle (red) is defined as the angle between the vertical cut plane and the Cobb axis (blue). 75

Figure 4.16: Anteroposterior views and lateral views of the tibias when Size C tibial components were implanted with the keel placed in the middle of the slot (a, b) and when

the keel was placed closer to the front of the slot (c,d). When the keel was placed in the middle of the slot, a hole was created in the anterior part of the tibia (a,b). 77

Figure 4.17: Mesh on the tibia (a) and on the tibial component (b). 79

Figure 4.18: The load was applied onto a load patch which represented the position of the bearing when it was 1 mm away from the wall and 8 mm posterior to the centreline. 80

Figure 4.19: Anteroposterior view (a) and lateral view (b) of the fractured (left) tibia of Patient 2 with a Size A component implanted at the post-operative position. The keel slot created holes in both the anterior and posterior cortex. 83

Figure 4.20: An example of the CAD model of the blocks used for testing. 85

Figure 4.21: Measurement of slot-cortex distance. The shortest distance between the keel slot surface and the exterior surface of the tibial was found in Solidworks 2022. 86

Figure 4.22: Slices of pre-operative computed tomography scans of Patient 1. The slices were taken at the proximal tibial plateau. Brighter regions which indicate sclerosis were shown in both tibias. Pixel size (0.781, 0.781). 88

Figure 4.23: Measurements of the medial proximal tibial angles and medial eminence lines (MELs) (blue) of the fractured and unfractured tibia of Patient 1. Both MELs penetrated the medial cortex. MA: mechanical axis. 89

Figure 4.24: Maximum principal stress plot of the unfractured tibia of Patient 1 when a 1000 N load was applied. 91

Figure 4.25: Material plot of the unfractured tibia of Patient 1, showing Young's Modulus of the tibia bone. 91

Figure 4.26: Maximum principal stress plot of the fractured (right) tibia of Patient 1 when a 1000 N load was applied. The keel slot cut through the tibia and made a hole. 92

Figure 4.27: Material plot of the fractured tibia of Patient 1 showing the Young's Modulus of the tibia bone. 92

Figure 4.28: Maximum principal stress plot of the fractured tibia of Patient 1 when a 1000 N load was applied. The keel slot was moved backwards by 1.81 mm to avoid making a hole in the bone. The figure is in the same scale as **Figure 4.26**. 93

Figure 4.29: Material plot of the fractured tibia of Patient 1. The front of the keel slot cut into the cortical bone, marked by the red circle. 93

Figure 4.30: Maximum principal stress plot of the unfractured tibia when the fractured cuts were replicated. 94

Figure 4.31: Material plot of the unfractured tibia when the fractured cuts were replicated. The front of the keel slot cut into the cortical bone. 94

Figure 4.32: The fractured tibia with Size C (left) or Size B (right) tibial component implanted with the same vertical and horizontal tibial resections. A better coverage and less medial and anterior overhang were shown when a Size B component was implanted. 95

Figure 4.33: Maximum principal stress plot of the fractured tibia when a Size B component was implanted with the same tibial resection. 96

Figure 4.34: Slices of pre-operative CT scans of Patient 2. The slices were taken at the proximal tibial plateau. Brighter regions which indicate sclerosis were shown in both tibias. Pixel size (0.781, 0.781) 97

Figure 4.35: Measurements of the medial proximal tibial angles (MPTAs) of the unfractured and the fractured tibias of Patient 2. 98

Figure 4.36: Medial eminence lines (MELs) of the fractured and unfractured tibia of Patient 2. Both MELs penetrated the medial cortex. AA: anatomical axis. 98

Figure 4.37: Maximum principal stress in the fractured tibia of Patient 2. 99

Figure 4.38: Maximum principal stress in the fractured tibia of Patient 2, in the same scale as **Figure 4.37**. 100

Figure 4.39: Maximum principal stress in the unfractured tibia of Patient 2. 100

Figure 4.40: Material plot of the fractured tibia of Patient 2. Keel slot cut through the anterior and posterior cortex. 101

Figure 4.41: Material plot of the unfractured tibia of Patient 2. 101

Figure 4.42: Maximum principal stress in the fractured tibia of Patient 2 when a Size AA component was implanted and loaded. 102

Figure 4.43: Maximum principal stress plot when the fractured cuts were replicated in the unfractured tibia of Patient 2. 102

Figure 4.44: Highest maximum principal stress in the tibia versus minimum slot-cortex distance (SCD) when the real bone material properties were applied. 103

Figure 4.45: Highest maximum principal stress in the tibia versus minimum slot-cortex distance (SCD) when the Sawbones material properties were applied. Dotted line: line of best fit. 104

Figure 4.46: Results from the load-to-fracture experiment with error bars showing a 95% confidence interval [164]. SCD: slot-cortex distance. Dotted line: line of best fit. 105

Figure 4.47: Load to fracture from the experiment against the highest maximum principal stress from the FE models 106

Figure 4.48: The tibial component rotates around the line connecting the anteromedial and posterolateral corners of the keel. 108

Figure 5.1: Position of incision for medial Oxford Unicompartmental Knee Replacement. The incision starts from the medial margin of the patella and extends to 3 cm distal to the joint line [32]. 114

Figure 5.2: The Oxford G-Clamp is used to decide the depth of the horizontal tibial resection. Figure adapted from [32] 115

Figure 5.3: Vertical and horizontal cuts for various changes in the position or orientation of the tibial component. 119

Figure 5.4: (a) Varus (b) standard and (c) valgus coronal placement of the tibial component. Changes in the varus-valgus orientation were made around the medial tibial spine. Figure adapted from [151] 120

Figure 5.5: Overlaying the five new smaller keel designs tested and the current keel design. Design c was the one tested in [117]. Designs c, d and e have the keel of the same size but placed at different positions, aligning to the front edge, back edge and middle line of the existing keel design. 122

Figure 5.6: Tibias were partitioned into the anterior part and the posterior part halfway across the keel slot in the anteroposterior direction 124

Figure 5.7: Highest maximum principal stress in the anterior and posterior part of the proximal tibia and the shortest anterior slot-cortex distance (SCD) in the unfractured tibia of Patient 1 and Patient 2 when the tibial component was translated in the mediolateral direction. 125

Figure 5.8: Highest maximum principal stress in the anterior and posterior part of the proximal tibia and the shortest anterior slot-cortex distance (SCD) in the unfractured tibia of Patient 1 and Patient 2 when the tibial component was translated in the proximal-distal direction. 126

Figure 5.9: Highest maximum principal stress in the anterior and posterior part of the proximal tibia and the shortest anterior slot-cortex distance (SCD) in the unfractured tibia of Patient 1 and Patient 2 when the tibial component was rotated in the internal-external direction. 127

Figure 5.10: Highest maximum principal stress in the anterior and posterior part of the proximal tibia and the shortest anterior slot-cortex distance (SCD) in the unfractured tibia of Patient 1 and Patient 2 when the tibial component was rotated in the varus-valgus direction. The tibial component was rotated into varus and valgus around the lateral edge of the keel slot. These rotations kept the component at roughly the same mediolateral and proximal-distal position. 128

Figure 5.11: Highest maximum principal stress in the anterior and posterior part of the proximal tibia and the shortest anterior slot-cortex distance (SCD) in the unfractured tibia of Patient 1 and Patient 2 when the tibial component was rotated in the varus-valgus direction while keeping the vertical cut next to the medial tibial spine. 129

Figure 5.12: Highest maximum principal stress in the anterior and posterior part of the proximal tibia when tibial components with small keel designs were implanted into the unfractured tibia of Patient 1 with the original tibial resection. The five new designs are Design a to Design e from left to right. 130

Figure 5.13: Highest maximum principal stress in the anterior and posterior part of the proximal tibia when two tibial components with smaller keels (Middle: Design c, Right: Design e) were implanted into the fractured tibia of Patient 1 with the original fractured tibial resection. 131

Figure 5.14: Highest maximum principal stress in the anterior and posterior part of the proximal tibia when tibial components with small keel designs were implanted into the unfractured tibia of Patient 2 with the original tibial resection. The five new designs are Design a to Design e from left to right. 132

Figure 5.15: Highest maximum principal stress in the anterior and posterior part of the proximal tibia when the tibial component with a small keel placed in the middle (Design e) was implanted into the fractured tibia of Patient 2 with the original tibial resection..133

Figure 5.16: Varus-valgus rotation of the component around the medial tibial spine is a combination of the change of its orientation and the change of its mediolateral position. (a) When the component is rotated into valgus around the medial tibial spine, it is more medially placed than when it is rotated around the lateral edge of the keel slot. (b) Similarly, when the component is rotated into varus around the medial tibial spine, it is more laterally placed than when it is rotated around the lateral edge of the keel slot. Figure adapted from [151]. 135

Figure 6.1: Lateral progression of osteoarthritis after Oxford Unicompartmental Knee Replacement. 143

Figure 6.2: The varus-valgus orientation of the bearing follows that of the tibial component.....144

Figure 6.3: The positions of the Oxford Unicompartmental Knee Replacement components were determined by virtually implanting the components into the tibia from which the cartilage and meniscus were built. The tibia was only used to find the positions of the components. It was not simulated in the FE model. 146

Figure 6.4: The femoral component and the femoral cartilage were brought downwards into contact with the meniscal bearing and the meniscus in the contact step. 148

Figure 6.5: The meniscus was sectioned into three layers based on their material properties. 150

Figure 6.6: Varus and valgus rotations of the component were made around the lateral superior edge of the tibial wall. 152

Figure 6.7: The bearing shifted medially when the tibial component was in varus and shifted laterally when the tibial component was in large valgus. 153

Figure 7.1: PRISMA flow diagram of the review. 162

Figure 7.2: Examples of (a) an AP radiograph and (b) a lateral radiograph that are not of optimal alignment for the assessment of subsidence. 171

Figure 7.3: After incomplete removal of the tibial plateau is made (Blue), a chisel is needed to remove the piece of bone left at the back, during which damage to the posterior cortex (Red) may be made. 173

Figure 7.4: Mesh was refined on the horizontal cut surface. 175

Figure 7.5: Position of the tibial component before (pink) and after (blue) migrations and rotations. 176

Figure 7.6: Bearing impingement model setup 178

Figure 7.7: When the femoral component was moved further laterally by 2 mm after the bearing hit the wall (overall 3 mm lateral movement), it was overhanging lateral to the bearing. 179

Figure 7.8: Damage to the posterior cortex of three different severity was modelled. Model 1 – Shallow damage to the medial and lateral cortex. Model 2 – Deep damage to the medial cortex only. Model 3 – Deep damage to the medial and lateral cortex. The blue regions represent the excessively removed bone. 182

Figure 7.9: Contact pressure (in MPa) in the bone after the tibial component was displaced into its subsided position under displacement control. 183

Figure 7.10: The bearing tipped into valgus under a 1000 N load when the femoral component was 1 mm lateral to its centre line. 184

Figure 7.11: The bearing tipped into valgus under a 1000 N load when the femoral component was 2 mm lateral to its centre line. 184

Figure 7.12: Contact pressure under the tibial tray when the femoral component was placed at different mediolateral positions. 185

Figure 7.13: Vertical displacement of the tibial component under a 1000 N load when the femoral component was placed at different mediolateral positions. Negative values indicate distal movements (into the page). 186

Figure 7.14: Contact pressure in the bone beneath the tibial component when a 5000 N load was applied. The femoral component was 3 mm lateral to its standard position. ... 187

Figure 7.15: Vertical displacement of the tibial component when a 5000 N load was applied. The femoral component was 3 mm lateral to its standard position. Negative values indicate distal movements (into the page). 187

Figure 7.16: Contact pressure in the bone when the posterior cortex was intact and when damage of different severity was made to the cortex. Model 1 – Shallow damage to the medial and lateral cortex. Model 2 – Deep damage to the medial cortex only. Model 3 – Deep damage to the medial and lateral cortex. 188

Figure 7.17: Vertical displacement of the tibial component under a 1000 N load when the posterior cortex of the tibias was damaged. Negative values indicate distal movements (into the page). Model 1 – Shallow damage to the medial and lateral cortex. Model 2 – Deep damage to the medial cortex only. Model 3 – Deep damage to the medial and lateral cortex. 189

List of Tables

Table 1.1: Indications and contraindications of Medial Oxford Unicompartmental Knee Replacement. ACL: Anterior cruciate ligament; PCL: Posterior cruciate ligament; MCL: Medial collateral ligament. 13

Table 1.2: Reasons for revisions in the first 1000 cementless Oxford Unicompartmental Knee Replacement (OUKR) cases performed by two designer surgeons (DWM, CAFD) at 15-year post-operation. OA: osteoarthritis. 16

Table 2.1: Studies conducted. Three pegs of two different levels of surface roughness and two diameters were studied. FEA: finite element analysis. PIPO: push-in-pull-out. 27

Table 2.2: Material properties of titanium pegs and plastic bone block. 30

Table 2.3: Maximum push-in and pull-out forces from experiments and finite element models of the 5.7 mm smooth peg with fracture strain (FS) of 0.28, 0.31 and 0.34. FS of 0.31 gave results that were closest to the experiments. 36

Table 2.4: Maximum push-in and pull-out forces for the 4.7 mm smooth and 4.7 mm porous peg from experiments and finite element (FE) models..... 38

Table 3.1: Coefficient of friction values. 54

Table 4.1: Relevant patient and surgical risk factors of periprosthetic tibial fracture. 64

Table 4.2: Parameters used in the conversion from Hounsfield Unit values from medical images to elastic modulus. 81

Table 4.3: Description of finite element models with modified tibial resections tested against the experiment. 84

Table 4.4: Summary of the comparison of the relevant patient-related risk factors of the fractured and unfractured tibia of Patient 1. 87

Table 4.5: Comparison of the bone quality and tibial size of the fractured and unfractured tibia of Patient 1. 88

Table 4.6: Positions and orientations of tibial resections in Patient 1. 90

Table 4.7: Summary of the comparison of the relevant patient-related risk factors of the fractured and unfractured tibia of Patient 2. 97

Table 4.8: Comparison of the bone quality and tibial size of the fractured and unfractured tibia of Patient 2. 97

Table 4.9: Positions and orientations of tibial resections in Patient 2. 99

Table 6.1: Material properties of Oxford Unicompartmental Knee Replacement components. 149

Table 6.2: Material properties of soft tissues in the lateral compartment. 149

Table 7.1: Patient, Intervention, Comparison, Outcome (PICO) framework of the review. 158

Table 7.2: Details of subsidence cases collected. BMI: Body mass index; OA: Osteoarthritis; Pre-op: pre-operative; Post-op: Post-operative; OKS: Oxford Knee Score; Y: Yes; N: No; N/A: Not applicable; AM: anteromedial. 164

Table 7.3: Summary of the proposed aetiology of tibial component subsidence. 167

Chapter 1. Introduction and Literature Review

1.1 The Knee

The knee, the synovial joint that connects the end of the femur and the top of the tibia (**Figure 1.1**), is one of the most complex joints in the human body and is involved in many daily activities [1]. It is comprised of two joints: the tibiofemoral joint and the patellofemoral joint. The tibiofemoral joint is the articulation between the medial and lateral condylar surfaces of the femur and the tibia and is responsible for the weight-bearing of the knee joint. It is known to transmit forces that peak at around three times body weight during normal level gait [2, 3]. The patellofemoral joint is the articulation between the patella and the femoral trochlea [4, 5]. These articulating surfaces are covered with smooth hyaline cartilage which reduces friction and allows smooth gliding motions between the surfaces during joint movement [6]. The other type of cartilage present in the knee is fibrocartilage. The knee menisci are two pieces of C-shaped fibrocartilage that adjust their shape to optimise load transmission in the knee joint between the femur and the tibia [7-9]. They are critical in maintaining the normal function of the knee joint and injured menisci can lead to the progression of degenerative lesions in the knee [10]. They have a concave superior surface that matches the convex surface of the femur and a flat inferior surface that fits the relatively flat tibial plateau and they create two congruent surfaces between the incongruent tibiofemoral cartilage surfaces [11]. This shape congruency at the articular surfaces on the femur and the tibia increases the contact area and reduces the chance of the joint surfaces receiving concentrated loads [12]. They also act as stabilisers of the knee joint during daily activities [4, 10, 13].

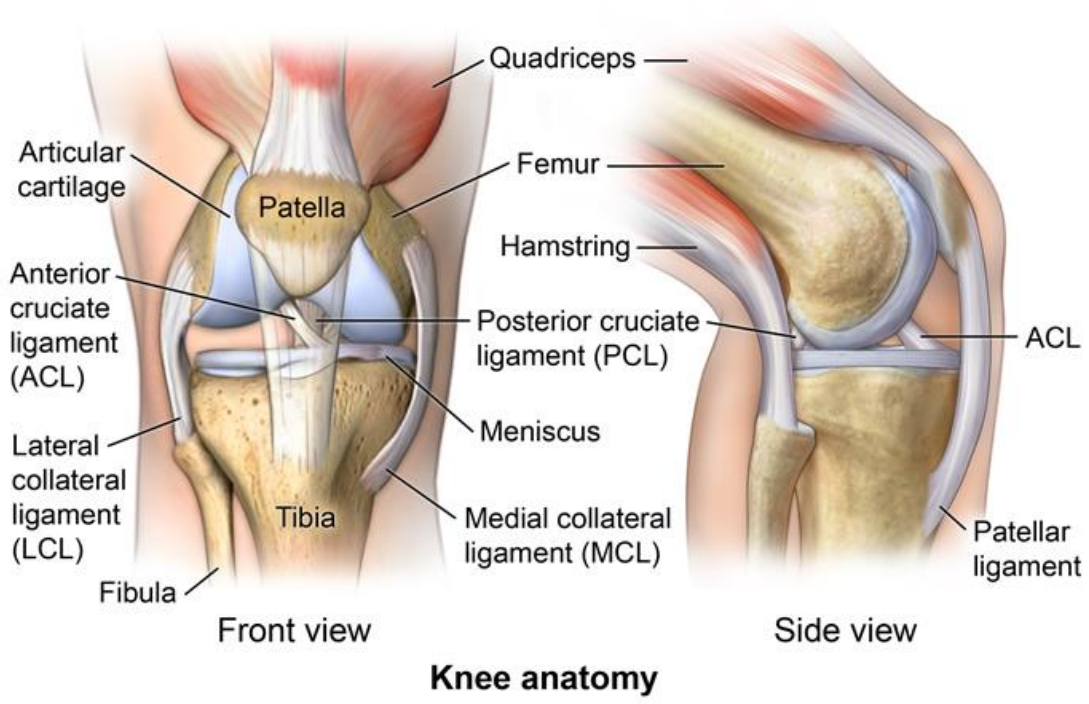

Figure 1.1: Anatomy of the knee joint [14].

Four main ligaments in the knee joint that connect the femur to the tibia are in charge of the main stability of the knee [4]. They are categorised into two types: cruciate ligaments and collateral ligaments [13]. The anterior cruciate ligament (ACL) and the posterior cruciate ligament (PCL) are located between the medial and lateral tibiofemoral articulations. ACL runs from the anterior part of the tibial intercondylar area to the posteromedial face of the lateral femoral condyle. It restrains excessive anterior displacement of the tibia and internal rotation in the knee joint. PCL extends from the posterior tibial intercondylar area to the lateral face of the medial femoral condyle. It is said to be twice as strong as the ACL and constrains excessive anterior movement of the femur during large knee flexion and pulls on the femur during knee extension, causing the femur to slide backwards as it is rolling forward [15-17]. The medial collateral ligament (MCL) is a flat and broad band that spans from the medial femoral epicondyle to the medial

side of the proximal tibia. It is the main stabiliser of the medial side of the knee, resisting large valgus stress and external rotation [15]. The lateral collateral ligament (LCL) runs from the lateral femoral epicondyle to the proximal end of the fibula [18, 19]. It stabilises the knee by constraining large varus movement [15, 16].

The patellar tendon extends from the quadriceps femoris tendon and connects the patella to the tibial tuberosity. The patella bone (sometimes called kneecap) slides around the distal and anterior surface of the femur during knee joint movements [13]. It restricts frictional contact between the tendon and the femur and enhances the extension capacity of the quadricep muscle by increasing the moment arm of the extensor [20].

The femur (thigh bone) which is the longest and heaviest bone in the human body is responsible for weight-bearing and stability of movements. The distal end of the femur, making up part of the knee joint, contains the medial and lateral condyles, separated by the intercondylar notch [21]. The tibia (shin bone) is the medial long bone of the lower leg, and it plays an essential role in weight-bearing. The proximal end of the tibia encapsulated in the knee joint contains the medial condyle, lateral condyle and intercondylar eminence. The medial and lateral condyles have flat surfaces called tibial plateaus that articulate with the femur [22].

1.2 Knee Osteoarthritis and Knee Replacement

Osteoarthritis (OA) is the most common type of joint disorder and the leading cause of pain and disability [23, 24]. It mostly happens in weight-bearing joints, e.g. knee joints [25]. This debilitating condition significantly affects a person's ability to perform daily activities and live independently [26, 27]. Increasing age, obesity and female gender are some common risk factors for OA [28]. With a rapidly ageing population and an increase in

obesity rates, it is estimated that the population suffering from OA in the UK will reach 17 million by 2030 [27, 29]. This affects both individuals' life quality and creates an increasing socioeconomic burden on healthcare systems.

The knee is the most commonly affected joint among OA [27], characterised by a breakdown of the articular cartilage at the ends of the bones [25]. This gradually leads to bone-on-bone contact, joint pain, joint stiffness, swelling and disability to conduct daily activities [30, 31].

Diagnosis of knee OA is usually conducted with radiographic examination [23, 31]. Preoperative weight-bearing anteroposterior (AP) radiographs, lateral radiographs, valgus-stress radiographs, and varus-stress radiographs are commonly taken to identify the amount of cartilage loss and the severity of OA [32]. Typical radiographic findings on patients with knee OA include narrowing of joint space, subchondral sclerosis, and formation of osteophytes (**Figure 1.2**) [23, 30, 31, 33].

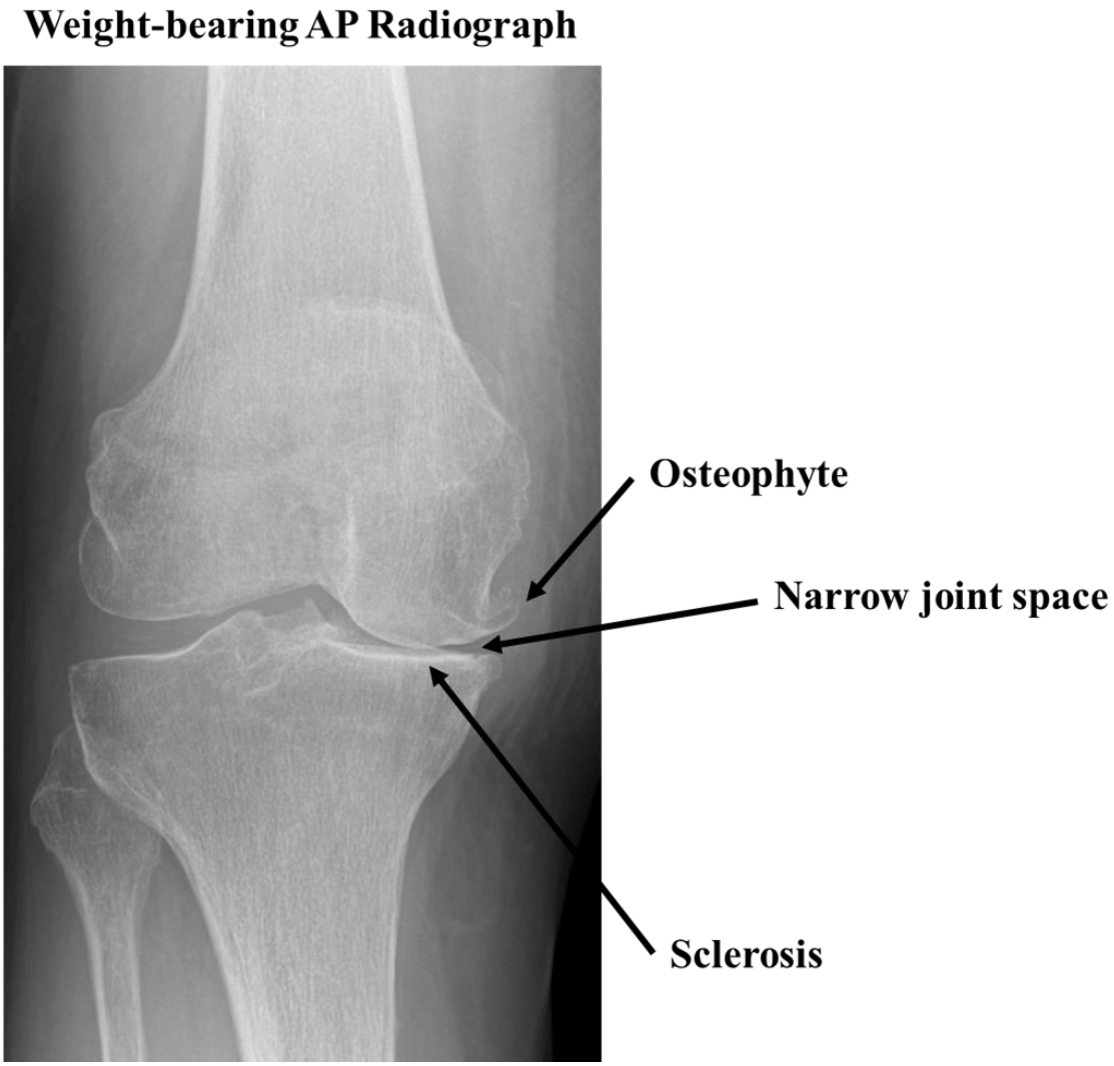

Figure 1.2: Weight-bearing radiograph of an anteromedial osteoarthritic knee. Subchondral sclerosis, formation of osteophytes and narrowing of joint space are shown.

There are three main types of treatment for knee OA: non-pharmacological, pharmacological, and surgical interventions [26, 27, 31]. Conservative non-pharmacological treatments mainly involve exercise, weight reduction, strengthening of surrounding muscles, or the use of orthotics like walking sticks or knee braces [23-25, 31]. Pharmacological treatments include the use of non-steroidal anti-inflammatory drugs, intake of supplements like glucosamine, or intra-articular injections of hyaluronic acid or corticosteroids [23-25, 31, 34]. If no improvement is seen after conservative treatments are

conducted, surgical interventions should be considered [24, 26, 27]. Knee replacement is an effective treatment for end-stage knee OA. This procedure removes the deteriorated articular surfaces of the joint and replaces them with implants [28]. The most widely used types of knee replacement are Total Knee Replacement (TKR), which replaces all articulation in the knee joint, and Unicompartmental Knee Replacement (UKR), which replaces only one compartment of the knee joint: medial tibiofemoral, lateral tibiofemoral or patellofemoral joint (**Figure 1.3**). Both procedures have demonstrated excellent long-term survival and functional outcomes [35]. Compared to TKR, UKR is less invasive [36], easier to revise when needed [37], displays a greater range of motion [38], shows less perioperative morbidity of stroke, thromboembolism, deep infection and myocardial infarction [36, 39, 40] and requires a shorter hospital stay and recovery time [41].

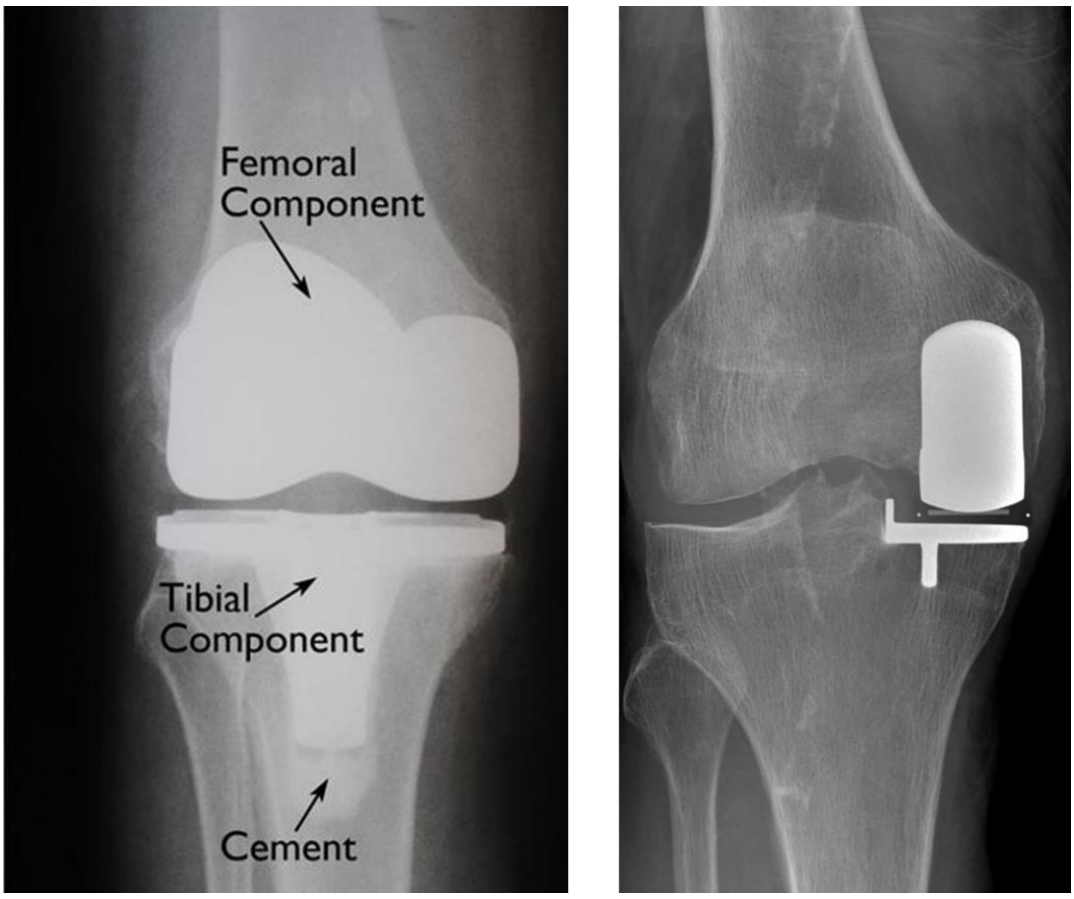

Figure 1.3: Post-operative anteroposterior (AP) radiographs of a Total Knee Replacement (TKR) (left, adapted from [42]) and a medial Unicompartmental Knee Replacement (UKR) (right).

As in most knee OA cases, the site of the lesion is limited to only one compartment of the knee joint, a great proportion of patients who undergo TKR are also eligible for UKR [11]. A previous study showed that nearly 50% of knee replacements conducted in the United Kingdom (UK) per year were also suitable for UKR and this could provide a cost saving of around £2k per case [43].

1.3 Cemented vs Cementless Fixation

Fixation of knee replacement components can be categorized into cemented fixation or cementless fixation (**Figure 1.4**). In cemented fixation, a cavity that is larger in volume than the fixation element on the implant is made in the hosting bone. Polymethylmethacrylate (PMMA) bone cement is inserted into the cavity to act as a grout between the bone and the implant. In cementless fixation, the fixation component on the implant is pressed into a cavity made in the host bone at an interference fit and seated with impaction. The difference in the dimension of the component and the dimension of the cavity is called interference.

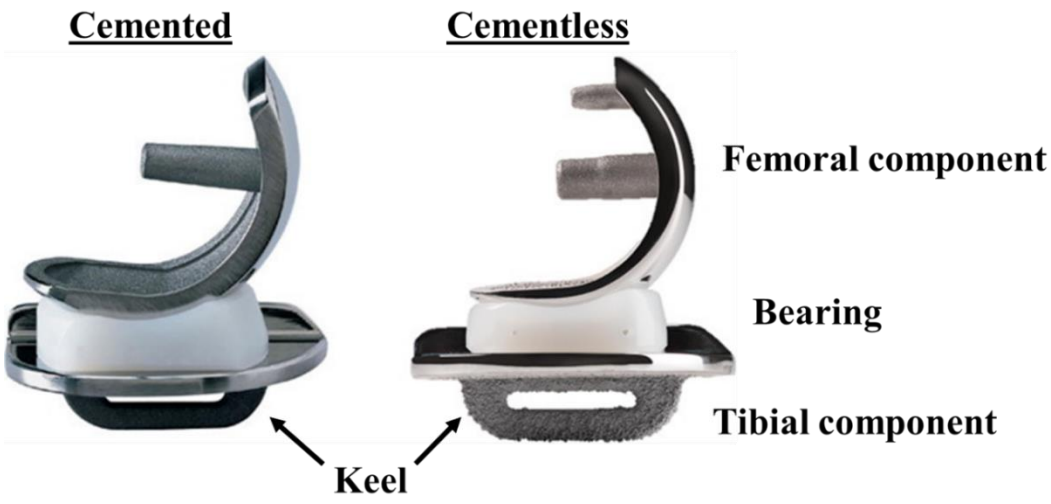

Figure 1.4: Cemented (left) and cementless (right) version of Oxford Unicompartmental Knee Replacement. Figure adapted from [44].

Interest in cementless TKR started to grow in the 1980s. Up to this point cemented TKR had been the gold standard and therefore the most common treatment for knee OA. Cemented TKR demonstrated excellent long-term functional outcomes and survivorship. However, in the early 1980s, there were increasing reports on implant failure and growing concerns about third-body wear from cement debris which might lead to osteolysis and implant loosening [45-47]. Cementless fixation was introduced to avoid cement-related complications while providing other potential advantages such as better bone preservation and better fixation through bone ingrowth to the porous implant surface [48]. However, the popularity of cemented TKR returned as poor early results and high rates of loosening were observed with cementless TKR [47]. Inadequate fixation and excessive micromotion were reported [47, 49]. National Joint Registry data shows that cemented TKR remains the most commonly performed primary knee procedure in the UK with excellent long-term outcomes. Cemented TKR accounted for 83% of all primary knee procedures in 2022 [50]. In contrast to the persistent popularity of its cemented counterparts, the use of cementless TKRs in the UK dropped from 3.6% of all TKR procedures to 2.5% between 2012 and 2022 due to concerns that arose from the high rate of failure [50, 51]. Nevertheless, the use of cementless TKR in the United States has increased from 2.2% to 20.5% in the past 10 years [52]. The advantages of cementless TKR are shorter operation time which reduces the risk of deep venous thrombosis and pulmonary emboli, and potential improvement in long-term fixation [46, 53]. Though cementless TKR is becoming less and less popular in the UK, the use of cementless/hybrid unicompartmental knee replacement (UKR) in the past decade increased, making up 14.8% of all UKRs in 2012 and 36.8% in 2022 [50].

To better facilitate bone ingrowth, the surface of the fixation elements on current cementless knee implant designs has a porous morphology to encourage bone ingrowth. These fixation components are also sprayed with a hydroxyapatite (HA) coating to further

enhance osseointegration. The porous surface also provides resistance to implant micromotion through frictional contact [46]. Introduction of better component designs and materials has motivated wider adoption of cementless fixation which offers several potential benefits: better bone stock preservation, reduced rate of cement-induced complications and better osseointegration on the implant surface [48, 54, 55]. Cementless UKR has demonstrated excellent long-term clinical and radiographic results, with a 10-year survival of 97% [56].

1.4 Primary and Secondary Stability of Implants

Implant stability can be categorised into primary stability and secondary stability. Primary stability (also called primary fixation) is the short-term fixation achieved by the mechanical response of bone after the component is seated in place [57]. As mentioned in **1.3,** primary stability of cemented implants is achieved through the use of PMMA bone cement which acts as a grout and anchors the implant to the host bone [58]. Primary stability of cementless implants comes from the stress induced in the periprosthetic bone when the component is press-fit into an undersized cavity with compression. This hoop stress and subsequent frictional force at the bone-implant contact interface hold the component in place [59]. It is achieved when the force dislodging the component is equal to or less than the force applied by the surrounding bone that holds it in place [60]. A satisfactory primary stability is the prerequisite for the secondary stability of the implant, which is achieved through osseointegration [61]. Secondary stability (also called secondary fixation) is the biological response of bone that anchors the implant to the bone. Implant stability is inversely related to its mobility and micromotion relative to periprosthetic bone [62]. Too much micromotion leads to the formation of fibrous tissue at the bone-implant interface in place of bone and

adversely affects the fixation of the components. This may further lead to aseptic loosening, failure and the need for expensive and more invasive revision operations [63]. The dominating stability shifts from primary to secondary stability at around 2-4 weeks postoperatively when new bone starts to form through remodelling (**Figure 1.5**) [57, 64].

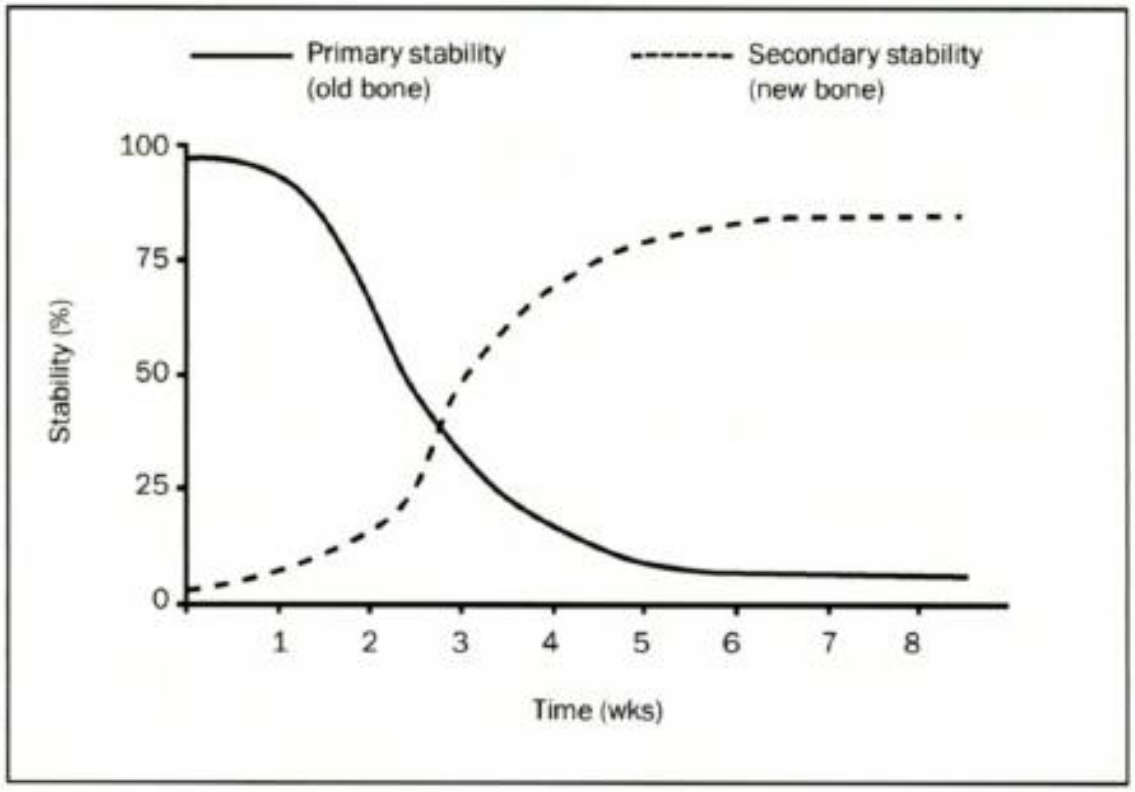

Figure 1.5: Onset of action of primary stability and secondary stability of implants. The dominating stability transits from the primary stability to the secondary stability at around 2-4 weeks post-operation [64].

Factors that affect a cementless press-fit component's primary stability are host bone quality, bone quantity [59, 61, 65, 66], surgical site preparation [67], implant geometry and design [68, 69], and the size of the interference [57, 70]. Previous studies concluded that cortical bone could provide implants with better support in the immediate post-operative bone-healing phase [59, 61, 65, 66]. Thus, implant location could be adjusted intraoperatively accordingly [67]. Higher surface roughness creates large friction at the surface and thus, resists micromotion of the implants [68]. The porous morphology also

gives a larger surface area which provides better fixation [69]. The size choice of interference is a trade-off between achieving an induced stress high enough to stabilize the implant and not creating excessive force that may cause bone fracture [57, 70, 71]. A previous study found an optimal interference range for the cementless tibial component of the Oxford Unicompartmental Knee Replacement with which satisfactory primary stability could be achieved without creating unnecessarily large stress in the bone thus not increasing the risk of fracture [72].

Factors that influence secondary stability are primary stability, bone remodelling and implant surface morphology [73]. As previously mentioned, satisfactory primary stability resists excessive micromotion which adversely affects osseointegration at the contact surface and creates fibrous capsules in place of bone [63]. Osseointegration of the implant to the bone is achieved by the remodelling of bone. Bone remodelling is a continuous cyclic process of bone formation and bone resorption and is an essential process for bone repair [74]. This process is controlled by the osteoclasts, which resorb old and damaged or obsolete bone, and osteoblasts, which lay down new bone where needed [75]. Early cementless designs used in the 1970s had smooth surfaces and showed poor outcomes due to high rates of loosening [76]. These prompted the development of better cementless prostheses. Porous coatings were introduced to increase the surface roughness of the implant to enhance the frictional contact between the bone and the implant [77]. The porous morphology not only improved the stability by creating larger interface friction but also by enabling mechanical interlocking between the bone and the implant through bone ingrowth [78]. HA coating is further applied to the porous surface to enhance osseointegration [79]. Thus, the optimal choice of surface roughness, bioactive coating material, interconnectivity of pores and pore size can potentially greatly improve the secondary stability of cementless implants [80].

1.5 Medial Oxford Unicompartmental Knee Replacement

Oxford Unicompartmental Knee Replacement (OUKR) is the most commonly used UKR implant in the UK [50] and medial OUKR is a treatment indicated for end-stage knee OA that is confined to the medial compartment of the knee joint. The main indication of medial OUKR is anteromedial OA (AMOA), while it is also an appropriate treatment for Spontaneous Osteonecrosis of the Knee (SONK) as long as no contraindication is observed (**Table 1.1**) [81]. OA in the medial compartment is generally limited to the anteromedial plateau where cartilage loss is seen on both femoral and tibial sides of the anterior part of the compartment. Full-thickness cartilage loss is best demonstrated on a varus-stressed AP radiograph (**Figure 1.6**) [32]. One key patient selection criterion of medial OUKR is that the lateral compartment should be intact with cartilage of full thickness. This is best shown by the presence of a normal joint space on a valgus-stressed AP radiograph (**Figure 1.6**) [32]. Though other contraindications, e.g. age, weight, and activity level, were suggested by Kozinn and Scott [82] for UKR in general, these do not apply to OUKR. OUKR can still be indicated as long as these specific criteria mentioned in **Table 1.1** are fulfilled [11].

Table 1.1: Indications and contraindications of Medial Oxford Unicompartmental Knee Replacement. ACL: Anterior cruciate ligament; PCL: Posterior cruciate ligament; MCL: Medial collateral ligament.

Indications	Contraindications
Full-thickness cartilage loss in the medial compartment showing bone-on-bone contact	Failure to show bone-on-bone contact in the medial compartment
Intact lateral compartment, showing preservation of lateral cartilage and meniscus	Lateral cartilage erosion
Functionally intact ACL	Damaged or absent ACL, PCL or MCL
Correctable intra-articular varus deformity	Not fully correctable intra-articular varus deformity
	Flexion deformity larger than 15 degrees, suggesting ACL deficiency
	Inflammatory arthritis
	Passive range of motion smaller than 100 degrees
	Mediolateral subluxation
	Deterioration in the lateral patellofemoral joint

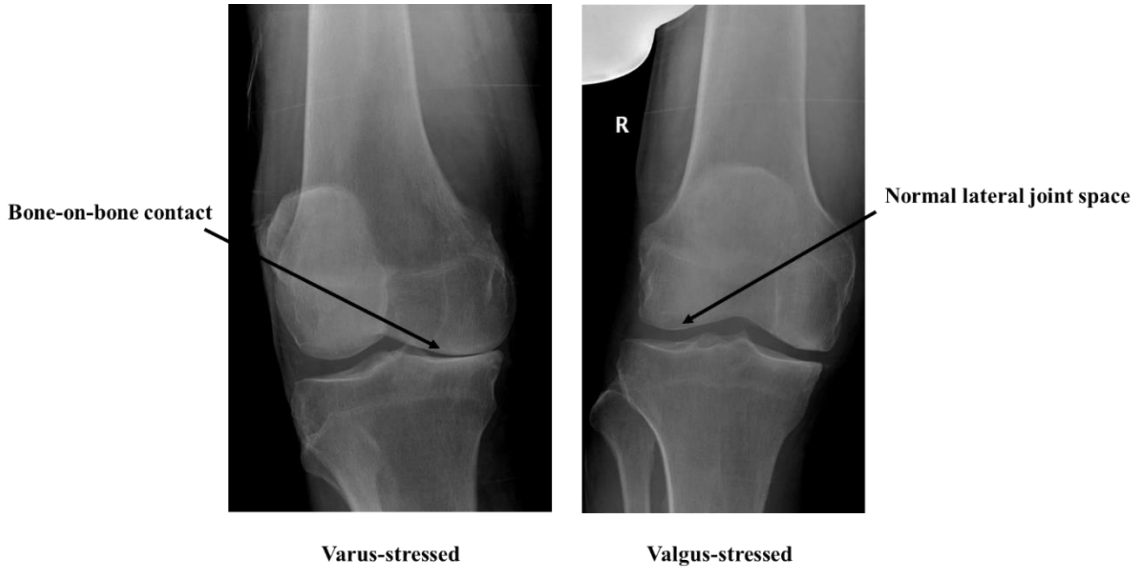

Figure 1.6: Varus-stressed (left) and valgus-stressed (right) anteroposterior radiographs of an osteoarthritic knee with anteromedial osteoarthritis. When a varus stress was applied to the knee, bone-on-bone contact was shown in the medial compartment. When valgus stress was applied, a normal joint space was shown in the lateral compartment.

Medial OUKR is comprised of a tibial component, a femoral component and a polyethylene meniscal bearing that is free to move between the two components (**Figure 1.4**). The mobile bearing has a spherical concave superior surface that is congruent with the spherical articular surface on the femoral component and a flat inferior surface that is in full contact with the superior surface of the tray during the full range of joint movement. These fully congruent contact surfaces minimise bearing wear and allow unrestricted bearing mobility [11].

The cementless version of OUKR was first introduced in 2004 to reduce the chance of unnecessary revision caused by misinterpretation of the radiolucency around cemented components. These physiological radiolucent lines at the bone-cement interface occurred in more than half of the cemented UKR cases [83] (**Figure 1.7**). Some cases were misinterpreted as loosening and sent for revisions when pain was reported, which were unnecessary [84]. The fixation of the cementless components is achieved through the interference fit at the keel, which is the vertical protrusion beneath the tibial tray, and the pegs on the femoral component.

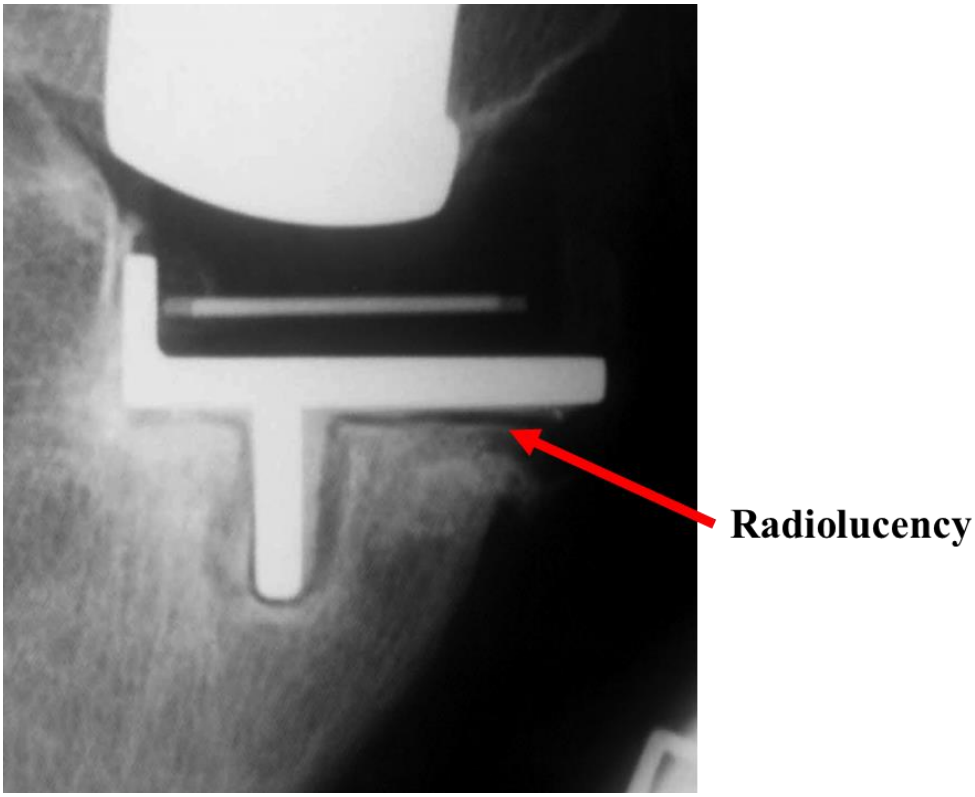

Figure 1.7: Radiograph showing a physiological radiolucent line beneath the tibial component. Figure adapted from [83].

Cementless OUKR has demonstrated excellent functional outcomes and a 14-year survival rate of 94% [85]. It also showed a lower risk of revision for aseptic loosening, pain and lysis which gave an overall risk of revision 24% less than that of its cemented counterparts at 10-year post-operation [84].

1.5.1 Complications of Cementless Medial Oxford Unicompartmental Knee Replacement

The most common reasons for revision in the first 1,000 consecutive cementless OUKRs performed through a minimally invasive approach by two designer surgeons (DWM, CAFD) at 15-year post-operation were lateral progression of OA, pain and bearing dislocation [85] (**Table 1.2**).

Table 1.2: Reasons for revisions in the first 1000 cementless Oxford Unicompartmental Knee Replacement (OUKR) cases performed by two designer surgeons (DWM, CAFD) at 15-year post-operation. OA: osteoarthritis.

	15-year revision rates of first 1000 cementless OUKR performed by designer surgeons
Lateral progression of OA	1.8%
Pain	0.9%
Bearing dislocation	0.8%
Deep infection	0.3%
Bearing fracture	0.2%
Tibial plateau fracture	0.2%
Femoral component loosening	0.1%

Two complications that are associated with primary fixation of the components are tibial component subsidence and periprosthetic tibial fracture. These two complications around the tibial component of OUKR will also be the focus of this thesis.

1.5.1.1 Tibial Component Subsidence

Tibial component subsidence is an uncommon complication after cementless medial OUKR. A few tibial components were found to have subsided during the early-recovery phase with pain reported [86-90]. The components typically subsided posteriorly and/or into valgus (**Figure 1.8**). Though in most cases, the components stabilised without further intervention in the first post-operative year, this complication caused pain and affected patients' mobility in the first few post-operative months [87, 88]. This abnormal radiographic phenomenon together with complaints about pain can lead to unnecessary

revision surgeries during the early recovery phase as in most cases the component will eventually become well-fixed without any surgical intervention. This also explains why no revision on this complication was seen at 15-yr post-operation (**Table 1.2**).

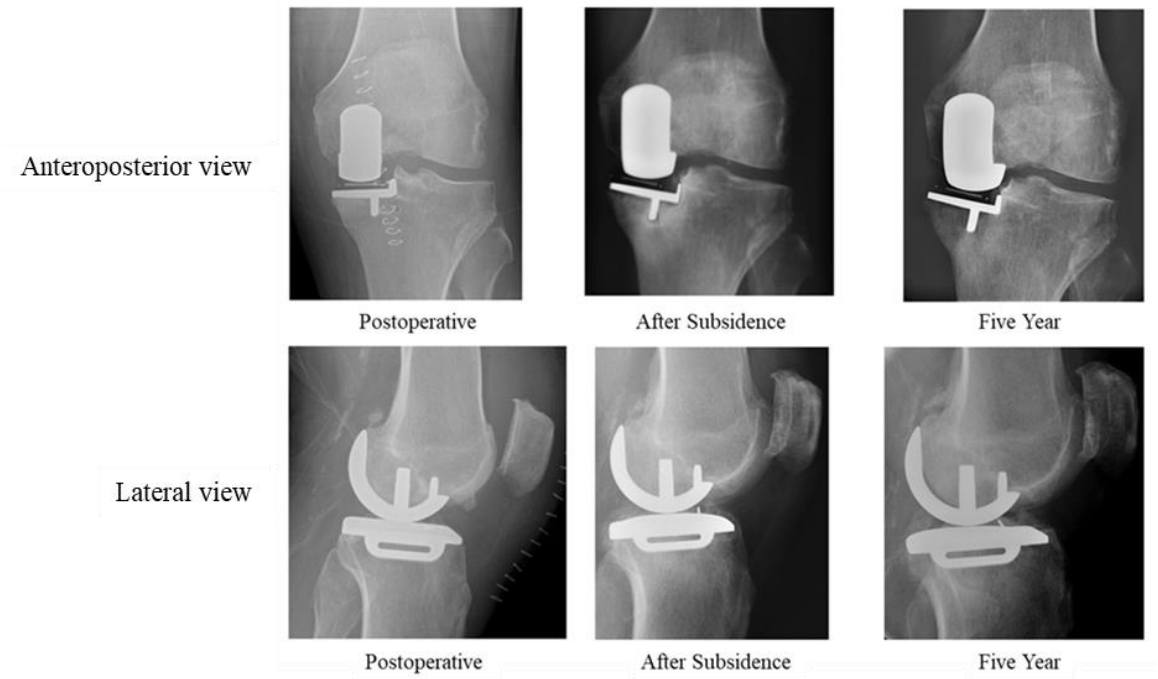

Figure 1.8: Anteroposterior and lateral radiographs of a subsidence case. The component subsided into valgus and fixated at the subsided position. Figure adapted from [87].

Secondary stability was successfully achieved in these patients as the component showed satisfactory fixation at one-year post-operation. However, primary stability was inadequate with the component tilting during the early recovery phase. What caused subsidence and what stopped it after a few months is unclear. One hypothesised cause of tibial component subsidence is the lateral placement of the femoral component relative to the tibial component which can occur when the vertical tibial cut is made too medial. This mismatch in the coronal alignment of the tibial and femoral components may lead to the impingement of the bearing onto the lateral tibial wall and elevate the compressive load beneath the lateral part of the tibial tray. The component tilts into valgus under the large compressive

load before the secondary stability is achieved. As the component continues to subside, the bearing moves away from the wall and impingement stops. The loading beneath the tibial tray becomes well-distributed again (**Figure 1.9**), bone remodelling continues, and secondary fixation is then achieved [87]. Kamenaga et al. [88] suggested that excessive external rotation of the tibial component may also lead to valgus subsidence. As the bearing moves back and forth during knee flexion and extension movement, excessive external rotation of the component might also lead to the impingement of the bearing on the posterior part of the lateral wall during deep flexion [91]. This creates a large compressive load under the posterior region of the tray lateral to the tibial keel and causes the component to tilt into valgus and posteriorly. This concentrated compressive load may cause the component to subside before adequate bone remodelling is achieved. Excessive vertical cut on the tibial plateau may also be a risk factor for subsidence [87]. This removes extra bone beneath the component and weakens the loading-bearing ability of the supporting bone (**Figure 1.10**).

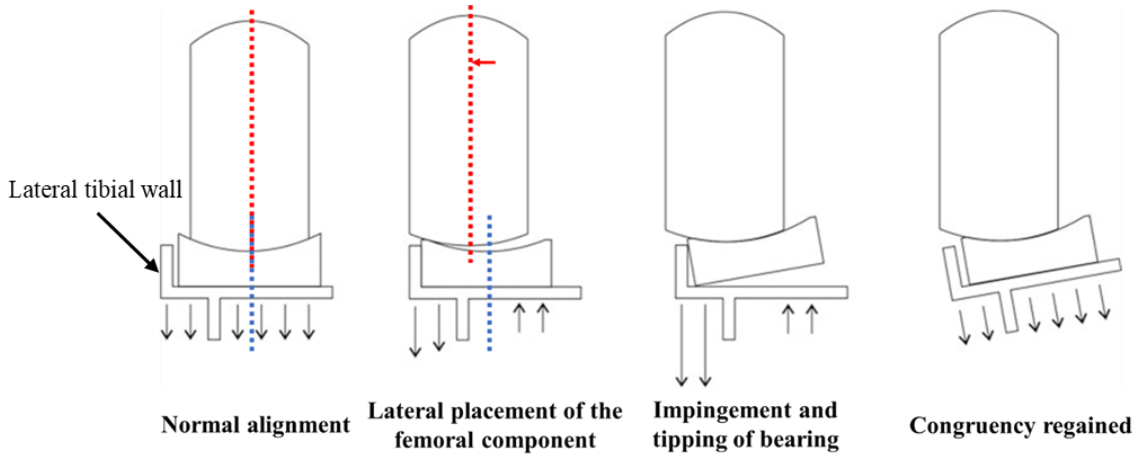

Figure 1.9: Proposed mechanism of tibial component valgus subsidence: lateral placement of the femoral component relative to the tibial component caused bearing impingement on the lateral wall of the tibial tray. This subsequently caused the bearing to tip and created a concentrated compressive load beneath the lateral side of the tibial tray. After the tibial component subsides into valgus, congruency between the bearing and the tibial component is regained. Figure adapted from [87].

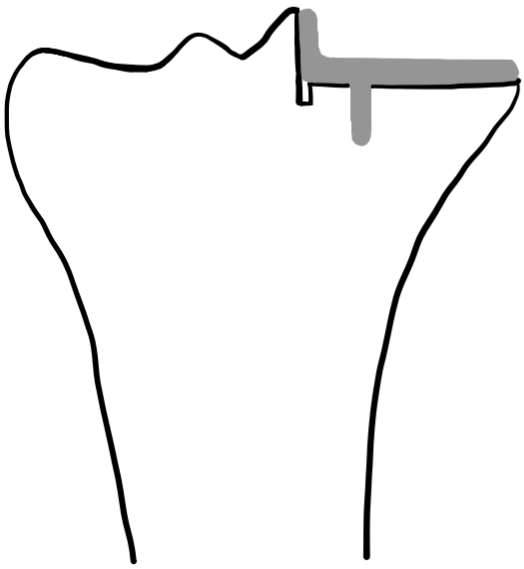

Figure 1.10: Vertical overcut potentially weakening the load-bearing ability of the bony support.

This complication will be studied in **Chapter 7**.

1.5.1.2 Periprosthetic Tibial Fracture

Periprosthetic fracture (PPF) is a severe complication after cementless medial OUKR with a revision risk of 0.26% reported in a 10-year study of 7,407 cementless OUKR cases from the National Joint Registry for England, Wales, Northern Island and the Isle of Man [84]. This was significantly higher than ($p = 0.01$) the revision risk of PPF in their matched cemented cohort (0.09%) [84]. Most PPF happened on the tibial side during the early post-operative phase (**Figure 1.11**). The interference fit around the keel and the impaction technique required to seat the component were considered the reasons that had caused these cases of early fracture around the tibial component [84, 92].



Figure 1.11: Anteroposterior radiograph of tibial periprosthetic fracture after a cementless medial Oxford Unicompartmental Knee Replacement [93].

PPF is a severe complication that usually requires revision to TKR with stem fixation [94], which is a more invasive procedure. This greatly affects patients' quality of life [92].

Despite the low revision rate reported in a Caucasian cohort (less than 1%), much higher rates (3.8% to 8%) have been reported in Asian cohorts [95-99]. One possible cause of the difference in the risk of revision for PPF between these two populations is the morphology of the tibial bone. Overhanging tibial plateau and small tibial size are two risk factors of PPF and these features are more commonly seen in Asian patients [92, 100, 101]. Also, as current OUKR components all have keels of the same depth regardless of their sizes, the

ratio between the dimension of the keel and the dimension of the medial tibial plateau is larger in patients that have small-size components implanted. These small patients showed a higher fracture rate [99]. A previous study reported that Asian patients generally used smaller components compared to Caucasian patients due to the difference in bone morphology [102]. Thus, Asian patients are at a higher risk of experiencing tibial PPF.

This complication will be studied with finite element analysis (FEA) in **Chapter 4** and **Chapter 5**.

1.6 Application of Finite Element Analysis in Orthopaedics

FEA was first used for orthopaedic applications in 1972 by Brekelmans et al. [103] to study the mechanical response of a femoral bone under various load cases. Finite element (FE) modelling has been extensively utilised as a powerful evaluation tool for various biomechanical purposes thereafter. The main uses of FEA in orthopaedics are implant design, pre-clinical testing and optimisation, mechanobiological analysis of tissue growth, and study of a particular musculoskeletal structure [104].

FEA around OUKR has been used to look at the effects of tibial component posterior inclination, varus-valgus inclination and coronal or sagittal alignment of the components on the stress in the bone [105-108], component design optimisation [109], and bone behaviour after implantation [110, 111].

Compared to traditional *in-vivo* and *in-vitro* studies, FEA has the advantages of:

- Being able to identify the isolated effects of specific variables (e.g. prosthesis design, surgical technique, lesion on skeletal structure) through sensitivity analysis without excessive expenses and time [112].

- Avoiding the uncertainties brought by variabilities in material properties between samples and being more repeatable [113].
- Being non-invasive when studying musculoskeletal structures compared to *in-vivo* experiments.

Despite these advantages, FEA should be used with care. Proper verifications and validations are essential to ensure that the model setup is valid and the results are meaningful [114].

FEA will be applied in the following chapters of this thesis to study clinical problems around cementless OUKR with the support of experimental validations.

1.7 Thesis Overview

1.7.1 Thesis Aim

The overall objective of this thesis is to investigate the causes of two complications of the cementless medial OUKR: periprosthetic tibial fracture and subsidence of the tibial component. This project was conducted as a combination of computational modelling and experiments.

The three aims of this thesis are:

1. Simulate the press-fit of cementless fixation components via computational modelling and understand the factors that contribute to adequate fixation (**Chapter 2** and **Chapter 3**).

2. Understand the causes of elevated risk of periprosthetic tibial fracture after cementless OUKR and investigate the optimal tibial component position in patients with smaller tibia, overhanging tibial plateau and/or tibia vara (**Chapter 4** to **Chapter 6**).

3. Determine the incidence and aetiology of OUKR tibial component subsidence via a systematic review and test the hypothetical mechanisms that might have led to subsidence via computational modelling (**Chapter 7**).

1.7.2 Thesis Structure

This thesis contains six experimental chapters that correspond to the three aims of this research mentioned in **1.7.1**.

In **Chapter 2**, the press-fit of cementless pegs of various dimensions and different surface morphology are simulated with explicit FEA. In **Chapter 3**, an experiment used to find the coefficients of friction (COFs) between various bone samples (plastic, animal and human cadaveric) and implants is presented. The results from this experiment are applied to the FE models in this thesis to improve their accuracy.

In **Chapter 4**, tibial PPF is studied with FEA. FEA of the fractured and unfractured tibias of two patients who experienced tibial PPF in one of their tibias after bilateral OUKR is presented. Relevant patient-related risk factors or surgical risk factors that might have caused PPF in these patients are reported. In **Chapter 5**, the influence of surgical errors in four directions (mediolateral position, proximal-distal position, internal-external rotation, and varus-valgus orientation) is investigated with FEA. Positioning of the implant that can potentially lower the risk of fracture is proposed. New keel designs that aim to lower the risk of fracture are also tested. **Chapter 6** evaluates whether changes in surgical techniques that can potentially lower fracture risk will bring adverse effects to other parts of the knee joint, i.e. cause lateral progression of OA.

Chapter 7 studies the incidence and aetiology of subsidence of cementless OUKR tibial components through a systematic review (Part A) and computational simulations (Part B) of hypothetical mechanisms that lead to subsidence.

Chapter 8 summarizes the key findings in the experimental chapters and explores possible directions for future work.

Chapter 2. Finite Element Analysis and Experimental Verification of Press-fit Component Primary Fixation

2.1 Introduction and Aim

Cementless implants are press-fit into bone. An undersized cavity that matches the shape of the fixation element on the implant is made in the bone. The difference in the dimensions of the cavity and the fixation element can be quantified by a value that is called interference. Load is required to establish press-fit fixation and it is often applied surgically by impacting the implant with a hammer. Primary fixation of cementless implants comes from the mechanical response of bone. It is achieved through the stress induced in the bone and the subsequent friction force at the interface which inhibits excessive early migration and micromotion. Secondary fixation of the implant is controlled by the biological response of bone and is achieved through bone ingrowth at the bone-implant contact interface [73, 115]. Successful primary fixation appears to be a prerequisite for a satisfactory secondary fixation. Excessive micromotion leads to the formation of fibrous tissue in place of bone at the contact interface and adversely affects long-term implant fixation [63, 116]. The maximum force required to push in the cementless component is commonly used as a measure of the risk of periprosthetic fracture. A higher push-in force implies more deformation and larger stress induced in bone which as a result weakens its load-bearing ability. The maximum force required to pull out the component is often used as a measure to assess primary fixation. This value determines the amount of component micromotion during early recovery and the bone healing stage. A lower pull-out force implies a lower force threshold that needs to be overcome to induce implant micromotion which may negatively affect fixation [72].

Finite element analysis (FEA) is a widely used tool when assessing the primary fixation of cementless component designs. When simulating the physical process of implant insertion, an implicit FE solver faces convergence problems due to nonlinearity in contact and material properties from extreme deformation in the host bone. Therefore, previous attempts at modelling press-fit implantation using FEA generally involved an interference fit contact algorithm with the resolution of an initial overclosure using an implicit solver [117, 118]. Bone is commonly modelled as a heterogeneous linear elastic or linear elastic-plastic material with elastic modulus assigned based on the bone density derived from pre-operative Computed Tomography (CT) scans of the bone. This method has a number of disadvantages and limitations. Firstly, it does not give an estimation of the push-in force as the physical insertion process is not simulated. Secondly, it cannot account for any material removal at the bone-implant interface which occurs in both implant insertion and extraction phases.

Bone, with a complicated cellular microstructure, shows asymmetric behaviour under compression and tension [119]. Their properties also vary greatly among individuals and resection sites [120]. This again creates large complexity when developing computational models of implant press-fit for the assessment of primary fixation. Analogues of trabecular bone, 20 pounds per cubic foot (PCF) polyurethane (PU) foam as an example, are frequently used to obtain insight into the effects of design and surgical factors on primary fixation [72, 121, 122]. The use of PU foam is also more accessible and controllable during benchtop experimental validations of the computational models. Thus, the press-fit behaviour of implants was modelled in PU foam rather than in trabecular bone in this chapter. PU foam is a homogeneous material and exhibits less variability compared to real bone. Furthermore, access to pre-operative CT scans from which the elastic modulus of bone can be calculated is not guaranteed for each individual. Thus, PU foam acting as an

analogue to human trabecular bone, rather than the real human or animal bone, was used in this study.

In a previous attempt that explicitly modelled cementless conical implant press-fit with FEA, the complexity of bone and its deformation necessitated the use of a customised damage model and a VUMAT subroutine [123]. The objective of this chapter was to develop a simple FE model that could simulate cementless implant press-fit and provide insights into their level of primary fixation. The press-fit of titanium pegs, a widely used fixation component in orthopaedics having a geometry simpler than the keel of the OUKR tibial component was simulated with an axisymmetric FE model. Push-in-pull-out (PIPO) of pegs of two levels of surface roughness (smooth/porous) and diameters (5.7/4.7 mm) were studied with this model (**Table 2.1**). To reflect the level of primary fixation after implantation, the model should be able to predict the maximum push-in forces and maximum pull-out forces of cementless implants in plastic bone analogues with good accuracy. The method was validated by comparing the results from the models to the corresponding experiment conducted in a PCF20 plastic bone analogue. The model should require minimal parameter inputs and should provide solutions within a reasonable time so that it can be further optimised and enhanced for clinical applications.

Table 2.1: Studies conducted. Three pegs of two different levels of surface roughness and two diameters were studied. FEA: finite element analysis. PIPO: push-in-pull-out.

Peg Diameter / Surface Roughness	5.7 mm	4.7 mm
Smooth	FEA vs Sawbones PIPO experiment of a 5.7 mm smooth peg	FEA vs Sawbones PIPO experiment of a 4.7 mm smooth peg
Porous		FEA (using mean/max peg diameter) vs Sawbones PIPO experiment of a 4.7 mm porous peg

2.2 Method

The push-in-pull-out (PIPO) of pegs was modelled with an axisymmetric model in ABAQUS/CAE (Dassault Systèmes, France). Excess distortion of plastic bone analogue elements during peg insertion can lead to failure in convergence and make it technically difficult and time-consuming to simulate the physical press-fit process with an implicit solver. Therefore, an explicit solver was used to avoid this issue.

Three straight titanium pegs each with a hemispherical tip and a circular cross-section were modelled: a 5.7 mm diameter smooth peg, a 4.7 mm diameter smooth peg and a 4.7 mm diameter porous peg as the thickness of a clinically used porous coating is approximately 0.7 mm [124].

A plastic bone block (Sawbones Solid Rigid PU Foam, PCF20, #1522-03, Malmö, Sweden) which acted as an analogue for trabecular bone with relatively predictable homogeneous material properties was modelled. The chosen density (PCF20) is most commonly used for biomechanical testing due to its porous structure and material behaviour similar to those of trabecular bone [72, 121, 122].

2.2.1 Model Geometry and Boundary Conditions

Due to the axisymmetric nature of the peg, a 2-dimensional (2D) axisymmetric model was built to save computational costs. A plastic bone cylinder of 22.45 mm in diameter and 35.00 mm in height was modelled. Holes of different diameters were modelled to simulate press-fit at surgically-relevant diametral interferences of 0.68, 0.70 and 0.92 mm with the 5.7 mm smooth peg. A smaller interference of 0.45 mm and a larger interference of 1.06mm were also tested. Interference of 0.60 mm was tested with the 4.7 mm smooth peg and the 4.7 mm porous peg. The porous peg had a mean diameter of 4.7 mm and a maximum diameter of 4.8 mm that considered the maximum height of the asperities on the surface.

The PIPO of a 4.8 mm porous peg was also modelled at an interference of 0.70 mm, taking the effect of the asperities on the rough surface into account. All holes were 15.0 mm in depth along the long axis of the cylinder. The plastic bone was constrained in the axial direction at the bottom edge and was constrained in the radial direction on the sidewall. All other degrees of freedom were set free. The peg was pushed into the hole by 9.0 mm and was pulled out completely through a vertical displacement applied to the top of the peg. All other degrees of freedom of the peg were constrained to avoid rigid body motion (**Figure 2.1**).

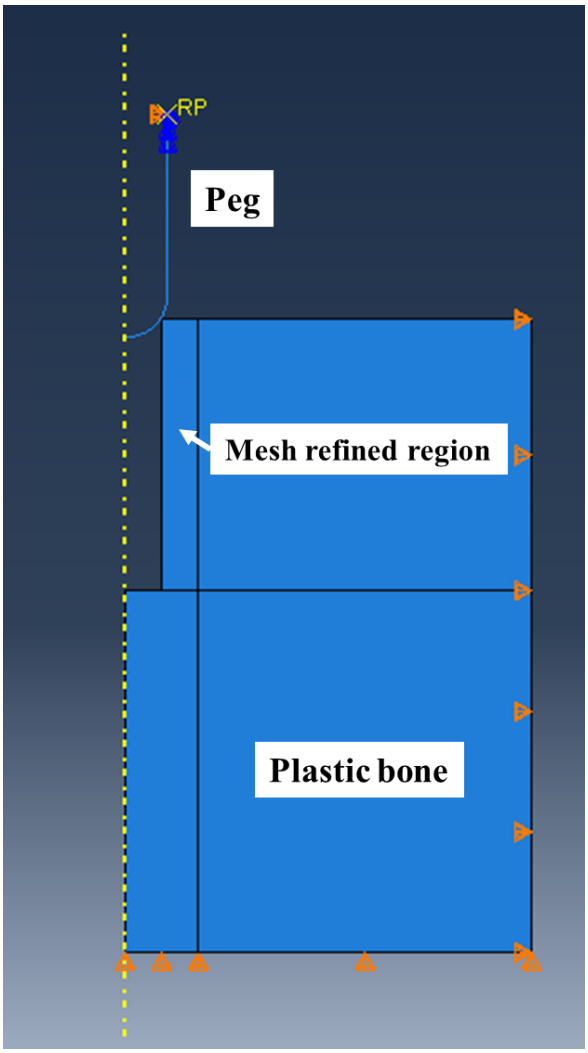

Figure 2.1: Axisymmetric finite element model setup.

2.2.2 Material

Table 2.2 lists the material properties of the titanium peg and the plastic bone simulated in the model [125, 126]. The Young's modulus of the plastic bone was obtained from a uniaxial compression test on the Sawbones PCF20 foam done by a fellow DPhil student (David Heath).

Table 2.2: Material properties of titanium pegs and plastic bone block.

	Young's modulus (MPa)	**Poisson ratio**
Titanium Peg	Rigid body	Rigid body
Plastic bone	160	0.3

As the elastic modulus of the titanium peg was several orders of magnitude larger than that of the plastic bone block, it was modelled as rigid. The geometry of the rigid peg was represented with lines. The plasticity of the plastic bone block was characterized by the material curve derived from the uniaxial compression test results (**Figure 2.2**). The curve shows the true stress and true plastic strain values derived from the average stress-strain data from six test repeats. It was modelled as a deformable material.

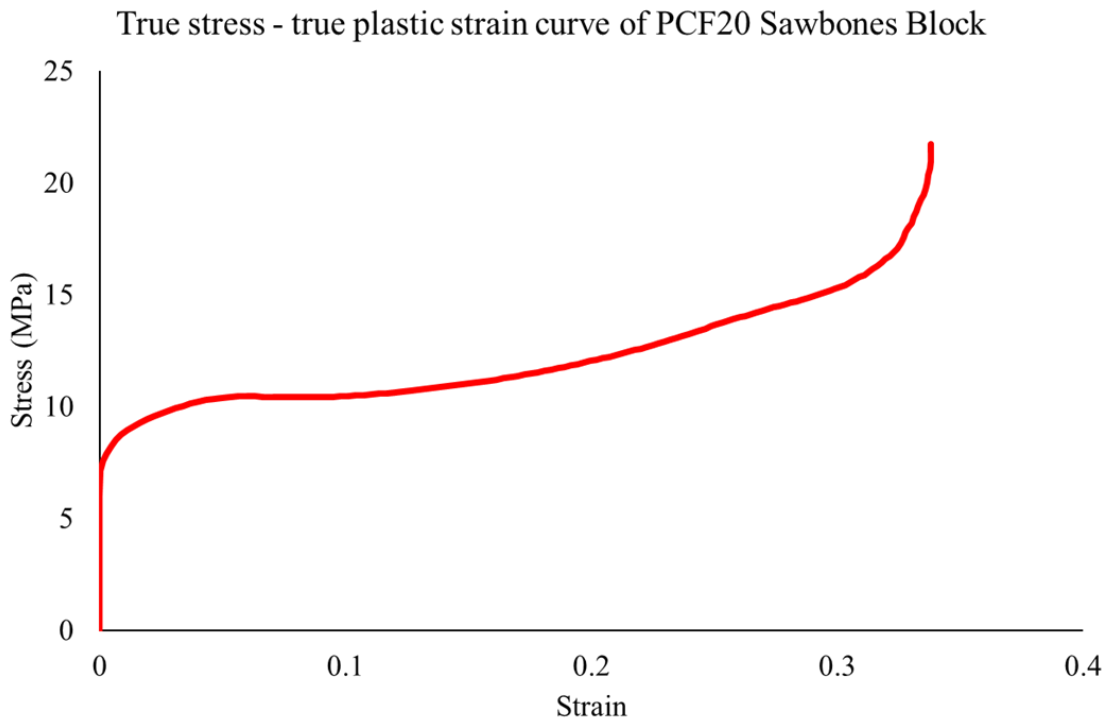

Figure 2.2: True stress-true plastic strain curve of the Sawbones foam [127]*. The upturn value is 0.31 at which the gradient of the curve greatly increases. PCF: pounds per cubic foot.*

Press-fit at interferences above a certain level causes both extreme deformation and removal of the material at the interface [128, 129]. Large distortion of elements during insertion leads to failure in analysis convergence. The ductile damage feature in ABAQUS was used to implement element deletion which could overcome the convergence issue that occurred with the implicit solver at high interferences. Element deletion combined the effects of material deformation and machining in the plastic bone near the interface. The removal of elements was controlled by the fracture strain, which was the threshold plastic strain value above which the element would be deleted. The fracture strain was tuned using results from the 5.7 mm smooth peg PIPO experiment. Fracture strain values of 0.31, 0.28 and 0.34 (-/+10% of the upturn value, 0.31) were tested with the 5.7 mm smooth peg. The maximum push-in forces and the maximum pull-out forces required in the simulations when each fracture strain was used were compared to those from the experiments. The value that gave results closest to the experiments was then applied to simulate the PIPO of

4.7 mm smooth and porous pegs at an interference of 0.60 mm and the PIPO of the 4.8 mm porous peg at an interference of 0.70 mm. PIPO of the smooth 5.7 mm peg at a higher interference of 1.06 mm and a lower interference of 0.45 mm were also tested with this fracture strain value.

2.2.3 Mesh

The plastic bone was meshed with axisymmetric elements (CAX4R). The mesh was refined in the region 2 mm radial from the hole surface. Mesh convergence studies were conducted at each interference for the 5.7 mm smooth peg: the change in the maximum push-in and pull-out force as the mesh size was gradually decreased was monitored. The mesh was considered to be converged when these measures were 5% of the previous values. The element sizes used for the interference of 0.68, 0.70, 0.92 and 1.06 mm were 0.05, 0.05, 0.06 and 0.05 mm, respectively. For interference of 0.45 mm, the pull-out force failed to converge to within 5% when the mesh size was reduced from 0.06 to 0.03 mm. As the model required excessive analysis time when 0.03 mm elements were used, elements of 0.04 mm were chosen. For the simulations of the 4.7 mm smooth peg, the percentage change was less than 5% when elements of 0.03 mm were used. The same mesh size was used for the porous peg. The wall of the peg was meshed with rigid axisymmetric elements (RAX2) of 0.5 mm and the tip was meshed with elements of 0.2 mm to capture the curvature.

2.2.4 Contact

A frictional contact was defined between the peg and the plastic bone block. The COFs applied were found from an experiment that is described in **Chapter 3**. The COFs between smooth implant and plastic bone block, and rough implant and plastic bone block were 0.27 and 0.56, respectively. An eroding surface contact was defined at the bone-implant interface

to constantly renew and update the contact surface so that a frictional contact was set up between the peg and the new plastic bone surface after machining.

Insertion of the porous peg using both the geometry with the mean diameter (4.70 mm) and the geometry with the maximum diameter (4.80 mm) of the peg was modelled. The same COF of 0.56 was used in both simulations.

2.2.5 Experimental Validation

To examine the accuracy and reliability of the FE model, a PIPO experiment on Sawbones was conducted (**Figure 2.3**). Straight 3-dimensional (3D)-printed titanium pegs (Cp-Ti Grade 2, AP&C, Saint-Eustache, Canada) with a circular cross-section and a hemispherical tip were pushed in and pulled out from pre-drilled holes in a Sawbones plastic bone block (Solid Rigid PU Foam, PCF20, #1522-03, Malmö, Sweden) using the DARTEC HC-10 servohydraulic material testing machine (ZwickRoell Ltd, Herefordshire, UK) and FSB-01 S-beam load cell (maximum load: 2.5 kN, Force Logic, Berkshire, UK). Tests with two peg designs were conducted: a 4.7 mm diameter smooth peg and a 4.7 mm diameter porous peg, as in the FE models (**Figure 2.4**) with each test repeated three times (n=3). The diameter of the 3D-printed porous peg simulated in the model was measured with a vernier calliper (500-196-20, Mitutoyo, Kawasaki, Japan) and the maximum diameter accounting for the height of the asperities was 4.8 mm. Results for the 5.7 mm diameter smooth peg were obtained from a previous test conducted by David Heath.

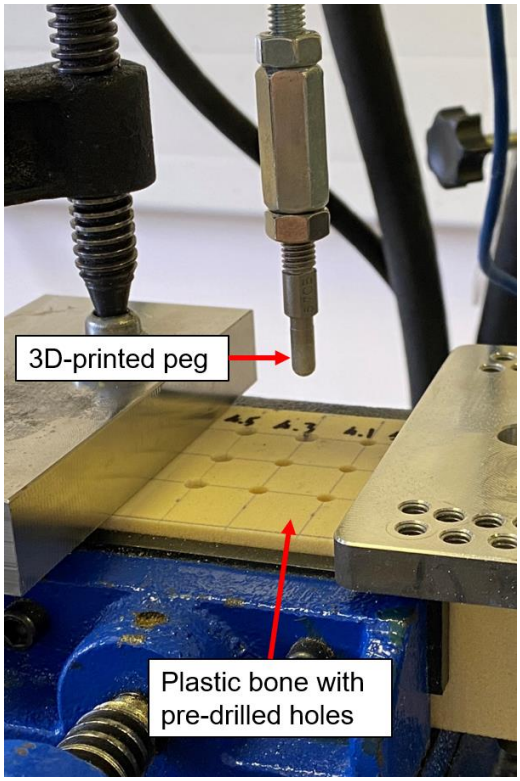

Figure 2.3: PIPO test experimental setup.



Figure 2.4: Pegs of smooth (left) and porous (right) surface finish.

Holes were prepared using a pillar drill (RS Pro Bench Pillar Drill, RS Components Ltd, Northants, UK). All holes were 15 mm deep, and the diameters corresponded to the

interferences tested in the FE simulations mentioned above. The test was repeated six times with each 4.7 mm peg at 0.6 mm interference.

The peg was aligned axially to the hole manually before each test. It was then pushed in by 9.0 mm at a speed of 10 mm/min and completely pulled out at the same speed under displacement control. The plastic bone block was constrained in the anteroposterior direction and the vertical direction. The vertical forces applied by the load cell were recorded at a frequency of 250 Hz.

2.3 Results

Results on the 5.7 mm diameter smooth peg were obtained from previous PIPO tests done by another member of the research group. Mean values of the maximum push-in and maximum pull-out forces at each interference were calculated. Results from the FE models when different fracture strain values were applied were compared to the experimental results in terms of percentage error (**Table 2.3**).

When a fracture strain value of 0.31 was defined, the differences in the forces from FEA and experiments in the surgical-relevant interference range (0.6-0.9 mm) were the smallest. The force-displacement curves from the PIPO experiment and the curves from the simulations with a fracture strain of 0.31 were plotted (**Figure 2.5** – **Figure 2.7**). The force gradually increased in the negative direction as the peg was pushed in by 9.0 mm. Then the force reached a maximum positive value which marked the maximum pull-out force while the peg was extracted from the hole. The gradients of the push-in force-displacement curve and the gradient of the pull-out force-displacement curve from the simulation (red) were similar to those from the experiments (grey).

Table 2.3: Maximum push-in and pull-out forces from experiments and finite element models of the 5.7 mm smooth peg with fracture strain (FS) of 0.28, 0.31 and 0.34. FS of 0.31 gave results that were closest to the experiments.

Interference (mm)		Push-in (N)	% error	Pull-out (N)	% error
0.45	**Experiment**	178.4 (SD = 4.9)	-	148.5 (SD=6.1)	-
	FS = 0.31	261.1	+46.4%	180.3	+21.4%
0.68	**Experiment**	244.5 (SD = 8.0)	-	179.5 (SD = 4.7)	-
	FS = 0.28	283.0	+15.7%	175.1	-2.5%
	FS = 0.31	289.6	+18.4%	172.8	-3.7%
	FS = 0.34	357.4	+46.2%	204.4	+13.9%
0.70	**Experiment**	270.2 (SD = 23.8)	-	184.6 (SD = 14.1)	-
	FS = 0.28	291.1	+7.7%	180.1	-2.4%
	FS = 0.31	297.8	+10.2%	179.2	-2.9%
	FS = 0.34	362.3	+34.1%	219.0	+18.6%
0.92	**Experiment**	349.4 (SD = 15.3)	-	206.9 (SD = 9.7)	-
	FS = 0.28	274.5	-21.4%	135.1	-34.7%
	FS = 0.31	344.0	-1.5%	192.7	-6.9%
	FS = 0.34	357.8	+2.4%	174.9	-15.5%
1.06	**Experiment**	373.9 (SD = 18.1)	-	201.1 (SD = 7.5)	-
	FS = 0.31	320.2	-14.4%	155.0	-22.9%

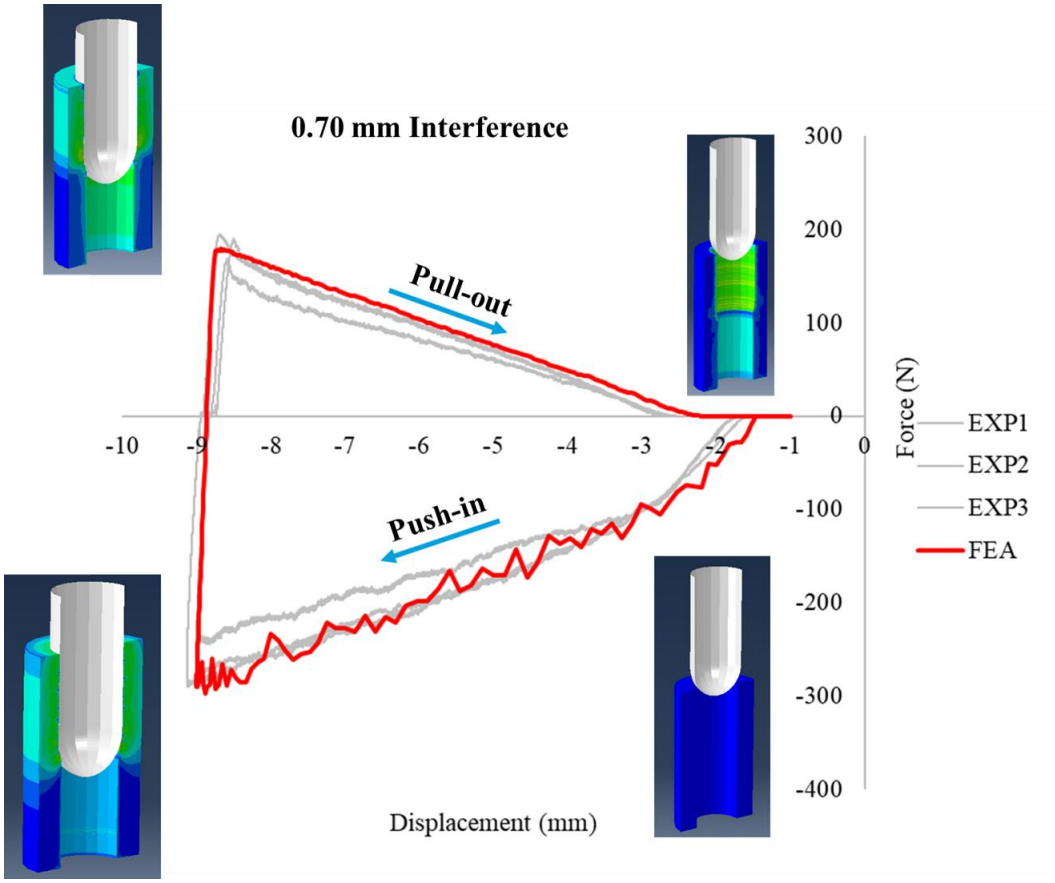

Figure 2.5: Force-displacement curves from experiments (grey) and finite element analysis (FEA) (red) of the PIPO of the smooth 5.7 mm peg at 0.70 mm interference with the fracture strain of 0.31 (red).

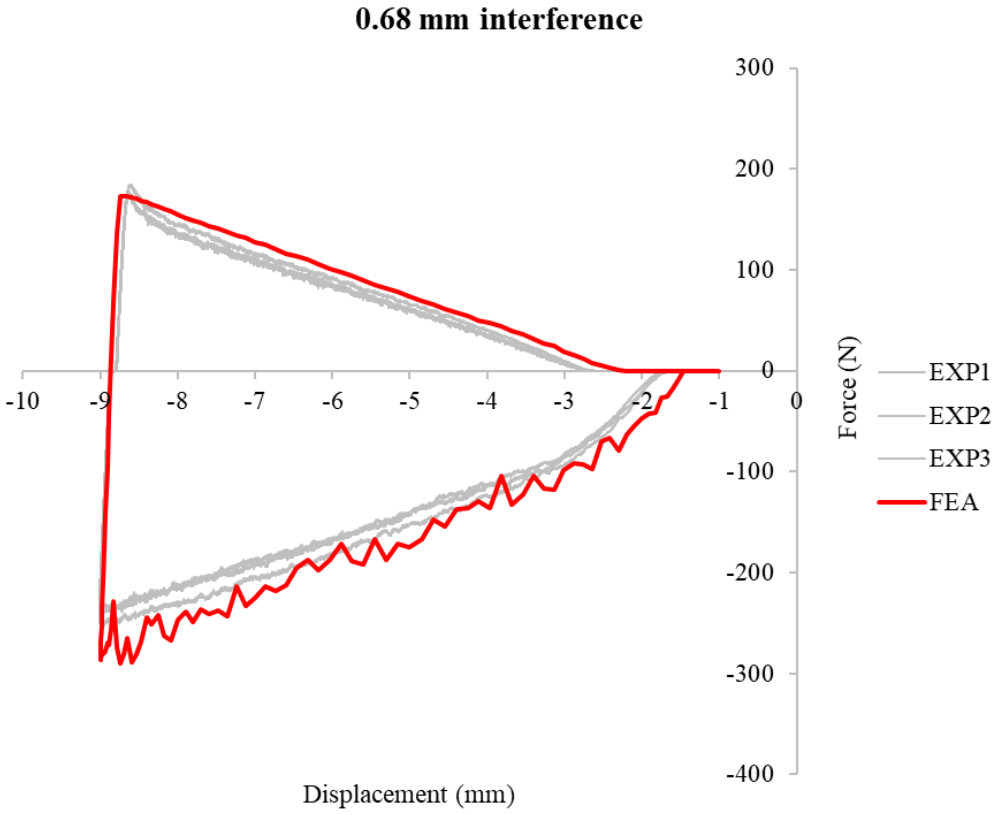

Figure 2.6: Force-displacement curve from experiments (grey) and finite element analysis (FEA) (red) of the PIPO of the smooth 5.7 mm peg at 0.684 mm interference with the fracture strain of 0.31.

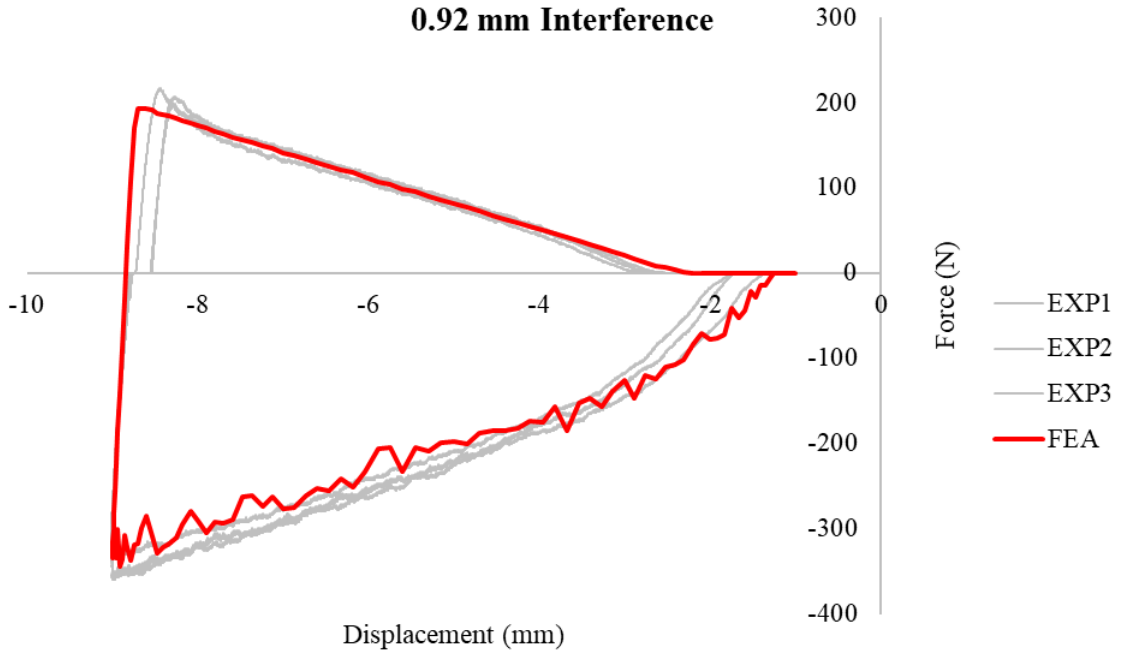

Figure 2.7: Force-displacement curves from experiments (grey) and finite element analysis (FEA) (red) of the PIPO of the smooth 5.7 mm peg at 0.92 mm interference with the fracture strain of 0.31.

When the same fracture strain value of 0.31 was used to simulate the PIPO of the 4.7 mm diameter smooth peg, the force-displacement curve from the FE model again corresponded well to the experimental results (**Figure 2.8**). The progression of force with displacement in the simulation and the experiments showed similar trends and the percentage error on the maximum push-in force and the maximum pull-out force were both within 14% (**Table 2.4**).

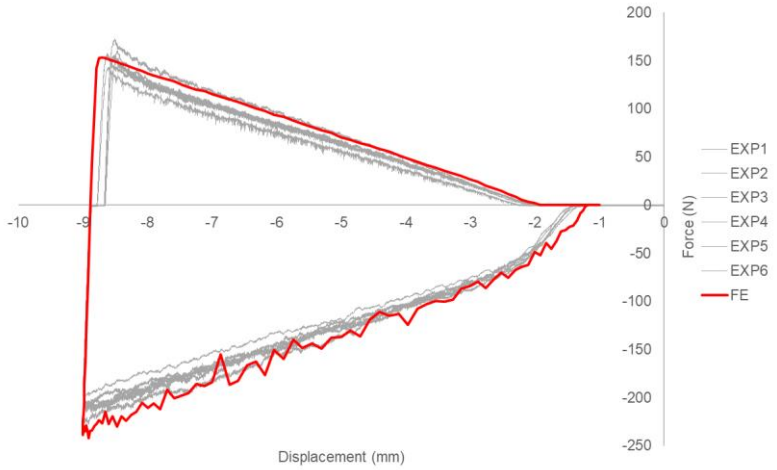

Figure 2.8: Force-displacement curve at 0.6 mm interference for the smooth 4.7 mm peg.

Table 2.4: Maximum push-in and pull-out forces for the 4.7 mm smooth and 4.7 mm porous peg from experiments and finite element (FE) models.

	Push-in			Pull-out			PO/PI ratio	
	Experiment (N)	**FE (N)**	**% error**	**Experiment (N)**	**FE (N)**	**% error**	**Experiment**	**FE**
4.7 mm smooth	212.7 (SD = 9.3)	241.2	+13.4%	157.8 (SD = 9.6)	153.4	-2.8%	0.742	0.636
4.7 mm porous	198.0 (SD = 3.8)	225.1	+13.7%	88.6 (SD = 6.6)	117.0	+32.1%	0.447	0.520
4.8 mm porous	198.0 (SD = 3.8)	216.6	+9.4%	88.6 (SD = 6.6)	101.6	+14.7%	0.447	0.469

As found in the experiment, the 4.7 mm porous peg showed a maximum push-in force and a maximum pull-out force lower than those of the 4.7 mm smooth peg when either the

mean diameter or the maximum diameter of the peg was used (**Figure 2.9**). The ratios between the pull-out force and the push-in force of the porous peg were smaller than that of the smooth one, which was shown in the experiment. When the diameter of the porous peg in the model was 4.7 mm, which was the mean diameter, the pull-out force was overestimated by 32%. When the diameter of the porous peg in the model was 4.8 mm which accounted for the height of the asperities on the rough surface, the percentage error in the push-in force was +9.4% and for the pull-out force, it was +14.7%. Using the maximum diameter of the porous peg gave both a maximum push-in force and a maximum pull-out force closer to the experimental results. However, a clear deviation was shown between the force-displacement curves from the experiment (red) and from the experiment (grey) (**Figure 2.10**).

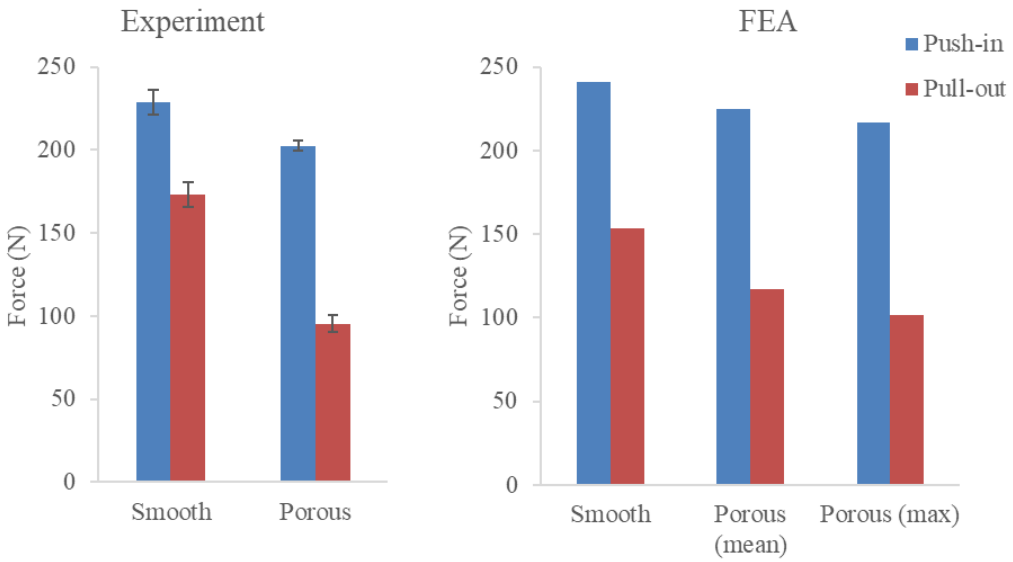

Figure 2.9: Push-in and pull-out forces from the experiment with a 95% confidence interval (left) and from finite element analysis (FEA) (right) of the smooth and porous pegs of 4.7 mm diameter. The porous peg was modelled with mean diameter (4.7 mm) and maximum diameter (4.8 mm).

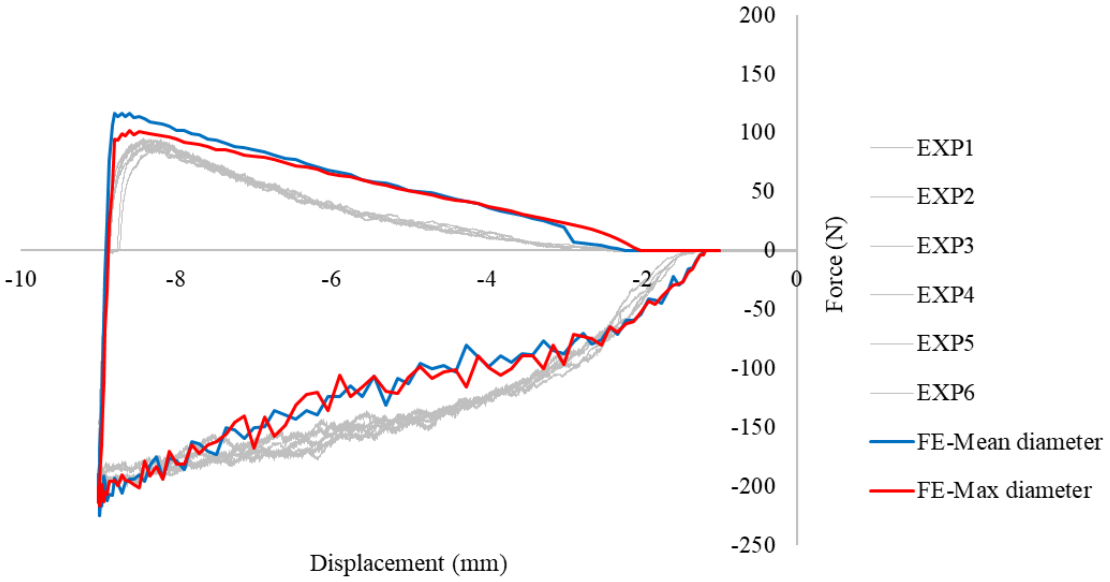

Figure 2.10: Force-displacement curve for the porous 4.7 mm peg. FEA simulation was conducted with both the mean diameter (at 0.60 mm interference) and the maximum diameter (at 0.70 mm interference) of the peg.

2.4 Discussion

This chapter investigated a method of modelling the press-fit of cementless fixation components with explicit FEA. FE modelling of cementless component press-fit is complex as 1) bone has a complicated cellular microstructure, shows non-linear and asymmetric behaviours under compression and tension [119], and is subject-specific, and 2) it is computationally difficult to simulate the physical process of press-fit due to nonlinearity from the large deformation in the periprosthetic bone at high interference. Therefore, this study focused on simplifying the computational simulations of complex material responses during press-fit with a single modelling technique.

An explicit solver was chosen to overcome the convergence issue that appears with an implicit solver when dealing with nonlinearity from large material deformation. The technique of element deletion was used to model the combined bone damage effect rather than attempting to capture individual responses under press-fit. Trabecular bone analogue

(PCF20 Sawbones foam), a homogeneous material that exhibits less variability compared to real bone was used to minimise the impact of complicated material definitions. It goes through three phases under compression: elastic stage, plateau stage, and densification stage [130]. In the plateau phase which is the part of the curve with small gradients in **Figure 2.2**, the material goes through plastic deformation and the cellular structure collapses. Once the cells in the cellular foam cannot collapse further (e.g. when the upturn plastic strain value of the curve in **Figure 2.2**, 0.31 is reached), the material starts to go through densification. The stress increases rapidly with little increase in strain. This behaviour was typically captured with damage models that required complex material definitions or with micro-FE models built from micro-CT scans, denoting the microstructure of the material [123, 131].

As an efficient alternative to introducing complicated material definitions of the plastic bone foam, element deletion was implemented to account for the combining effect of plastic bone deformation and removal at the contact surface under press-fit. This chapter demonstrated that using a strain-based element deletion criterion to simulate the press-fit of metal pegs into a plastic bone analogue with an explicit solver, a satisfactory prediction of the maximum push-in and maximum pull-out forces could be derived.

Results close to experimental findings were achieved. A 5% change was used as the criterion for mesh refinement, and these 5% changes corresponded to one to two standard deviations from the mean values in the experimental results. With the fracture strain of 0.31, which correlates to the upturn value on the true stress-true strain material curve of the PCF20 Sawbones foam, the results from the FE models were in good accordance with the experiment at surgically-relevant interferences of 0.6-0.9 mm for smooth pegs. The progression of push-in and pull-out forces with displacement also showed a similar trend to the experiment. Moreover, when the same fracture strain value of 0.31 was used to

simulate porous pegs PIPO, maximum push-in force, maximum pull-out force and pull-out force/pull-in force ratio all reduced compared to the 4.7 mm smooth peg, as observed in the experiment (**Table 2.4**). When the maximum diameter of the porous peg was used to take the height of the asperities on the porous surface into account, the simulation gave results closer to the experimental results compared to when the mean diameter was used. As the press-fit of pegs removes the material around the hole, the peak height of asperities determines the amount of foam material that will be machined away.

While the model in this study provided satisfactory results that agreed well with experiments, the study should be considered in the context of its limitations. Firstly, the results from the model gave less accurate results at interferences that were outside the medium range (0.6-0.9 mm). Less accurate results were observed at interferences of 0.45 and 1.06 mm and it was also hard to achieve mesh convergence at low interference. This could be attributed to the difference in damage mechanism at different levels of interference. At lower interferences, deformation may be more dominated by elasticity, while at higher interferences, deformation is more dominated by damage and material removal [128]. Press-fit at a higher-interface can result in more permanent periprosthetic bone removal through compression beneath the nose of the peg while press-fit at a lower interference generates more circumferential elastic deformation in the bone than permanent damage [128]. As in this study, the combined effect of different forms of deformation (elastic deformation, plastic deformation, permanent damage) was simplified and simulated with a single fracture strain threshold value, this value might have not differentiated their respective proportion of material behaviour attributed to each type of deformation at each interference levels. Secondly, this model did not distinguish between compressive and tensile deformation and assumed that the plastic bone acted as an isotropic material. Press-fit components are held in place by tensile hoop stress induced in the periprosthetic bone

after implantation. In future studies of press-fit in real bone, when the primary fixation of implants is assessed in terms of periprosthetic stress, characterisation of the tensile and anisotropic properties of bone should be included and this will further improve the accuracy of the simulations. Thirdly, deviation in the shape of the force-displacement curves of the porous peg was shown between FEA and experimental results when either diameter was used while similarity was shown between the FEA and experimental curves of the smooth peg. The progression of forces with displacement of the porous peg depends on the morphology of the asperities along the length of the peg. Thus, it was difficult to achieve the same curve shape with a simple surface contact definition controlled by a single COF value. Despite the slight differences in force-displacement curve shape, the similarity in FEA and experimental maximum push-in force, maximum pull-out force and pull-out force/push-in force ratio when the maximum diameter was used implied that this simple model could efficiently assess and compare the primary fixation of different porous component designs within a reasonable time.

2.5 Chapter Summary

This chapter introduced an FE model of press-fit peg insertion in plastic bone analogue. It required only two sets of inputs: the uniaxial material curve of the plastic bone from which the fracture strain value could be found, and the COF between the plastic bone and the implant, both of which could be determined experimentally. The results from the FE models agreed well with the experimental results, showing percentage errors from 1.5% to 18.4% for three peg designs. The method developed in this chapter can be further optimised and enhanced for the clinical modelling of real bone by introducing real bone material

properties. It can be applied to efficiently computationally assess implants' primary fixation, and test/optimise new fixation component designs prior to experimental testing.

Chapter 3. Experimental Characterisation of Coefficient of Friction at Bone-implant Interface

3.1 Introduction and Aim

Fixation of cementless orthopaedic components is achieved through press-fit at an interference. The keel of the OUKR tibial component, which is the vertical protrusion beneath the tray, acts as the fixation component. Excessive micromotion of the implants adversely affects their fixation by forming fibrous tissue at the contact interface in place of bone [73, 116, 132]. A rough, porous surface on the fixation component inhibits excessive early migration and micromotion and is therefore beneficial to long-term fixation [77]. For the OUKR tibial component, friction force induced at the bone-porous keel interface results in low micromotion and adequate mechanical interlock and helps achieve primary and secondary stability.

The previous chapter (**Chapter 2**) mentioned that the coefficient of friction (COF) was one of the inputs in the simulations of cementless component press-fit. COF values ranging from 0.4 to 0.95 have been used in other work when modelling the contact between bone and cementless implants [117, 133-136]. Some other studies conducted sensitivity analyses on COF when modelling cementless implantation as the exact value was unknown. COF was found to greatly affect the results of the press-fit model in terms of reaction forces, implant micromotion and implantation torque [123, 137, 138].

To better characterise the frictional behaviour at the bone-implant contact interface in the computational analysis conducted in **Chapter 2**, an experiment was designed to measure COF. Establishing an accurate frictional relationship at the contact interface would improve

the reliability of the computational simulations while improving the efficiency of the analysis by eliminating the need for sensitivity studies on COF.

Previous attempts at characterising COF usually required the use of multiple load cells or multi-axial load cells [128, 139]. These tests were also conducted with a piece of material that resembled the surface finish of the fixation component rather than the actual implant used in the surgery.

This chapter aimed to experimentally characterise the COF between bone and implant. To the best of the author's knowledge, no studies have been conducted to characterise the COF between cementless OUKR and plastic bone analogue/real bone. Thus, COFs between four types of bone (plastic bone analogue, porcine bone, bovine bone, cadaveric bone) and three types of implant surface roughness (3D-printed smooth implant, 3D-printed rough implant, and cementless tibial component of OUKR) were measured. The former two implants had the same surface finishes as the pegs tested in **Chapter 2**. The results of this study would provide better insights into the frictional behaviour at the bone-implant interface. The results provided input values for the COF parameter to the models mentioned in **Chapter 2** where titanium pegs were press-fit into Sawbones foam, and for the OUKR-implanted proximal tibia models that will be covered in **Chapter 4** – **Chapter 7** to improve simulation accuracy and efficiency.

3.2 Method

A method was developed to find the COF at the bone-implant interface by finding the ratio between the normal force and the friction force at the contact surface (**Figure 3.1**).

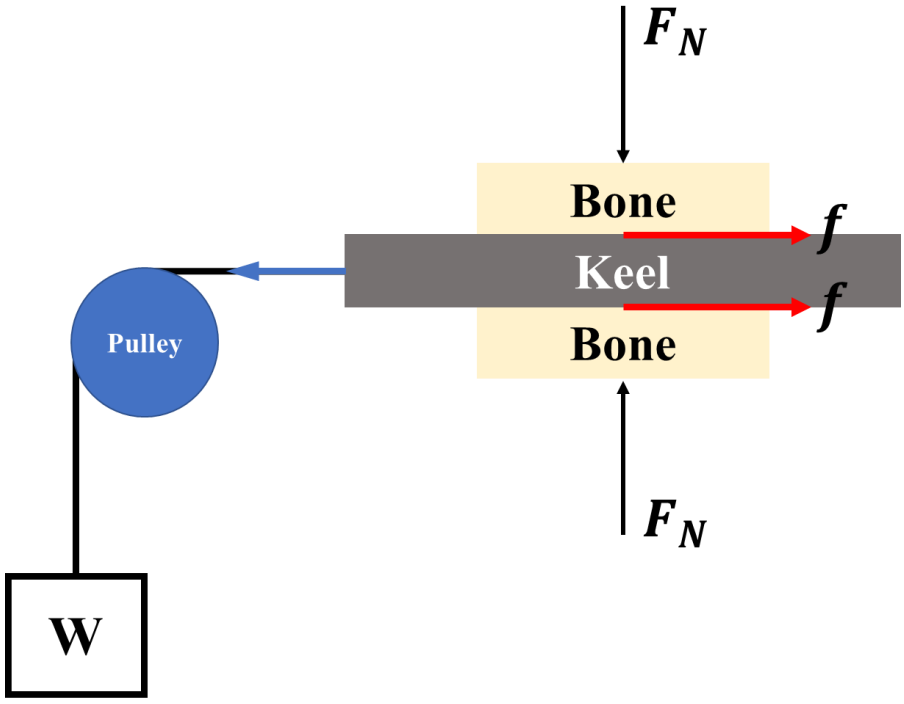

Figure 3.1: Schematic of the experimental setup. W: weight of the suspended mass, f: friction force, F_N: normal force.

Plastic bone foam (Sawbones Solid Rigid PU Foam, PCF20, #1522-03, Malmö, Sweden), the same material used in the simulations and the experiments covered in **Chapter 2** was used in this test. Fixation components of three different surface roughness were tested: a smooth 3D-printed keel additively manufactured from powdered titanium (Cp-Ti Grade 2, AP&C, Saint-Eustache, Canada), a rough 3D-printed keel additively manufactured from powdered titanium, and the keel of the actual cementless OUKR tibial component which has a porous coating (**Figure 3.2**). The smooth and rough 3D-printed keel had the same surface finish as the 3D-printed pegs used in the PIPO tests in **Chapter 2**.

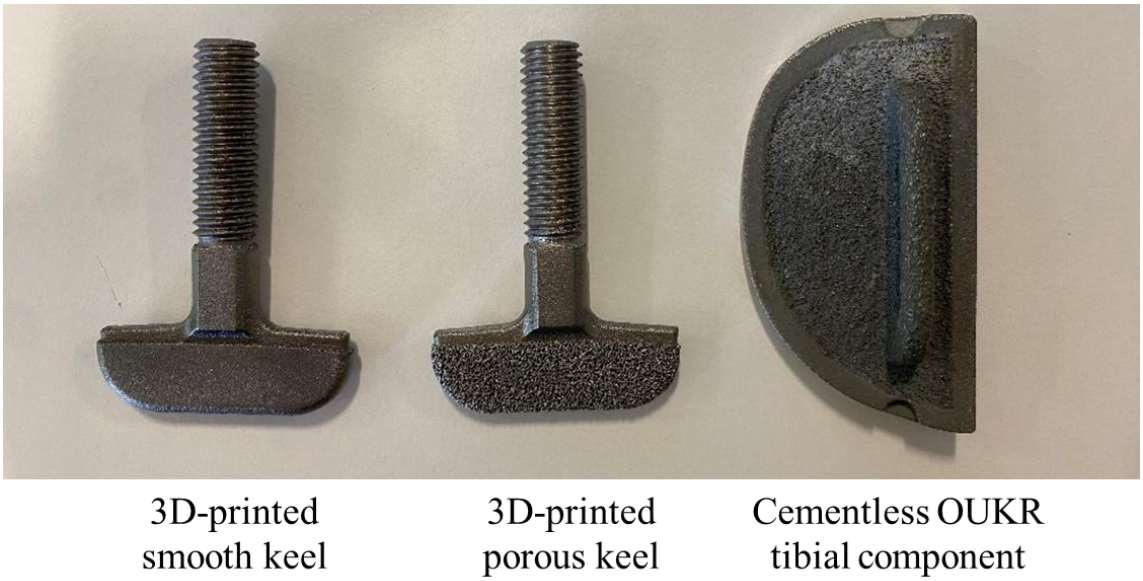

Figure 3.2: 3D-printed smooth keel (left), 3D-printed porous keel (middle), cementless Oxford Unicompartmental Knee Replacement (OUKR) tibial component (right)

Images of the surface microstructure of the porous components taken with Scanning Electron Microscopy by Azmi Rahman and Jack Aspinall [124] showed that the pore size was around 300-500 μm on the 3D printed component and around 100-200 μm on the OUKR tibial component (**Figure 3.3**), which were similar to the pore sizes on other cementless orthopaedic components in use [140].

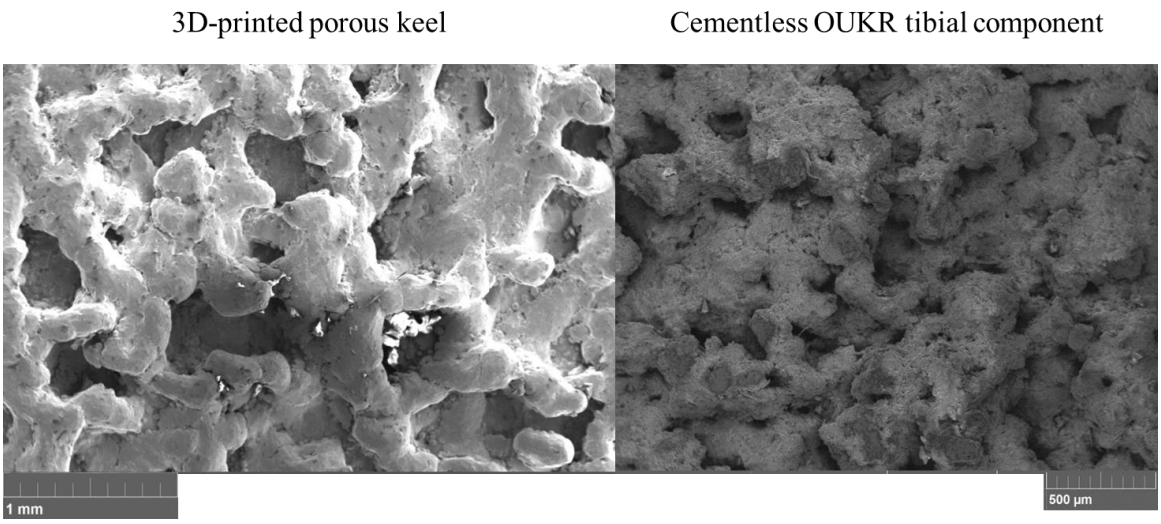

Figure 3.3: Surface microstructure of the 3D-printed porous keel (left) and the cementless Oxford Unicompartmental Knee Replacement (OUKR) tibial component (right).

The test rig is shown in **Figure 3.4**. The whole device was 3D-printed with Polylactic Acid (PLA).

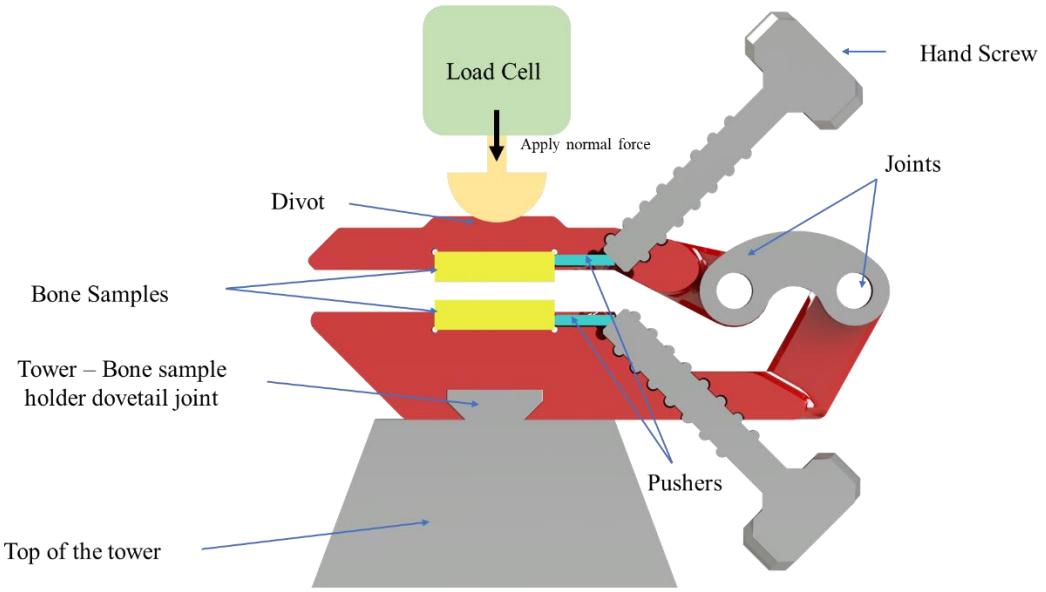

Figure 3.4: Schematic of the bone sample holder. Figure adapted from [141].

The plastic bone was cut into samples of approximately 15x15x5 mm³ using the MICRO bandsaw MBS 240/E (PROXXON GmbH, Föhren, Germany). The test was completed in the DARTEC HC-10 servohydraulic material testing machine (ZwickRoell Ltd, Herefordshire, United Kingdom). The tested component was clamped between two pieces of plastic bone before each test by a normal load applied through a vertical load cell (FSB-01 S-beam load cell, Force Logic, Berkshire, United Kingdom). Then a 2 kg mass was connected to the tested component through a piece of string and a pulley to apply a constant horizontal force (**Figure 3.5**). A keel holder was designed to secure the fixation of the 3D-printed tested components to the string (**Figure 3.6**). When the OUKR tibial component was tested, the string was directly connected to the component through the window on the keel (**Figure 3.5**). A spirit level was used to ensure that only force in the horizontal direction was applied to the tested component. A minimum clearance of 1 mm was ensured between the bottom of the tray and the rig so that no surfaces other than the keel faces were touching the rig or the bone samples to avoid any extra friction force.

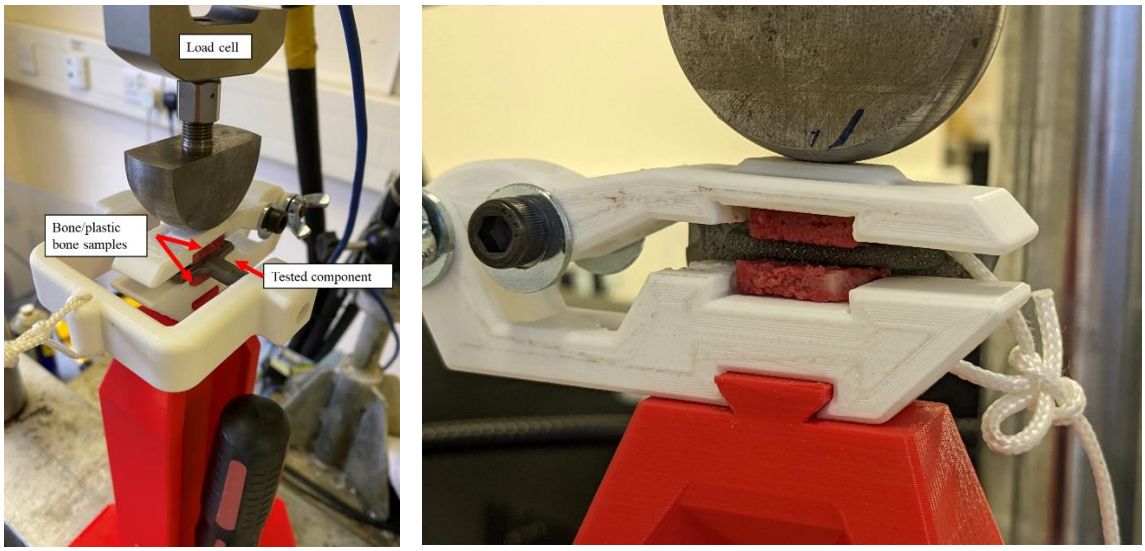

Figure 3.5: Equipment setup. The tested fixation component was clamped between two pieces of samples through the load applied by the vertical load cell. The 3D-printed component was held by the holder which was connected to the weight via a piece of string and a pulley (left). The string was directly connected to the keel of the Oxford Unicompartmental Knee Replacement tibial component (right).

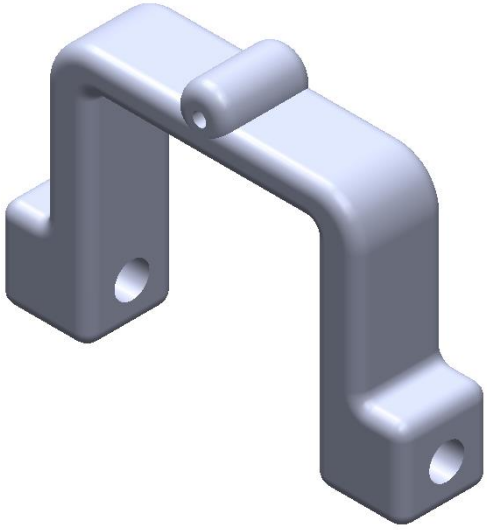

Figure 3.6: CAD model of the keel holder.

The load from the load cell was then gradually reduced through a downward ramp until the tested components started to slip between the samples and were freed from the clamp. This vertical load applied by the load cell was recorded, and the COF was derived using **Equation 3.1**. W is the weight of the suspended mass (2 kg x 9.81 N/kg), f is the friction force, μ is the COF between the plastic bone and the tested component, and F_N is the vertical load applied by the load cell.

$$W = 2f$$

$$W = 2\mu F_N$$

$$\mu = \frac{W}{2F_N} \qquad [3.1]$$

The hypothesis was that COF was around 0.2 between the plastic bone sample and a smooth implant, and around 1.0 between the plastic bone sample and a rough implant [142]. This means that the smooth and rough tested components were likely to start to slip at normal

forces of 50 N and 10 N, respectively. Thus, a pre-load of 80 N was applied to ensure that the tested component was securely clamped between bone samples before the test.

Tests on each fixation component were repeated six times with Sawbones and samples were not reused. The debris of bone on the tested components was cleaned after each test to make sure it would not affect the next repeat.

The same testing protocol was repeated with animal cancellous bone and human cancellous bone samples resected from fresh porcine, fresh bovine and defrosted cadaveric proximal tibias (Ethical approval: 16NW0859). Bovine samples were retrieved from three separate proximal tibias. The bone samples were resected along the long axis of the tibias, the same direction in which the keel of the OUKR tibial component would be implanted into the proximal tibia (**Figure 3.7**). This aimed to replicate the contact between the bone and the keel of the OUKR tibial component in the actual surgery. This also captured any effects brought by bone's anisotropic nature. The size of each sample was approximately 15x15x5 mm^3 (**Figure 3.8**). The number of tests conducted with animal and human bone depended on the number of samples that could be resected from each tibia. All experiments with animal bone and human bone were conducted immediately after samples were resected. Samples were tested on each side once and they were not reused.

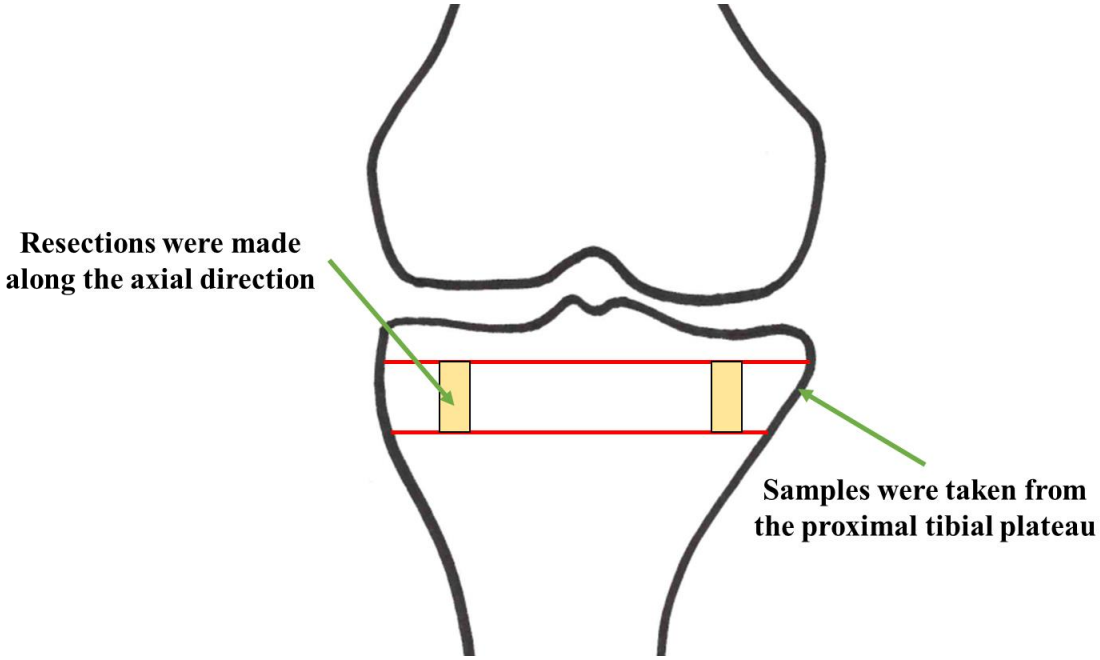

Figure 3.7: Schematic of bone sample collection. The samples were resected from the proximal tibial plateau along the axial direction of the tibia.

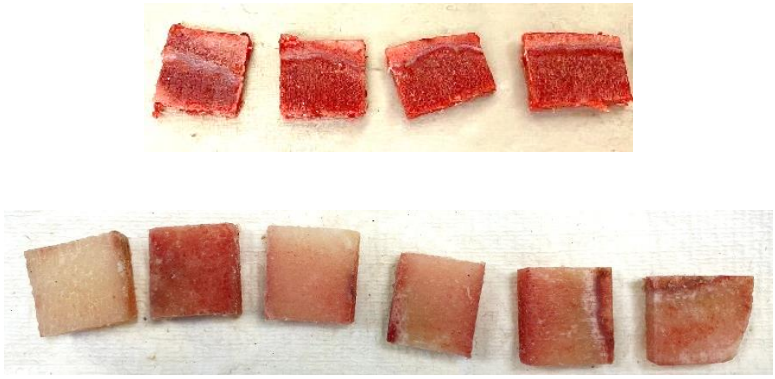

Figure 3.8: Examples of porcine samples (top) and bovine samples (bottom) tested in the experiment.

3.3 Results

The force and displacement data from each test were plotted as force-displacement graphs. The vertical loads under which the tested components started to move were found from the force-displacement curve as the point where the force abruptly decreased, implying the tested component was freed. The COFs were found using **Equation 3.1**.

Table 3.1 lists the COF values at each bone-implant contact interface.

Table 3.1: Coefficient of friction values.

			Coefficient of friction	
Bone sample	**Implant**	**n**	**Mean**	**Standard deviation**
Sawbones	Smooth keel	6	0.27	0.03
Sawbones	3D-printed porous keel	6	0.56	0.11
Sawbones	OUKR tibial component keel	6	0.99	0.09
Porcine	Smooth keel	4	0.54	0.06
Porcine	OUKR tibial component keel	7	0.93	0.18
Bovine Tibia 1	Smooth keel	2	0.46	0.02
Bovine Tibia 1	OUKR tibial component keel	3	1.00	0.03
Bovine Tibia 2	OUKR tibial component keel	3	0.68	0.09
Bovine Tibia 3	OUKR tibial component keel	3	0.20	0.01
Cadaveric	Smooth keel	3	0.41	0.08
Cadaveric	OUKR tibial component keel	5	0.99	0.14

For all types of bone, other than bovine tibia 3, the COF at the bone-OUKR keel interface was higher than that at the bone-smooth keel interface. COF between Sawbones and the 3D-printed porous keel was lower than that between Sawbones and the porous keel of the actual tibial component.

COF values were similar at the contact interfaces between cementless OUKR tibial component and plastic, porcine and human bone, all around 0.9-1.0. For bovine samples, large variability was shown among the three tibias, with mean values ranging from 0.2 to 1.0.

3.4 Discussion

In this chapter, a novel experimental method of determining the COF at the bone-implant interface was developed. Compared to prior methods described by Bishop et al. [128] and Grant et al. [139], this simple setup, with only one load cell needed, enables the

characterisation of COF between fixation components on real implants and bone samples from the region of interest where fixation of the real implants is provided. The contact area between the keel and the sample was approximately 15x10 mm² and the normal stress was about 0.1-0.4 MPa at the surface when the component was freed from the clamp, similar to the normal pressure applied in previous studies [139, 143, 144]. Similar COF values between human trabecular bone and porous implants were shown in a previous study that was conducted with multi-axial load cells (0.99 in the current study vs. 0.86-1.08 in [142]). This implies that the current method can provide valid COF results with a relatively simpler setup when access to the multi-axial load cells or multiple load cells is limited.

COF values found at the bovine bone-OUKR tibial component interface showed large variability, with mean values ranging from 0.2 to 1.0. During bone sample preparation, it was noticed that bovine tibia 3 was noticeably different in the quality of bone. This might have explained the small COF values found with bovine tibia 3 compared to the values found with the other two bovine tibias. These results may imply that the frictional contact between the implant and pathological bone can be different to that between the implant and healthy bone. Thus, this differentiation in contact at the interface should be accounted for in future studies. Previous studies also displayed large variability in COF values among samples [139, 142, 144-146]. The COF between human trabecular bone and smooth implants varied between 0.16 to 0.43 [139, 142, 145, 146]. In two studies that measured the COF between human trabecular bone and smooth polished implants, the values were 0.37 (Standard deviation (SD) = 0.02) and 0.16 (SD = 0.05) [139, 142]. In the same studies, the reported COFs between human trabecular bone and beaded porous implants with a roughness of 32.6 μm were 0.42 (SD = 0.01) and 0.86 (SD = 0.02). Some other studies reported the COFs between human trabecular bone and beaded porous implants while not specifying the roughness of the surface. The values ranged from 0.53 to 0.68 [144-146].

These variations in COFs found from the current and prior studies might come from the variability of material properties between resection sites of the tested samples or between individuals.

Though this method provided a relatively simple way of finding the COF at the bone-implant interface, some limitations require further investigation. All tests on plastic bone were conducted under dry conditions. In the actual surgery, blood and fat are present at the contact surface. This may also explain why different COFs were found between plastic bone-smooth implant interface (0.27) and real bone-smooth implant interface (0.41-0.54), while similar COFs at the contacts with porous implant were found (0.99 for plastic bone-OUKR keel vs. 0.93-0.99 for porcine and cadaveric bone-OUKR keel). Debris from the plastic bone surface might have acted as small spheres that allowed the tested smooth component to roll on the surface, creating a lower friction force. While this effect was less obvious with real bone, a larger COF was shown between real bone and the smooth implant. Asperity on porous implants dominates the frictional behaviour at the contact surface. While for smooth implants, the presence of blood and fat tissue may have a relatively more significant effect on the friction force. A similar difference was also shown in [139], in which the COFs at the plastic bone-smooth implant interface reported were generally smaller than those at the human trabecular bone-smooth implant interface (0.08 vs. 0.40). Future studies can adjust the testing conditions based on the application of the results. Also, no statistical analysis was performed in this study due to the limited number of samples that could be retrieved from each proximal tibia. Despite the limited number of repeats, the COF values found can provide a more accurate characterisation of the frictional behaviour at the bone-implant interface in computational modelling. This enables more reliable FE simulations by minimizing the uncertainty brought by the unknown contact behaviour and improves analysis efficiency by eliminating the need for a sensitivity study on COF.

To the best of the author's knowledge, this is the first study that experimentally characterises the COFs between the porous coating on the tibial component of OUKR (the most used cementless UKR in the UK [50]) and PCF20 Sawbones (a widely used biomechanical test material) and human cadaveric bone. This provides numerical values on COF that can be widely applied in future computational analysis around OUKR.

3.5 Chapter Summary

This study proposed a novel experimental method of measuring COF at the bone-implant surface. This enables the characterisation of COF at the interface between bone and the actual component used in the surgery with a relatively simple setup using one load cell. The results were similar to previous findings from experiments conducted with multiple load cells or multi-axial load cells. Combinations of fixation components of three different surface roughness (3D-printed smooth/3D-printed porous/OUKR cementless tibial component porous) and four types of bone (plastic trabecular bone analogue/porcine bone/bovine bone/human cadaveric bone) were tested. The COF is 0.27 (SD = 0.03) between the 3D-printed smooth component and plastic bone analogue, 0.56 (SD = 0.11) between the 3D-printed rough component and plastic bone analogue and 0.99 (SD = 0.09) between the porous OUKR tibial component and plastic bone analogue. The COF is 0.99 (SD = 0.14) between the porous OUKR tibial component and human cadaveric bone. This experimental characterisation of COF at the interface between bone and cementless implants enables more accurate and more efficient simulations of cementless implantation. The COF values found in this chapter were applied to the FE models covered in **Chapter 2** and **Chapter 4** – **Chapter 7**.

Chapter 4. Finite Element Analysis of Periprosthetic Tibial Fractures after Cementless Oxford Unicompartmental Knee Replacement

4.1 Introduction and Aim

Surgical techniques for tibial resection (vertical cut and horizontal cut) in cemented OUKR and cementless OUKR are the same. In cemented OUKR, the tibial component is fixed with a small amount of PMMA bone cement which acts as grout. In the cementless version, a keel slot narrower than the keel is made in the tibia. The primary fixation of the cementless tibial component is achieved through an interference fit. The interference is defined as the difference in the width of the keel and the width of the keel slot. The component is impacted carefully with a hammer until fully seated. Excessive impaction may cause a large 'splitting' force in the tibia plateau and subsequently lead to a periprosthetic stress fracture [92]. The interference fit fixation and impaction needed to seat the implant may create a higher risk of fracture. This may explain why cementless OUKR show a higher rate of periprosthetic tibial fracture (1.22%, 95% Confidence Interval (CI): 0.60-2.49) than the cemented version (0.99%, 95% CI: 0.62-1.59) [92].

Tibial periprosthetic fracture (PPF) is a severe complication of cementless OUKR which compromises functional outcomes and recovery. It usually requires conversion to more invasive implants, e.g. stemmed TKR [94, 98, 147]. Most fracture cases after cementless OUKR were non-traumatic fractures and happened within three months post-surgery [92]. Compared to the ~1% incidence rate in Caucasian populations [97, 98, 148], higher incidences were reported in Asian populations, ranging from 3.8% to 8.0% [95, 96, 99].

This difference in outcomes between different populations may come from the diversities in tibia morphology. The tibial size of the Asian population was shown to be relatively smaller compared to a Caucasian cohort [149]. The incidence of tibial vara and overhanging medial tibial condyle has also been shown to be higher in studies on Asian cohorts [100, 101, 150-153]. Ruangsomboon et al. [154] and Wang et al. [102] reported that small tibial components (Size A and AA) were used in around 50% of the cases in their Chinese and Thai cohorts while small-sized components are less commonly used in the Western populations. Hiranaka et al. [99] reported that in Japanese patients, very small cementless components (Size A and AA) showed a fracture risk seven times higher than that of the larger sizes. OUKR tibial components of all sizes have the same keel depth, which means the keel can be relatively closer to the cortex in patients using smaller components (**Figure 4.1**). This gives less bony support under the component.

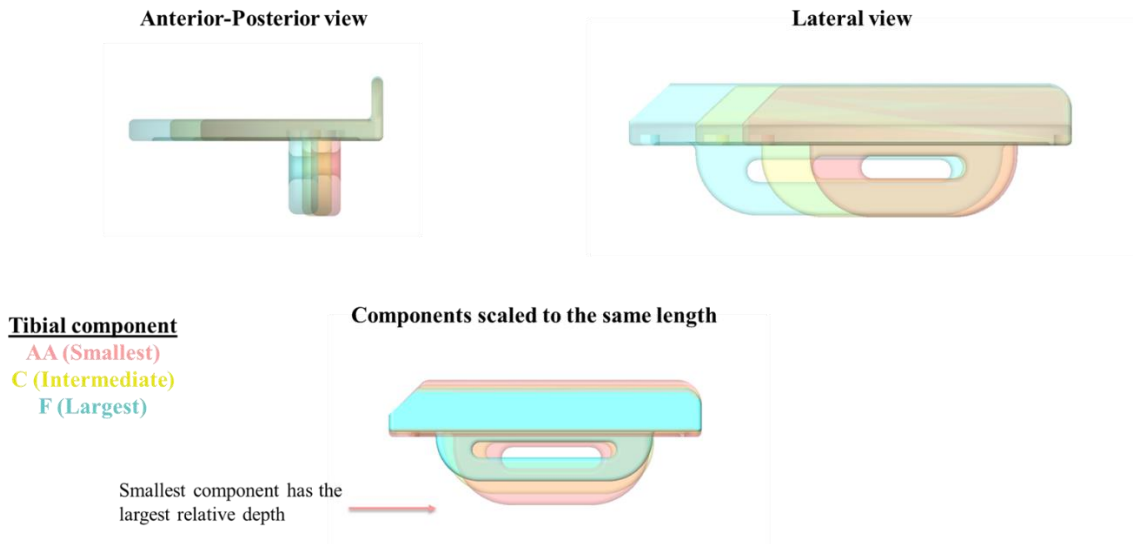

Figure 4.1: Oxford Unicompartmental Knee Replacement tibial components of Size AA, Size C, and Size F. When the components are scaled to have the same length, the smallest component (Size AA) has the largest depth, implying the depths of smaller components are relatively larger. Figure adapted from [124].

Two cases of PPF were reported in two female Japanese patients who had received bilateral OUKR. In both cases, tibial components of the same size were used in both knees while only one of them developed fracture.

- Patient 1 received Size C cementless OUKR tibial components in both knees and the right knee fractured (**Figure 4.2**). The component in the fractured knee was overhanging medially and anteriorly. A medium femoral component and a medium bearing were used in each knee.

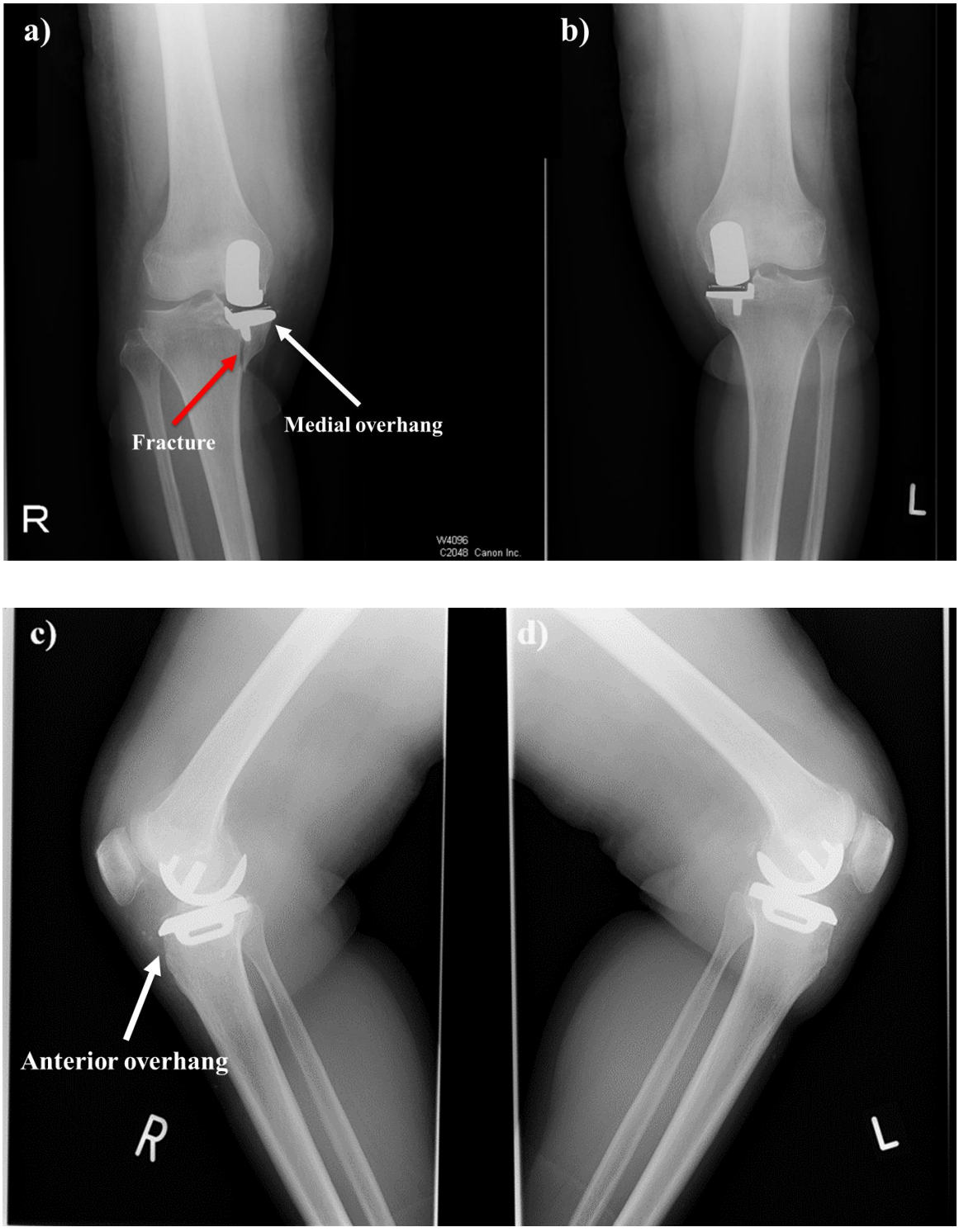

Figure 4.2: Post-fracture anteroposterior (a, b) and lateral (c, d) radiographs of Patient 1, showing periprosthetic fracture in the right tibia (a). Medial and anterior overhang was shown in the right leg (a, c).

- Patient 2 received a Size A cementless OUKR tibial component in the right knee which did not fracture and received a Size A cemented component in the left knee that fractured (**Figure 4.3**). As previously mentioned, the cementless tibial component is seated by impaction with a hammer into a slot with interference. This interference fit fixation may make the cementless version more prone to fracture [84]. Compared to the cemented version, cementless OUKR showed a higher rate of revision due to PPF [84]. Thus, this fractured tibia would have had an even larger chance of experiencing fracture if a Size A cementless component was implanted. A senior surgeon assessed the position of the component based on post-operative radiographs. It was concluded that the cuts in the fractured tibia were made noticeably too medial and too distal. The component was overhanging significantly medially. It could be seen from the post-operative radiograph that the keel penetrated the posterior cortex. An extra-small (X-small) femoral component and an X-small bearing were used in each knee.

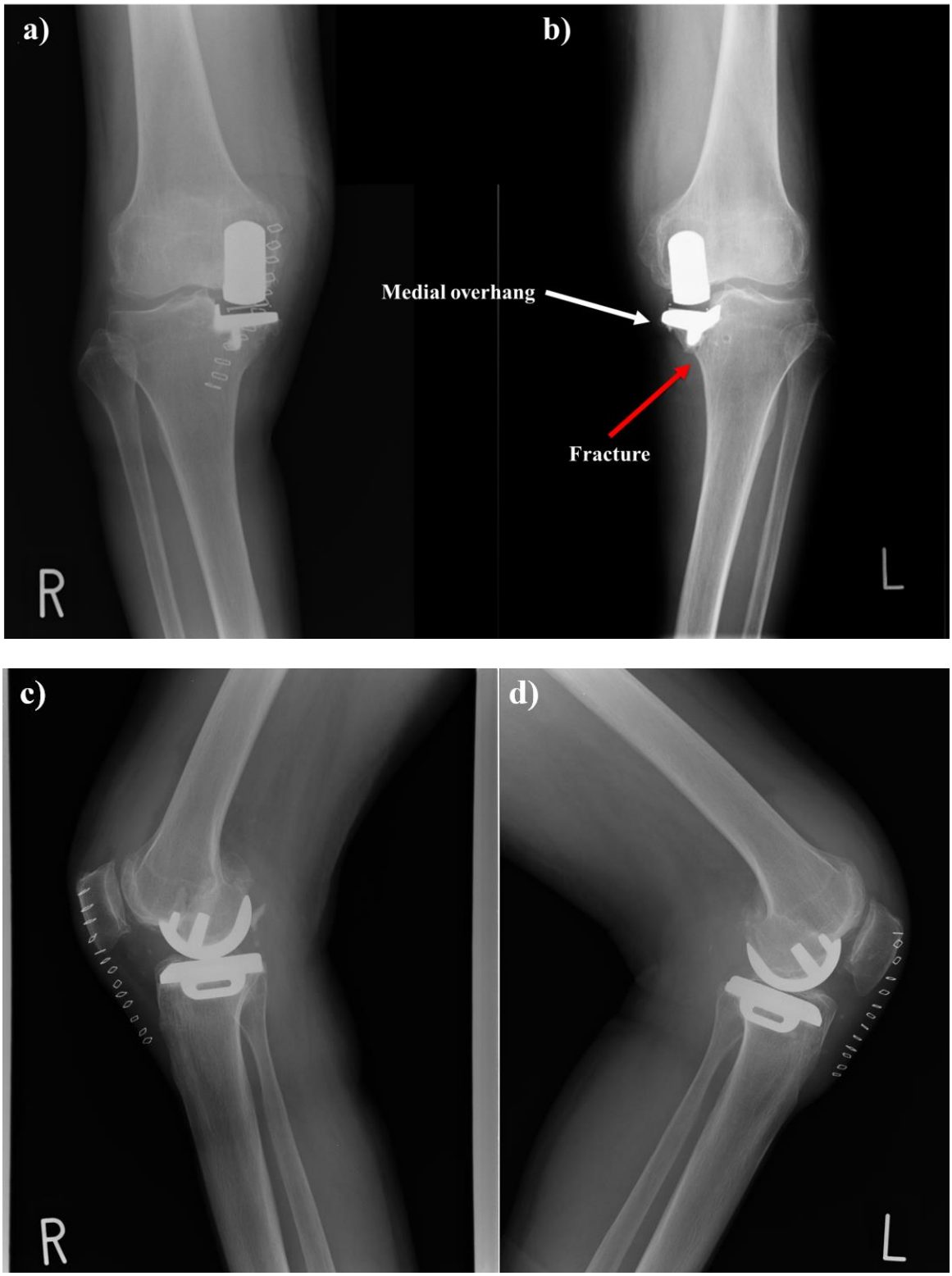

Figure 4.3: Post-fracture anteroposterior (a, b) and lateral (c, d) radiographs of Patient 2, showing periprosthetic fracture in the left tibia (b). Medial overhang of the tibial component is shown in the left tibia (b).

Previously reported risk factors of PPF include female gender, higher BMI, greater age, smaller tibia, an overhanging tibial condyle, use of under- or over-sized components and excessive tibial bone resection [92]. Smaller tibial plateaus or tibias with overhanging medial condyles are at higher risk of experiencing fracture due to the lack of bone stock supporting the tibial component. As these two cases are both fractures in one tibia of the patients who received bilateral OUKR, the comparison of the fractured and the unfractured tibias within the patient excludes the effect of gender, BMI, and age. The relevant risk factors can be classified into patient factors and surgical factors. The patient factors were poor proximal tibial bone quality or osteoporosis, small tibial size and overhanging medial tibial condyle. The surgical factors were excessive tibial bone resections and component over- or under-sizing [92] (**Table 4.1**).

Table 4.1: Relevant patient and surgical risk factors of periprosthetic tibial fracture.

<table>
<tr><th>Patient factors</th><th>Surgical factors</th></tr>
<tr><td>Poor bone quality/Osteoporosis</td><td rowspan="2">Excessive tibial bone resection</td></tr>
<tr><td>Small tibial size</td></tr>
<tr><td>Overhanging medial plateau</td><td>Component oversizing or undersizing</td></tr>
</table>

Yoshikawa et al. [95] introduced an auxiliary line that could be used to assess the risk of fracture after cementless medial OUKR radiographically. This medial eminence line (MEL) passes the tip of the medial tibial eminence and extends parallel to the tibial anatomical axis (**Figure 4.4**). Tibias can be classified into extramedullary type or intramedullary type based on the position of the MEL relative to the medial tibial cortex. The tibia is termed extramedullary type if MEL passes the medial cortex, otherwise, intramedullary type. Patients with extramedullary tibia were found to have a higher risk of tibial fracture than the others after cementless OUKR [95].

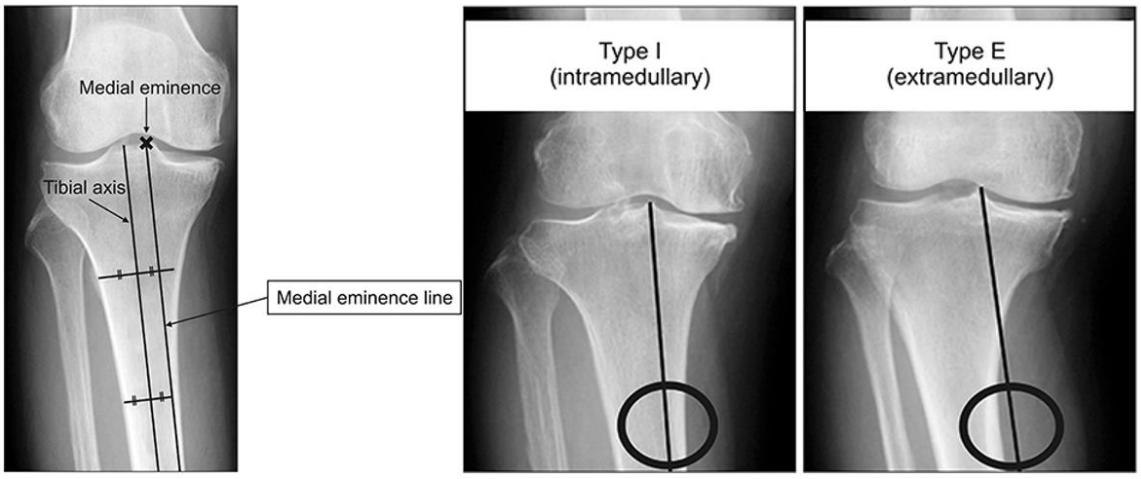

Figure 4.4: The medial eminence line (MEL) is defined as the line that starts from the medial tibial spine and extends parallel to the tibial anatomical axis. In the intramedullary-type tibia, MEL does not pass through the medial cortex. In the extramedullary-type tibia, MEL passes through the medial cortex [95].

The medial proximal tibial angle (MPTA) is the angle between the tangent to the tibial plateau and the tibial mechanical axis (MA) (**Figure 4.5**). Mullaji and Shetty [155] suggested that varus deformity larger than 10 degrees might adversely affect the outcomes and survival of UKR. Erlichman et al. [156], thus, defined tibia vara as MPTA smaller than 80 degrees. Patients with tibia vara are likely to have an overhanging medial plateau and these patients are at higher risk of experiencing fracture [95].

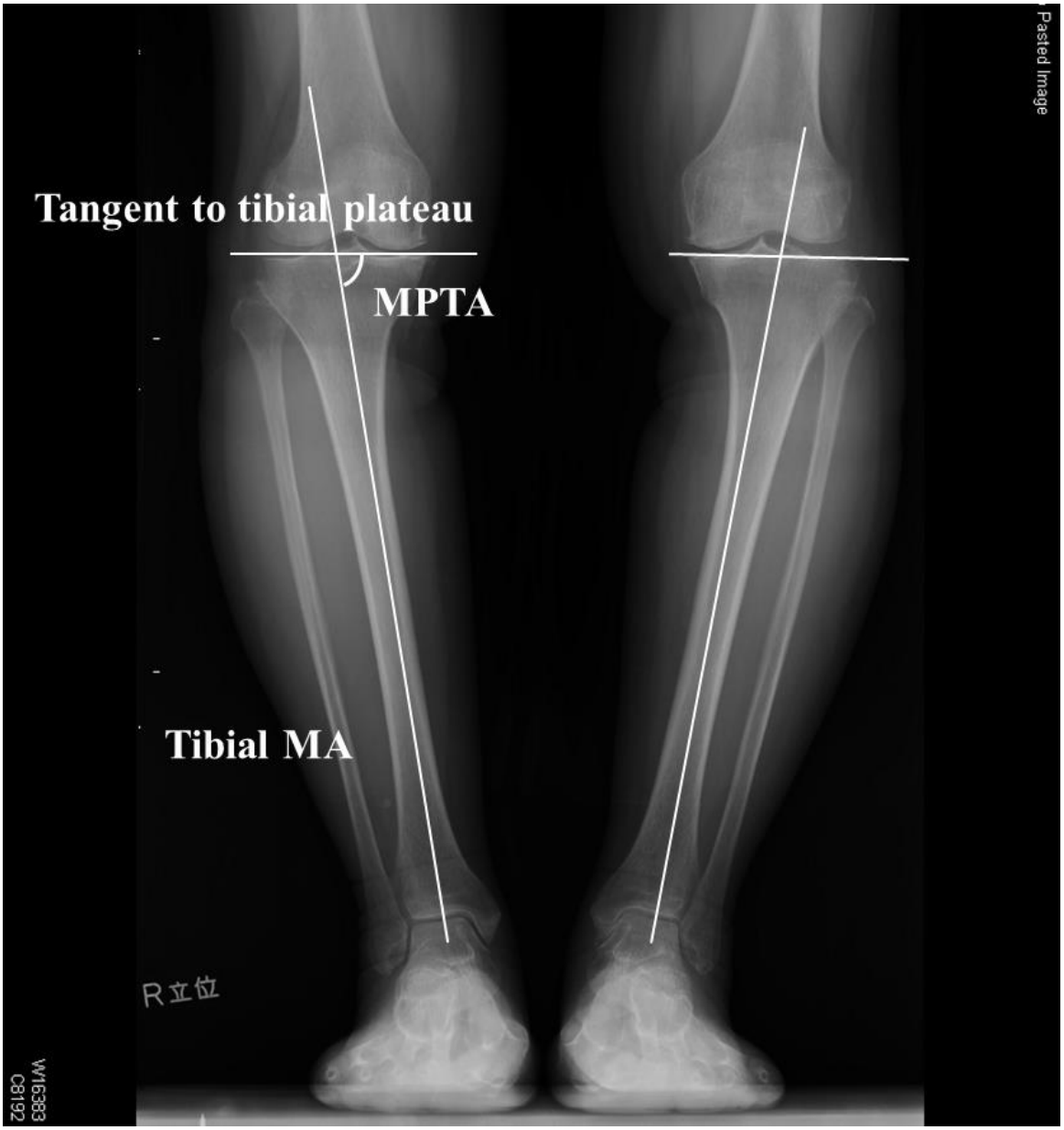

Figure 4.5: Medial proximal tibial angle (MPTA) is the acute angle between the tangent to the tibial plateau and the tibial mechanical axis (MA).

During the surgery, the patient lies supine, and the operated leg hangs with a 30° hip flexion and a 110° knee flexion on the leg holder. The vertical tibial saw cut should be immediately medial to the apex of the medial tibial spine and should point towards the anterior superior iliac spine (ASIS) (**Figure 4.6**). The horizontal saw cut should be 2 or 3 mm below the

deepest region of the erosion or above the bottom of the erosion if the defect is very deep [11, 32].

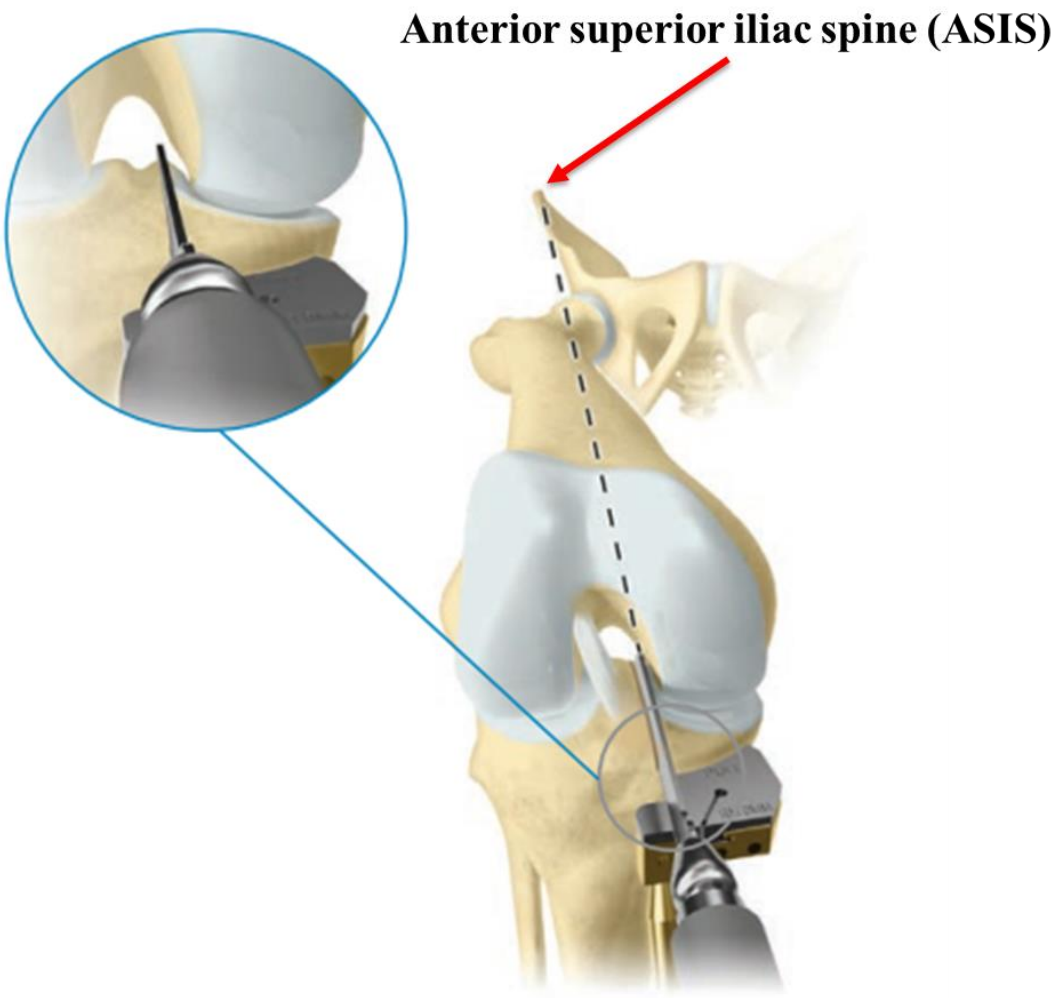

Figure 4.6: The vertical tibial saw cut should be immediately medial to the medial tibial spine and should point towards the anterior superior iliac spine (ASIS). Figure adapted from [32].

Regarding the sizing of the tibial component, the surgical guide suggests that the component should match the width and the length of the excised plateau, showing good coverage. The medial margin of the component should be flush with the medial cortex or show an overhang of less than 2 mm. The posterior margin should also either be flush with the posterior cortex or show a < 2 mm overhang. The anterior corner of the tibial component should be flush with the anterior cortex or underhang by less than 5 mm. Thus, a

satisfactory component size choice should fulfil these criteria (**Figure 4.7**). Inappropriate saw cuts that place the component too medial, too distal, and inappropriate tibial component size choice are both risk factors of PPF [92, 157].

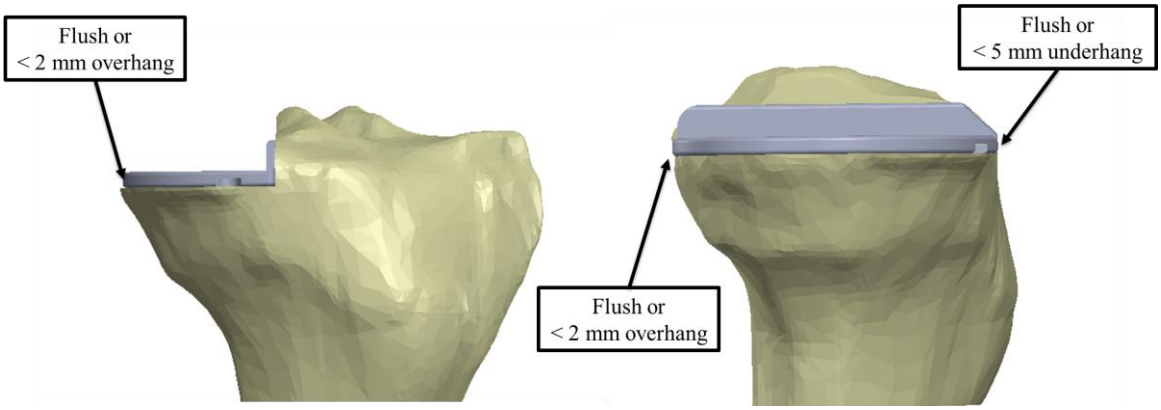

Figure 4.7: Criteria for the positioning and sizing of the Oxford Unicompartmental Knee Replacement tibial component.

A previous study showed that patients who experienced PPF after cementless OUKR generally had a shorter distance between the keel and the posterior cortical bone compared to those patients without fractures (**Figure 4.8**) [96]. Placement of the tibial component too medial or too distal shortens this posterior keel-cortex distance (KCD) and subsequently increases the risk of fracture [96]. Kamenaga et al. [158] suggested that varus implantation of the tibial component could increase KCD and could potentially lower the risk of PPF, especially in patients with overhanging medial tibial plateaus.

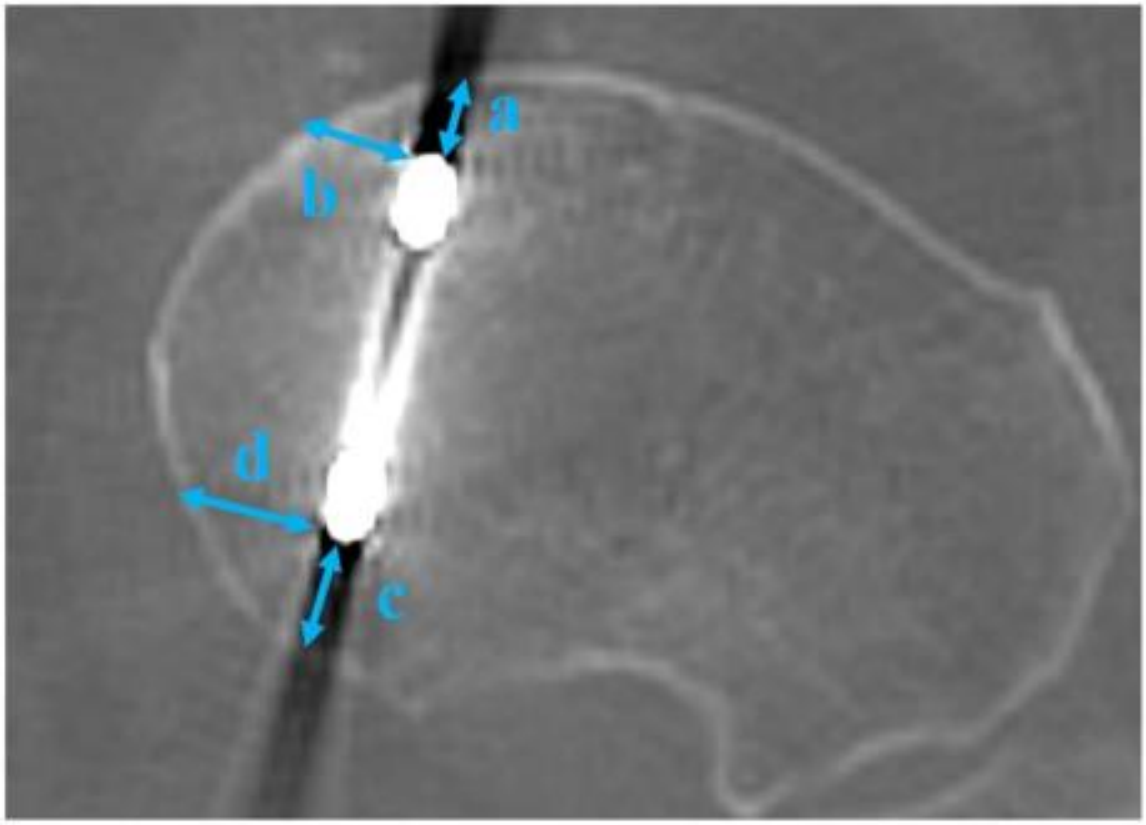

Figure 4.8: Measurements of keel-cortex distances (KCDs) made in different regions: a) anterior, b) anteromedial, c) posterior, and d) posteromedial [96].

The aim of this chapter was to investigate the relevant patient and/or surgical factors that caused the difference in outcomes in the fractured and unfractured tibias of these two patients who experienced PPF in one of their tibias after receiving bilateral OUKR. Patient factors, which are poor bone quality, small tibial size and overhanging tibial plateau, and surgical factors, which are excessive bone resection and component over- or under-sizing were compared between the fractured and unfractured tibia in both patients. FEA was then conducted on the tibias with the tibial component implanted at their post-operative positions. The tibial resections in the fractured tibias were also replicated in their unfractured counterparts to eliminate the effects of patient factors. Finally, the choice of using maximum principal stress as an indication of the risk of fracture was justified by comparing the computational results from FE models to the results of a previous load-to-

fracture experiment on Sawbones plastic bone analogue conducted by a colleague (Lachlan Arthur).

4.2 Methods

All patient data used in this study was anonymised.

4.2.1 Patient 1

The two tibias of Patient 1 were compared regarding the relevant patient-related risk factors for periprosthetic fracture (**Table 4.1**): poor bone quality (osteoporosis), small tibial size and overhanging medial condyle. Bone quality at the resection sites was assessed by comparing the Young's modulus of the trabecular bone and cortical bone at the tibial plateau, and by checking if there was sclerotic bone resulting from osteoarthritis at the plateau from the CT scans. The size of the tibia was compared in terms of the width, length, and aspect ratio of the tibia plateau. The morphology of the medial condyle was compared using the MPTA of the two tibias. Also, these two tibias were classified into either extramedullary type or intramedullary type. MELs were marked from the medial tibial eminence point and extended distally parallel to the tibial anatomical axis. Their position relative to the medial cortex was assessed.

The tibial preparations in the two tibias were then compared based on relevant surgical-related risk factors of periprosthetic fracture: excessive tibial bone resection and component over- or under-sizing. The mediolateral position, proximal-distal position, varus-valgus orientation and internal-external rotation of tibial resections in the fractured and unfractured tibia were compared (**Figure 4.9** and **Figure 4.10**).

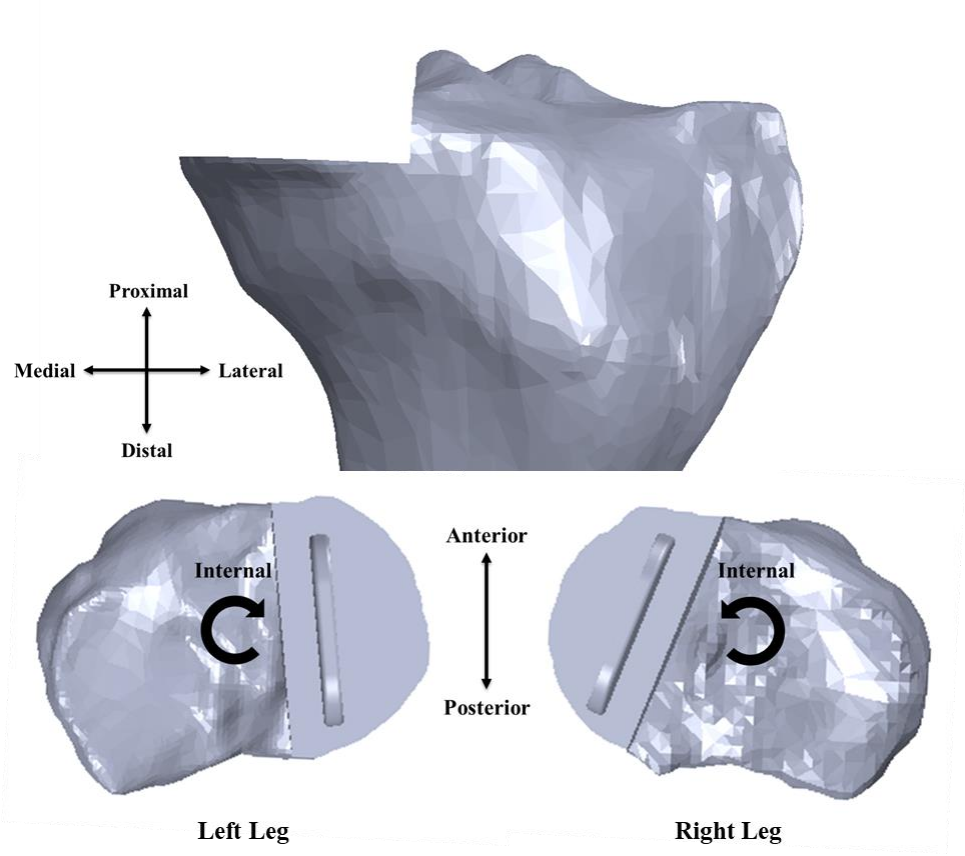

Figure 4.9: Anatomical directions on tibias resected for medial Oxford Unicompartmental Knee Replacement.

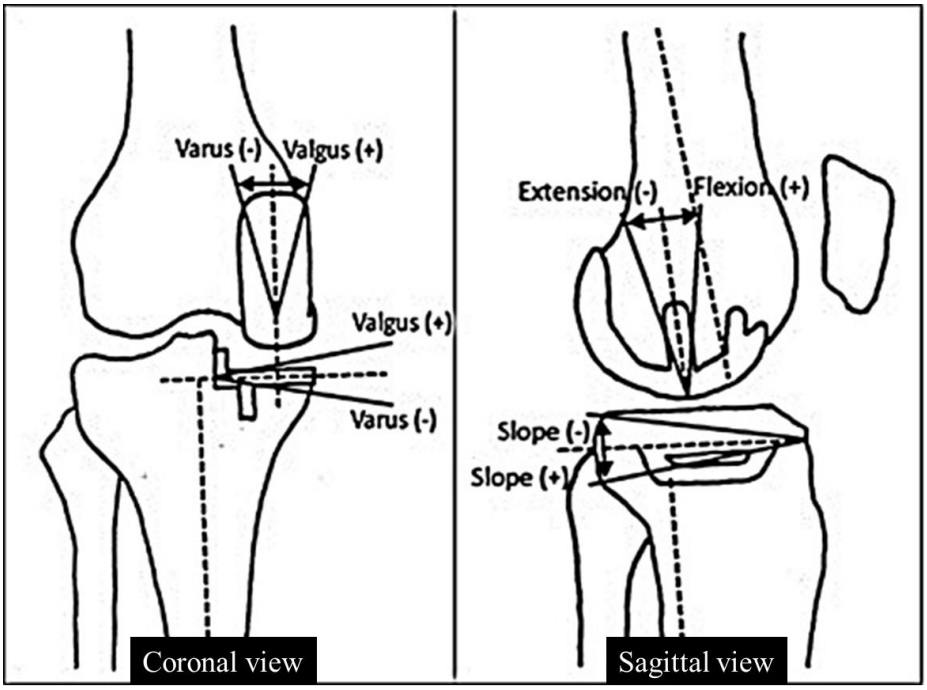

Figure 4.10: Alignments of the tibial and femoral components. Figure adapted from [159].

The vertical and horizontal bone cuts define the position and orientation of the tibial component. Geometries of the tibias were reconstructed from the preoperative CT scans with Mimics (version 23, Materialise, Leuven, Belgium). The tibial components were virtually implanted in their post-operative position. The mediolateral position of the vertical cut was measured as the distance from the Cobb axis, an anatomical tibial axis defined by Cobb et al. [160]. The Cobb axis is the perpendicular bisector of the line connecting the centres of the medial and lateral tibial condyles (**Figure 4.11**).

A best-fit circle was found with 11 data points picked on the periphery of the lateral articular surface. The centre of this circle was defined as the lateral condyle centre (LCC). Similarly, 11 data points were taken around the medial condyle on a plane 20 mm below the medial tibial eminence. The medial condyle centre (MCC) was the centre of the best-fit circle of these 11 data points [160].

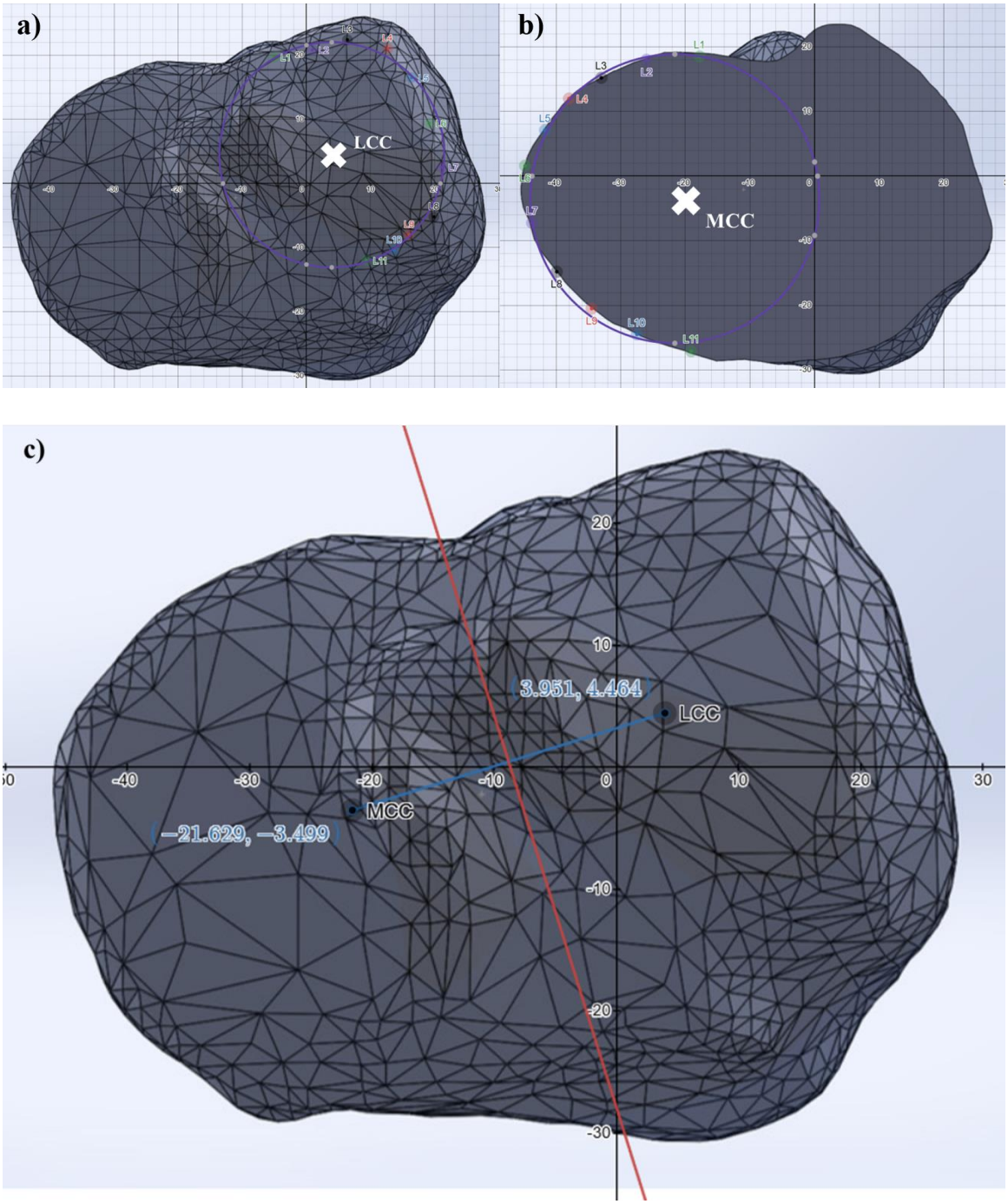

Figure 4.11: Definition of (a) lateral condyle centre (LCC), (b) medial condyle centre (MCC), (c) Cobb axis (Red) is the perpendicular bisector of the line connecting LCC and MCC.

The mediolateral position of the vertical cuts was defined with the perpendicular distance from the middle point of the anteroposterior (AP) cut to the Cobb axis on the horizontal cut plane (**Figure 4.12**). The proximal-distal position of the horizontal cut was defined using

the distance from the proximal tibial centre, which is the intercondylar eminence, to the horizontal cut plane (**Figure 4.13**). The varus-valgus orientation of the cuts was defined with the angle between the vertical cut plane and the tibial long axis, which connected the centre of the talus and the proximal tibial centre (**Figure 4.14**). The internal-external rotation was defined using the angle between the vertical cut plane and the Cobb axis (**Figure 4.15**).

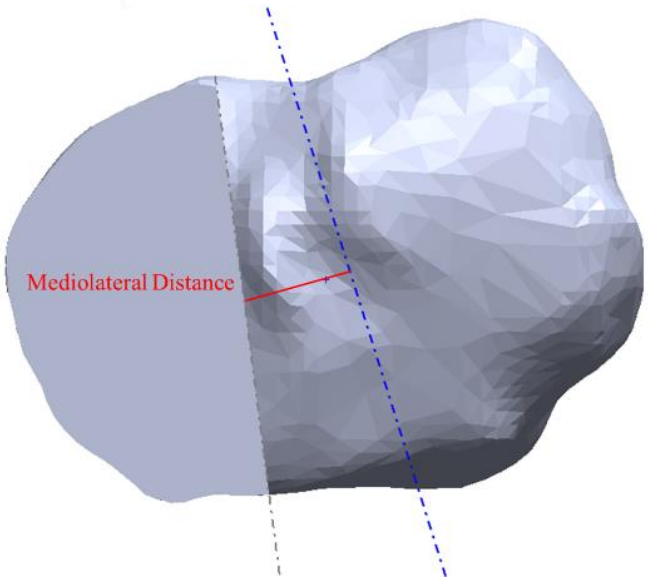

Figure 4.12: Measurement of the mediolateral position of the tibial cuts. The mediolateral distance (Red) is defined as the distance between the midpoint of the AP cut and the Cobb axis's projection on the horizontal cut plane (Blue).

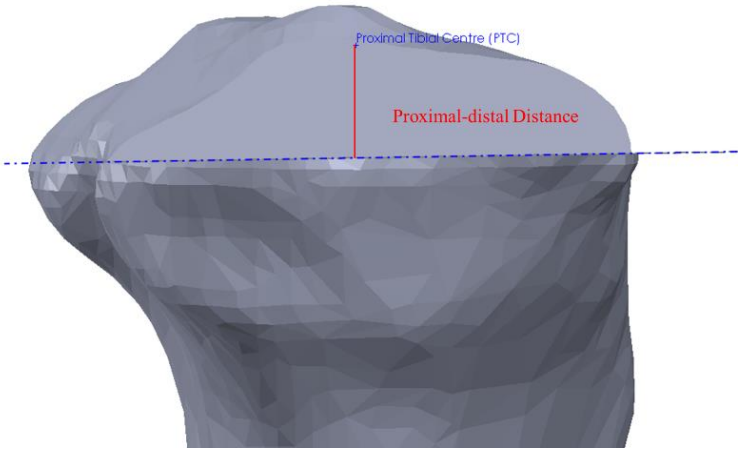

Figure 4.13: Measurement of the proximal-distal position of the tibial cuts. The proximal-distal distance (Red) is defined as the distance from the proximal tibial centre to the horizontal cut plane.

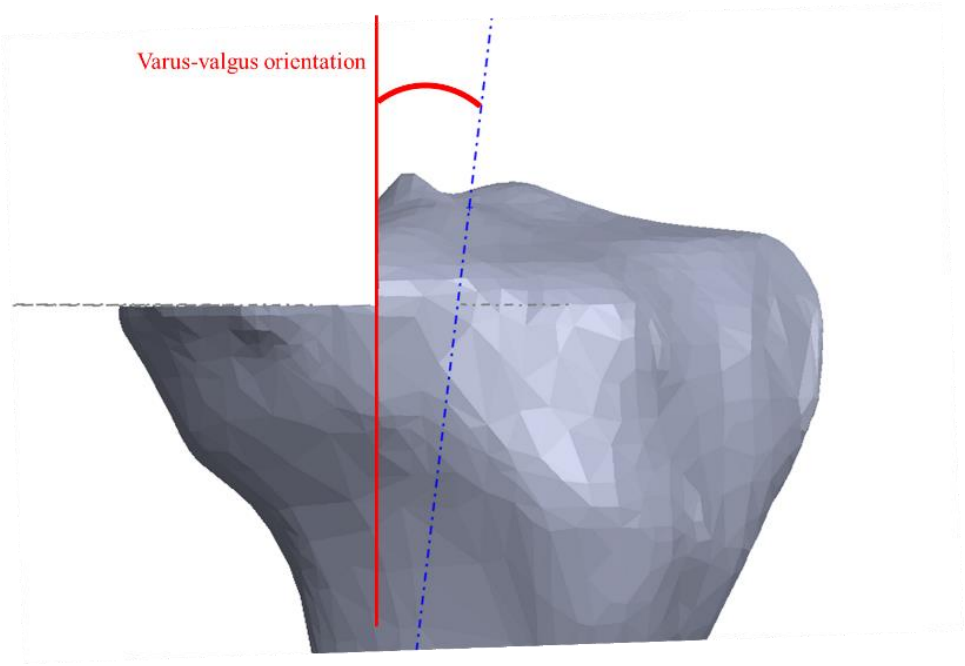

Figure 4.14: Measurement of the varus-valgus orientation of the tibial cuts. The varus-valgus angle is defined as the angle between the vertical cut plane and the tibial long axis (Blue).

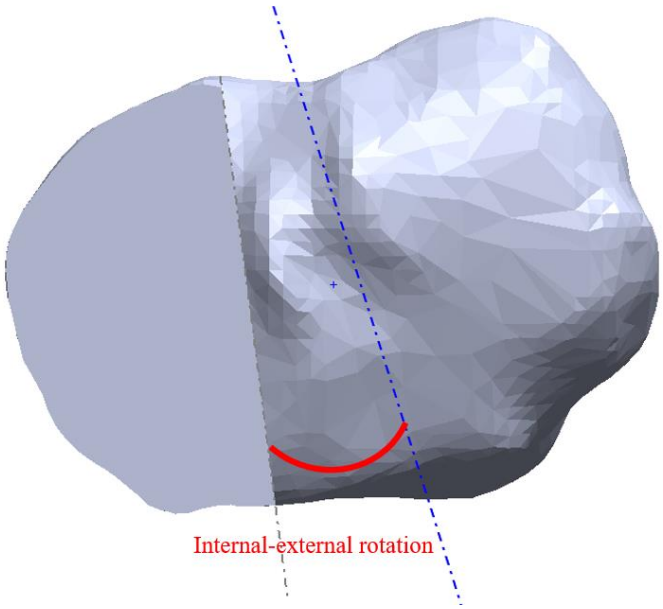

Figure 4.15: Measurement of the internal-external rotation of the tibial cuts. The internal-external angle (red) is defined as the angle between the vertical cut plane and the Cobb axis (blue).

The tibial component in the fractured tibia was overhanging anteriorly and medially. Thus, a tibial component one size smaller (Size B) was tested with the same tibial resections. The posterior margin of the tibial tray was flush with the posterior tibial cortex.

4.2.1.1 Finite Element Modelling

4.2.1.1.1 Geometry and Mesh

Finite element (FE) models of the fractured and unfractured tibia with the tibial component implanted in its post-operative position were built in ABAQUS/CAE 2020 (Dassault Systèmes, France). The tibial geometries segmented from the pre-operative CT scan of this patient with Mimics (version 23, Materialise, Leuven, Belgium) were imported to the FE models. A previous study claimed that a shortened tibia model would improve computational speed without affecting outcomes [161]. Also, truncating the tibia to the current length did not create a stress concentration at the bottom face of the shortened tibia affecting the stress near the tibial resection. Thus, only the proximal tibias were modelled in this study for analysis efficiency. The tibial resections were made with the revolve cut feature and the keel slots were created virtually using the Boolean function in Abaqus/CAE 2020 (Dassault Systèmes, France) with a Python script adapted from the previous work of Pegg et al. [110] (**Appendix A**). The positions of the vertical and horizontal cuts were found by replicating the position and orientation of the implanted tibial component referring to the immediate post-operative radiographs. It was assumed that the cuts were perfectly orthogonal to each other with no gaps between the component and the cut surface. Size C components were then virtually implanted in the FE models with the posterior margin flush with the back of the tibia.

In the PPF (right) tibia, when the component was positioned with its posterior margin flush with the posterior cortex and the keel being in the middle of the keel slot as suggested in the surgical techniques guide, the keel slot cut through the anterior cortex (**Figure 4.16 a, b**). The post-operative radiographs did not show clearly if the keel slot penetrated the cortex. Thus, a second scenario in which the keel slot was moved backwards by 1.81 mm so that

no hole (penetration through the tibial bone) was created in the tibia was also modelled. In this case, the component was still placed at the same position with the posterior margin flush with the posterior cortex. The keel was closer to the front of the keel slot than to the back and no hole was created in the tibia (**Figure 4.16 c, d**). This was intended to provide a more conservative estimate of the maximum stress in the tibia that fractured.

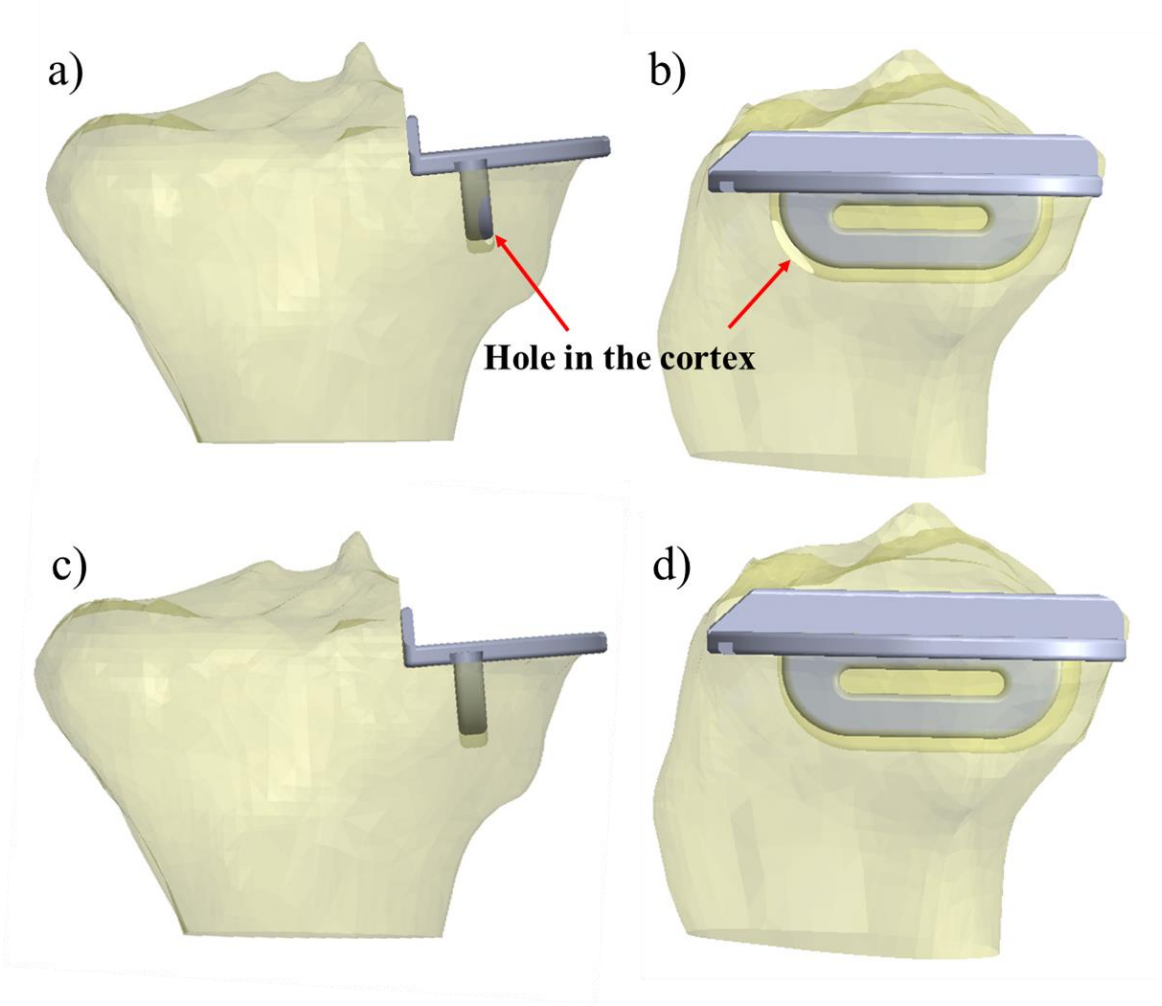

Figure 4.16: Anteroposterior views and lateral views of the tibias when Size C tibial components were implanted with the keel placed in the middle of the slot (a, b) and when the keel was placed closer to the front of the slot (c,d). When the keel was placed in the middle of the slot, a hole was created in the anterior part of the tibia (a,b).

Bone was found to behave more like a brittle material than a ductile material [162] and maximum tensile principal stress is generally used to assess brittle failure [163]. Thus, maximum principal stress, the maximum normal stress on a material when it is under loads, was used to indicate the risk of fracture.

The finite element mesh was created in the ABAQUS/CAE 2020 (Dassault Systèmes, France). The tibias were deformable and were meshed with quadratic tetrahedral elements (C3D10M) of 2.4 mm. Given the thickness of cortical bone at the medial proximal tibial diaphysis was found to be around 5-6 mm in an elderly Japanese cohort (61-83 years old) [164], 2.4 mm elements should be able to capture the geometry of the peripheral cortical bone at the medial plateau. The mesh was refined to 0.5 mm at the keel slot in the fractured tibia and 0.6 mm in the unfractured tibia. The percentage changes in the highest maximum principal stress in the tibia were 2% in both models of the fractured tibia when 0.4 mm elements were used. Thus, mesh refinement with elements of 0.5 mm was applied at the keel slot. Similarly, the results converged from a mesh size of 0.6 mm in the unfractured tibia. Thus, 0.6 mm elements were used to save analysis time. As the tibial components were orders of magnitude stiffer than trabecular bone, they were modelled as rigid and meshed with quadrilateral rigid elements (R3D4) of 2.4 mm. The mesh on the keel was refined to 0.8 mm to better capture the curvature on the edge (**Figure 4.17**).

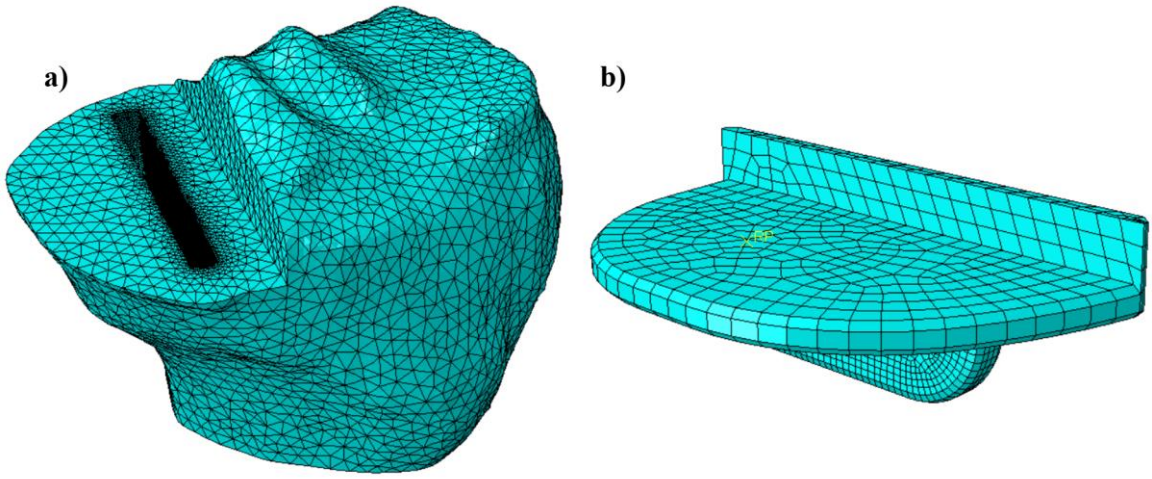

Figure 4.17: Mesh on the tibia (a) and on the tibial component (b).

4.2.1.1.2 Contact

Interference fit at the keel was simulated by the resolution of an initial overclosure. An interference of 0.16 mm was applied in both tibias [109]. Before the analysis, the tibial component elements were penetrating those of the tibia at the keel slot walls. Then the implantation of the tibial component at an interference fit was modelled by removing this overclosure between the bone and the implant. While the overclosure was resolved in this 'interference fit' step, the contact between the tibia and the implant was set as frictionless. The COF between the porous surface of the tibial component and the bone was changed to 0.99 thereafter [141].

4.2.1.1.3 Boundary Conditions and Loads

In each model, the distal end of the proximal tibia was fully constrained in all degrees of freedom throughout the analysis. A vertical load of 1000 N was applied to the tibial component to simulate the loading in the medial compartment of the knee joint during gait [165]. The load position was chosen as the position of the bearing when it was 1 mm away from the tibial wall and 8 mm posterior to the middle line of the implant. This is the

posterior-most position of the bearing during step-up movements [166], and it tends to occur in [167]. The load was perpendicular to the superior surface of the tibial component to simulate the load transferred from the bearing and it rotated with the tibial component. The tibial component was fully constrained in all degrees of freedom in the interference fit step and was free to move during the loading step.

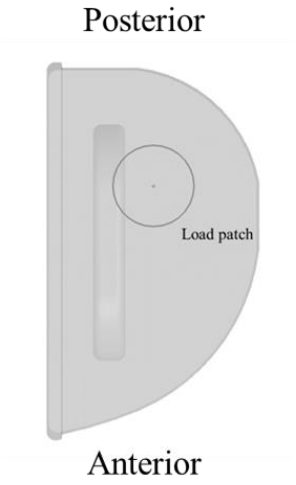

Figure 4.18: The load was applied onto a load patch which represented the position of the bearing when it was 1 mm away from the wall and 8 mm posterior to the centreline.

4.2.1.1.4 Material Properties

The material properties of bone were assigned to the tibia models through the py_bonemat_abaqus python package [168]. This software tool assigned elements with Young's modulus converted from the Hounsfield unit (HU) read from the CT scans using **Equation 4.1** and **Equation 4.2**. a and b are calibration parameters used to convert the CT HU values into the apparent density of bone (ρ_{app}). c, d and e are parameters of the power equation used to calculate Young's Modulus (E) from the apparent density of bone. Values of these parameters were taken from previous studies in the group on the same radiographs

and are listed in **Table 4.2**. This modelled the tibia as a heterogeneous linear elastic material with 600 material modulus intervals and a Poisson ratio of 0.35.

$$\rho_{app} = a + b * HU \quad [4.1]$$

$$E = c + \left(d * \rho_{app}\right)^{e} \quad [4.2]$$

Table 4.2: Parameters used in the conversion from Hounsfield Unit values from medical images to elastic modulus.

Parameter	Values
a	$\begin{cases} -1022.7580833244992, & if\ HU \leq 1937 \\ 451.47970926711076, & if\ HU > 1937 \end{cases}$
b	$\begin{cases} 1.13113537358083325, & if\ HU \leq 1937 \\ 0.5377649909145973, & if\ HU > 1937 \end{cases}$
c	$\begin{cases} 0, & if\ HU \leq 1200 \\ -6142, & if\ HU > 1200 \end{cases}$
d	$\begin{cases} 0.58, & if\ HU \leq 1200 \\ 14, & if\ HU > 1200 \end{cases}$
e	$\begin{cases} 1.3, & if\ HU \leq 1200 \\ 1, & if\ HU > 1200 \end{cases}$

The CT scans were recorded in the format of Digital Imaging and Communications in Medicine (DICOM). They were taken with a slice thickness of 2 mm and the pixel spacing was (0.781, 0.781) in the transverse plane.

The material modulus distribution was visualised with a Python script developed by Slawomir Polanski.

4.2.1.2 Finite Element Modelling of Fractured Tibial Resection in the Unfractured Tibia

With the differences in the position and orientation of the tibial components found, the cuts in the fractured tibia (right tibia) were replicated in the unfractured tibia by moving and changing the orientation of the original cuts. These changes were achieved by altering the definition of the position and orientation of the horizontal and vertical cut planes in the Python code (**Appendix B**). The tibia was loaded with a 1000 N load perpendicular to the superior surface of the tibial tray in an identical fashion to the fractured tibia as in **4.2.1.1.3**.

4.2.2 Patient 2

The same evaluation method was repeated on the second patient who experienced PPF in the left tibia after bilateral medial OUKR.

Same as for Patient 1, the patient-related factors of the two tibias were analysed. The tibial geometries were segmented from the pre-operative CT scans and the position of the tibial components in both tibias were found by referring to the immediate post-operative AP and lateral radiographs. Size A tibial components were virtually implanted into the two tibias in ABAQUS/CAE 2020 (Dassault Systèmes, France) following the same procedure used for Patient 1. The difference in the position of the tibial components was measured in terms of their mediolateral position, distal-proximal position, valgus-varus orientation, and internal-external rotation using the same measuring protocol used for Patient 1.

In the fractured (left) tibia, the keel slot cut through the cortex and created holes in both the anterior and posterior parts of the tibia (**Figure 4.19**).

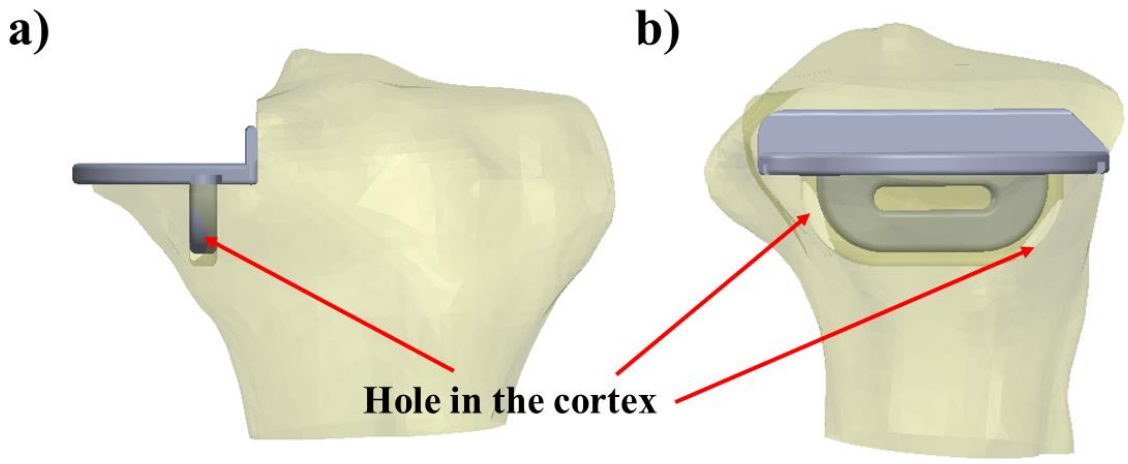

Figure 4.19: Anteroposterior view (a) and lateral view (b) of the fractured (left) tibia of Patient 2 with a Size A component implanted at the post-operative position. The keel slot created holes in both the anterior and posterior cortex.

The same FEA model template was conducted on the two OUKR-implanted tibias. The boundary conditions, contact settings, and material properties were kept the same as those in the models of Patient 1 (see **4.2.1**). The tibias were deformable and were meshed with quadratic tetrahedral elements (C3D10M) of 2.4 mm. The same mesh convergence study was conducted with the same criterion used in **4.2.1.1.1**. The mesh at the keel slot was refined to 0.6 mm.

The horizontal and vertical saw cuts in the fractured tibia (left tibia) were again replicated in the unfractured tibia (right tibia) with the measurements made about the differences in the tibial resection positions.

As the Size A tibial component was significantly overhanging medially, a tibial component one size smaller (Size AA) was also tested in the fractured tibia.

4.2.3 Validation of Finite Element Model against Experiment

To assess the validity of the FE models and to assess if the highest maximum principal stress value is a valid indication of risk of fracture, the results from a series of FE models were compared to a biomechanical experiment using PCF20 Sawbones Blocks.

As the surgical error in tibial resection is a proposed risk factor of tibial PPF, it was hypothesised that changes in the position of the tibial component would affect the stress the surrounding bone withstood under loads.

Modifications to the surgical cuts in the unfractured tibia of Patient 1 were made by modifying the position and orientation of the vertical and horizontal cut planes (**Table 4.3**). To prevent unintended and immature failure of the Sawbones tibias during sample preparation which might happen when the keel was press-fit into the keel slot at an interference, all models with cut modifications were made for a Size B tibia component. It was assumed that the AP position of the implants was determined by aligning the posterior margin of the tray to the posterior cortex. Keel slots with the same 0.16 mm interference were made in each model correspondingly [109]. The fractured cut was also replicated for both Size B and Size C components.

Table 4.3: Description of finite element models with modified tibial resections tested against the experiment.

Model Name	Modification to Component Position	Component Size
Unfractured Cut_C	None	C
Unfractured Cut_B	None	B
Medial 3 mm_B	Move the component medially by 3 mm	B
Distal 3 mm_B	Move the component distally by 3 mm	B
Valgus 5 degrees_B	Rotate the component into valgus around the lateral edge of the keel slot by 5 degrees	B
External 20 degrees_B	Rotate the component externally around the mid-point of the AP cut by 20 degrees	B
Fractured Cut_B	Move the component into the fractured cut position based on the measurements found in **4.2.1**	B
Fractured Cut_C	Same as above	C

The CAD models were then mirrored horizontally as these models were of the left tibia of Patient 1 while only Right Size B and Size C medial tibial components were available for biomechanical testing. CAD models of these flipped tibias were turned into blocks with one medial plateau on each side for testing by Chris Hunt (**Figure 4.20**). The geometries of the blocks were machined from the PCF20 Sawbones block (Heritage Engineering Ltd, Bicester, UK).

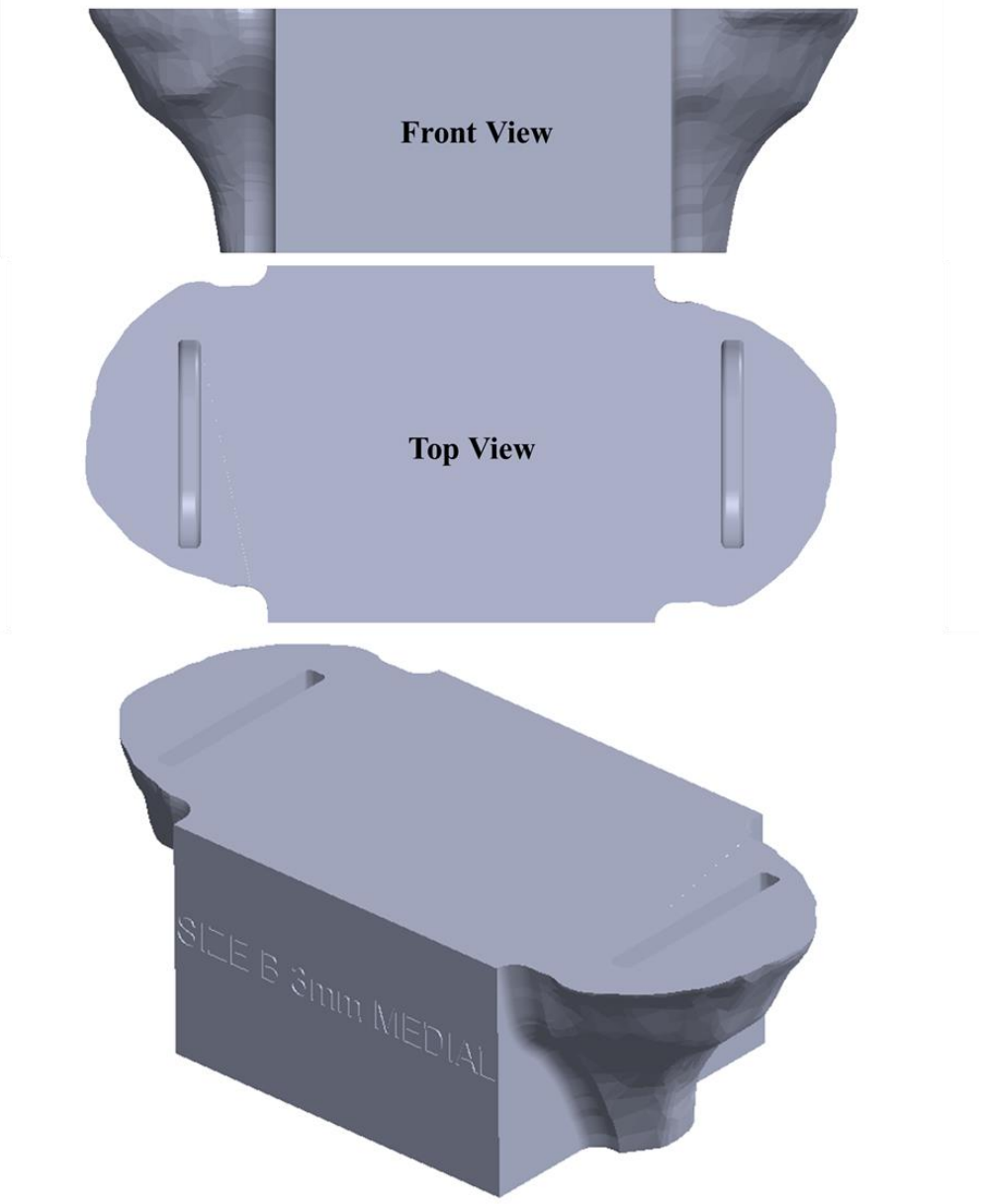

Figure 4.20: An example of the CAD model of the blocks used for testing.

The load-to-fracture experiment was conducted on these Sawbones blocks by Lachlan Arthur. The load under which the Sawbones tibia fractured for each tibia model was recorded [169].

FEA was conducted on these eight tibia models using the same method described in **4.2.1.1**. Other than using the heterogeneous material properties of bone based on elastic modulus mapped from bone density as in previous models, the models were also run with the material properties of Sawbones (PCF20). Sawbones was modelled as a homogeneous linear elastic material with a Young's Modulus of 240 MPa and a Poisson ratio of 0.3 [126, 170]. The changes in the highest maximum principal stress in the tibia brought by the cut modifications were compared to those in load to fracture from the experiment.

The 3D models of the tibias with the tibial resection and keel slot created were imported into SolidWorks 2022 (Dassault Systèmes, France). The shortest distances between the keel slot and the posterior and anterior surfaces of the tibia were measured with the Evaluate-Measure feature (**Figure 4.21**). This measurement will be referred to as the slot-cortex distance (SCD) from this point forward.



Figure 4.21: Measurement of slot-cortex distance. The shortest distance between the keel slot surface and the exterior surface of the tibial was found in Solidworks 2022.

4.3 Results

4.3.1 Patient 1

Table 4.4 lists the results of the comparison of the patient-related PPF risk factors of the two tibias in Patient 1. No large difference was found between the bone quality, tibial size and medial condyle morphology of the fractured and unfractured tibia (**Table 4.5**). The elastic modulus of the trabecular and cortical bone was read from the FE models after heterogeneous material properties were applied with the py_bonemat_abaqus Python package. Both tibias showed trabecular bone and cortical bone of similar elastic modulus and the aspect ratios of the two tibial plateaus were both around 1.5. In the preoperative CT scans, both tibias had sclerosis at the proximal tibia plateau (**Figure 4.22**). The MPTAs of the fractured and unfractured tibia were both 80° and MELs penetrated the medial cortex in both tibias, indicating that both tibias were extramedullary type tibia (**Figure 4.23**).

Table 4.4: Summary of the comparison of the relevant patient-related risk factors of the fractured and unfractured tibia of Patient 1.

Patient factors	Evaluation Methods	Difference
Poor bone quality/ Osteoporosis	Bone stiffness	No
	Existence of sclerotic bone from OA	No
Small tibial size	Width, length and aspect ratio of tibia plateau	No
Overhanging medial plateau	Medial proximal tibial angle (MPTA)	No
	Extramedullary or intramedullary	No

Table 4.5: Comparison of the bone quality and tibial size of the fractured and unfractured tibia of Patient 1.

	Unfractured (Left)	**Fractured (Right)**
Trabecular bone stiffness	~200 – 2000 MPa	~200 – 2000 MPa
Max. Cortical bone stiffness	24.5 GPa	24.2 GPa
Aspect ratio of plateau	1.46	1.52

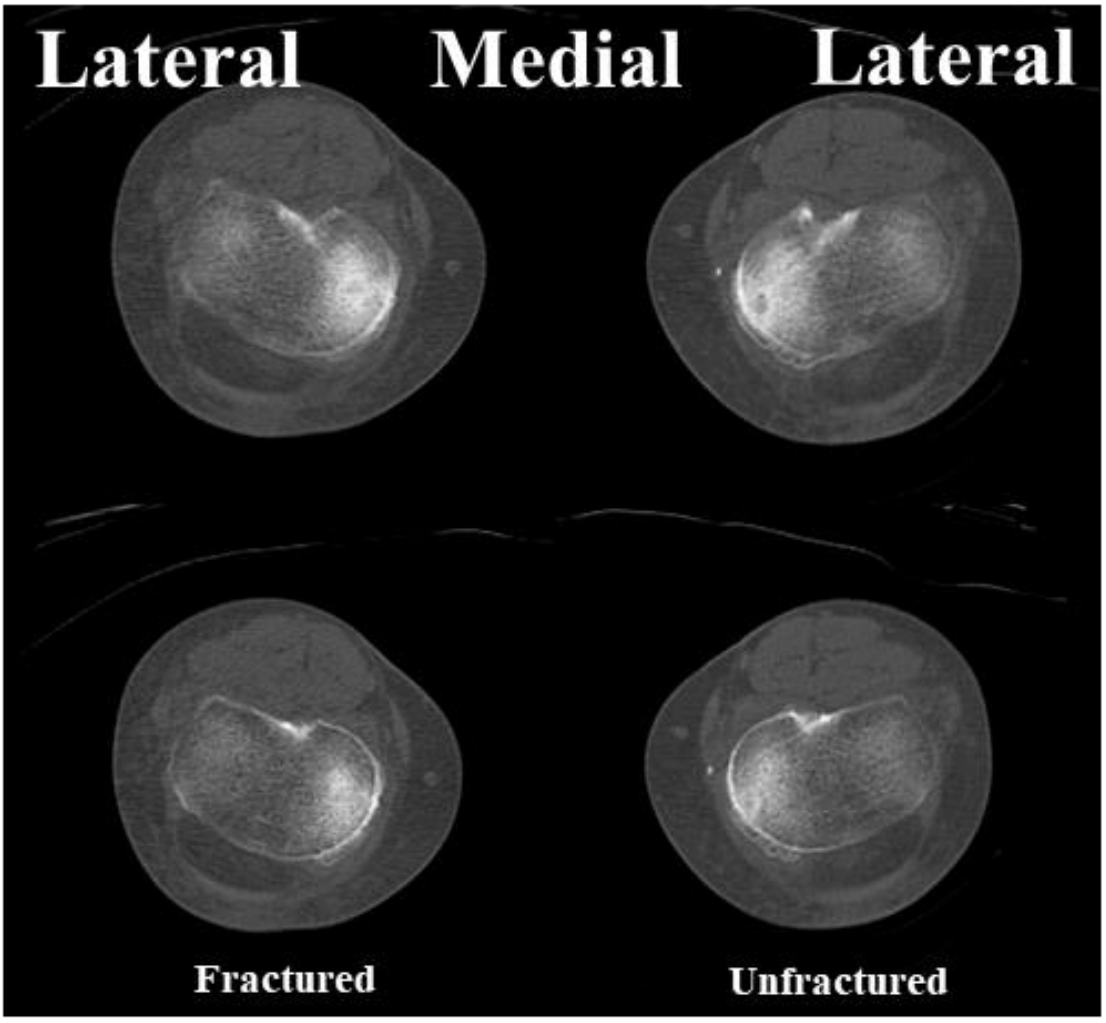

Figure 4.22: Slices of pre-operative computed tomography scans of Patient 1. The slices were taken at the proximal tibial plateau. Brighter regions which indicate sclerosis were shown in both tibias. Pixel size (0.781, 0.781).

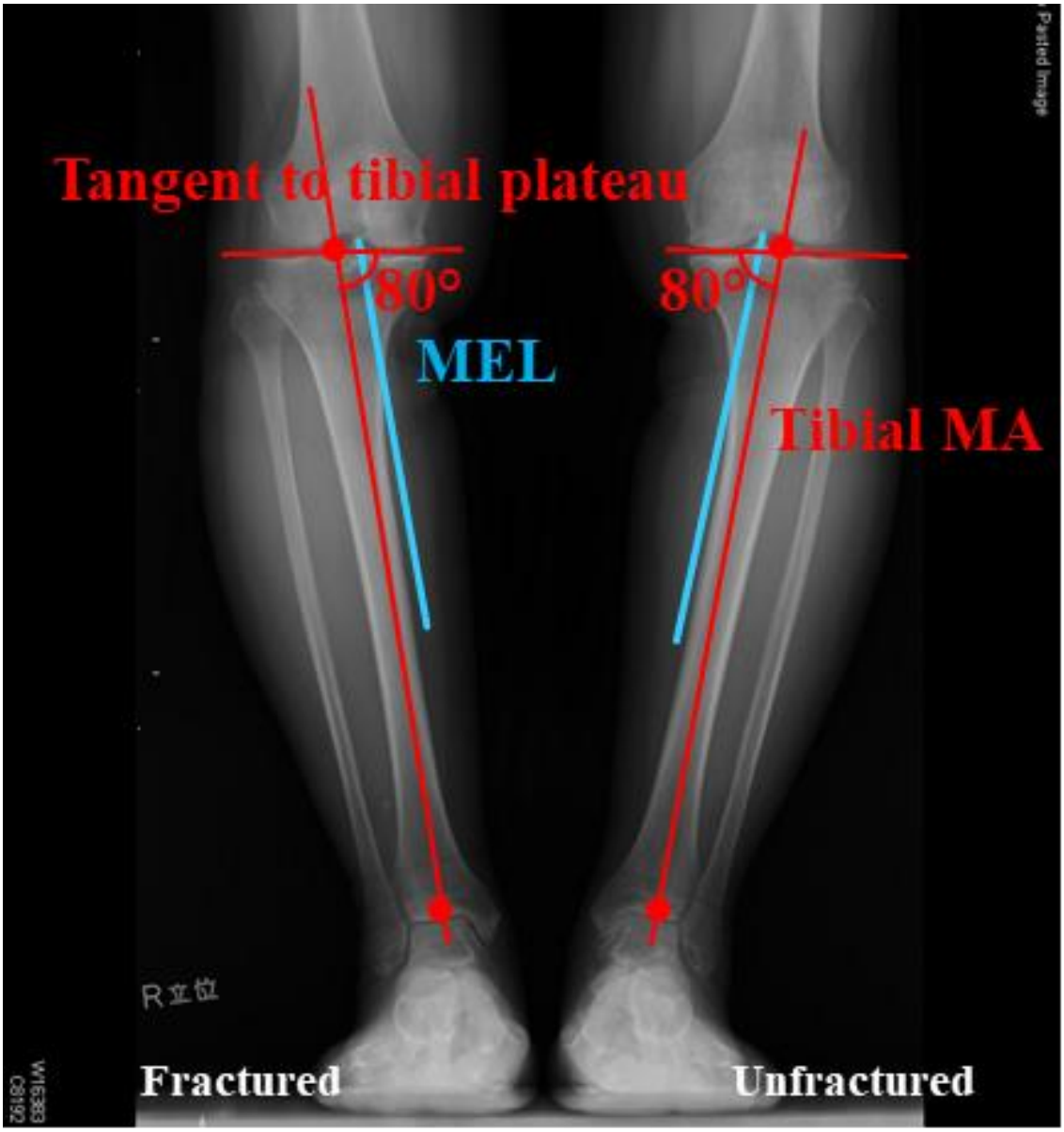

Figure 4.23: Measurements of the medial proximal tibial angles and medial eminence lines (MELs) (blue) of the fractured and unfractured tibia of Patient 1. Both MELs penetrated the medial cortex. MA: mechanical axis.

Compared to the component in the unfractured tibia (left), the tibial component in the fractured tibia (right) was 0.74 mm more medial, 2.44 mm more distal, 1.73° more valgus and 18.83° more externally rotated (**Table 4.6**).

Table 4.6: Positions and orientations of tibial resections in Patient 1.

	Right Leg (Fractured)	Left Leg	Comparison
Posterior slope	9.78°	10.16°	Very small difference (fractured cut less posterior by 0.38°)
Internal-External Rotation	8.77° External to the Cobb Axis	10.06° Internal to the Cobb Axis	Fractured cut is more externally rotated by 18.83°
Medial-Lateral position	• Anterior Cut Point 9.36 mm medial • Posterior Cut Point 16.86 mm medial • Mid-point 13.11 mm medial to the Cobb Line	• Anterior Cut Point 16.72 mm medial • Posterior Cut Point 8.02 mm medial • Mid-point 12.37 mm medial to the Cobb Line	There is no large difference in the medial lateral position of the mid-point of the AP cut (fractured cut is 0.74 mm more medial). As the difference in external/internal rotation is large, the anterior cut point in the fractured tibia is 7.36 mm more lateral. The posterior cut point in the fractured tibia is 8.84mm more medial
Proximal-Distal position	12.57 mm	10.13 mm	Fractured cut 2.44 mm deeper
Varus-Valgus Rotation	3.50° Varus	5.23° Varus	Fractured cut 1.73° more valgus

Figure 4.24 shows the maximum principal stress in the unfractured (left) tibia of Patient 1 when a 1000 N load was applied perpendicular to the superior surface of the tibial tray. All stress plots from this point, unless mentioned, are shown in the unit of MPa. The highest stress, which was 49.1 MPa was seen at the anteromedial corner of the keel slot. No large increase in stress was seen in any particular region of the tibia. **Figure 4.25** shows the Young's modulus of the bone in the tibia. The stiffer bone at the periphery marks the stiffer cortical bone. The keel slot was away from the cortical bone. All material plots mentioned later are in the unit of MPa.

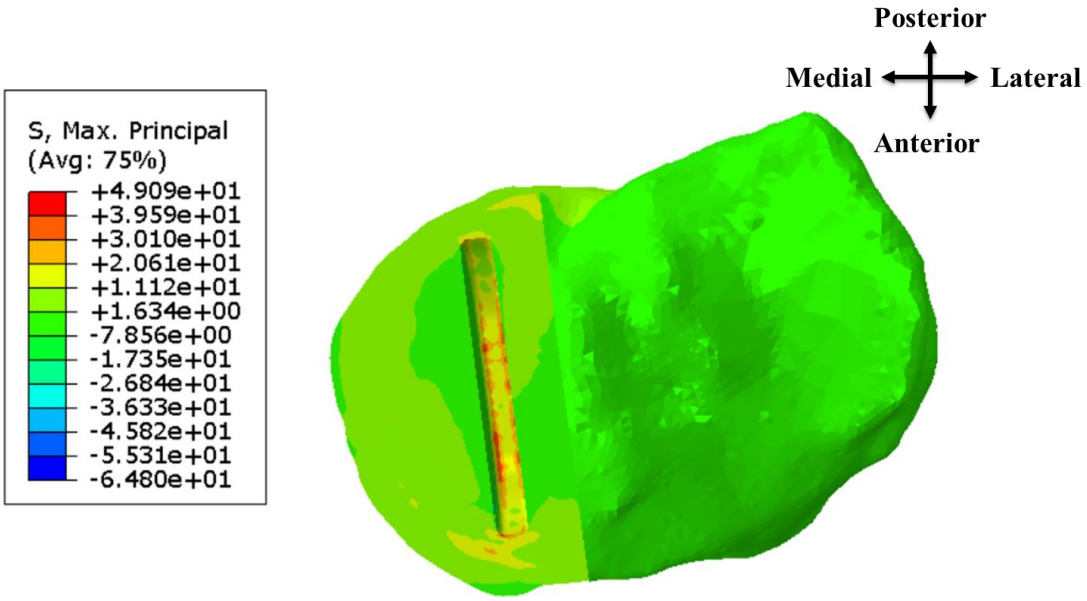

Figure 4.24: Maximum principal stress plot of the unfractured tibia of Patient 1 when a 1000 N load was applied.

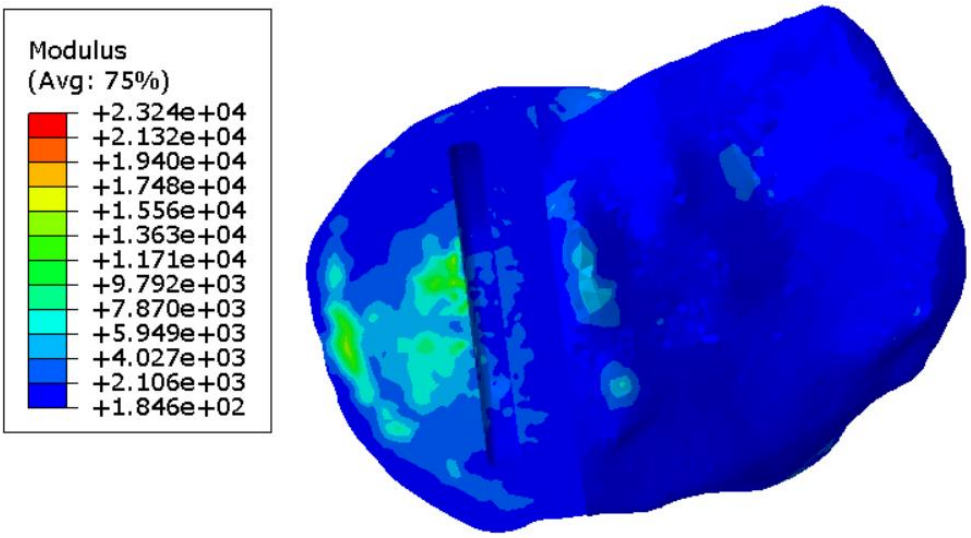

Figure 4.25: Material plot of the unfractured tibia of Patient 1, showing Young's Modulus of the tibia bone.

Figure 4.26 shows the maximum principal stress in the proximal tibia of the fractured tibia when the keel slot penetrated the bone. This happened when the posterior margin of the tray was flush with the posterior cortex and when the keel was placed in the middle of the keel slot in the AP direction. The highest maximum principal stress was 157.1 MPa and

appeared at the anteromedial corner of the keel slot. The keel slot cut through the medial cortical bone (**Figure 4.27**).

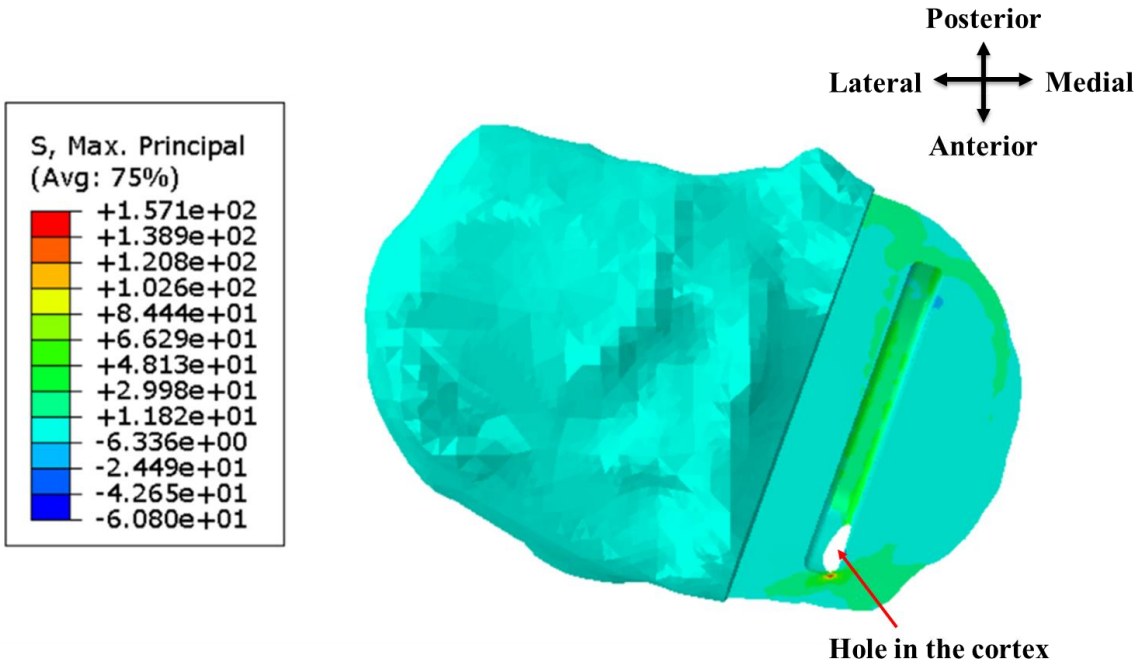

Figure 4.26: Maximum principal stress plot of the fractured (right) tibia of Patient 1 when a 1000 N load was applied. The keel slot cut through the tibia and made a hole.

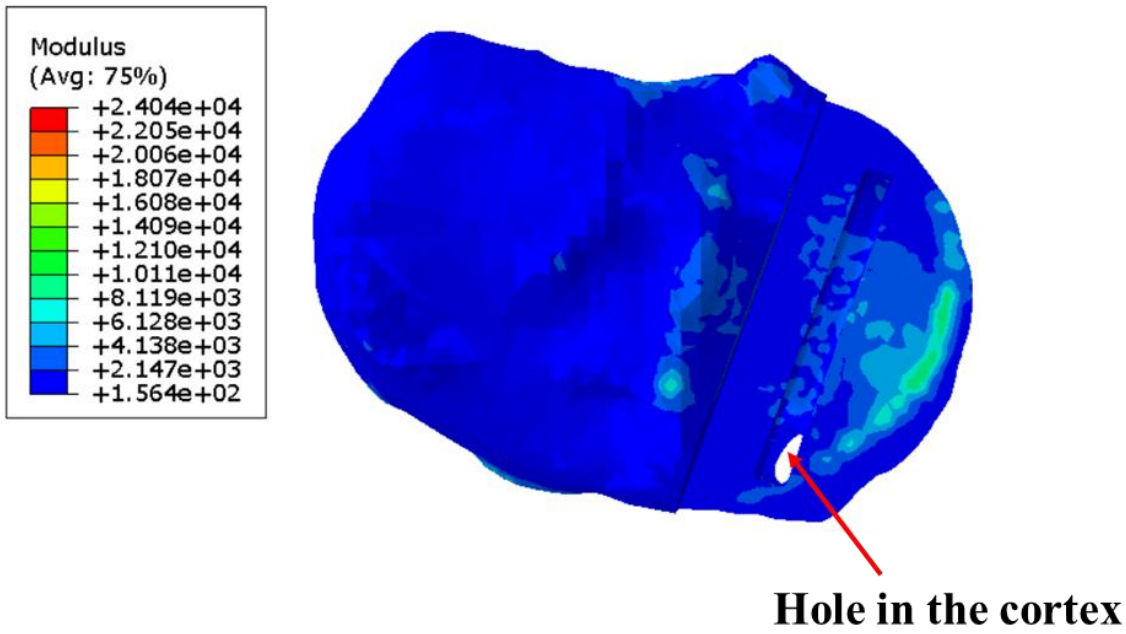

Figure 4.27: Material plot of the fractured tibia of Patient 1 showing the Young's Modulus of the tibia bone.

Figure 4.28 shows the maximum principal stress in the bone when the keel slot was moved backwards by 1.81 mm so that no hole was created in the bone during keel slot preparation. The highest stress was 152.6 MPa at the anteromedial corner of the keel slot. Though there was no hole in the tibia, the keel slot still cut into the cortex (**Figure 4.29**).

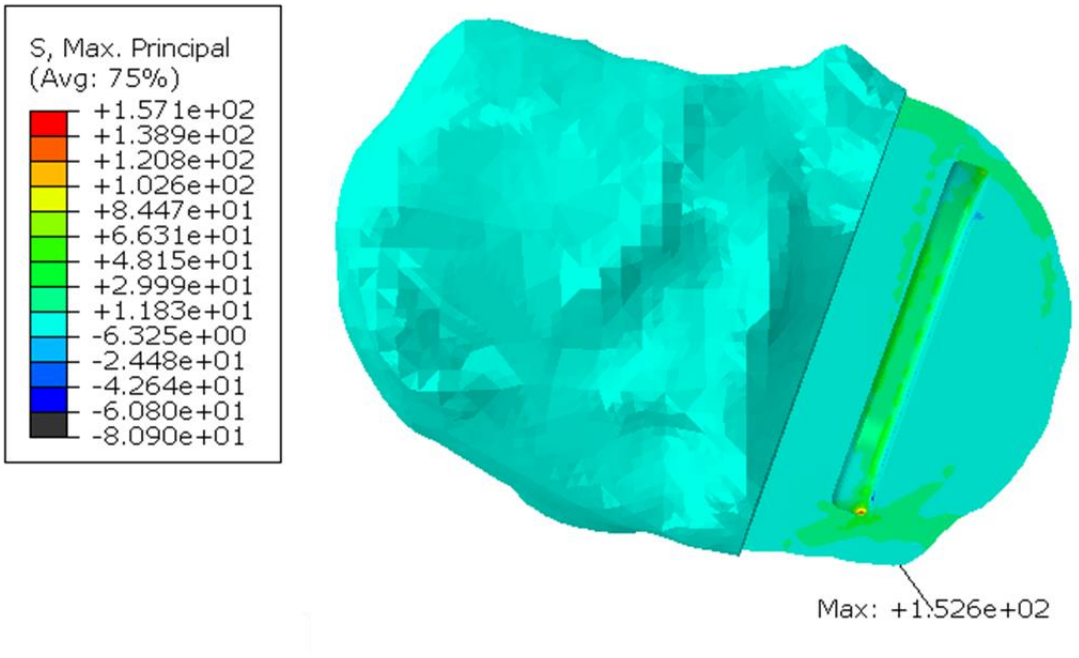

Figure 4.28: Maximum principal stress plot of the fractured tibia of Patient 1 when a 1000 N load was applied. The keel slot was moved backwards by 1.81 mm to avoid making a hole in the bone. The figure is in the same scale as ***Figure 4.26****.*

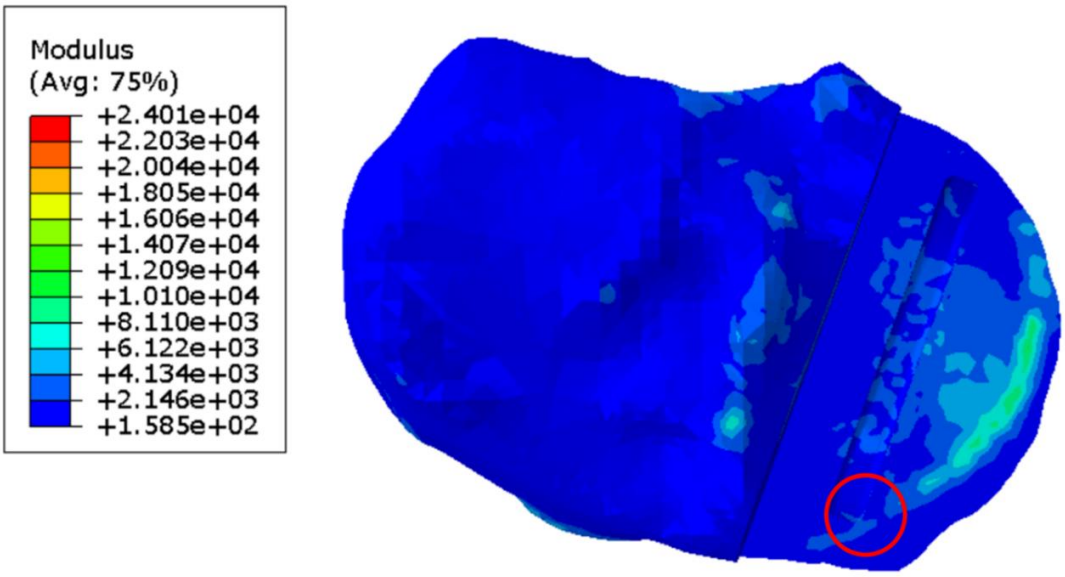

Figure 4.29: Material plot of the fractured tibia of Patient 1. The front of the keel slot cut into the cortical bone, marked by the red circle.

When the tibial resection in the fractured tibia was replicated in the unfractured tibia, the highest maximum principal stress value in the tibia was 2.4 times the stress when the component was implanted at the standard position (117.2 vs 49.1 MPa). This was again found at the anteromedial corner of the keel slot (**Figure 4.30**), similar to what happened in the fractured tibia (**Figure 4.29**). The material plot showed that with this tibial component positioning, the keel slot would cut into the stiffer cortical bone regardless of the tibia they were made in (**Figure 4.31**).

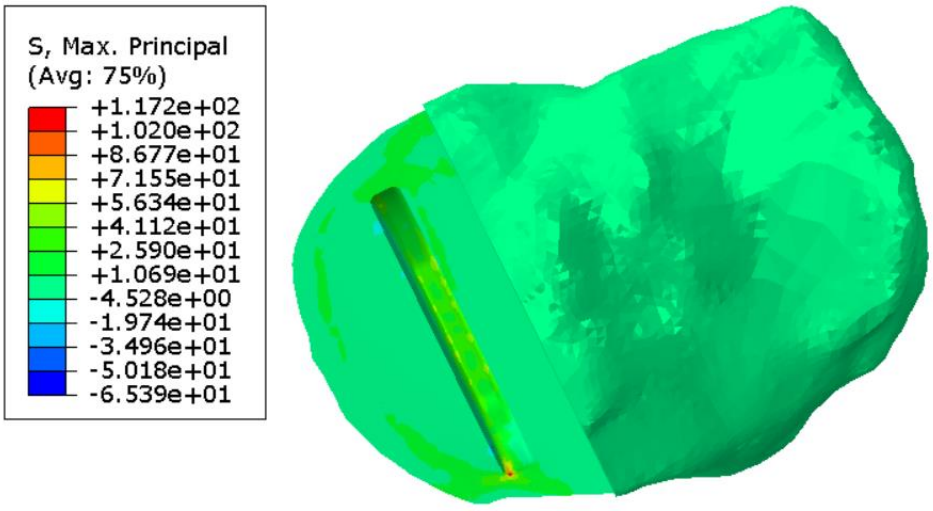

Figure 4.30: Maximum principal stress plot of the unfractured tibia when the fractured cuts were replicated.

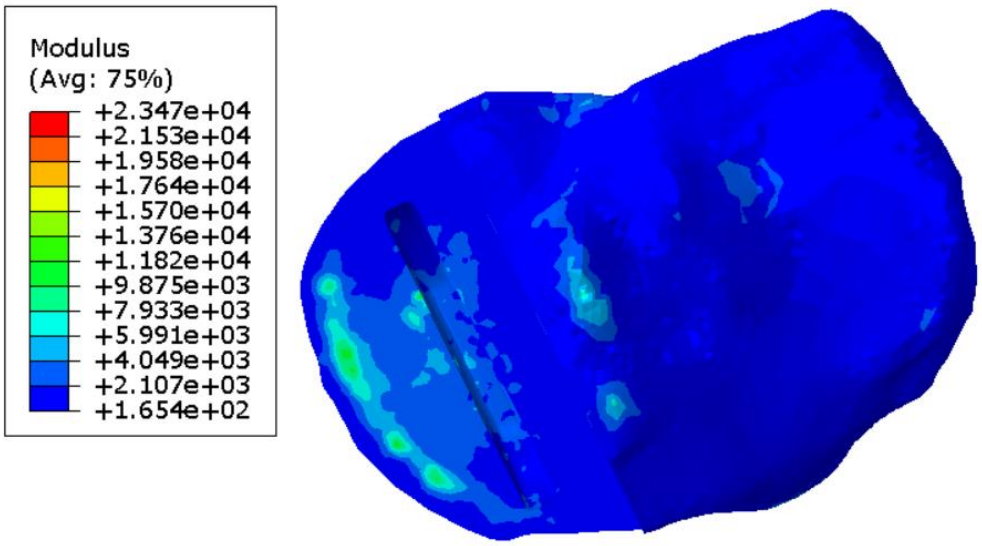

Figure 4.31: Material plot of the unfractured tibia when the fractured cuts were replicated. The front of the keel slot cut into the cortical bone.

When a Size B tibial component was implanted in the fractured tibia, better coverage was achieved with less medial and anterior overhang (**Figure 4.32**). The highest maximum principal stress, which was shown at the anteromedial corner of the keel slot was lowered by 60% (152.6 MPa vs 62.0 MPa). No significant rise in stress was found in the tibia and the stress level was similar in the anterior and posterior part of the medial condyle (**Figure 4.33**).

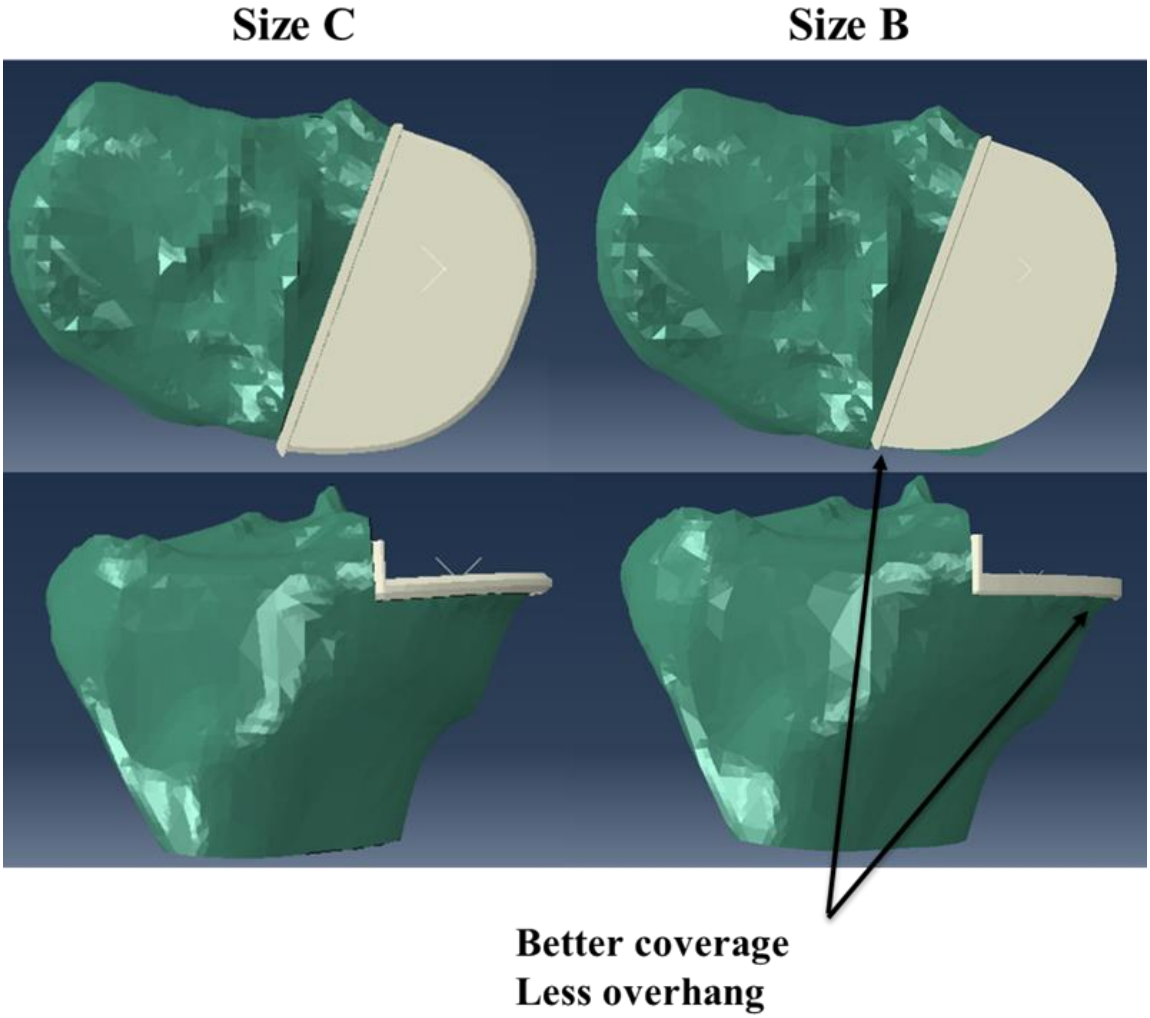

Figure 4.32: The fractured tibia with Size C (left) or Size B (right) tibial component implanted with the same vertical and horizontal tibial resections. A better coverage and less medial and anterior overhang were shown when a Size B component was implanted.

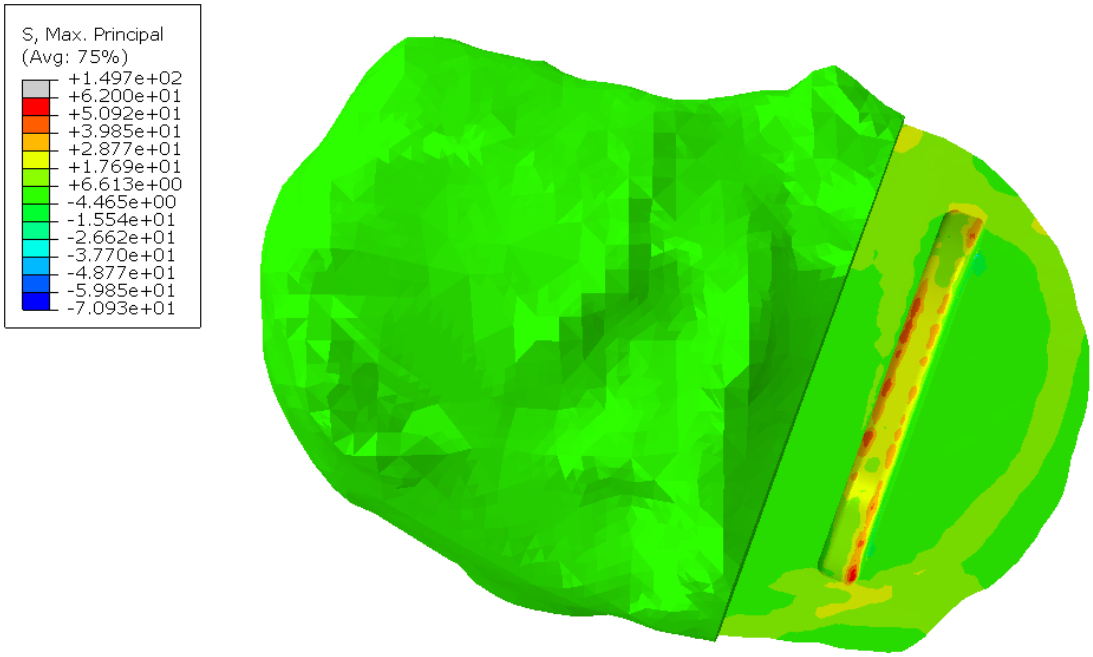

Figure 4.33: Maximum principal stress plot of the fractured tibia when a Size B component was implanted with the same tibial resection.

4.3.2 Patient 2

No difference in the patient factors was found between the fractured and unfractured tibia of Patient 2 (**Table 4.7**). The left (PPF) and right (non-PPF) tibia showed similar trabecular and cortical bone elastic modulus and both tibias showed sclerosis at the medial plateau (**Table 4.8**, **Figure 4.34**). The aspect ratio of the fractured tibia (left) and unfractured tibia (right) were both around 1.55. MPTAs of both the right tibia and the left tibia were 79° (**Figure 4.35**). MEL passed the medial cortex in both tibias, thus, both tibias were extramedullary type tibia (**Figure 4.36**).

Table 4.7: Summary of the comparison of the relevant patient-related risk factors of the fractured and unfractured tibia of Patient 2.

Patient factors	Evaluation Methods	Difference
Poor bone quality/Osteoporosis	Bone stiffness	No
	Existence of sclerotic bone from OA	No
Small tibial size	Width, length and aspect ratio of tibia plateau	No
Overhanging medial plateau	Medial proximal tibial angle (MPTA)	No
	Extramedullary or intramedullary	No

Table 4.8: Comparison of the bone quality and tibial size of the fractured and unfractured tibia of Patient 2.

	Fractured (Left)	Unfractured (Right)
Trabecular bone stiffness	~50 – 2000 MPa	~60 – 2000 MPa
Max. Cortical bone stiffness	23.7 GPa	24.7 GPa
Aspect ratio of plateau	1.55	1.55

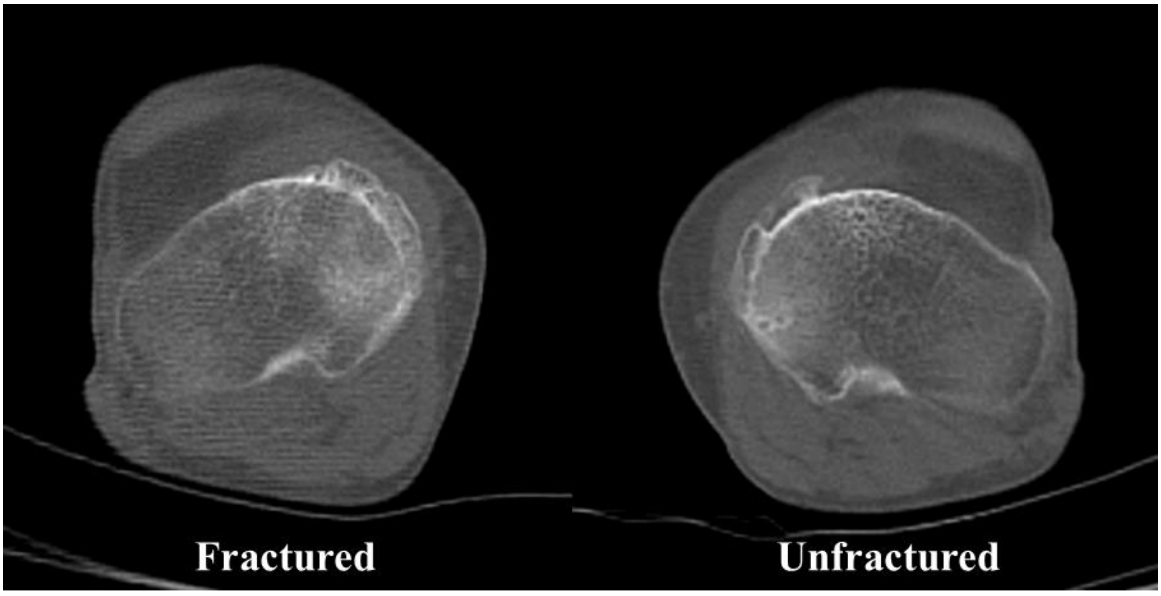

Figure 4.34: Slices of pre-operative CT scans of Patient 2. The slices were taken at the proximal tibial plateau. Brighter regions which indicate sclerosis were shown in both tibias. Pixel size (0.781, 0.781).

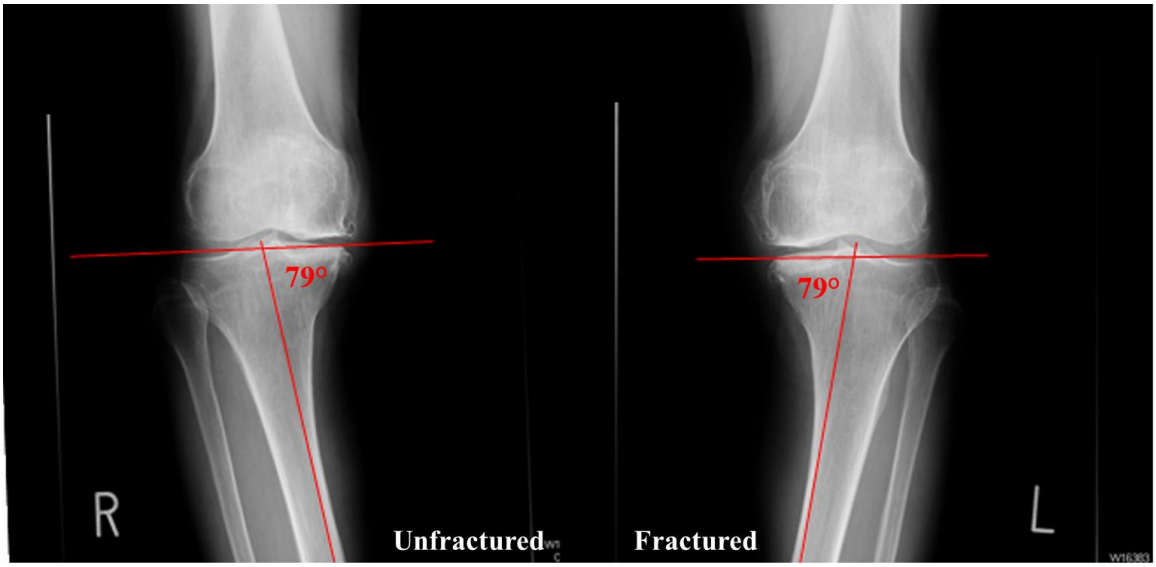

Figure 4.35: Measurements of the medial proximal tibial angles (MPTAs) of the unfractured and the fractured tibias of Patient 2.

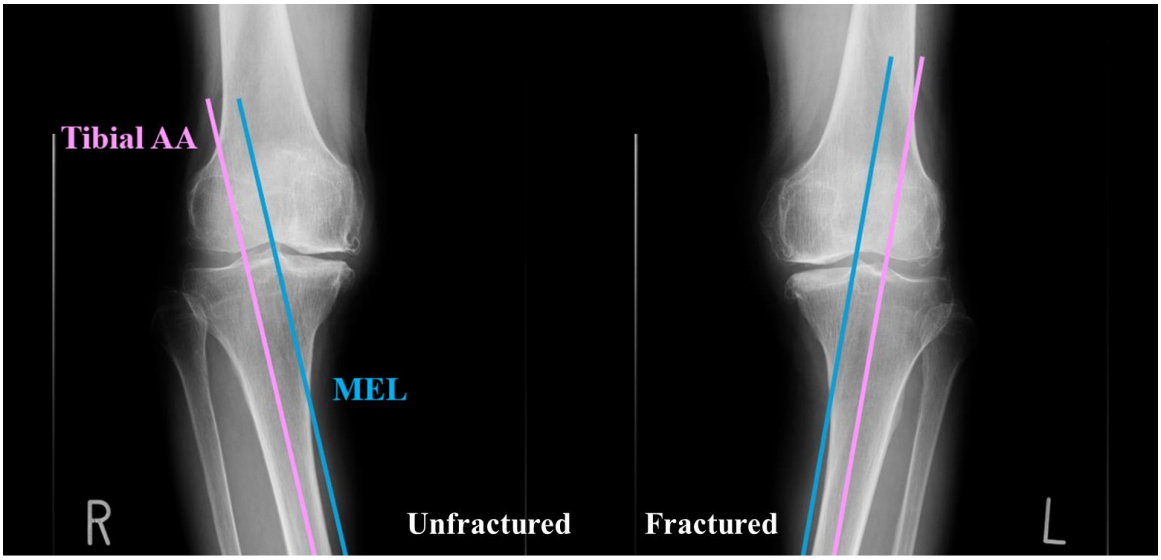

Figure 4.36: Medial eminence lines (MELs) of the fractured and unfractured tibia of Patient 2. Both MELs penetrated the medial cortex. AA: anatomical axis.

Compared to the tibial resection in the right tibia which did not fracture, the horizontal and vertical cuts in the left tibia were 3.95 mm more medial, 1.36 mm more distal, 1.47° more valgus and 16.4° more internally rotated (**Table 4.9**).

Table 4.9: Positions and orientations of tibial resections in Patient 2.

	Right Leg	Left Leg (Fractured)	Comparison
Posterior slope	8.53°	7.32°	1.21° less posteriorly sloped
Internal-External Rotation	12.87° External to the Cobb Axis	3.53° Internal to the Cobb Axis	Fractured cut is more internally rotated by 16.40°
Medial-Lateral position	• Anterior Cut Point 3.60 mm medial • Posterior Cut Point 13.95 mm medial • Mid-point 8.78 mm medial to the Cobb Axis	• Anterior Cut Point 14.05 mm medial • Posterior Cut Point 11.41 mm medial • Mid-point 12.73 mm medial to the Cobb Axis	Mid-point of the AP cut: fractured cut is 3.95 mm more medial.
Proximal-Distal position	16.09 mm	17.45 mm	Fractured cut 1.36 mm deeper
Varus-Valgus Rotation	6.10° Varus	4.63° Varus	Fractured cut 1.47° more valgus

Maximum principal stress plots of the fractured and non-fractured tibia are shown in **Figure 4.37** and **Figure 4.39**. The highest maximum principal stress in the fractured (left) tibia was 701.9 MPa. This value was found at the anteromedial corner of the keel slot and extended to the hole in the anterior cortex. A very high stress (311.8 MPa) was also shown in the posterior cortex near the posterior hole. The highest maximum principal stress in the unfractured (right) tibia was 63.1 MPa, which was 9.0% of that of the fractured tibia and was found at the anteromedial corner of the keel slot.

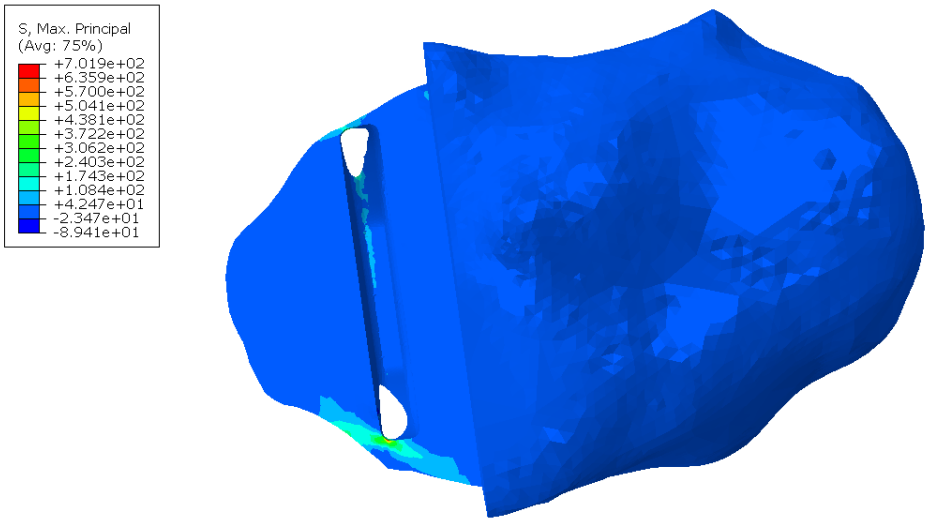

Figure 4.37: Maximum principal stress in the fractured tibia of Patient 2.

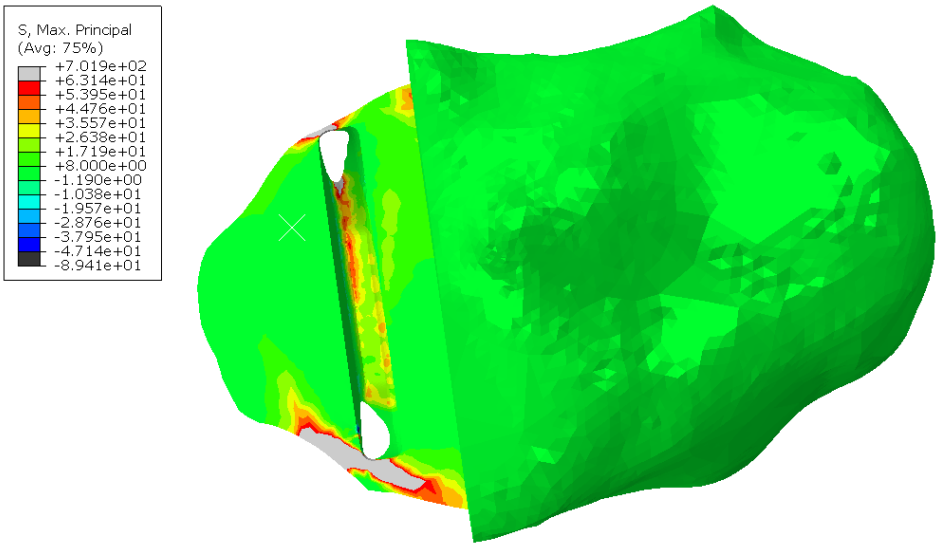

Figure 4.38: Maximum principal stress in the fractured tibia of Patient 2, in the same scale as ***Figure 4.37****.*

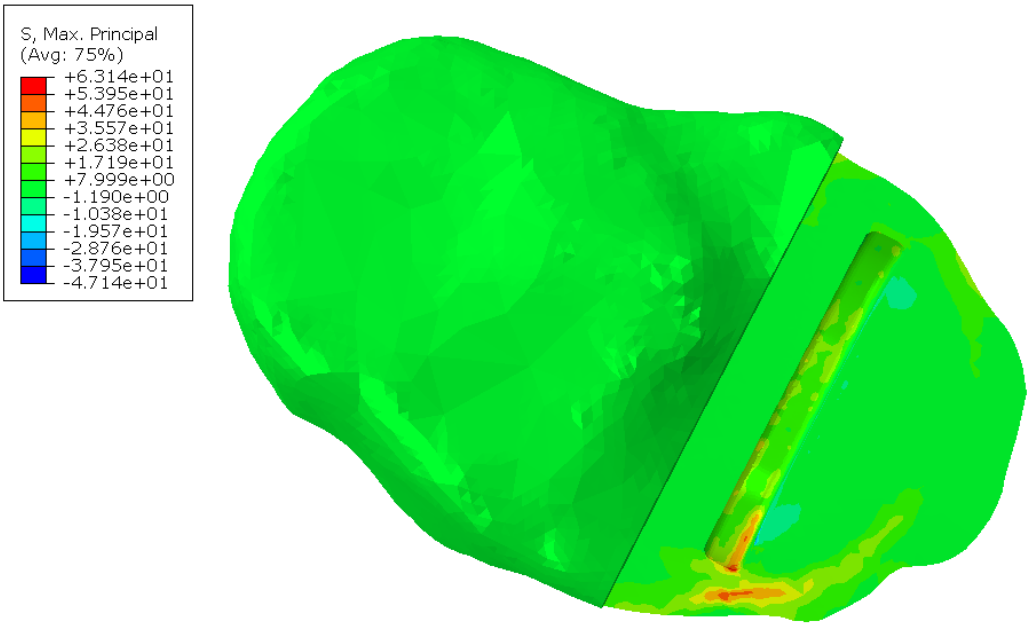

Figure 4.39: Maximum principal stress in the unfractured tibia of Patient 2.

Figure 4.40 and **Figure 4.41** show the elastic modulus of the bone in the two tibias. The keel slot in the fractured tibia cut through the cortex while that in the unfractured tibia was away from the cortex, though cut into the anterior sclerotic bone.

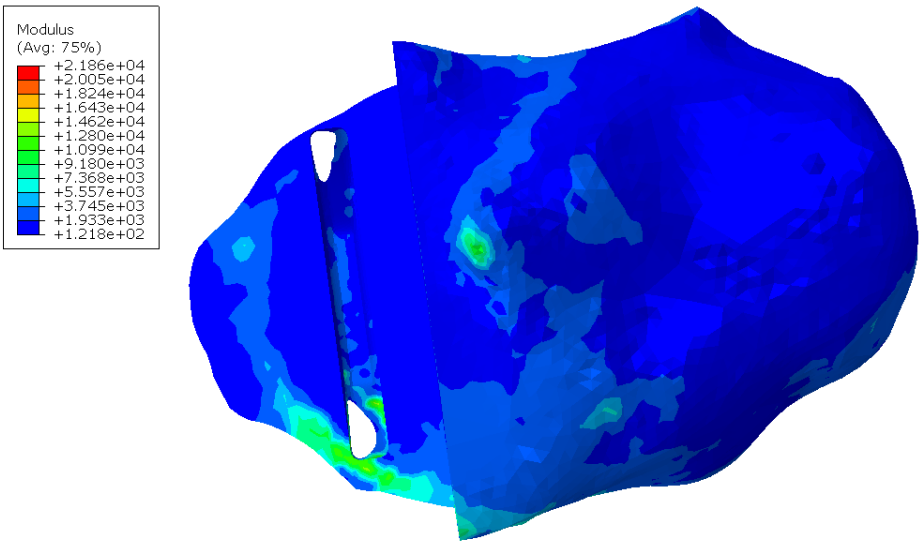

Figure 4.40: Material plot of the fractured tibia of Patient 2. Keel slot cut through the anterior and posterior cortex.

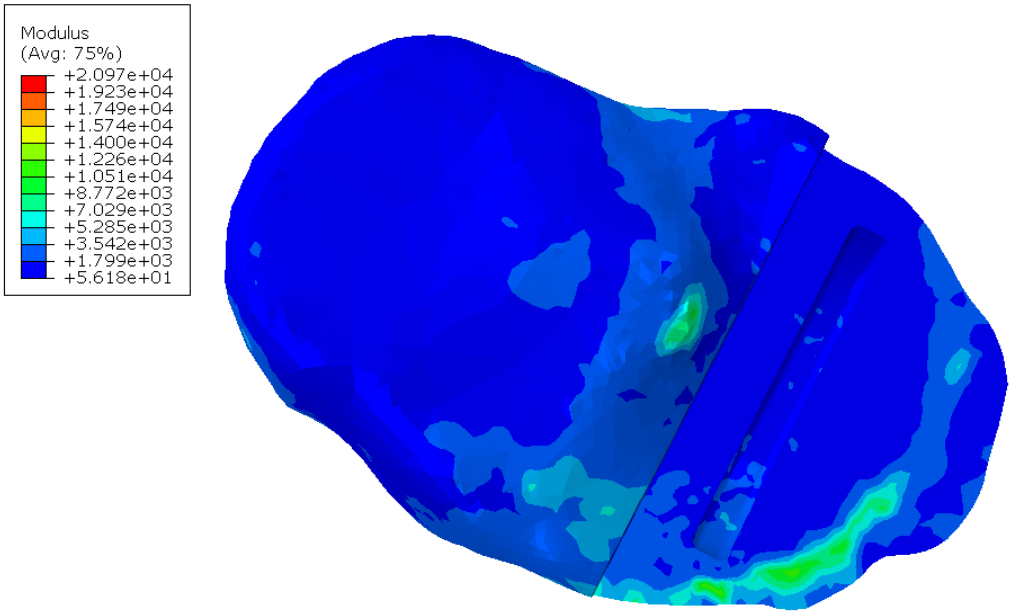

Figure 4.41: Material plot of the unfractured tibia of Patient 2.

Figure 4.42 shows the maximum principal stress in the fractured tibia when a Size AA component was implanted with the same tibial resection. The highest value was 689.7 MPa at the anterior corner of the keel slot, near where the hole was made.

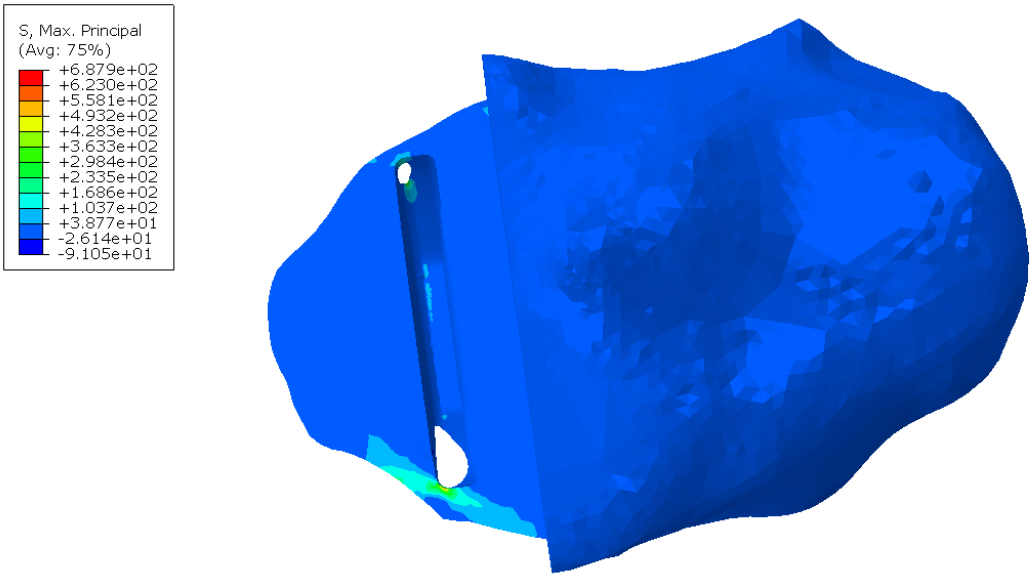

Figure 4.42: Maximum principal stress in the fractured tibia of Patient 2 when a Size AA component was implanted and loaded.

When the vertical and horizontal cuts in the fractured (left) tibia were replicated in the unfractured (right) tibia, the keel slot cut through both the anterior and posterior cortex. The highest maximum principal stress was 930.0 MPa at the anteromedial corner of the keel slot near the hole (**Figure 4.43**).

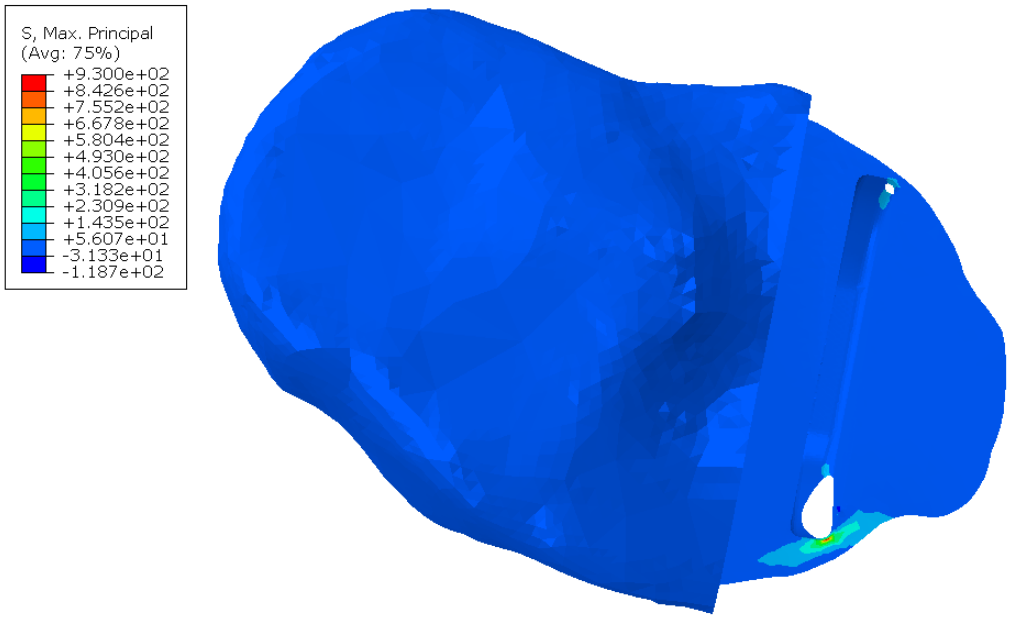

Figure 4.43: Maximum principal stress plot when the fractured cuts were replicated in the unfractured tibia of Patient 2.

4.3.3 Validation of Finite Element Model against Experiment

Figure 4.44 shows the highest maximum principal stress in the tibias with fractured, unfractured and modified tibial resections when the real bone properties were applied with the py_bonemat_abaqus Python package. All highest values appeared at the anteromedial corner of the keel slot. Anterior SCD was smaller than the posterior one when a Size C component was implanted (Fractured Cut_C and Unfractured Cut_C). The posterior SCD was smaller in all other cases. The highest maximum principal stress value was notably higher in the model where a Size C component was implanted with the fractured tibial resection than in other models. SCD was also smaller than those in other models, below 2 mm. Other models all showed a highest value of around 30 to 60 MPa, similar to that in the original unfractured tibia of Patient 1 with a Size C component implanted (49.1 MPa).

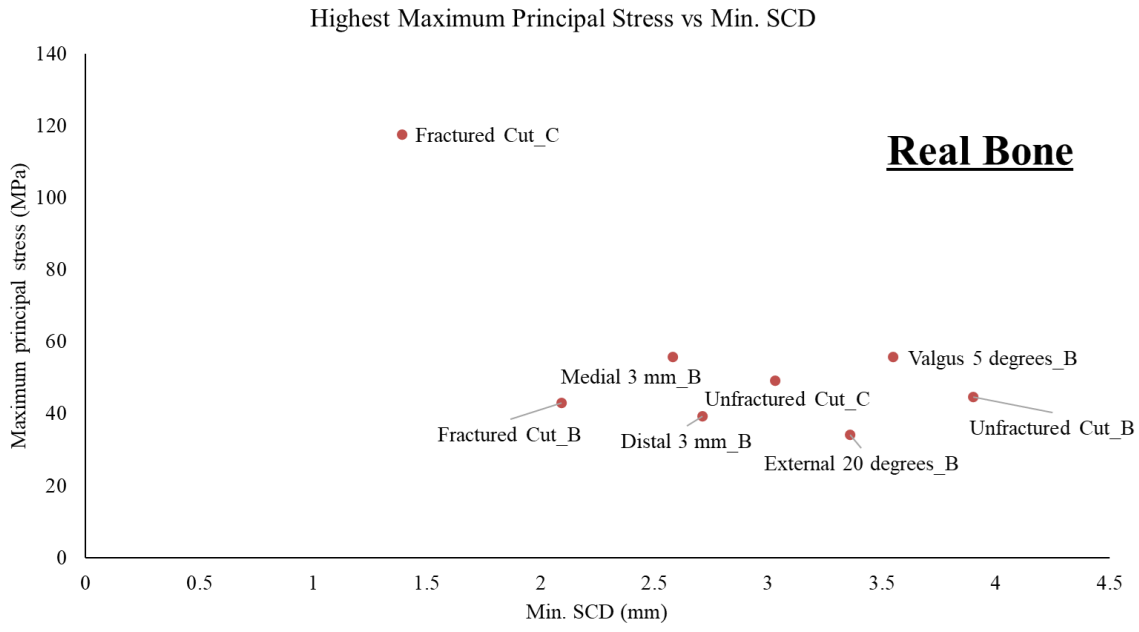

Figure 4.44: Highest maximum principal stress in the tibia versus minimum slot-cortex distance (SCD) when the real bone material properties were applied.

The highest maximum principal stress at the anteromedial corner of the keel slot in the eight tibia models when the homogeneous Sawbones properties were applied is shown in **Figure 4.45**. All the highest stress values were found at the anteromedial corner of the keel slot. A strong negative correlation was shown between the highest maximum principal stress and the minimum SCD (Pearson correlation coefficient, r = -0.95). Compared to the original scenario, i.e. unfractured cuts with a Size C component implanted, rotating the component externally by 20 degrees had a minor influence on the highest stress value (less than 10%). Turning the component into valgus by 5 degrees increased the stress by 15%. Medial movement and distal movement of 3 mm both increased the highest maximum principal stress in the tibia by around 40%. Using a Size B component with the fractured cuts induced a 25% smaller stress than using a Size C component with the same cuts.

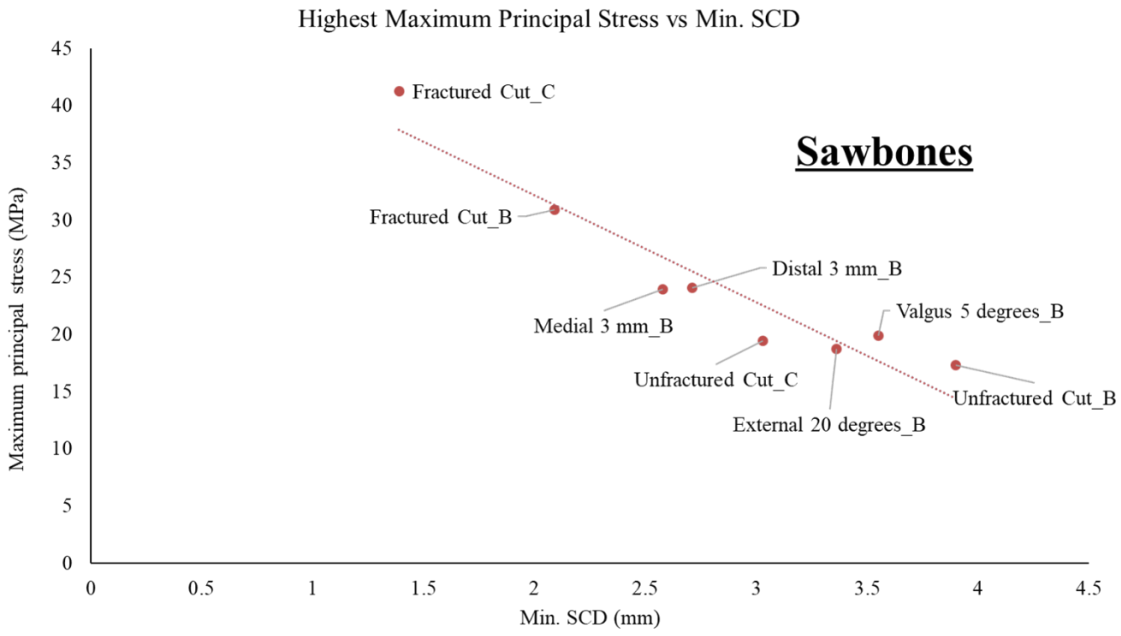

Figure 4.45: Highest maximum principal stress in the tibia versus minimum slot-cortex distance (SCD) when the Sawbones material properties were applied. Dotted line: line of best fit.

Figure 4.46 shows the results of the load-to-fracture experiment [169]. A strong positive correlation was shown between load to fracture and minimum SCD (Pearson correlation coefficient, r = 0.88).

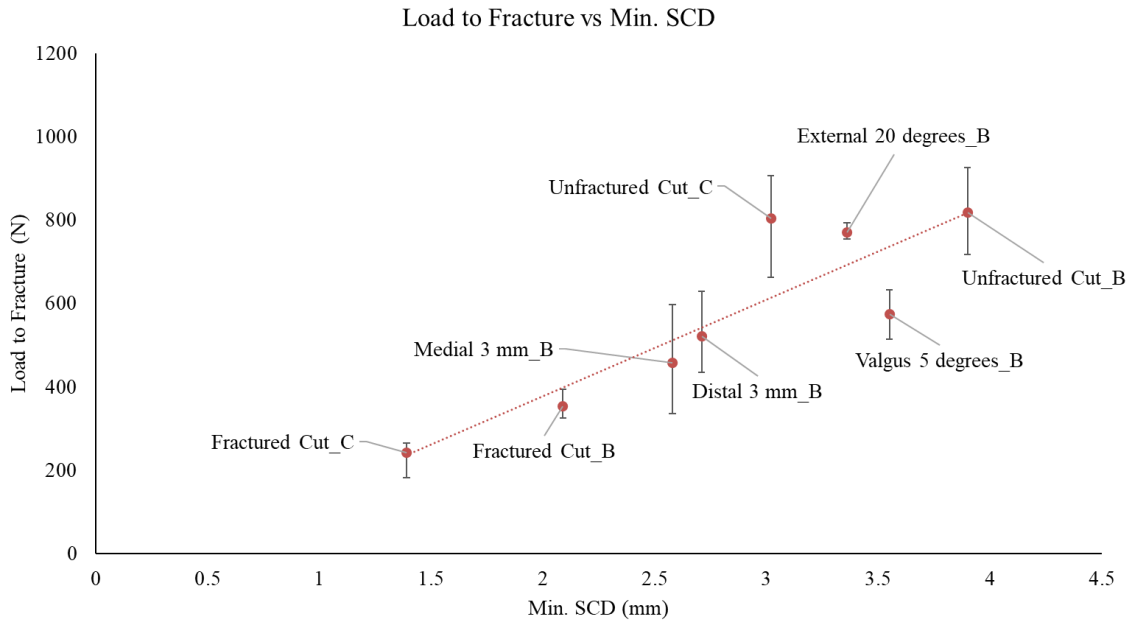

Figure 4.46: Results from the load-to-fracture experiment with error bars showing a 95% confidence interval [169]. SCD: slot-cortex distance. Dotted line: line of best fit.

When plotting load to fracture against the highest maximum principal stress, a strong negative correlation was shown (Pearson correlation coefficient, r = -0.90) (**Figure 4.47**).

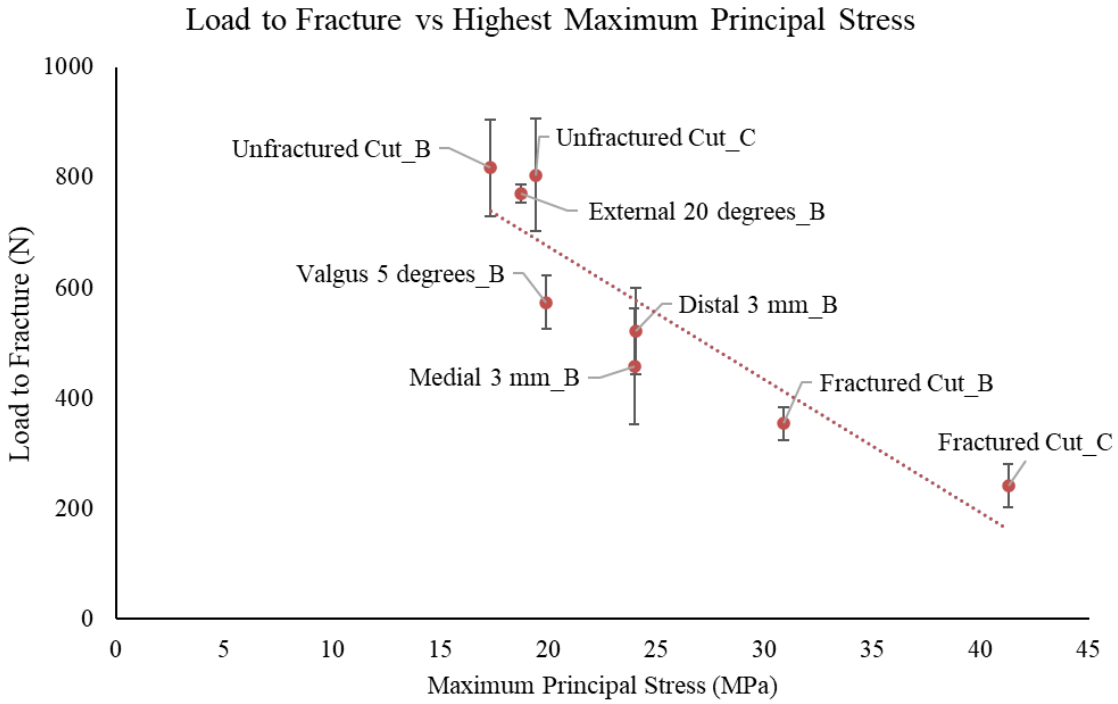

Figure 4.47: Load to fracture from the experiment against the highest maximum principal stress from the FE models.

4.4 Discussion

This chapter investigated the possible risk factors that might have led to the difference in outcomes in the tibias of two patients who received bilateral OUKR but experienced PPF in one of their tibias. Patient-related risk factors, which are poor bone quality, small tibial size and overhanging tibial plateau, and surgical risk factors, which are excessive bone resection and component over- or under-sizing were examined. Results showed that in both Patient 1 and Patient 2, no large differences in the quality of the bone, size of the tibias and the morphology of the tibial plateaus were found between the fractured and unfractured tibias. Both pairs of tibias showed MPTA of 80° or less which indicated tibia vara. Thus, the abovementioned patient factors were unlikely to be the cause of periprosthetic fracture in these two fractured tibias. Tibial resections in the two pairs of tibias, which were the

vertical cut and horizontal cut made on the tibial plateau, were compared in terms of their mediolateral position, proximal-distal position, varus-valgus orientation and internal-external rotation. These cuts determined the position and orientation of the tibial components. Large differences were found between the position and orientation of the resections in the two tibias in both Patient 1 and Patient 2 (**Table 4.6** and **Table 4.9**). In both cases, the cuts in the fractured tibia were made more medial and more distal than the ones in their unfractured counterpart. These surgical errors caused a larger removal of bone stock in the fractured tibias which was deemed one of the risk factors of PPF after cementless OUKR [92, 99]. The tibial component in the fractured tibia of Patient 1 was placed around 19° more externally rotated than the one in the unfractured tibia. While in Patient 2, the tibial component in the fractured tibia was placed around 16° more internally rotated. In both cases, the keel slot either breached the anterior cortex or was very close to the anterior cortex. This suggests that it was not the direction of rotation but the damage in the cortex that was the determining factor of fracture in these two cases. A previous review on PPF after UKR also supports the finding that tibias with weakened cortical bone are more prone to fracture [92].

The highest maximum principal stresses in the two unfractured tibia were both around 50-60 MPa. In the fractured tibia of Patient 1, the keel slot was either very close to or had cut through the anterior cortical bone (**Figure 4.16**). In either scenario, the highest maximum principal stress was around 155 MPa, which was more than three times that of the highest value in the tibia that did not fracture (49.1 MPa). In both scenarios, the highest stress was seen at the anteromedial corner of the keel slot, which was also near the position of the hole. As the surgical guide suggests that the posterior margin of the tibial component should be flush with the posterior cortex, this makes sure that there is a fixed distance between the back of the keel and the back of the tibia. However, if a tibial component too large is

implanted or if surgical errors are made which results in the component not being in the optimal position, the front of the keel can get very close to the cortex. The keel slot which is theoretically 2 mm larger than the keel in the sagittal plane will cut into the cortex which is around two orders of magnitude stiffer than the trabecular bone (**Table 4.5**). Damage in the cortex significantly increases the local stress. This might explain why the highest value of maximum principal stress appeared at the anterior corner of the keel slot in both fractured cases. Also, the elastic modulus of the bone at the anterior part of the tibial plateau was higher due to the existence of sclerotic bone coming from osteoarthritis. Press fitting the keel created a higher stress in the anterior part of the keel slot than at the posterior part.

As the load was applied at the position of the bearing when it was 1 mm away from the wall and 8 mm posterior to the centreline, the load position was medial to the keel (**Figure 4.48**). As the tibial component was loaded, the keel acted as a lever in the keel slot and the component tended to rotate towards the posteromedial corner around the line that connects the anteromedial corner and posterolateral corner of the keel slot. This further increased the tensile stress at the anteromedial corner of the keel slot.

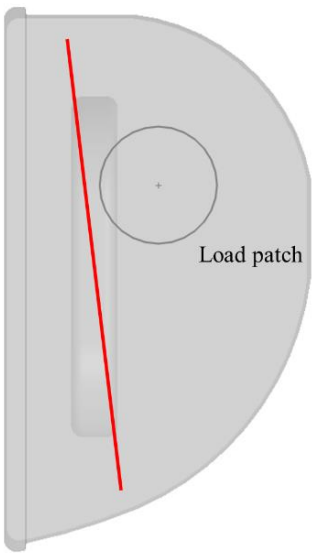

Figure 4.48: The tibial component rotates around the line connecting the anteromedial and posterolateral corners of the keel.

In the fractured tibia of Patient 2, the highest stress was again found at the anteromedial corner of the keel slot. A Size A cemented component was implanted in this tibia. Previous studies showed that compared to its cemented counterpart, cementless OUKR is more prone to PPF [84, 92]. Primary fixation of the cementless components which are seated through impaction is achieved through an interference fit. This introduces extra 'splitting force' in the bone compared to cemented fixation, in which the component is grouted with PMMA bone cement. This implies that though a cemented tibial component was implanted into the fractured tibia in Patient 2, implanting a cementless component at the same position would have had an even larger chance of causing a fracture. Keel slot created holes in both the anterior and posterior cortex and large concentrated stress was shown near the damage in the bone (**Figure 4.39** vs **Figure 4.38**). Despite the fact that this was a small patient with low BMI, using a Size AA implant still showed damage in the cortex and unacceptable anterior and medial overhang with these tibial cuts (**Figure 4.40** and **Figure 4.42**). When a Size AA component was implanted and loaded, though the highest maximum principal stress value was slightly lower than that when a Size A component was used (687.9 MPa vs 701.9 MPa), the value was still around 11 times the highest value in the unfractured tibia. Also, the other tibia that did not fracture with a Size A component implanted demonstrated that a Size A component would fit if put in a satisfactory position. This suggests that inappropriate bone cuts that removed excessive bone stock were made in the fractured tibia of Patient 2.

When the same fractured cuts were repeated in the unfractured tibias, both cases showed a large increase in stress and the keel slots cut into the cortical bone. These simulations eliminated the effects of patient-related factors on the risk of fracture. Thus, the results demonstrated that the tibial resections in the fractured tibias would have had a much higher chance of damaging the cortex and causing fracture even in the unfractured tibias.

The trend in the changes in the highest maximum principal stress in the tibia with the minimum SCD when different modifications were made to the tibial cuts (**Figure 4.45**) was similar to that in the changes in the load to fracture from the experiment (**Figure 4.46**). The minimum SCD was found at the anterior part of the tibial plateau when a Size B component was implanted and was found at the posterior part of the tibial plateau when a Size C component was used. When the Sawbones material properties were applied, all the highest maximum principal stresses were found at the anteromedial corner of the keel slot. Both sets of results showed that in the Sawbones tibia, external rotation of 20 degrees had a small effect on the stress or load to fracture value (changes within 10%). The next more detrimental error in this tibia was a 5-degree rotation into valgus, supported by both FE and experimental results. Medial or distal movement of 3 mm created the largest changes in both stress and load to fracture. In FE simulations, the effects of these two movements were similar while in the experiment, medial movement led to a slightly lower load to fracture. However, as experimental results of the medial movement samples and distal movement samples both showed large confidence intervals (CIs) with large overlap, the deviation in results might come from the uncertainties of the experiment.

These results along with the strong linear correlation between the highest maximum principal stress and the load to fracture also imply that the highest maximum principal stress values found from the FE models could be used as an indicator of the risk of fracture with confidence.

The difference between **Figure 4.44** and **Figure 4.45** again reinforces the idea that the risk of fracture in the tibia is not solely related to the geometry of the tibia but also related to local material properties. When the real bone properties were applied, the risk of fracture was greatly related to the shortest distance between the keel slot and the tibial surface, i.e., how close the keel slot was to the cortex. As demonstrated in **Figure 4.44**, there exists a

threshold SCD value (around 2 mm) below which the highest maximum principal stress will significantly increase, thus, making the tibia more prone to fracture. This value is likely to be the thickness of the peripheral cortical bone. The results from these simulations and their comparison to the experimental results suggest that though certain surgical errors in tibial resections may not cause detrimental effects structure-wise, they may trigger responses of the stiffer material locally which could act like stress-risers. Thus, combined with the effect of the high tensile stress at the anteromedial corner of the keel slot due to the bending motion around the keel as mentioned above, this elevated stress in the stiff anterior cortical bone greatly increases the risk of fracture.

This study has several limitations. Firstly, only one load case, which was the posterior-most position of the bearing during step-up movements was simulated. In real life, the bearing moves back and forth while the knee flexes and extends and the load varies accordingly. As this study focuses on the risk of fracture, the worst-case scenario which tends to create the largest load was modelled [167]. Future studies can look at the position of the bearing at different time points during gait and apply the corresponding load. Secondly, the press-fit process was modelled by applying an interference fit contact algorithm. Simulating the actual press-fit process would greatly increase the complexity of the model due to element distortion and subsequent convergence issues. This would also greatly increase the analysis time of each model. As this study compares the risk of fracture in several tibias with OUKR implanted with the same interference, the contact algorithm used was sufficient to provide information on the factors that affected fracture. Thirdly, the tibial bone was modelled as a heterogeneous linear elastic material while the actual bone exhibits plastic behaviour [171]. However, as the material definitions were consistent across models, this gave us enough insights into the effects of component positioning on the risk of tibial PPF. Lastly, the physical process of fracture initiation and propagation was not modelled, and the highest

maximum principal stress was used as an indication of the risk of fracture. The numerical value of the highest stress found in some models might be well above the stress that the bone could withstand [172] and the tibia might have fractured before the 1000 N load was fully applied. However, the comparison of these highest maximum principal stress values between models implied relatively how likely fracture was about to happen when the tibial component was placed at that position.

4.5 Chapter Summary

This chapter investigated the patient-related risk factors and surgical risk factors that might have caused the tibial PPF in two patients who received bilateral OUKR while experiencing fracture in one tibia through FEA. In both patients, no large differences were found in the bone properties, tibial size, and proximal tibia morphology between the two tibias. The tibial resections were made more distal and more medial in the fractured tibias in both cases. In both fractured tibias, high maximum principal stresses an order of magnitude higher than those in the unfractured tibias were seen at the anteromedial corner of the keel slot. The keel slot was very close to the anterior cortex or had penetrated the cortex. Keel slot cutting into the cortical bone due to surgical errors in tibial resections that led to unsatisfactory component positioning was suggested as the main cause of PPF in these two cases.

The comparison between results from FEA and a biomechanical experiment in Sawbones demonstrated that load-to-fracture values from the experiment were linearly negatively correlated to the highest maximum principal stress found from FEA. Therefore, the highest values of maximum principal stress in the tibia were used as an indication of the risk of experiencing tibial PPF after cementless OUKR throughout this thesis.

Chapter 5. Effects of Tibial Component Positioning and Design on Risk of Periprosthetic Tibial Fracture after Cementless Oxford Unicompartmental Knee Replacement

5.1 Introduction and Aim

Results from **Chapter 4** suggest that placing the keel slot, which has a 2 mm offset from the keel in the sagittal plane (**Figure 4.13**) too close to the cortical bone can be a risk factor for tibial PPF after cementless OUKR. Leaving a short distance between the keel slot and the cortex creates a higher chance of cutting the keel slot into the cortex which would greatly reduce the load-bearing ability of the bone. Thus, changes that move the keel and keel slot further away from the cortical bone may help reduce the chance of having a fracture.

Current OUKR surgery applies Microplasty Instrumentation that implements a minimally invasive technique. The surgery is performed through a small incision from the medial margin of the patella to 3 cm below the joint line (**Figure 5.1**). This minimally invasive technique allows the patella to not be dislocated intraoperatively, which enables faster recovery in flexion ability and reduces post-operative pain [11, 32].



Figure 5.1: Position of incision for medial Oxford Unicompartmental Knee Replacement. The incision starts from the medial margin of the patella and extends to 3 cm distal to the joint line [32].

Despite the abovementioned advantages of this minimally invasive technique, the small incision limits the exposure of the knee compartments and makes it a more demanding surgical approach for surgeons, providing limited space for operation.

The current guidance on surgical techniques suggests that the vertical saw cut should sit right next to the apex of the medial tibial spine and should point towards the anterior superior iliac spine (ASIS) [11, 32]. This defines the mediolateral position and the internal-external rotation of the component. Large variations in the internal-external rotation of the tibial components were observed when using this anatomical landmark as a reference. Lee et al. [173] and Gao et al. [174] reported a range of 1.9°-25.2° and -1.0°-19.1° respectively on the angle between the vertical tibial cut and the Akagi line. The Akagi line is a reference AP axis that connects the middle of the posterior cruciate ligament (PCL) and the medial edge of the patellar tendon [175]. One possible cause of these wide ranges is that ASIS is difficult to identify accurately and consistently intraoperatively, especially in obese patients. The position of ASIS might also vary based on the rotation of the hip joint and on how the leg is positioned on the holder [173, 176]. The components in the two fractured tibias studied in **Chapter 4** were rotated towards different directions compared to the ones in the unfractured tibias. The effect of the internal and external rotation of the component on the risk of fracture is still unknown. The vertical cut also determines the varus-valgus orientation of the component. It is made with the tibial saw guide and should be parallel to the mechanical axis of the tibia [32].

The horizontal tibial saw cut should be 2 to 3 mm below the deepest point of the erosion on the medial tibial plateau. The resection made using the femoral sizing spoon, tibial saw guide and a 3 or a 4 G-clamp can accurately establish a horizontal cut at a level appropriate for a Size 3 or Size 4 bearing to fit in (**Figure 5.2**) [32].

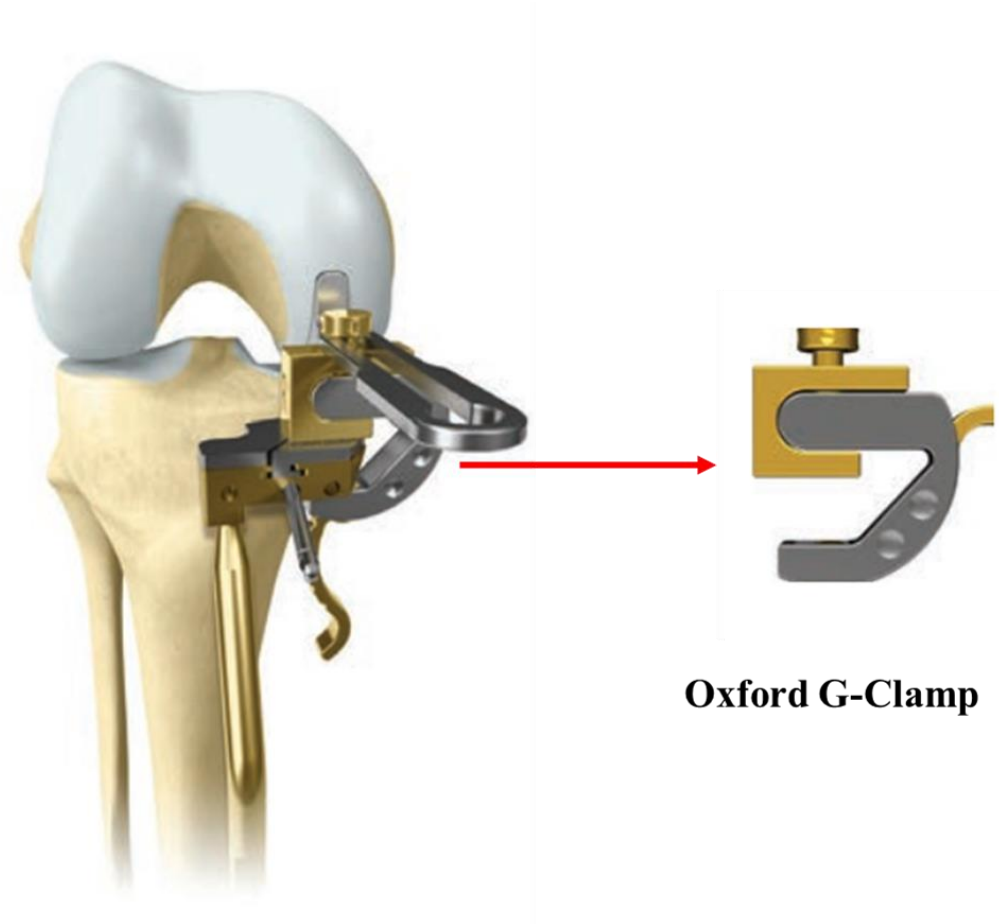

Figure 5.2: The Oxford G-Clamp is used to decide the depth of the horizontal tibial resection. Figure adapted from [32].

Tibial component underhanging may lead to component subsidence and loosening as the component would sit on the trabecular bone instead of the stiffer peripheral cortical bone. Thus, when perfect coverage cannot be attained, positioning the component with a slight overhang is recommended [32, 174, 177]. However, this increases the chance of making the vertical cut too medial which leaves relatively less supporting bone stock underneath the tray. Putting the component too medial or too distal, which happened in the two fractured tibias in **Chapter 4**, reduces the amount of bony support.

Thus, the effects of the mediolateral position, proximal-distal position, internal-external rotation and varus-valgus orientation of the tibial component on the risk of fracture were

investigated. The significance of the accuracy of the cut position in these four dimensions was assessed in terms of their effects on the slot-cortex distance (SCD) and the highest maximum principal stress in the tibia.

Current OUKR tibial components, regardless of their sizes, have keels of the same width and depth. The length of the keel increases as the size goes up. Therefore, the ratio between the size of the keel and the size of the tibia is larger in tibias requiring smaller tibial components. As shown in **Figure 4.1**, when the components of Size AA (smallest), C (intermediate) and F (largest) are scaled to have the same tray length, the Size AA component has the keel of the largest relative depth. This implies that the relative amount of bone stock remaining after the tibial component is implanted is less in smaller tibias. Hence, some authors have suggested that small tibial components should have smaller keels accordingly [99]. A previous study demonstrated that using a small porous keel design which was 4 mm shorter at the back and 3 mm shallower than the current OUKR cementless keel design (**Figure 5.5 c**) created similar or slightly smaller sagittal micromotion compared to the existing keel. Thus, using a smaller keel on the tibial component could provide equal, if not better, primary fixation [124]. As this study only tested one shorter keel design which was shorter at the back, and results of **Chapter 4** showed that the anterior cortex was at a higher risk of initiating fracture, this chapter investigates the optimal location of the small keel on the tibial component that could potentially lower the risk of PPF with FEA.

The aim of this chapter was to determine in which direction or orientation surgical errors had the largest impact on the risk of PPF and to investigate changes that can be made to component design or surgical procedure that would help minimize the risk of tibial PPF after cementless OUKR. The effects of component positioning on the risk of tibial PPF were studied with a parametric FE study. The tibial resections in the unfractured tibia of

Patient 1 and Patient 2 which represented satisfactory positioning of the tibial component were moved or rotated in the mediolateral, proximal-distal, internal-external and varus-valgus directions to evaluate the effects of surgical errors in these four dimensions on the stress in the bone and the shortest SCD. Five new small keel designs which should provide larger SCDs than the current design were also tested in the unfractured tibias with a FE study. The designs that provided the largest reduction in stress and the largest increase in SCD were implanted into the fractured tibias to assess if they could reduce the risk of fracture when surgical errors were made.

5.2 Methods

5.2.1 Effects of Component Positioning on Risk of Fracture

The effects of the tibial component's mediolateral position, proximal-distal position, varus-valgus orientation and internal-external rotation on the risk of fracture were assessed in terms of the highest maximum principal stress in the bone and the distance between the keel slot and the outmost surface of the tibial bone.

The position and orientation of the surgical cuts in the two unfractured tibias of Patient 1 (left) and Patient 2 (right) mentioned in **Chapter 4** were used as references. Based on the experience of a senior surgeon/surgical instrument designer, changes in cut position in clinical settings were usually applied in an interval of 3 mm. Thus, changes around 3 mm were made to the position of the tibial component. The cuts in the two tibias were moved medially by 1 mm, 3 mm and 5 mm, laterally by 1 mm, 3 mm and 5 mm, distally by 1 mm, 3 mm and 5 mm, or proximally by 1 mm, 3 mm and 5 mm from their original position (**Figure 5.3**). The cuts were also rotated by 5 degrees, 10 degrees and 15 degrees both internally and externally. 5-degree, 10-degree and 15-degree rotation of the tibial

component in the varus or valgus orientation were also tested. The mediolateral movement was made along the horizontal cut plane and the proximal-distal movement was made along the vertical cut plane. The internal-external rotation was made about the midpoint of the AP cut. The varus-valgus rotation was made around the lateral edge of the keel cut to make sure there was no large translation in the mediolateral or proximal-distal position of the components. As the surgical guide suggests that the vertical cut should be right next to the apex of the medial tibial spine, the scenarios in which the vertical cuts were moved medially or laterally after varus/valgus rotation to sit right next to the tibial spine were also modelled (**Figure 5.4**).

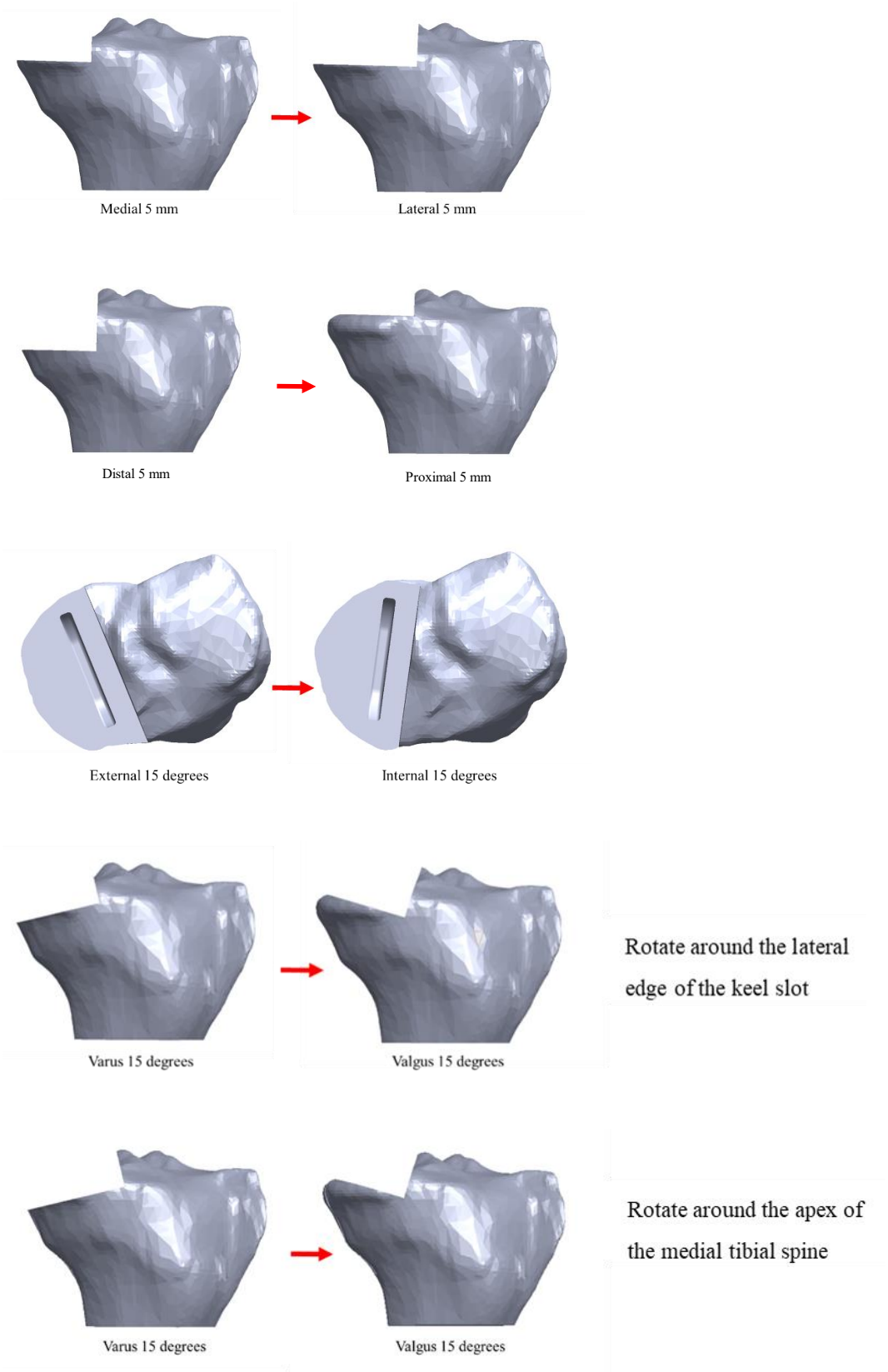

Figure 5.3: Vertical and horizontal cuts for various changes in the position or orientation of the tibial component.

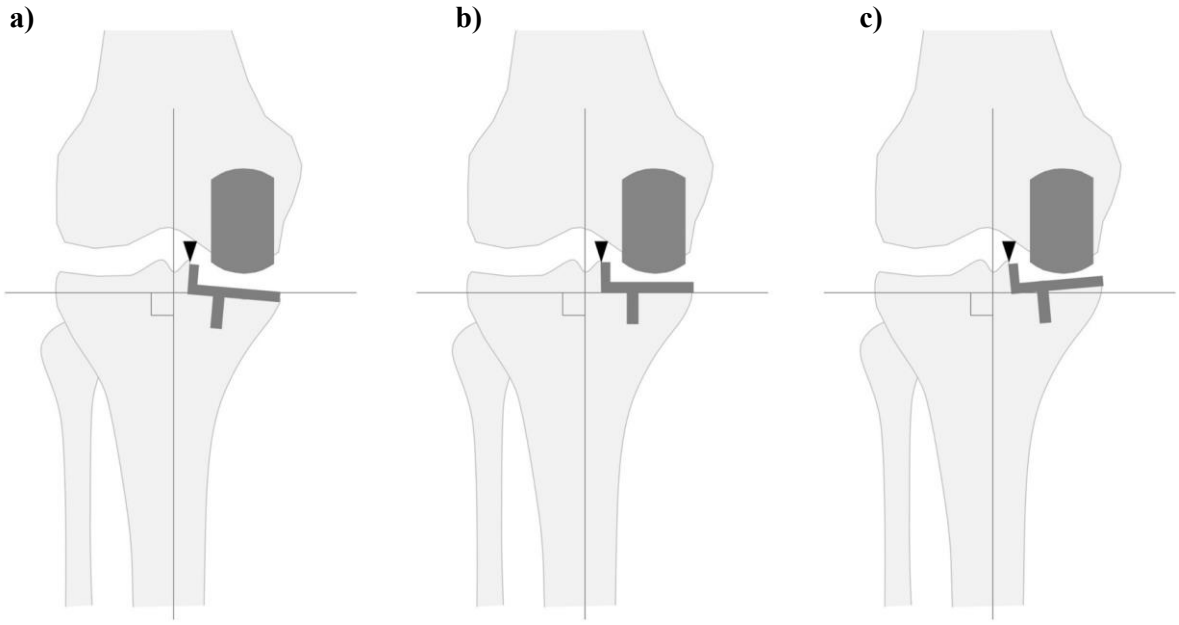

Figure 5.4: (a) Varus (b) standard and (c) valgus coronal placement of the tibial component. Changes in the varus-valgus orientation were made around the medial tibial spine. Figure adapted from [158].

FE models were built with the Python script adapted from the one used to replicate the fractured cuts in **4.2.1.2** (**Appendix B**). For the movement in the medial and distal direction, if the change resulted in the keel slot cutting through the bone, then a movement 1 mm smaller was tested instead. The same FEA model template used in **4.2.1.1** was repeated on these two OUKR-implanted tibias with modified tibial resections. The same boundary conditions, contact, and material properties settings used in the models in **Chapter 4** were applied. The elastic modulus and the Poisson ratio of the tibias were assigned with the py_bonemat_abaqus python package [166]. An interference fit of 0.16 mm was applied in each model [109]. The same mesh size used in the FE models of these two tibias (2.4 mm and 0.6 mm mesh refinement at the keel slot) was again applied.

A 1000 N load was applied perpendicular to the superior surface of the tibial tray in each model. The load position was the same as in **Chapter 4**: the position of the bearing when it was 1 mm away from the wall and 8 mm posterior to the middle line [166]. It was

assumed that the corresponding placement of the femoral component and bearing thickness choice would be made accordingly with the position of the tibial component to ensure that the bearing was placed at its optimal position which would not cause bearing impingement onto the vertical tibial wall throughout the full extension-flexion motion. It was assumed that the mediolateral position of the femoral component would move with the tibial component, thus the loading point would remain the same when the tibial component was moved medially or laterally. As the superior spherical surface of the bearing stays congruent with the spherical femoral component, when the tibial component was orientated in the varus-valgus direction, the bearing would rotate around the centre of the femoral component with the inferior surface staying in full contact with the tibial component. When the component was moved proximally or distally, bearings of appropriate thickness would be inserted to restore the natural tension of the ligaments. Therefore, it was assumed that the location at which the load was applied would stay the same relative to the tibial component. As the rotation of the femoral component was determined by the intramedullary rod which went through the intramedullary canal of the femur, it was fairly consistent and not easy to alter. Therefore, when the tibial component was rotated in the internal-external direction, scenarios in which the femoral component rotated and did not rotate with the tibial component were both tested. When the femoral component did not rotate, which implies that the relative position between the femoral component and the tibia would remain the same, the loading position on the tibial component was changed as the tibial component rotated (**Appendix C**).

After the modifications in vertical and horizontal cuts were made and the keel slot was created, the 3D models of the tibias were imported into SolidWorks 2022 (Dassault Systèmes, France). SCDs were then found in each tibia model.

5.2.2 Testing of Smaller Keel Designs

Five new keel designs were tested to investigate the effect of keel length, keel depth and the AP position of the keel relative to the component on the risk of PPF (**Figure 5.5**). Designs *a* and *b* were 3 mm shallower and 4 mm shorter, respectively. The keel in design *b* was placed in the middle, aligning with the middle line of the current keel design. Designs *c, d,* and *e* all had keels that were 3 mm shallower and 4 mm shorter but placed at different AP positions. In Design *c*, which was the component tested in a previous biomechanical experiment investigating the primary fixation of various keel designs [124], the back of the keel was moved forward by 4 mm. While in Design *d*, the front of the keel was moved backwards by 4 mm. The keel was again in the middle in Design *e*.

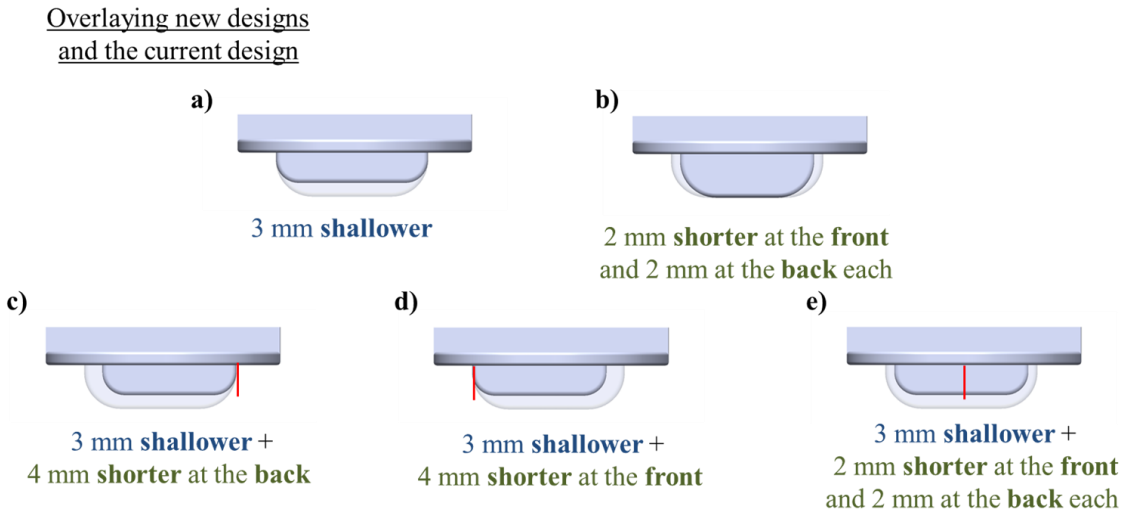

Figure 5.5: Overlaying the five new smaller keel designs tested and the current keel design. Design c was the one tested in [124]. Designs c, d and e have the keel of the same size but placed at different positions, aligning to the front edge, back edge and middle line of the existing keel design.

These small keel designs were virtually implanted into the FE models of the two tibias that did not fracture in Patient 1 and Patient 2. The same vertical and horizontal cuts were made in the tibia which means the components were placed at the same position with the same orientation. The size of the keel slot was reduced accordingly, still maintaining a 2 mm

offset from the margin of the keel. The keel slots were made in the tibias with the Boolean function in ABAQUS/CAE 2020 (Dassault Systèmes, France). When the posterior margin of the component was flush with the posterior cortex, the keel was in the middle of the keel slot in the AP direction.

The same FEA workflow used in **5.2.1** was repeated on these models with small keel tibial components implanted. The same boundary conditions, contact, and material properties settings were applied, and the same mesh size was used. A 1000 N vertical load was applied to the superior surface of the tibial component at the same loading position used in **4.2.1.1** [165]. The distance between the keel slot and the surface of the tibia (SCD) was measured in SolidWorks 2022 (Dassault Systèmes, France) using the same method described in **5.2.1** and the highest maximum principal stress value in each model was recorded. Designs that showed the largest increase in SCD and the largest reduction in stress were then implanted in the two tibias that experienced PPF (right tibia in Patient 1 and left tibia in Patient 2). The same vertical and horizontal cuts as before were made and the size of the keel slots were reduced to fit the shape of the keel.

For ease of analysis, each tibia model was partitioned into the anterior part and the posterior part along the middle line across the keel slot in the AP direction (**Figure 5.6**).

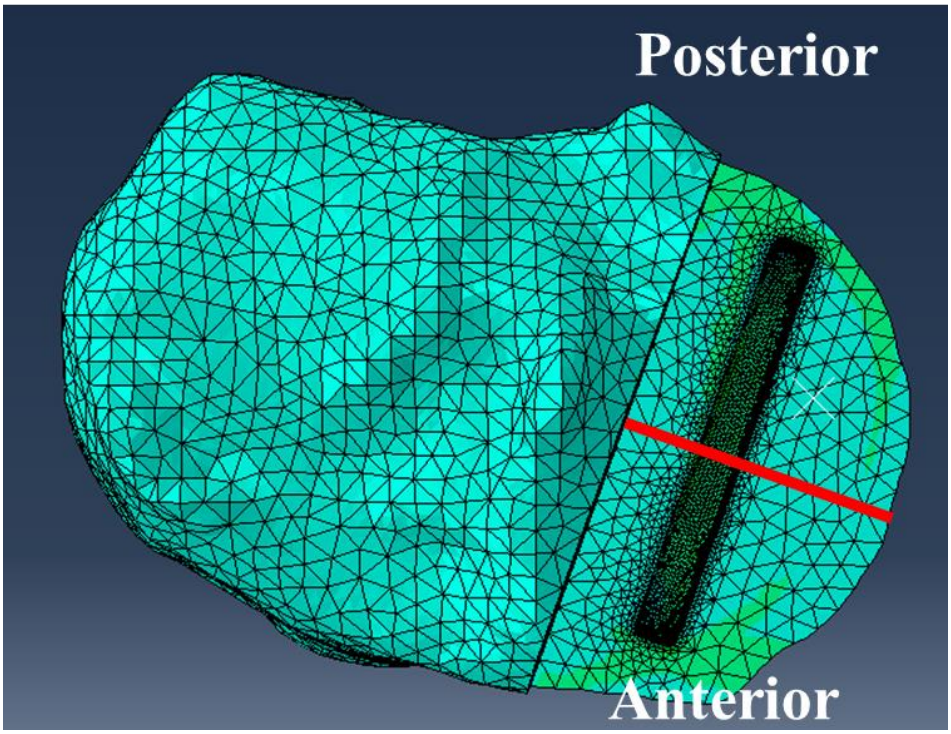

Figure 5.6: Tibias were partitioned into the anterior part and the posterior part halfway across the keel slot in the anteroposterior direction.

5.3 Results

5.3.1 Effects of Component Positioning on Risk of Fracture

The values of the highest maximum principal stress and their locations in each model were recorded.

5.3.1.1 Medial-lateral Movements

When the component was moved in the mediolateral direction relative to the reference position (original post-operative component position), the highest stress in the anterior part of the tibia was always higher than that in the posterior part apart from the Patient 1 1-mm medial movement model in which the stresses were at the same level anteriorly and posteriorly (**Figure 5.7**). The highest stress increased as the component moved more medially. The highest stress in the bone was under or around 50 MPa until the component

was moved medially by 3 mm in Patient 1 and by 2 mm in Patient 2, at which point abrupt increases in stress were shown. When the component was moved medially by 5 mm in Patient 1, the highest stress reached 307 MPa, which was more than 6 times that when the component was placed at the reference position. The highest stress reached almost three times that of the reference stress value (179 MPa vs 63 MPa) when the component was moved medially by 2 mm in Patient 2. SCD decreased with the medial translation. The stress doubled in Patient 1 when the SCD was reduced to 1.5 mm as the component was moved medially by 3 mm. In Patient 2, the keel slot breached the cortex when moved medially by 3 mm or above.

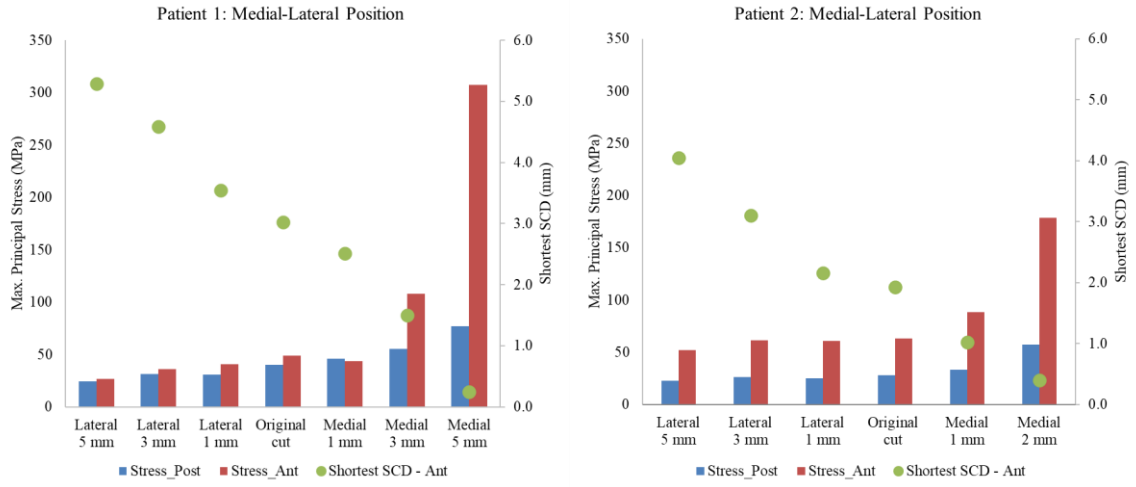

Figure 5.7: Highest maximum principal stress in the anterior and posterior part of the proximal tibia and the shortest anterior slot-cortex distance (SCD) in the unfractured tibia of Patient 1 and Patient 2 when the tibial component was translated in the mediolateral direction.

5.3.1.2 Proximal-Distal Movements

The maximum principal stress at the anterior part of the keel slot retained the highest in the tibia when the component was moved in the proximal-distal direction in both patients other than the case when the component was 5 mm proximal to the reference position in Patient

2 (**Figure 5.8**). In this case, similar stress levels are seen in the anterior and posterior parts of the tibia and the highest value was found at the posterolateral corner of the keel slot. In Patient 1, the highest stress was around 50 MPa until the component was moved distally by 5 mm, at which point the maximum stress in the anterior part of the tibial suddenly doubled. The SCD decreased with the distal translation of the component and the highest stress doubled when the SCD was below 1.8 mm. In Patient 2, the highest stress increased and the anterior SCD decreased as the component was moved distally and the keel slot created holes in the tibia when the component was moved distally by 4 mm or above.

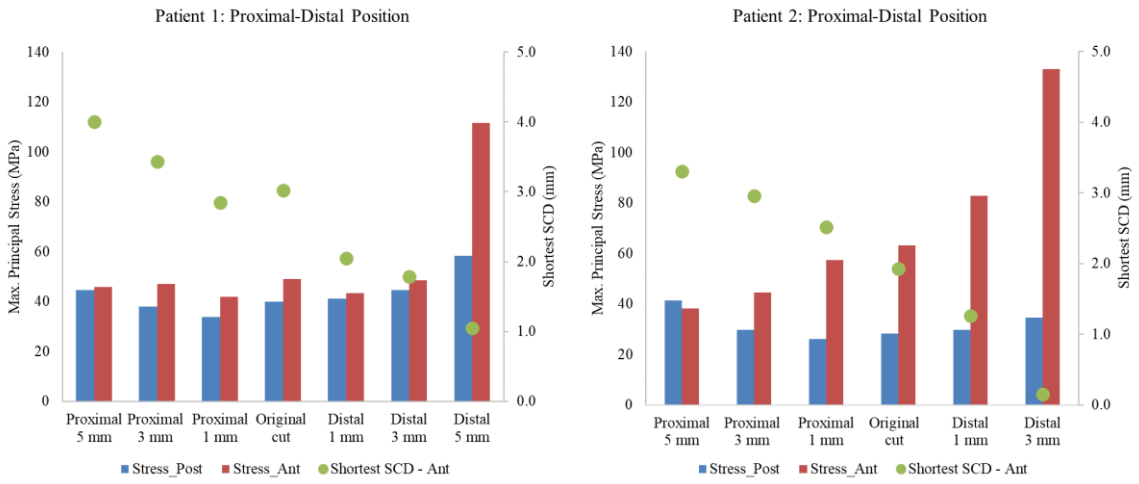

Figure 5.8: Highest maximum principal stress in the anterior and posterior part of the proximal tibia and the shortest anterior slot-cortex distance (SCD) in the unfractured tibia of Patient 1 and Patient 2 when the tibial component was translated in the proximal-distal direction.

5.3.1.3 Internal-External Rotations

In Patient 1, the highest stress was shown when the component was internally rotated by 15 degrees or externally rotated by 10 degrees when altering the internal-external direction of the implant while keeping the loading position the same (**Figure 5.9**). These were also the positions where the shortest SCDs were seen. Though when the component was further

externally rotated into 15 degrees, the highest maximum principal stress in the anterior part of the bone decreased, the stress in the posterior part increased by 39%. This also corresponded to the decrease in posterior SCD from 10-degree external rotation to 15-degree external rotation.

When the loading position was changed based on the rotation of the tibial component as described in **5.2.1** (**Appendix C**), the difference in the maximum principal stress found was within 1 MPa (less than 2.5% of the stress value) from the results in **Figure 5.9** and did not change the trend in SCD nor stress as the component was rotated internally or externally.

As changing the loading position based on the internal-external rotation of the tray had a minor effect on results, the loading position was kept the same for Patient 2. The highest stress showed an increasing trend as the component was rotated either internally or externally. Posterior SCD decreased as the component was more externally rotated while anterior SDC showed the opposite trend. Within a rotation of 15 degrees in either internal or external direction, the highest maximum principal stress remained under 90 MPa.

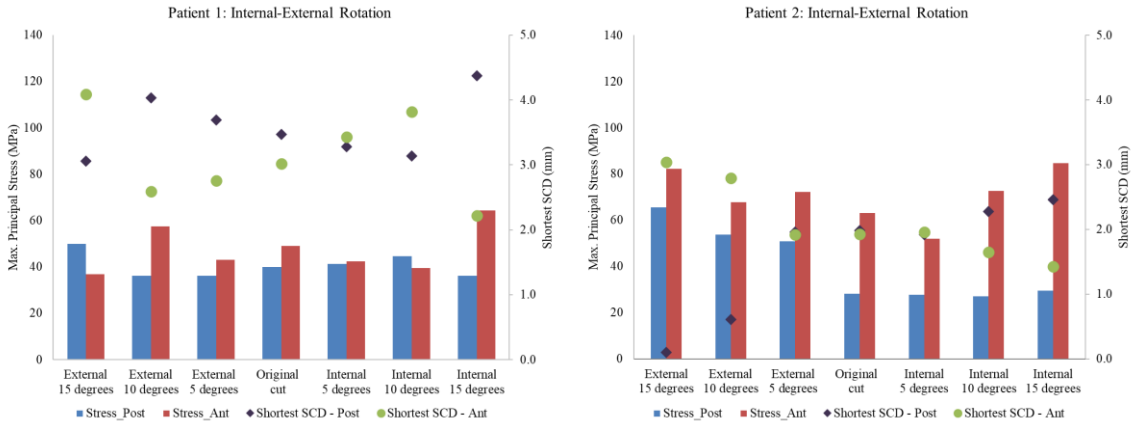

Figure 5.9: Highest maximum principal stress in the anterior and posterior part of the proximal tibia and the shortest anterior slot-cortex distance (SCD) in the unfractured tibia of Patient 1 and Patient 2 when the tibial component was rotated in the internal-external direction.

5.3.1.4 Varus-Valgus Rotations

Rotating the component around the lateral edge of the keel slot (i.e. the centre of the component remained at roughly the same mediolateral and proximal-distal position) showed changes of within 30% in stress in either the varus or valgus direction (**Figure 5.10**).

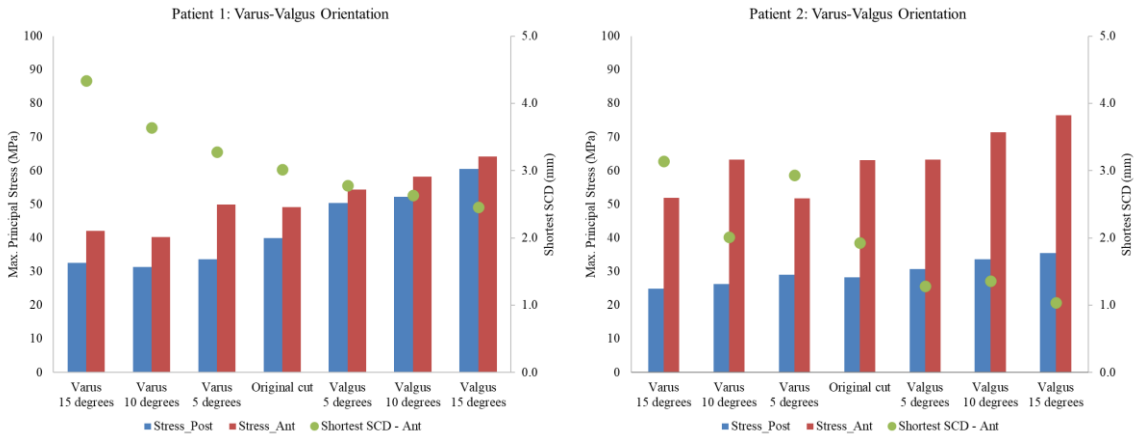

Figure 5.10: Highest maximum principal stress in the anterior and posterior part of the proximal tibia and the shortest anterior slot-cortex distance (SCD) in the unfractured tibia of Patient 1 and Patient 2 when the tibial component was rotated in the varus-valgus direction. The tibial component was rotated into varus and valgus around the lateral edge of the keel slot. These rotations kept the component at roughly the same mediolateral and proximal-distal position.

When the varus-valgus orientation of the tibial component was altered while keeping the vertical cut right next to the medial tibial spine, putting the component in valgus created significantly higher stress than when putting it in varus in both cases (**Figure 5.11**). The keel slot penetrated the anterior cortex when the component was in 15-degree valgus in Patient 2. Putting the component in a 5-degree valgus could increase the highest stress by up to 98%.

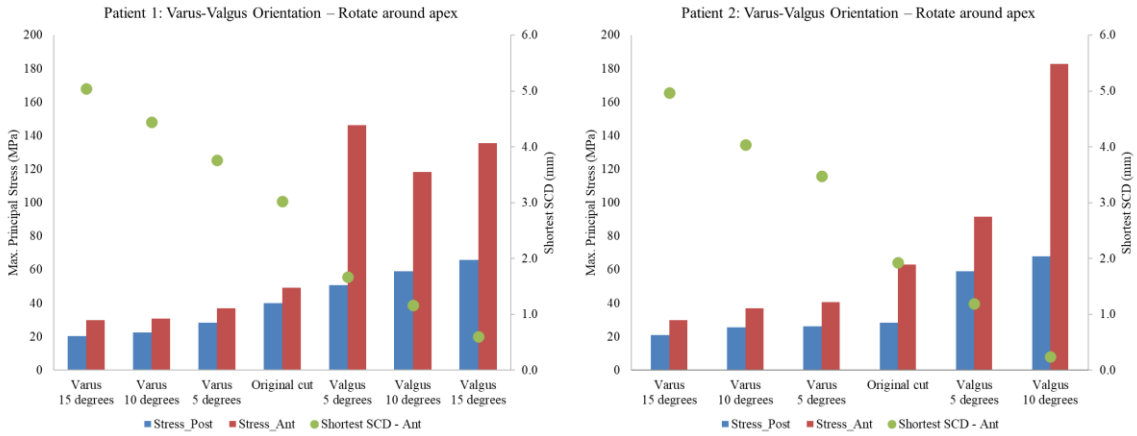

Figure 5.11: Highest maximum principal stress in the anterior and posterior part of the proximal tibia and the shortest anterior slot-cortex distance (SCD) in the unfractured tibia of Patient 1 and Patient 2 when the tibial component was rotated in the varus-valgus direction while keeping the vertical cut next to the medial tibial spine.

5.3.2 Testing of Smaller Keel Designs

Figure 5.12 shows the highest maximum principal stress value in the anterior and posterior part of the proximal tibia when tibial components with smaller keel designs were implanted into the unfractured tibia of Patient 1 in the same post-operative position. Compared to the current design, the keel that was 4 mm shorter while having the same depth (Design *b*), and the keel that was 4 mm shorter at the front and 3 mm shallower in depth (Design *d*) showed an increase in the highest stress level. The 3-mm shallower keel (Design *a*) showed a reduction in stress, but only by 8%. Placing the 4-mm shorter and 3-mm shallower keel in the middle (Design *e*) or at the front (Design *c*) gave the lowest stress, showing a 59% to 69% reduction in the maximum value at both the anterior and posterior part of the proximal tibia.

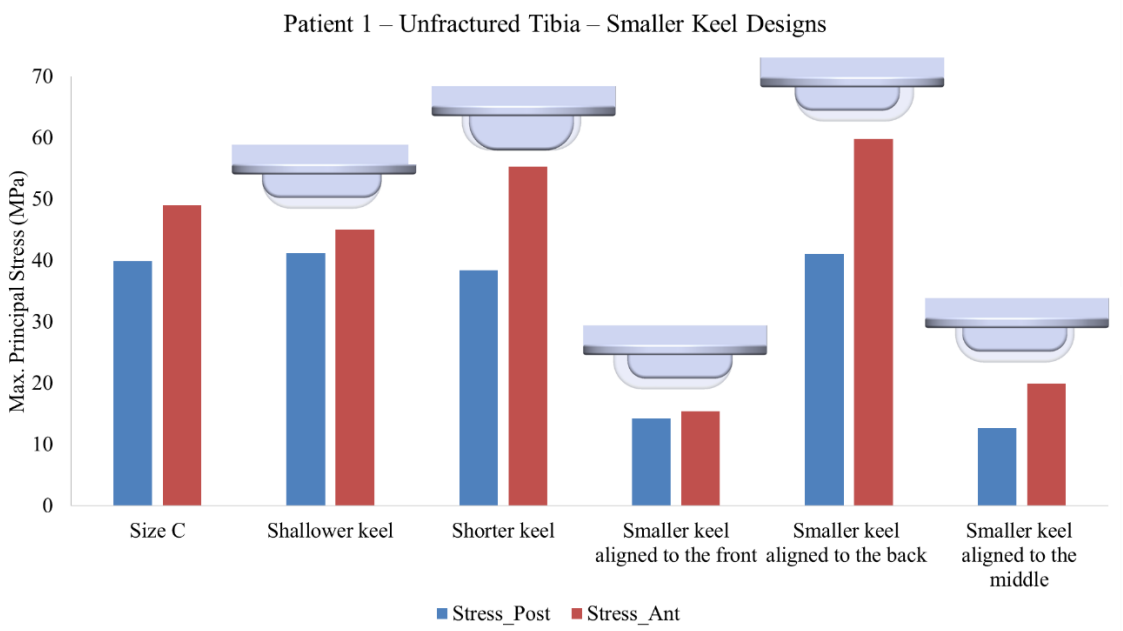

Figure 5.12: Highest maximum principal stress in the anterior and posterior part of the proximal tibia when tibial components with small keel designs were implanted into the unfractured tibia of Patient 1 with the original tibial resection. The five new designs are Design a to Design e from left to right.

As the smaller keel designs with the keel aligned to the front (Design *c*) and the middle line (Design *e*) of the current keel showed the lowest maximum principal stress, these two designs were tested in the fractured tibia of Patient 1. Using these two designs both showed a reduction in the highest stress (**Figure 5.13**). Placing the keel in the middle showed a larger decrease in stress compared to when placing the keel at the front (69% vs 30%). The highest stress was 55 MPa at the bottom of the posterior part of the keel slot when the keel was placed in the middle, similar to the highest stress value in the other tibia that did not fracture when a standard Size C component with the current keel design was used (49 MPa).

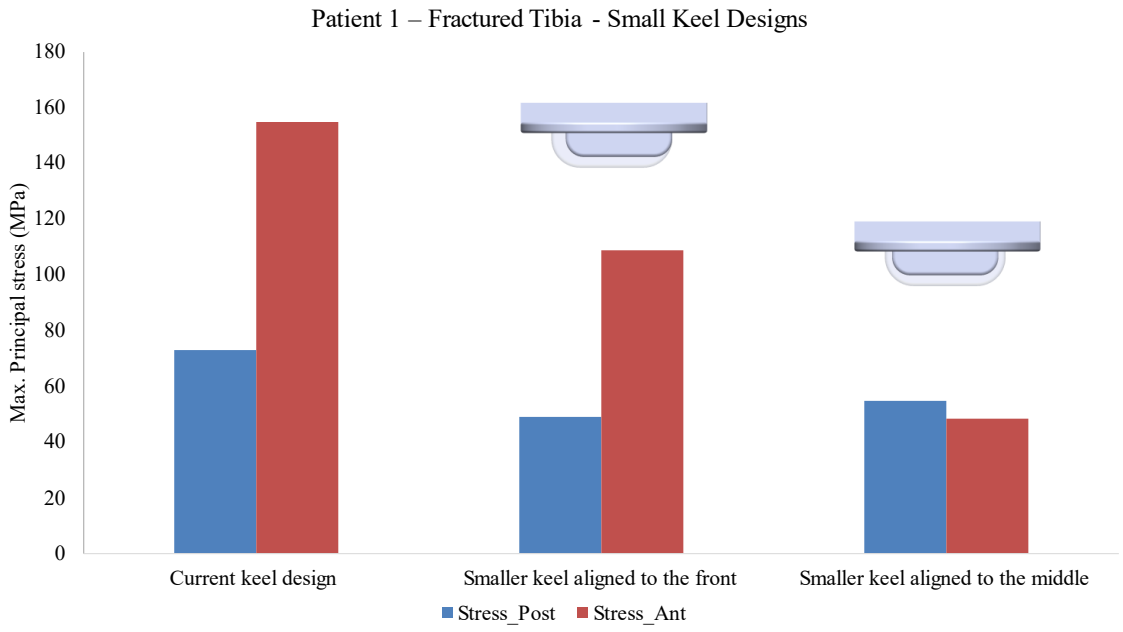

Figure 5.13: Highest maximum principal stress in the anterior and posterior part of the proximal tibia when two tibial components with smaller keels (Middle: Design c, Right: Design e) were implanted into the fractured tibia of Patient 1 with the original fractured tibial resection.

When the tibial components with small keel designs were implanted into the unfractured tibia of Patient 2, all designs showed a reduction in the highest value of maximum principal stress in the bone (**Figure 5.14**). The keel that was 2 mm shorter at the front and 2 mm shorter at the back (Design *b*), the small keel placed at the back (Design *d*), and the small keel placed in the middle (Design *e*) showed the largest reduction in stress.

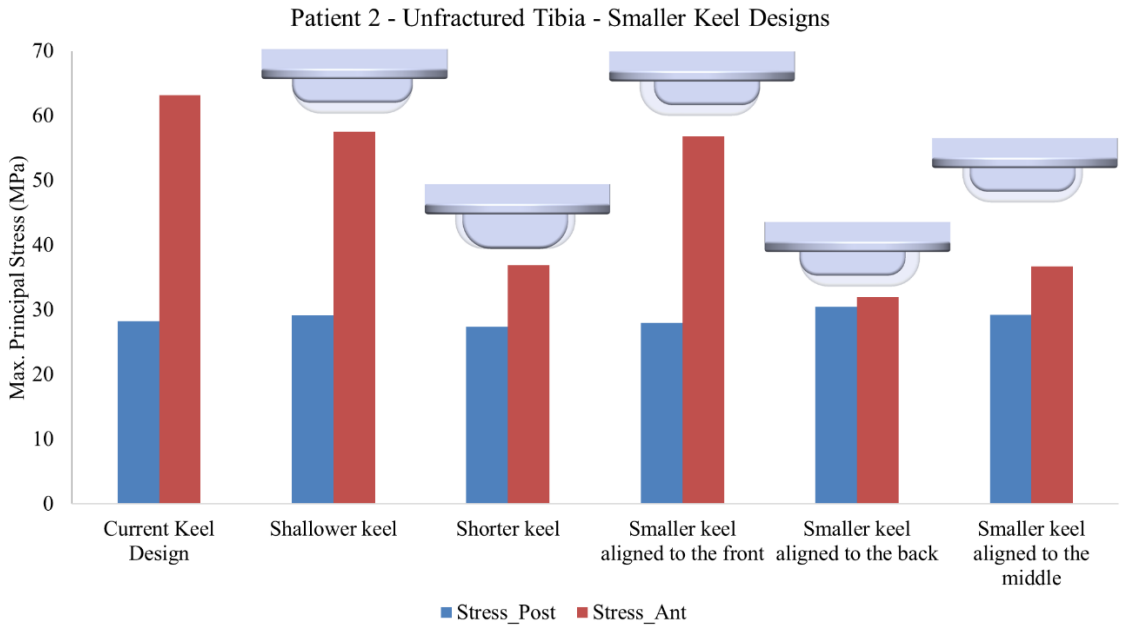

Figure 5.14: Highest maximum principal stress in the anterior and posterior part of the proximal tibia when tibial components with small keel designs were implanted into the unfractured tibia of Patient 2 with the original tibial resection. The five new designs are Design a to Design e from left to right.

These three tibial components with smaller keels were then implanted into the fractured tibia of Patient 2 with the original tibial resection. However, the keel slot cut through the bone and created holes in the tibia when Design *b* and Design *d* were used. When the small keel was placed at the centre (Design *e*), no holes were created in the bone and the highest stress was shown at the anteromedial corner of the keel slot (**Figure 5.15**).

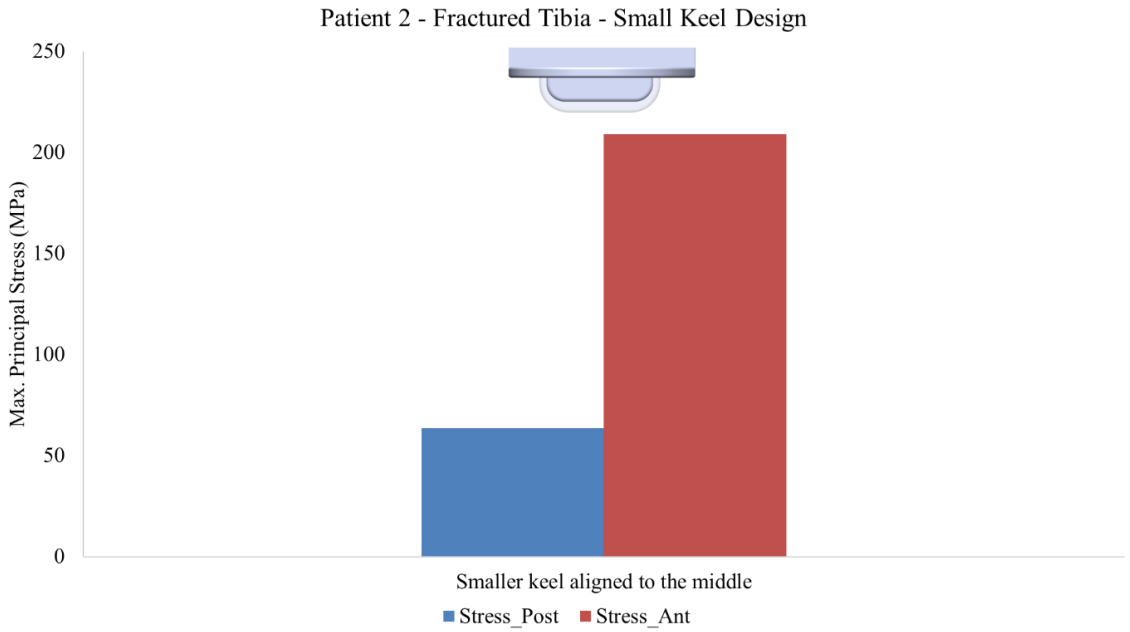

Figure 5.15: Highest maximum principal stress in the anterior and posterior part of the proximal tibia when the tibial component with a small keel placed in the middle (Design e) was implanted into the fractured tibia of Patient 2 with the original tibial resection.

5.4 Discussion

This chapter investigated the effects of tibial component position and orientation on the risk of tibial PPF after cementless OUKR. The position and orientation of the tibial components in the unfractured tibias of Patient 1 and Patient 2 mentioned in **Chapter 4** were altered in terms of their mediolateral position, proximal-distal position, internal-external rotation, and varus-valgus orientation.

The highest maximum principal stress in the unfractured tibia and fractured tibia of Patient 1 were 49.1 MPa and 152.6 MPa, respectively. This implies that when the position of the component was changed, if the maximum stress was around 50 MPa or smaller, then it was unlikely to fracture. If the stress was around 150 MPa or larger, the tibia would have a high chance of experiencing fracture. The mediolateral and proximal-distal translation of the component resulted in a large increase in stress when the component was moved medially

by more than 3 mm (increased by 184%) or moved distally by more than 5 mm (increased by 129%). This suggested that surgical errors that placed the component 3 mm or more too medial, or 5 mm or more too distal would greatly increase the risk of fracture. The SCD fell below 2 mm in these cases, consistent with the approximate threshold SCD value found in **Chapter 4**, below which a sudden increase in stress was seen (**Figure 4.44**). Internal or external rotation of the tibial component within 15 degrees around the mid-point of the AP cut did not show an increase in maximum stress by more than 30.6%. The highest values were 64 MPa and 57 MPa when the component was internally rotated by 15 degrees or externally rotated by 10 degrees. These were also the positions where SCDs were the shortest. The highest stresses found in the bone after changes in the component's internal-external rotation also suggested that a short SCD in either the anterior part or the posterior part of the tibia would lead to an increase in the high tensile stress at the anteromedial corner of the keel slot due to the bending motion around the keel as described in **4.4**. Thus, compared to large surgical errors that placed the component too medial or too distal, internal-external rotations around the mid-point of the AP cut which kept the vertical cut roughly next to the medial tibial spine were less likely to cause fracture. Varus-valgus rotation around the lateral edge of the keel slot showed small changes in the highest maximum principal stress, with the values ranging from 40 to 64 MPa. The mediolateral position and the proximal-distal position of the component remained roughly at the same place when it was rotated around the lateral edge of the keel slot. SCD remained above 2.5mm throughout the rotation. However, when the varus-valgus orientation was altered while keeping the vertical cut next to the apex of the medial tibial spine, placing the component in valgus significantly increased the stress. SCD was smaller than 2 mm when the component was rotated into valgus by 5 degrees or more. The highest maximum principal stress was around 120 to 150 MPa when the component was put in valgus by 5-

15 degrees. This implies that placing the component more in valgus than the current orientation was very likely to cause PPF in this patient. Large differences in results were shown when the tibial component's varus-valgus orientation was changed around two different landmarks. When the component was rotated around the apex of the tibial medial spine (**Figure 5.4**), the centre of the component moved laterally when it was placed in varus and moved medially when it was placed in valgus (**Figure 5.16**). The vertical cut planes were 1 mm, 2 mm and 3 mm more medial respectively when the component was rotated by 5, 10 and 15 degrees into valgus, compared to those with the components rotated around the lateral edge of the keel slot. Similarly, the vertical cut planes were 2 mm, 3 mm, and 4 mm more lateral when rotated into varus. Thus, changing the varus-valgus orientation of the tibial component while keeping the tibial wall next to the medial tibial spine was a combination of varus-valgus rotation and mediolateral translation.

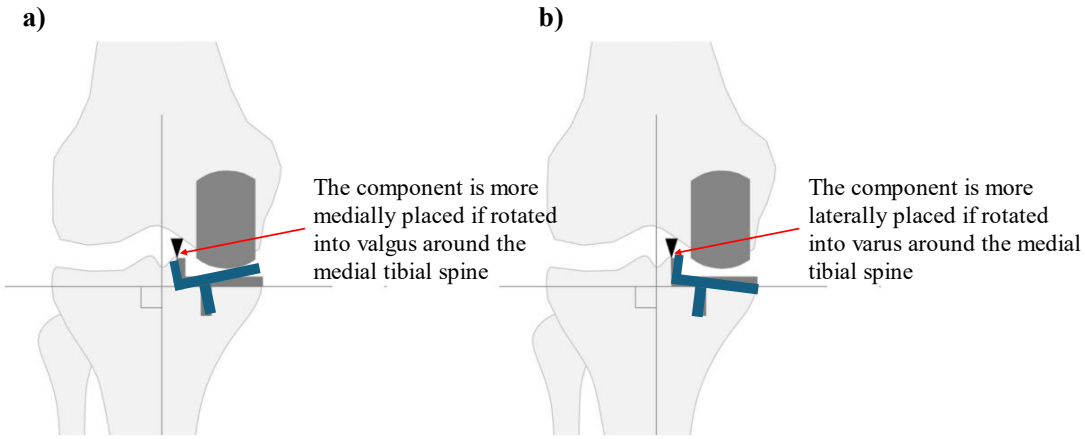

Figure 5.16: Varus-valgus rotation of the component around the medial tibial spine is a combination of the change of its orientation and the change of its mediolateral position. (a) When the component is rotated into valgus around the medial tibial spine, it is more medially placed than when it is rotated around the lateral edge of the keel slot. (b) Similarly, when the component is rotated into varus around the medial tibial spine, it is more laterally placed than when it is rotated around the lateral edge of the keel slot. Figure adapted from [158].

The results suggest that placing the tibial component in valgus while making the surgical cut next to the medial tibial spine was the least forgiving surgical error in these two high-

risk patients with small tibias and overhanging tibial plateaus. Even a 5-degree rotation was very likely to cause PPF. The second most detrimental surgical error was the medial placement of the tibial component. SCD decreased and the highest stress significantly increased when the component was put more medially than the reference position by around 3 mm or more. Making the horizontal cut 5 mm or more deeper than the reference position which placed the component too distally also increased the risk of PPF, doubling the maximum principal stress at the anteromedial corner of the keel slot. Internal or external rotation of the component within 15 degrees in each direction around the mid-point of the AP cut showed maximum stress of around 40-60 MPa, which was unlikely to cause PPF. While the component was rotated, the vertical cut remained roughly next to the medial tibial spine. However, rotation within 5 degrees in each direction is recommended as this makes the smallest change in SCD and stress and allows the surgical cuts to be more forgiving to surgical errors in other directions.

The same modifications to the tibial cuts were made in the unfractured tibia of Patient 2. The keel slot penetrated the bone when the cut was made 3 mm more medial or 4 mm more distal than the reference position. Varus placement of the component was more favourable compared to valgus placement and valgus rotation of the component around the medial tibial spine should be avoided. The shortest SCD decreased when the component was rotated by more than 5 degrees internally or externally around the midpoint of the AP cut. This made the tibia more prone to fracture if surgical errors in other directions or orientations were made. Thus, large internal or external rotations should be avoided.

Modifications to the tibial resections in Patient 1 and Patient 2 both showed that the component should not be placed more into valgus compared to their current location. Though the increase in stress was less obvious when the rotation was made around the lateral edge of the component, which roughly kept the original mediolateral position of the

component, a further surgical error in the medial direction would greatly elevate the risk of PPF. As the components were already in varus by around 5 degrees in these two tibias (**Table 4.6** and **Table 4.9**), the results suggest that the tibial component should be placed in varus in patients with overhanging tibial plateaus or small MPTAs. Placing the tray orthogonal to the tibial mechanical axis which is the standard position suggested in the surgical technique guidance (0-degree varus/valgus) [11] would elevate the risk of tibial PPF and also make it more sensitive to the mediolateral position of the vertical cut. Thus, a coronal placement in varus should be aimed for, which is also supported by the findings of Kamenaga et al. [158]. The next least forgiving surgical error was the medial placement of the component, followed by the distal placement of the component. When these surgical errors were made, the component showed medial overhang which indicated that the keel was getting relatively closer to the medial cortex. Overhang was also seen when component oversizing happened as described in **Chapter 4**. Thus, if severe overhang is shown when the trial component is tested, which may infer that the vertical cut was made too medial, the horizontal cut was made too distal or a tibial component too large was chosen, adjustments should be made accordingly either by making a more lateral vertical cut or using a smaller component to make sure a satisfactory coverage is achieved. Between mediolateral movement and proximal-distal movement, SCD decreased more rapidly as the component was moved medially than when it was moved distally. Thus, the tolerance to a horizontal cut too distal is slightly higher than the tolerance to a vertical cut too medial. Internal or external rotations of the tibial component around the mid-point of the AP cut which roughly maintain the component's mediolateral position showed the least detrimental effects. However, large rotations should be avoided as this greatly reduces the distance between the keel slot and the surface of the bone. This infers that further errors in

the mediolateral direction, proximal-distal direction or varus-valgus orientation would drastically increase the stress in the bone, and subsequently increase the risk of fracture.

Five small keel designs were tested (**Figure 5.5**): one that was 3 mm shallower (Design *a*), one that was 4 mm shorter (Design *b*) and three that were 3 mm shallower and 4 mm shorter than the current keel design (Design *c, d and e*). The three shorter and shallower ones were aligned to the front margin (Design *c*), back margin (Design *d*), and middle line (Design *e*) of the current keel design, respectively. In Patient 1, using the small keel which was placed in the middle (Design *e*) could reduce the stress in the fractured tibia to 55 MPa, which was the same stress level as that shown in the unfractured tibia when the current standard component was used (49 MPa). This implies that using this small keel Design *e* was highly unlikely to cause PPF in this tibia even with the same unsatisfactory tibial resection. In Patient 2, as the tibial resection was made too distal and too medial, the maximum stress was still three times that of the unfractured tibia when the small keel Design *e* was used. However, this design was the only one of the five designs and the current design that did not create penetration in the bone. Thus, placing the small keel in the middle gave the lowest risk of fracture among the six designs and was the only one of them that might have prevented fracture if used. The results from both Patient 1 and Patient 2 suggest that reducing the depth and length of the current keel design could reduce the risk of tibial PPF. The keel should be kept in the middle, i.e. the middle line of the small keel should align with the middle line of the current large keel on the tibial component. The size of the small keel was chosen to maintain the same surface area as the current keel design [124]. The current design of the cementless keel has a window in the middle (**Figure 1.3**) which was kept from the cemented version of the OUKR tibial component. This slot was designed for cement in-fill in the cemented version. As there is no substantial evidence showing that the window on the cementless keel is assisting or improving the fixation of the component, the

window was removed from the small keel designs. The smaller keels were 3 mm shallower in depth and 4 mm shorter in length to maintain the same surface area as that of the current keel for osseointegration [124]. This aimed to maintain the level of primary stability and secondary stability which could be achieved through bone ingrowth on the porous keel surface. This study by Rahman [124] also proved that one of the small keel designs (Design *c*) could provide similar, if not better, primary fixation as the current keel design, suggesting keels of this dimension are unlikely to compromise primary stability.

This study has some limitations that require further investigation. The same FEA model template used in **Chapter 4** was again applied in this study. Thus, the same limitations mentioned in **4.4** still exist. Despite having these limitations, this FE method provided enough insights into the effects that changes in surgical cuts and implant designs would bring to the risk of tibial PPF efficiently with reasonable model setup time and solving time. Other than the abovementioned limitations, only four tibia geometries from these two Japanese patients were studied and thus, the findings might not be generally applicable to all OUKR patients. However, these two high-risk patients are the representative cases that experienced post-operative tibial PPF after OUKR. A previous study in a Belgian cohort showed a mean MPTA measurement of 87.04° (SD = 2.07°) among 500 adults [178], which is 7 degrees larger than the mean in this study. Compared to other general tibia models, tibias in this study are more representative of Asian patients who have smaller tibias and more overhanging medial tibial plateaus. Also, as the pre-operative CT scans of these two patients were available, the elastic modulus of the bone could be derived from the density of the bone. This bone material assignment was more realistic and more representative of patients with AMOA. To the best of the author's knowledge, this is the first study that studied the effects that changes in surgical cuts and component designs would bring to the

risk of PPF after OUKR with heterogeneous bone elastic modulus assignment based on the density of the bone in small tibias that fractured.

5.5 Chapter Summary

This chapter studied how surgical errors in four directions (mediolateral, proximal-distal, internal-external rotation, varus-valgus orientation) affected the risk of tibial PPF after medial OUKR. Surgical errors in the varus-valgus direction are the least forgiving in patients with overhanging tibial plateaus. In patients with overhanging medial plateaus and small MPTAs, the component should be implanted in varus with the vertical cut abutting the medial tibial spine. Surgical cuts that place the component too medial or too inferior are the next two least forgiving errors. Moving the component medially would rapidly reduce the shortest SCD and when this reaches the threshold SCD value, i.e. when the slot is cut into the cortex, the risk of fracture immensely increases. Therefore, the surgical technique guidance should be strictly followed when deciding the mediolateral and proximal-distal position of the vertical and horizontal bone cut. Extreme internal or external rotation of the component should be avoided as this reduces the shortest distance between the keel slot and the cortex. This makes the tibias more sensitive to errors in the other three dimensions. Medial overhang is a sign of surgical errors and if shown when a trial component is put in, adjustment to the cuts or the size choice should be made.

This chapter also tested five small keel designs. The keel that showed the greatest reduction in the risk of fracture was 3 mm shallower and 4 mm shorter than the current design. This design has the same surface area as the current keel design, intending to keep the same level of primary stability and secondary stability. The margin of the keel should be as far away from both the anterior and posterior cortex as possible to minimise the risk of

accidentally damaging the cortex when making the keel slot. Thus, the keel should be placed in the middle of the tray in the AP direction with the middle of the new small keel aligned to the middle line of the original keel. This small keel design reduces the risk of fracture while in the meantime maintaining adequate primary fixation as demonstrated in a previous study [124].

Chapter 6. Risk of Lateral Progression of Osteoarthritis after Varus Placement of Tibial Component

6.1 Introduction

One conclusion from the study in **Chapter 5** was that the OUKR tibial component should be placed in varus in patients with tibia vara, small tibia or overhanging tibial plateau with the vertical cut abutting the medial tibial spine. Placing the tibial component in varus decreases the highest maximum principal stress induced in the tibia and therefore, reduces the risk of tibial PPF after cementless OUKR. This placement increases the shortest distance between the slot and the cortex, making it more forgiving to surgical errors by reducing the chance of accidentally damaging the cortex when creating the keel slot. Placing the tibial tray orthogonal to the tibial mechanical axis as suggested in the surgical guide or placing them in valgus could greatly increase the stress experienced by the bone and thus, elevate the risk of tibial PPF.

Despite its advantage of reducing the risk of PPF, there are concerns about whether placing the tibial component in varus would lead to medial subluxation of the femur and subsequently cause lateral progression of OA, which is the most common complication of cementless OUKR [56, 85] (**Figure 6.1**).

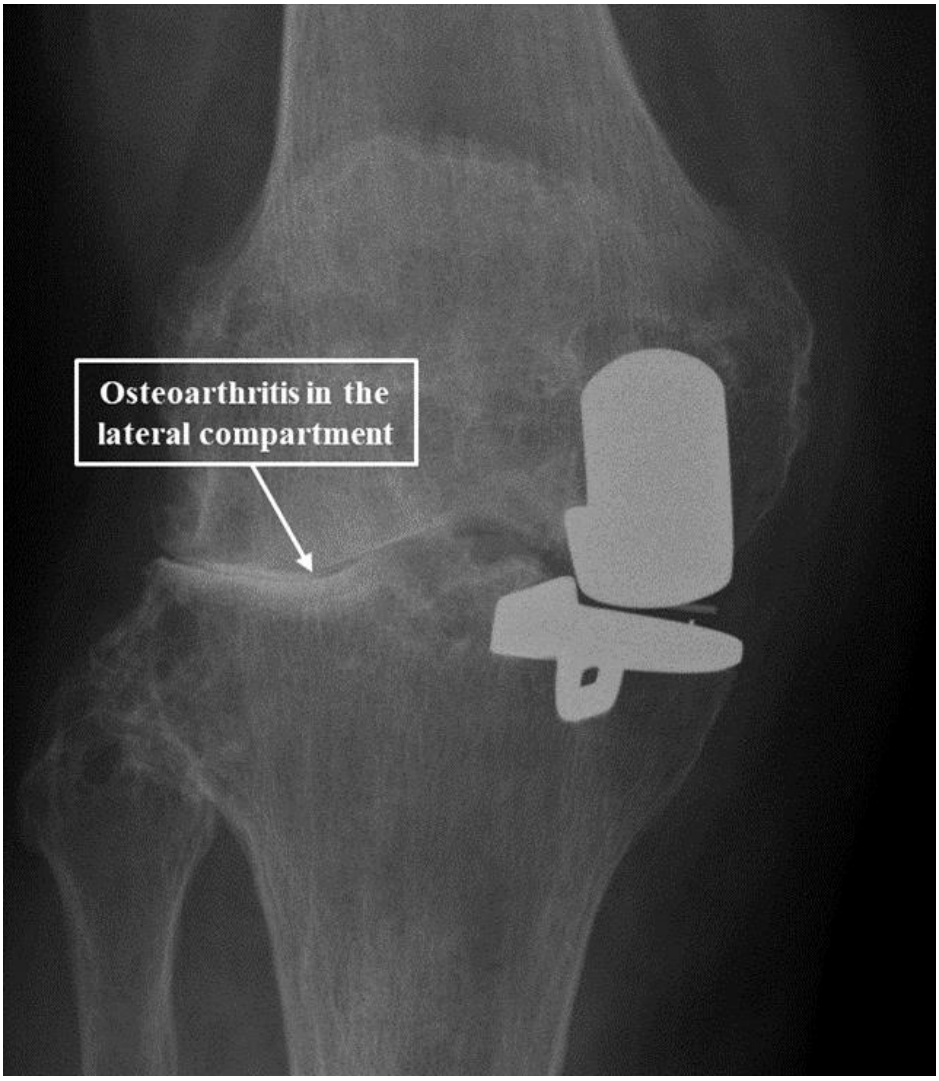

Figure 6.1: Lateral progression of osteoarthritis after Oxford Unicompartmental Knee Replacement.

As the inferior flat surface of the bearing is in full contact with the superior surface of the tibial tray while the bearing moves, the bearing would also be in varus relative to the tibial mechanical axis when the tibial component is placed in varus. The upper surface of the bearing which is concave and spherical would stay congruent with the spherical femoral component (**Figure 6.2**).

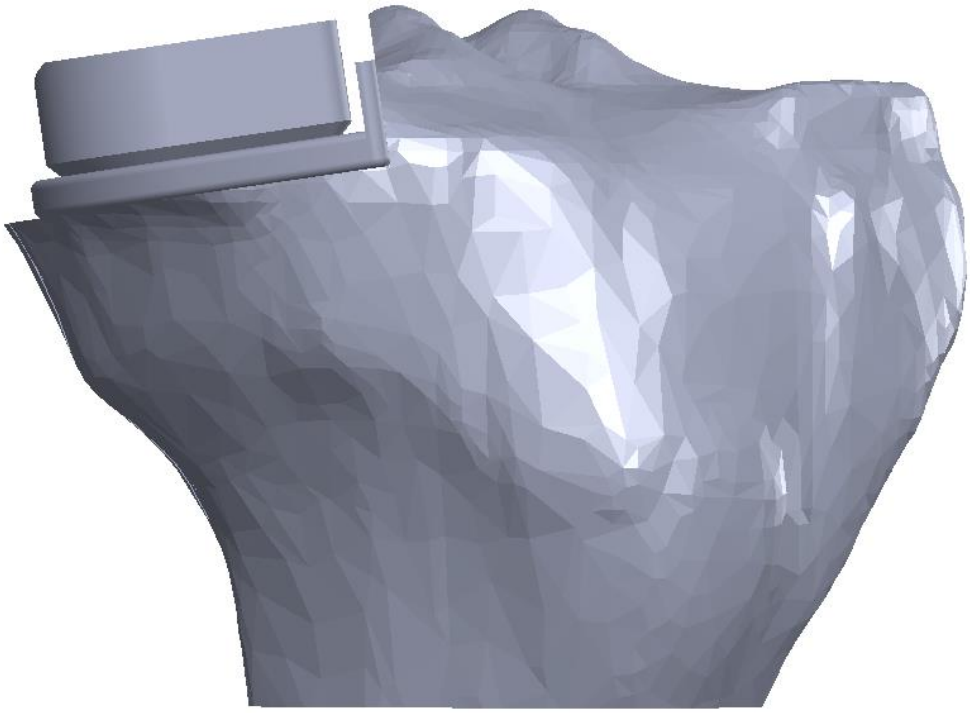

Figure 6.2: The varus-valgus orientation of the bearing follows that of the tibial component.

When the knee is loaded as the patient is completing daily activities, the femoral component transfers the load to the tibial component through a compressive load on the bearing. The bearing transfers this load to the superior surface of the tibial component which is at an angle with the tibial mechanical axis when the component is placed in varus. This reaction force has a horizontal component pointing medially which might push the bearing and cause it to slide medially. As theoretically, the femoral component is in full congruency with the concave surface of the bearing, together with the effect of the compressive load from the femur to the tibia, the femur might slide medially with the bearing. This could cause the femur to undergo medial subluxation. When the femur moves medially above a certain distance, the medial face of the lateral condyle in the intercondylar fossa may come into contact with the lateral tibial spine. Repetitive contact and abrasion between these two surfaces can induce erosion of cartilage and eventually lateral progression of OA.

Though concerns about lateral progression of OA following varus placement of the tibial component were raised by surgeons, no clinical evidence nor experimental or computational justification has been given. The objective of this computational study was to gain an understanding of the effects that changes in surgical factors of medial OUKR may bring to the lateral knee compartment. FEA was conducted to monitor the movement of the meniscal bearing in a medial OUKR-implanted knee when changes were made to the tibial component position. As the tibial components were placed at about 3-6° varus in the two cases studied in **Chapter 4** (**Table 4.6** and **Table 4.9**), varus and valgus placements of 3 and 6 degrees were tested. The results of this exploratory study provided insight into possible adverse effects that changes in component position made for a reduction in risk of fracture might bring to other parts of the knee joint.

6.2 Methods

6.2.1 Finite Element Analysis of Standard Placement of Tibial Component

OUKR tibial components in this model were placed at the standard recommended positions with no varus or valgus [11].

6.2.1.1 Model Setup

The OUKR tibial component, femoral component and meniscal bearing were virtually implanted into an FE model consisting of lateral femoral cartilage, lateral meniscus and lateral tibial cartilage. The geometries of the femoral cartilage, meniscus and tibial cartilage were taken from a previous study [179]. The positions of the OUKR components relative to these tissues in the lateral compartment were decided by virtually implanting the components into the tibia from which the cartilages and meniscus were built in SolidWorks

2022 (Dassault Systèmes, France) (**Figure 6.3**). Then this relative position between the medial OUKR components and the lateral compartment was replicated in the FE model in ABAQUS/CAE 2020 (Dassault Systèmes, France). The knee was at around 30° flexion based on the orientation of the femoral cartilage relative to the tibial cartilage in the lateral compartment. Therefore, the bearing was placed 1 mm away from the wall and 6 mm posterior to the middle line of the bearing in the AP direction [166].

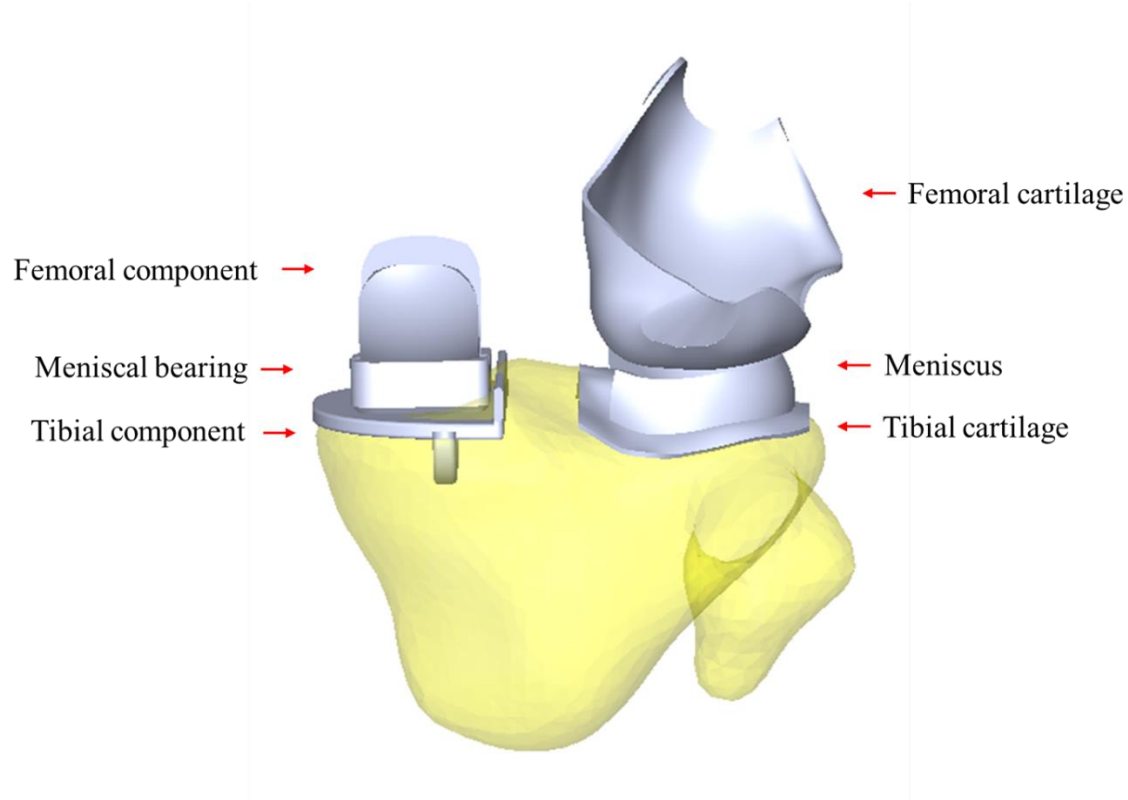

Figure 6.3: The positions of the Oxford Unicompartmental Knee Replacement components were determined by virtually implanting the components into the tibia from which the cartilage and meniscus were built. The tibia was only used to find the positions of the components. It was not simulated in the FE model.

6.2.1.2 Boundary Conditions and Loads

The tibial component was fixed in all degrees of freedom throughout the simulation. The bottom surface of the tibial cartilage, which is the inner surface that is connected to the proximal end of the tibial bone was coupled to a reference point and constrained in all

degrees of freedom. This assumed that the tibia stayed stationary. The upper surface of the femoral cartilage which is the inner surface that is attached to the distal end of the femoral bone was coupled to a reference point. In real life, both the lateral femoral cartilage and the OUKR femoral component are attached to the femur and their relative positions should remain the same given the component is well-fixed. Therefore, the femoral cartilage was coupled to the femoral component. This coupling ensured that the femoral component would move with the femoral cartilage.

Analysis failed when proper contact could not be achieved between the meshed surfaces of the femoral component and the meniscal bearing. When contact between the inferior surface of the femoral component and the superior surface of the bearing was not successfully established, the femoral component was not constrained in the vertical direction. This inadequate definition of boundary conditions led to failure in analysis convergence. At the start of the analysis, the femoral component was placed above, but not in contact with the bearing (**Figure 6.4**). Then the femoral cartilage and the femoral component were moved vertically downwards to bring them into contact with the meniscus and the tibial component, respectively. The initial distance between the femoral component and the meniscal bearing and the distance between the femoral cartilage and meniscus were adjusted by monitoring the contact pressure on the lateral tibial cartilage and the mediolateral movement of the bearing. All other degrees of freedom of the femoral cartilage and the component were constrained in this step. This process is defined as the 'Contact' step. This 'Contact' step is not a representation of an actual joint motion but a preparation step necessary for successful computational simulations. Then a 2000 N vertical force was applied to the femoral component and femoral cartilage altogether to simulate the load in the knee joint during gait [165]. This study assumed that the reaction force transferred from the femur to the tibia acts in the same direction as the body weight

which is vertically downwards. After the knee was loaded, the contact pressure on the tibial cartilage should be roughly evenly distributed beneath the meniscus and the bearing should not experience large mediolateral translation as the knee joint was stable [180]. If a concentrated pressure was seen on the tibial cartilage which indicated that the initial distance between the femoral cartilage and the tibial cartilage was too small, the femoral cartilage would be moved upwards until the pressure concentration disappeared. The femoral cartilage and the femoral component were allowed to move in the mediolateral and proximal-distal direction and were constrained in the other four degrees of freedom. This assumed that the rotational motion of the femoral head was not constrained.

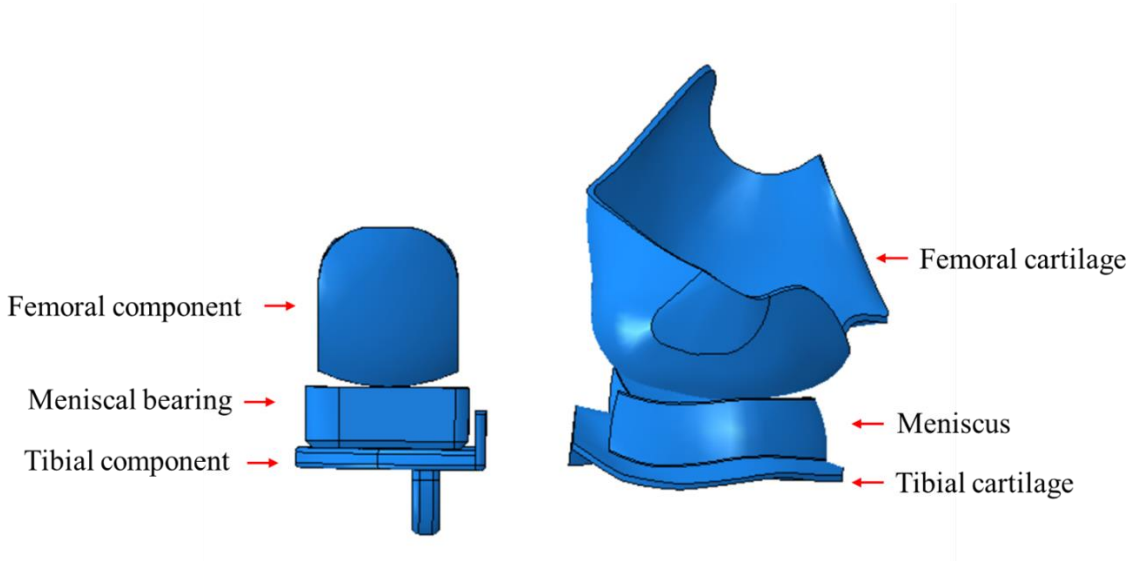

Figure 6.4: The femoral component and the femoral cartilage were brought downwards into contact with the meniscal bearing and the meniscus in the contact step.

As the bottom surface of the meniscus was already in congruency with the femoral cartilage, which represented its appropriate mediolateral position and AP position when the knee joint was under load, the bottom face of the meniscus was constrained in these two dimensions. It was assumed that the bottom of the meniscus was already in the place it would be under load and would not be pushed further outwards in the radial direction. It was free to move

in the distal-proximal direction to fill the gap between the meniscus and the tibial cartilage in case of small offset in their geometrical shapes.

The OUKR meniscal bearing was constrained in the AP direction in the contact step and was free to move thereafter when the knee was loaded.

6.2.1.3 Material Properties

The material properties of each part are listed in **Table 6.1** and **Table 6.2**. All three OUKR components were modelled as linear elastic materials. The tibial and femoral cartilage was modelled as Neo-Hookean hyper-elastic material and the meniscus was sectioned into three layers (**Figure 6.5**) as in previous studies [179, 181]. The internal layer was more compressible and softer than the stiffer external layers on the top and bottom.

Table 6.1: Material properties of Oxford Unicompartmental Knee Replacement components.

	Young's Modulus (MPa)	**Poisson ratio**
CoCrMr Tibial Component [182]	220000	0.3
CoCrMr Femoral Component [182]	200000	0.3
Polyethylene Meniscus Bearing [108]	700	0.3

Table 6.2: Material properties of soft tissues in the lateral compartment.

Neo-Hookean Model	C_{10}	D_1
Cartilage [179]	1.667	0
Meniscus – Outer Layer [179]	2.614	0.008
Meniscus – Internal Layer [179]	2.256	0.205

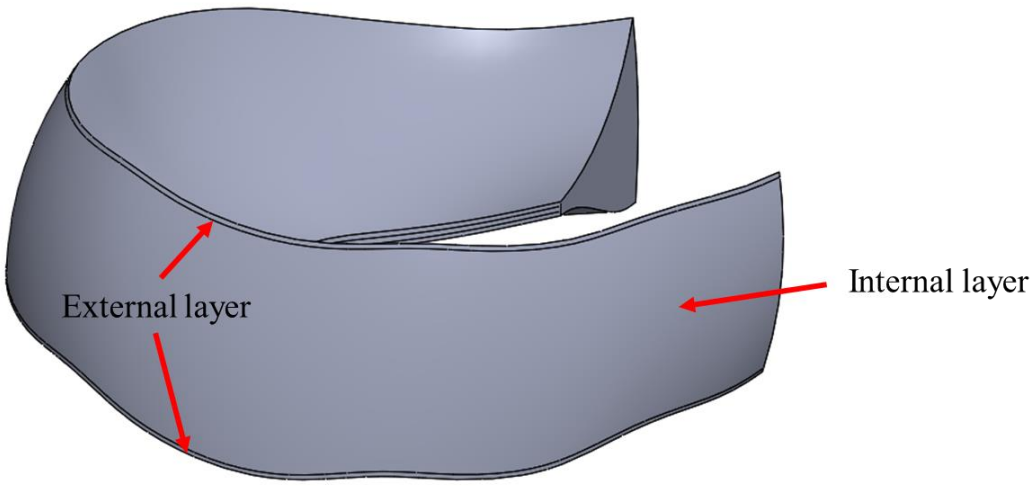

Figure 6.5: The meniscus was sectioned into three layers based on their material properties.

6.2.1.4 Mesh

The femoral cartilage and tibial cartilage were meshed with 1.5 mm 8-node brick elements (C3D8RH). This captured the curvature of the two geometries. All other parts were meshed with 10-node quadratic tetrahedral elements (meniscus, tibial component and femoral component: C3D10H, meniscal bearing: C3D10M). The meniscus was meshed with 1 mm elements. The meniscal bearing was meshed with 1.6 mm elements. The femoral component was meshed with elements of 2.5 mm and the tibial component was meshed with elements of 2.0 mm.

6.2.1.5 Contact

The COF between the meniscal bearing and the femoral and tibial components was 0.04 [183]. The COF was 0.02 between the two cartilage and between the cartilage and the meniscus [184].

6.2.2 Finite Element Analysis of Varus and Valgus Placements of Tibial Component

6.2.2.1 Model Setup

To simulate the varus placements of the OUKR tibial component which were suggested in **5.5** to reduce the risk of tibial PPF, the tibial components were rotated around the lateral superior edge of the tibial wall by 3° and 6° respectively (**Figure 6.6**). This assumed that the vertical cuts were made immediately next to the apex of the medial tibial spine in all models. As the femoral component was placed perpendicular to the superior surface of the tibial tray in the surgery, it was rotated by the same amount as the tibial component. The bearing stayed on the tibial component at the same relative position.

Valgus placements of 3° and 6° around the same axis were also tested.

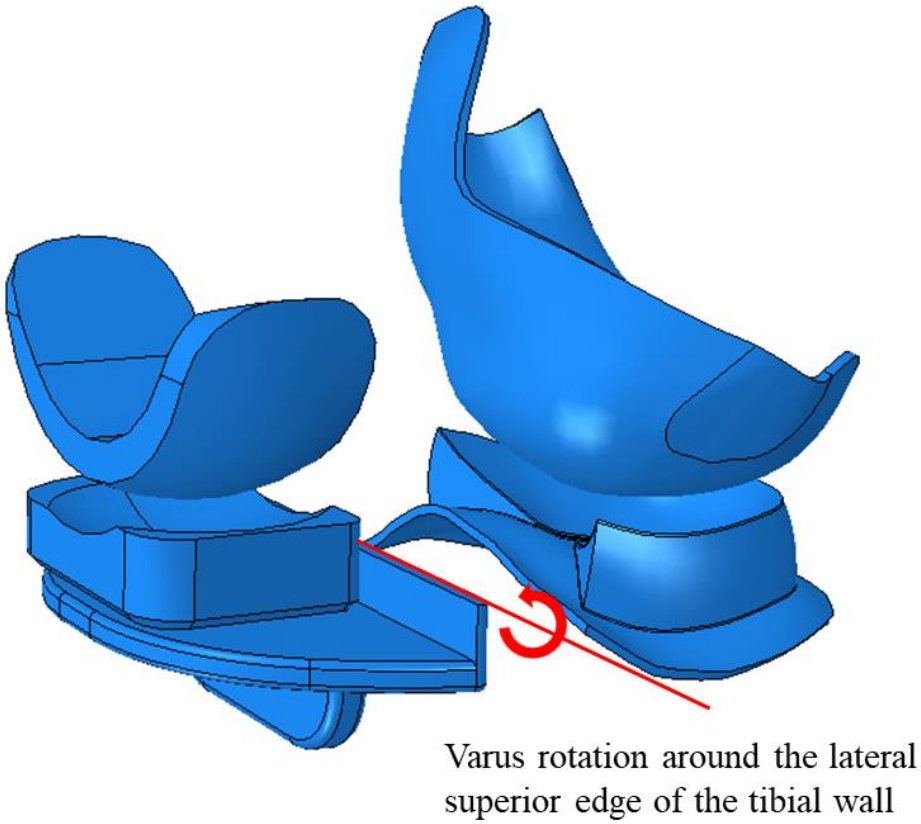

Figure 6.6: Varus and valgus rotations of the component were made around the lateral superior edge of the tibial wall.

6.2.2.2 Boundary Conditions

The femoral component moved in the same proximal-distal direction relative to the whole skeletal system as in **6.2.1**. The femoral component and the femoral cartilage were still displaced and loaded in the same direction – the vertical direction before the components were placed in varus or valgus.

6.3 Results

Compared to its original mediolateral position, which was 1 mm away from the tibial wall, the bearing shifted medially by 1.12 mm and 1.38 mm when the tibial component was placed in 3-degree and 6-degree varus, respectively, which indicated a medial subluxation of the femur relative to the tibia (**Figure 6.7**). The bearing did not move when the tibial component was at its standard position and in 3-degree valgus. It impinged the wall when the tibial component was placed in 6-degree valgus.

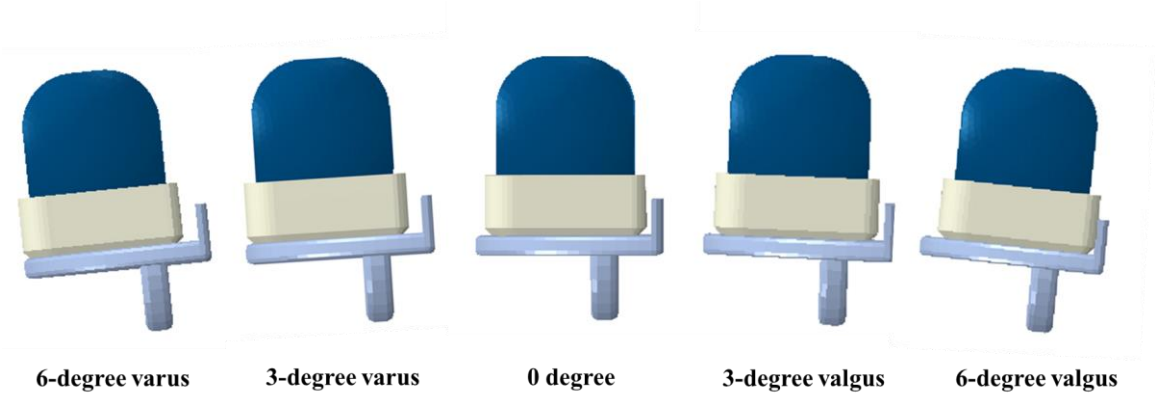

Figure 6.7: The bearing shifted medially when the tibial component was in varus and shifted laterally when the tibial component was in large valgus.

6.4 Discussion

The results of this chapter suggest that the femur has a tendency to move medially when the tibial component is placed in varus. This can subsequently cause the lateral face of the femoral intercondylar fossa to contact the lateral tibial spine. Overloading of the lateral compartment and repetitive impingement at these two surfaces may cause the cartilage to wear down and lead to lateral progression of OA [185, 186]. This implies that though varus placement of the tibial component was recommended for small patients with overhanging tibial plateau to reduce the risk of tibial PPF after cementless OUKR in [158] and in **5.4**,

this needs to be conducted with care. This model could be further enhanced and applied to monitor the contact pressure and load bearing in each compartment. If the 3D model of a natural knee joint is available, the normal contact pressure in a healthy knee joint can be studied with FEA and used as a reference to assess if a specific positioning of the component will lead to a large change in load distribution in the joint. This can provide us with more information on the adverse effect that a specific component positioning will bring to the other compartments of the knee joint (e.g. lateral progression of OA).

This exploratory study has some limitations that should be noted. Firstly, only one timeframe of knee flexion-extension (30° flexion) was simulated. The load distribution in the knee joint varies as the knee flexes. As the results based on one timeframe already showed medial movement of the femur relative to the tibia, these simulations at 30° flexion demonstrate that there is an increased risk of lateral progression of OA as the tibial component is placed in varus. Secondly, this model does not consider any ligaments, tendons or muscles associated with the knee joint. In the knee joint, soft tissues constrain the movement of bones as mentioned in **1.1**. However, musculoskeletal modelling is another level of complexity and is outside the scope of this study. The movement of the femur as the varus-valgus orientation of the tibial component is altered is the focus of this study. The direction of movement is likely to remain the same in a full musculoskeletal model when the same settings of soft tissues (insertion points, strength, etc.) are used across all simulations. Thirdly, this study assumes that the load transfers from the femur to the bearing is in the vertical direction. Again, musculoskeletal modelling is needed to fully understand the direction of joint contact load, especially in patients with tibia vara about which little is known. This is outside the scope of this project, so a simplified loading case was modelled. As the loading direction was kept the same in all simulations, the comparative results imply that placing the tibial component in varus is more likely to cause

medial movement of the femur than placing it in valgus. Lastly, the bottom surface of the meniscus was constrained to ensure complete contact between the meniscus and the tibial cartilage while the menisci are free to move in the natural knees with their movements constrained by their insertions on the tibia at the anterior and posterior horns. This boundary condition might have limited the range of motion of the femur in the mediolateral direction. However, as the top of the meniscus was free to move and expand in the radial direction, this should not have significantly affected the mobility of the femur. Nevertheless, more practical boundary conditions on the meniscus should be applied in future models that contain more realistic geometry of the soft tissues.

6.5 Chapter Summary

Placing the tibial component in varus can cause the femur to slide medially relative to the tibia. This can potentially lead to repetitive contact between the femoral intercondylar fossa and the lateral tibial spine during daily activities. This increased contact and overloading at these regions may lead to an increase in the risk of lateral progression of OA after medial OUKR. Thus, large varus should be avoided to prevent the chance of developing lateral OA.

Chapter 7. Risk Factors of Cementless Oxford Unicompartmental Knee Replacement Tibial Component Subsidence

7.1 Introduction and Aim

As previously discussed in **1.5**, cementless OUKR has demonstrated excellent survival of 94% at 14 years post-operation [85], providing better implant fixation compared to the cemented version [187]. Valgus subsidence of the tibial component which was briefly introduced in **1.5.1.1** is an uncommon complication of cementless OUKR that usually happens during the early recovery stage. It causes pain and constrains the mobility of the patient. The causes of valgus subsidence still require further investigation.

7.1.1 Symptoms of Cementless Tibial Component Subsidence after OUKR

Symptoms of diagnosis are mainly patient-reported pain and radiographic evidence of large component tilting.

Clinical: Most subsidence patients reported pain in the initial recovery period. However, pain improved with modified partial weight-bearing and without further surgical intervention by one-year post-operation in most cases [87, 88].

Radiographic: Large tilting of the tibial component was seen on AP and lateral radiographs taken at later follow-ups when compared to the immediate post-operative radiographs. Tilting of these components, which is generally several degrees, is different to those found in RSA studies of component fixation, where the migrations (in mm) and rotations (in degrees) are in order of magnitude of 0.01-0.1 mm or degree. These small movements are likely to be the ‘bedding-in’ process of the tibial components which are not fully seated

intra-operatively [188]. Cementless tibial components are usually left slightly proud of the horizontal cut surface to avoid unnecessarily large impaction force which increases the risk of tibial PPF [188]. Conversely, a notable change in position can be seen when comparing immediate post-operative radiographs of these subsidence patients to those from later follow-ups (**Figure 1.8**).

However, in most subsidence cases, the components became well-fixed showing good fixation at one-year follow-up. No radiographic evidence of further subsidence was shown after the initial identification [87, 88]. In the few cases that were revised, osseointegration and bony ingrowth around the keel were observed [87].

Scarce publications were found on subsidence after cementless OUKR and to the best of the author's knowledge, no reviews on this complication were conducted. Therefore, this chapter studied the possible causes of the subsidence of cementless OUKR tibial components through a systematic review (Part A) and some hypothesised risk factors were investigated through computational simulations (Part B).

7.2 Part A: Systematic Review on Tibial Component Subsidence after Cementless OUKR

The first part of this chapter (Part A) investigated the risk factors for the subsidence of cementless OUKR tibial components through a review.

7.2.1 Methods

A review was conducted on the topic of 'Causes and incidence of subsidence and migration of the tibial component in UKR' in a systematic manner. The aim was to identify all subsidence cases in the literature and collect their radiographs for radiographic studies.

The PICO (Patient, Intervention, Comparison, Outcome) framework was applied (**Table 7.1**).

Table 7.1: Patient, Intervention, Comparison, Outcome (PICO) framework of the review.

Patients	Adult patients (>18 years old) with unicompartmental knee osteoarthritis or osteonecrosis that were refractory to conservative treatments and required surgical interventions
Intervention	Surgical treatment using medial OUKR
Control	N/A
Outcomes	Primary outcomes: • Incidence of notable tibial component migration or subsidence • Causes and risk factors for tibial component migration or subsidence Secondary outcomes: • Level of subsidence and distance of migration • Time points of subsidence shown • Patient-Reported Outcome Measures (PROMs): Oxford Knee Scores of subsidence or migration patients • Subsidence mode (e.g. valgus, posterior) • Was pain reported? • Progression of OA? • Ethnical factor? • Radiolucency?

7.2.1.1 Search Strategy

Screening was conducted in Embase, Medline, Scopus, PubMed, Web of Science and Cochrane Library. Results from manual searches were also included. The search in Embase, Medline, Scopus, and Cochrane Library was conducted on the 11th of March 2022. The same search strategy was repeated in PubMed on the 4th of April 2022. A manual search for additional papers and grey literature was completed on the 26th of April 2022.

The search strategy was composed with the assistance of an experienced librarian. Keywords and phrases used for searches were: 1) knee replacement, 2) unicompartmental, 3) migration or subsidence, 4) primary stability or secondary stability, 5) Radiostereometric analysis. Radiostereometric analysis (RSA) is a technique developed to examine implants' fixation through the measurements of their migrations [189]. During surgeries, radiopaque tantalum marker beads are embedded into the bone. The positions of these marker beads are then used to find the change in the position and rotation of the components in three dimensions relative to the host bone with an RSA software package. Thus, the results of RSA studies can provide information about the early migration of implants [189]. Articles on RSA studies were included intending to identify any large early tibial component migration which might indicate subsidence. These keywords were then expanded to build search strings in Embase as below.

Embase Search Strings

1 Arthroplasty, Replacement, Knee/
2 Knee Prosthesis/
3 1 or 2
4 (Unicompartment* or Uni-compartment*).ti,ab.
5 (Unicondyl* or Uni-condyl*).ti,ab.
6 partial.ti,ab.
7 (UKA or UKR or PKA or PKR or UCA or UCR).ti,ab.
8 4 or 5 or 6 or 7
9 3 and 8
10 migrat*.mp.
11 subsid*.mp.
12 (RSA or Radiostereo* or "roentgen stereo*").mp.
13 ("primary fixation*" or "secondary fixation*" or "primary stability" or "secondary stability").mp.
14 10 or 11 or 12 or 13
15 9 and 14

The search strings were then modified for each database (**Appendix D**). The reference lists of relevant results were further explored.

7.2.1.2 Eligibility Criteria and Study Selection

Inclusion criteria: This systematic review considered all studies that mentioned subsidence, migration or early movement of the tibial component of any UKR or partial knee replacement. As the mechanism of subsidence might be universal among different implants, included studies were not limited to those about medial OUKR.

7.2.1.3 Data Collection and Extraction

Search results with full references were imported to EndNote 20 for screening. Duplicates were removed after which the titles and abstracts were examined. Full texts of shortlisted studies were extracted.

The following information was collected from each study:

- First author
- Publication year
- Fixation type of the subsided implant, i.e. cementless or cemented
- The number of subsidence cases identified
- Gender of the subsidence patients
- Age at operation
- Diagnostic criteria for subsidence
- Time points of diagnosis
- Mode of subsidence, e.g. posterior, valgus
- If revision surgery was performed
- If progression of lateral OA was shown
- If pain was reported
- Pre-operative and post-operative PROM scores
- Evidence of radiolucency on post-operative radiographs
- Ethnic group

- Hypothesis about the aetiology of subsidence

AP and lateral radiographs of the reported cases were collected. If they were not available in the published material, the authors of the study were contacted to obtain post-operative radiographs if possible.

7.2.2 Results

7.2.2.1 Literature Search Results

643 articles were identified from the databases searched and five other studies were found from manual searches (**Figure 7.1**). 241 articles remained after duplicates were removed, 45 of which were included for full-text retrieval after titles and abstract screening. 29 articles were excluded after the full-text assessment (details listed in **Appendix E**).

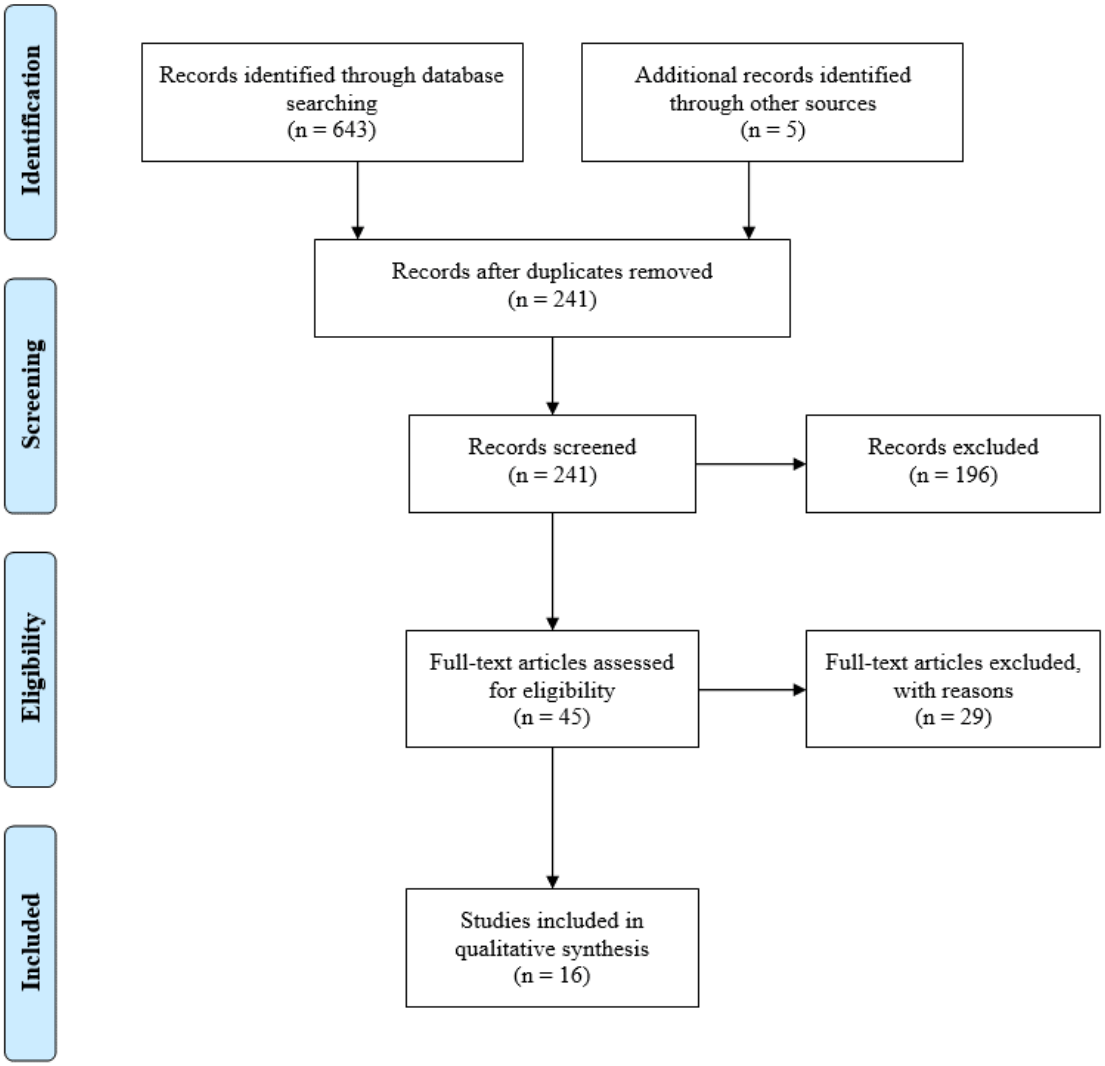

Figure 7.1: PRISMA flow diagram of the review.

16 eligible studies were identified. 23 cases of subsidence that showed notable tibial component tilting after cementless OUKR were identified from the literature and five other cases were identified in a cohort from the designer centre (Oxford) in a radiographic study conducted by Arthur et al. [190]. One case from [86] showed varus subsidence, one case from [89] showed posterior-only subsidence and one case from the designer centre showed varus and posterior subsidence [190]. All other cases developed various degrees of valgus subsidence in their early recovery period. Some valgus cases also showed combined

posterior subsidence. Details of these 28 cases are listed in **Table 7.2**. The incidence ranged from 0.3% to 5%.

Table 7.2: Details of subsidence cases collected. BMI: Body mass index; OA: Osteoarthritis; Pre-op: pre-operative; Post-op: Post-operative; OKS: Oxford Knee Score; Y: Yes; N: No; N/A: Not applicable; AM: anteromedial.

	First Author	Year of publication	Incidence	Case number	Mode of subsidence	Age at the time of operation	Gender	BMI	Progressive to lateral OA	Revision	Pain reported	Pain gone	Distance of subsidence	Pre-op OKS	Post-op OKS
1	**Liddle**	**2013**	**4/1000**	**1**	Valgus	61	Female	-	N	N	-	-	-	Mean 24.7	Mean 39.3
2				**2**	Valgus	-	-	-	N	N	-	-	-		
3				**3**	Valgus	-	-	-	N	N	-	-	-		
4				**4**	Varus	64	Male	-	N	N	-	-	-	-	30
5	**Liddle**	**2014**	**-**	**1**	Valgus	79	Male	-	N	N	4-month: pain deep within knee	In the first post-operative year	4-month: from 4 degrees varus to 8 degrees valgus relative to the mechanical axis	-	3-year: 39
6				**2**	Valgus	66	Male	-	N	N	4-week: AM pain	8-week post-op after two weeks of partial weight-bearing	4-week: valgus subsidence	-	-
7				**3**	Valgus	66	Male	-	N	Revision to cemented tibial component	6-week: medial pain	N/A	6-week: valgus subsidence	-	-
8				**4**	Valgus and posterior	65	Male	-	N	to TKA	6-month: progressive pain with stiff knee	N/A	6-month: valgus-posterior subsidence	-	-
9				**5**	Valgus	62	Female	-	N	N but debridement at 15-month post-operatively - switching to a 2mm thicker bearing	6-month: AM tibial pain and femoral pain with reduced mobility	In the first post-operative year	6-month: valgus subsidence	-	10-month after debridement: 35
10				**6**	Valgus and posterior	76	Male	-	N	N	2-week: AM pain on weight-bearing	3-month	3-month: valgus-posterior subsidence	-	2-year: 36

11	**Kamenaga**	**2019**	**6/120**	**1**	Valgus	72.7 ± 7.7	5 females/ 1 male	-	N	N	-	Before 12 months	(2-degree theshold) 3-month: valgus angle: 3.4 ± 0.9; two showed more than 2 degrees of posterior subsidence	24.7 ± 7.1	3-month: 23.5 ± 9.7; 12-month: 33.7 ± 7.6
12				**2**	Valgus			-	N	N					
13				**3**	Valgus (reported as valgus but more like posterior)			-	N	N					
14				**4**	Valgus			-	N	N					
15				**5**	Valgus			-	N	N					
16				**6**	Valgus			-	N	N					
17	**Hefny**	**2020**	**4/158**	**1**	Valgus and posterior	mean 76 (70 to 83.9)	-	-	Y	to TKA at 2-year postoperatively due to lateral progression	Medial pain during early recovery period	N/A	posterior subsidence of 5 mm at year 1 to 9 mm at year 2; valgus subsidence of 7 degrees	-	-
18				**2**	Valgus and posterior		-	-	N	N	Medial pain during early recovery period	-	-	-	Two had 5-year OKS of 38 and 43; one died after 12 months post-op
19				**3**	Valgus and posterior		-	-	N	N	Medial pain during early recovery period	-	-	-	
20				**4**	Posterior		-	-	N	N	Medial pain during early recovery period	-	-	-	
21	**Panzram**	**2020**	**2/192**	**1**	Valgus and posterior	-	-	-	-	Bearing change due to dislocation	-	-	2-degree posterior and 5-degree valgus	-	-
22				**2**	Valgus and posterior	-	-	-	-	N	N	N/A	1.8-degree posterior and 5.1-degree valgus	-	-

23	**Hefny**	**2020**	**1/61**	**1**	Valgus	67	Female	-	N	N	Patient reported increased pain at 8 weeks post-operation	Pain disappeared by one year post-operation	3.2 degrees of valgus subsidence in the first two months; no further subsidence	-	1-year: 44
24	**Arthur**	**2023**	**5/94**	**1**	Valgus and posterior	71	Male	34	N	N	N	N/A	2.7 degrees of valgus, 6.0 degree of posterior subsidence in the first year post-operatively, no further subsidence	-	5-year: 26
25				**2**	Valgus and posterior	65	Male	-	N	N	N	N/A	2.8 degrees of valgus, 1.6 degrees of posterior subsidence in the first year post-operatively, no further subsidence	-	2-year: 48
26				**3**	Valgus and posterior	74	Female	39	N	Femoral fracture at 5-year followup	N	N/A	2.4 degrees of valgus, 2.7 degrees of posterior subsidence in the first year post-operatively, no further subsidence	-	5-year: 31
27				**4**	Valgus and posterior	69	Male	29	N	N	N	N/A	4.9 degrees of valgus, 1.0 degrees of posterior subsidence in the first year post-operatively, no further subsidence	-	5-year: 48
28				**5**	Varus and posterior	57	Female	24	N	N	N	N/A	1.6 degrees of varus, 3.8 degrees of posterior subsidence in the first year post-operatively, no further subsidence	-	5-year: 45

7.2.2.2 Proposed Aetiology of Subsidence

Out of the 28 reported cases, radiographs of 18 cases were collected (18 AP radiographs and 14 lateral radiographs). The proposed causes of tibial component subsidence are listed in **Table 7.3**. Radiographs and more details are listed in **Appendix F**.

Table 7.3: Summary of the proposed aetiology of tibial component subsidence.

Patient-related factors	Surgical or mechanical factors
Lower local bone density and poor metaphysis bone quality in the tibias of elderly patients (> 70-year-old) [89, 191]	Lateral placement of the femoral component relative to the tibial component [87-89]
	Excessive external rotation of the tibial component [88]
	Damage to the horizontal cut face due to deep vertical saw cut [87]
	Damage to the posterior cortex [87]

None of these studies reported evidence of infection in subsidence patients.

Lateral placement of the femoral component relative to the tibial component and excessive external rotation of the tibial component both could potentially lead to the impingement of the mobile bearing against the lateral wall of the tibial tray, which subsequently might lead to valgus subsidence [87]. This mechanism was briefly introduced in **1.5.1.1** (**Figure 1.9**). The bearing tends to stay away from the lateral wall of the tibial tray when the knee is at extension, which is the position at which post-operative AP radiographs are taken [192]. Thus, contact or impingement of the bearing with the wall may not be visible on these radiographs. The bearing moves posteriorly and laterally from 0° to 60° knee flexion. Then during knee flexion from 60° to 120°, in the mediolateral direction, the bearing may move towards the wall or move away from the wall. In some cases, the bearing would contact the wall at deeper flexion [91]. When the femoral component was placed laterally relative to

the tibial component, the femoral component would displace the bearing further laterally and eventually lead to impingement of the bearing against the wall.

7.2.2.3 Revisions

Revision surgeries were conducted on six knees out of the 28 subsidence cases, though three of which were revised due to reasons unlikely to be related to subsidence (one debridement at 15 months post-surgery, one bearing dislocation after subsidence was identified, and one femoral fracture at five-year post-surgery) [87, 90, 190]. One revision case reported by Liddle et al. [87] was revised to a cemented tibial component while the other case was revised to TKR. The former was found loose in the revision surgery with incomplete osseointegration, showing bone ingrowth only around the keel. The latter was an undersized tibial component which was found well-fixed in revision. However, an occult non-displaced fracture of the posterior cortex was identified during the conversion to a TKR [87]. The other subsidence case revised to a TKR was reported by Hefny et al. [89]. This case showed continuous notable migration of the implant after one-year post-operation (5 mm at one-year and 9 mm at two-year post-operation follow-ups). A 7-degree subsidence into valgus which caused lateral progression of OA was also seen. The tibial component was placed more medially relative to the femoral component in this patient. All other 20 cases were treated conservatively. With partial weight-bearing, pain in most cases settled in the first post-operative year with adequate fixation of the component at the subsided position [87, 88, 191].

7.2.3 Discussion

This study compiled all cases of tibial component subsidence after cementless OUKR in a systematic manner. 23 cases were reported in the literature and 5 more cases were obtained

from the designer centre (Oxford). The incidence of tibial component subsidence after cementless OUKR ranged from 0.3% to 5%.

Though three of the cases were revised to cemented OUKR or to TKR, only one of them was operated after showing progressive subsidence after one year [89]. The other two either showed partial osseointegration at the keel or complete bone remodelling with good fixation at the time of revision surgeries [87]. The authors stated that these two cases could also have been treated conservatively considering the satisfactory outcomes of other subsidence cases treated without surgical interventions [87]. Conservative treatments were suggested in most studies to avoid unnecessary revisions. Though abnormal movements of the tibial components were seen on the radiographs and pain was reported in some patients, most of these subsided components settled in one year without undergoing further interventions. Pain also subsided in the meantime, with patients reporting satisfactory Patient-Reported Outcome Measures (PROMs). Thus, modified partial weight bearing and close follow-ups on radiological and clinical outcomes were advised.

However, no studies provided experimental or computational verification for their proposed causes of subsidence. Thus, so far from the review, no conclusions could be drawn on the aetiology of this uncommon complication. No recommendations could be made to the indications and contraindications of OUKR to avoid subsidence based on the results from this systematic review as no common factors were identified between the cases reported in these studies. Though Hefny and his colleagues suggested that elderly patients might be at a higher risk of subsidence after cementless OUKR due to poor local bone quality at the proximal tibia and cemented OUKR should be considered instead [89, 191], this causal relationship was not evident in other studies. Also, a previous study stated that good functional outcomes were shown in cementless medial OUKR patients in all age groups (< 55, 55 to < 65, 65 to < 75 and ≥ 75 groups) with low revision rates. Thus, old

age is not necessarily a contraindication of cementless OUKR regarding tibial component subsidence.

There are a few limitations in this review. Though this review was conducted in a systematic manner, as subsidence of the tibial component in UKR is not a widely identified complication, there are limited research papers available for inclusion and analysis. The 28 subsidence cases identified came from seven studies and no statistical analysis was conducted. Also, these seven studies all came from large volume centres (> 30 UKR/year) or were performed by surgeons with high-volume UKR practice. Three of these seven studies were published from the designer centre [86, 87, 190]. Most studies on outcomes of a specific procedure presented results through reports of the number of cases revised for various complications. As some subsidence patients do not experience pain and the components stabilise without further intervention, they may not be identified and/or reported. Also, subsidence is currently not well-noted by surgeons in general as a complication of cementless UKR. Thus, some cases from lower volume centres or by less experienced surgeons may have been overlooked. Moreover, as the incidence of 0.3% to 5% is reported from high-volume centres where procedures were performed by experienced surgeons and less-experienced surgeons new to OUKR are more likely to make surgical errors [110], the incidence may have been underestimated. Secondly, the identification of subsidence greatly depends on the quality of post-operative radiographs. To be able to identify subsidence, both the immediate post-operative radiograph and radiographs from later follow-ups of that patient should be properly aligned (i.e. the x-ray beam should be parallel to both the horizontal tibial tray and the vertical tibial wall in the AP radiographs, and parallel to the tray while perpendicular to the tibial wall in the lateral radiographs). Not all the cases studied had radiographs of adequate accuracy in alignment (**Figure 7.2**). Also, lateral radiographs are intended to be taken with the x-ray beam perpendicular to the

femoral component as shown in **Figure 7.2 b**, which makes it hard to interpret the position of the tibial component in some cases. Therefore, the incidence of 0.3% to 5% may be an underestimation of the actual number. Also, though attempts were made to contact the authors of the studies when radiographs were not provided in the original publications, 10 sets (immediate post-operation and later follow-ups) of AP radiographs and lateral radiographs were unavailable.

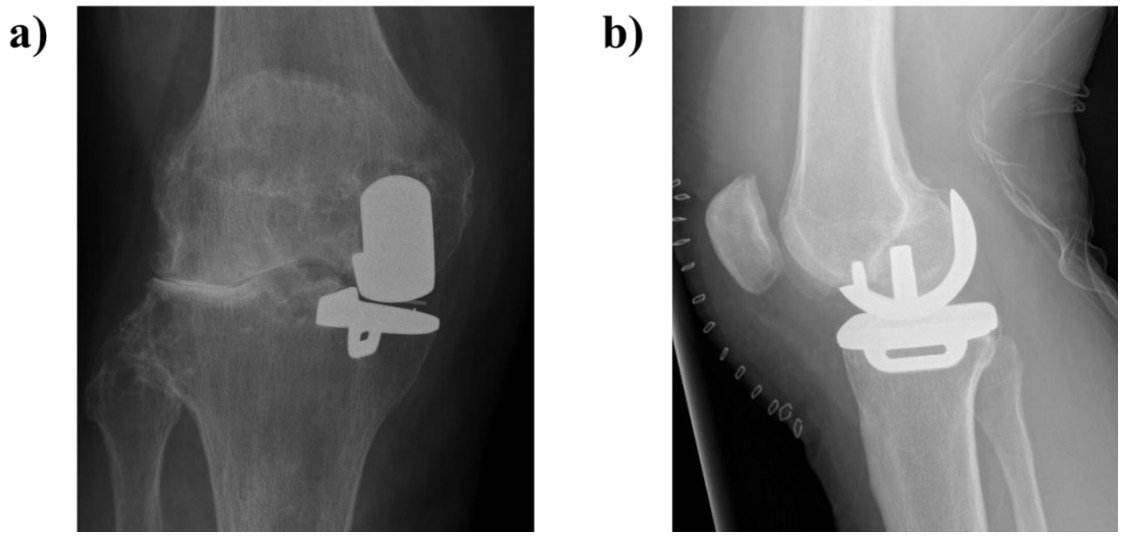

Figure 7.2: Examples of (a) an AP radiograph and (b) a lateral radiograph that are not of optimal alignment for the assessment of subsidence.

7.3 Part B: Computational Analysis of Hypothesised Causes of Subsidence

7.3.1 Introduction and Aim

As described in the results of the review in **7.2.2**, one of the mechanical factors that might have caused the valgus and posterior subsidence of the cementless OUKR tibial component was the impingement of bearing against the lateral tibial wall. This can happen when the

femoral component is placed too laterally relative to the tibial component [87]. However, this hypothesis has not been verified through experiments or computational simulations.

Also, signs of fracture in the posterior cortex were shown in one revision surgery [87]. Damage to the cortex might have weakened the load-bearing ability of the bone and subsequently led to the component subsiding posteriorly. When making tibial resection, if the horizontal cut is incomplete (the horizontal cut does not meet the vertical cut to separate the resected bone from the tibia completely), the eroded medial plateau (i.e. 'the biscuit') may not be removed completely in one attempt and some bone may be left at the back. Then a chisel will be needed to remove this part of the bone for a proper placement and seating of the tibial component. However, this can lead to excess removal - a larger chunk of bone including the posterior cortex is removed (**Figure 7.3**). These occult fractures are hard to identify on radiographs. Therefore, posterior cortex fracture could also have happened in other subsidence patients but could not have been discovered in the absence of revision surgeries. However, it was unclear if a fracture in the posterior cortex was the determining factor in this subsidence case.

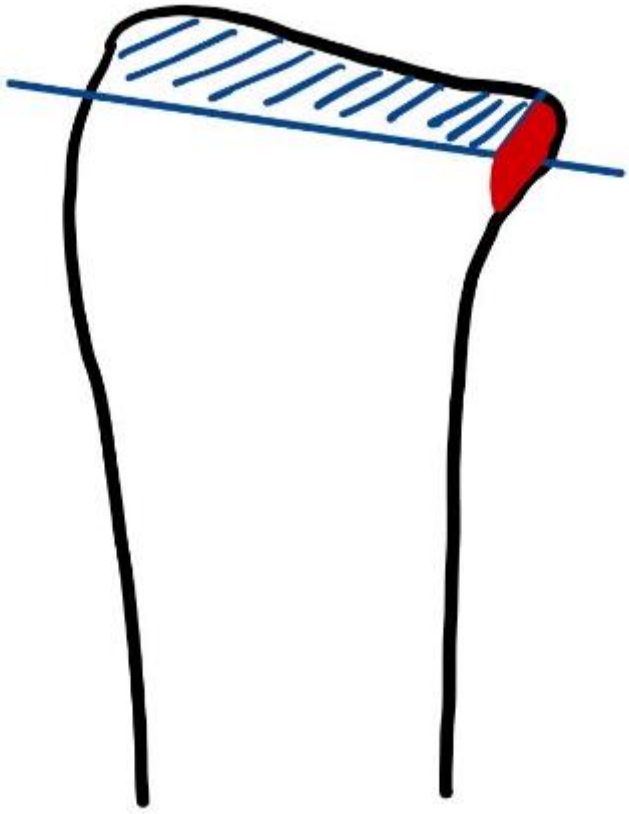

Figure 7.3: After incomplete removal of the tibial plateau is made (Blue), a chisel is needed to remove the piece of bone left at the back, during which damage to the posterior cortex (Red) may be made.

No hypotheses around the onset of subsidence have been validated with experimental or computational studies. Thus, the second part of this chapter was an exploratory study that tested the abovementioned hypothesised causes of tibial component subsidence through computational simulations. Also, little was known about the deformation in bone after the onset of subsidence. Thus, an FEA in which the component was forced into its post-subsidence position was also simulated to gain insight into what type of changes in loading would lead to this specific type of movement of the tibial component after cementless OUKR. The goal was to gain insight into what might be the determining risk factors (e.g.

bone defect, abnormal loading, and non-typical mechanobiological response of bone) for tibial component subsidence.

7.3.2 Methods

7.3.2.1 Forced Subsidence Model

An FE model was built to investigate the mechanical response of bone after the onset of subsidence: the tibial component was displaced into the subsided position. The load required to achieve this movement and the resulting deformation in bone were monitored.

7.3.2.1.1 Model Setup and Mesh

As the geometry and material distribution of the tibias of Patient 1 and Patient 2 were already available from **Chapter 4** and **Chapter 5**, the unfractured tibia (left tibia) of Patient 1 was used in the simulations in this chapter. As there was currently no radiographic or clinical evidence suggesting that a specific position or orientation of the tibial component would lead to subsidence, the tibial component was virtually implanted in the same reference position, i.e., the post-operative position. This model used the same element types and the same element sizes used in **4.2.1.1.1**. As the subsidence of the tibial component was accompanied by the local deformation of the bone beneath the tray, the horizontal cut surface was refined with 0.6 mm elements (**Figure 7.4**).

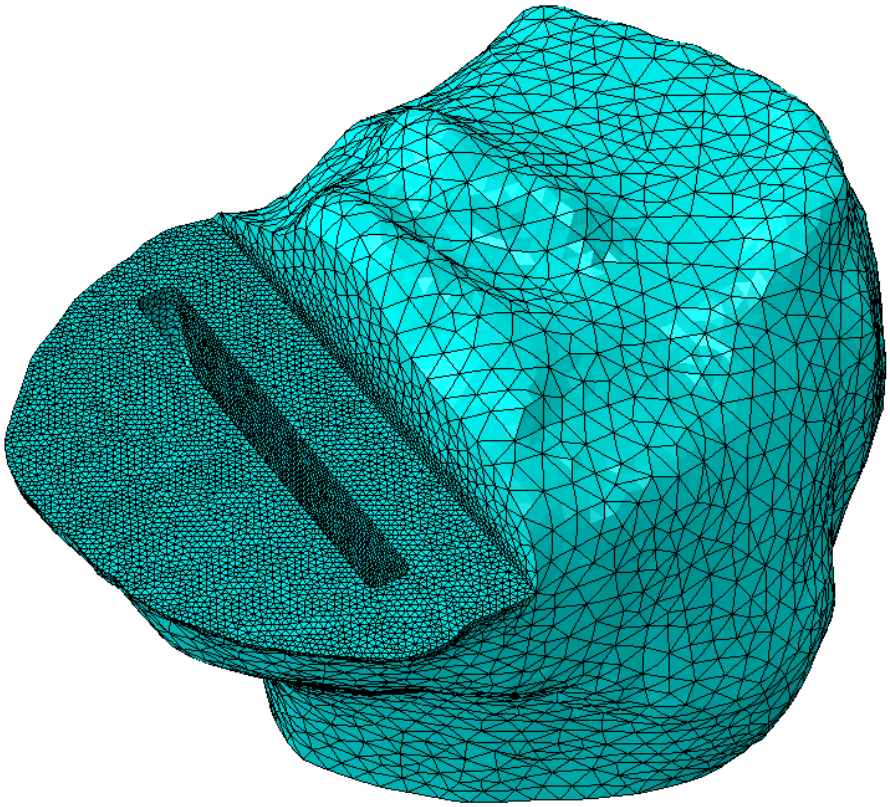

Figure 7.4: Mesh was refined on the horizontal cut surface.

7.3.2.1.2 Boundary Conditions and Loads

The base of the tibia was constrained in all degrees of freedom throughout the whole analysis.

The coordinate system around which the subsided components migrate and rotate is still unclear. Thus, the movements and rotations of the tibial component that had the largest maximal total point motion (MTPM) in an RSA study [193] were used as reference values. Compared to its immediate post-operative position, the component translated laterally by 0.2258 mm, distally by 0.5196 mm, and posteriorly by 0.2481 mm by one-year post-operation. The component tilted posteriorly by 1.5196°, rotated internally by 0.9446° and tilted into valgus by 0.7762° around the centre of the component (**Figure 7.5**) [193].

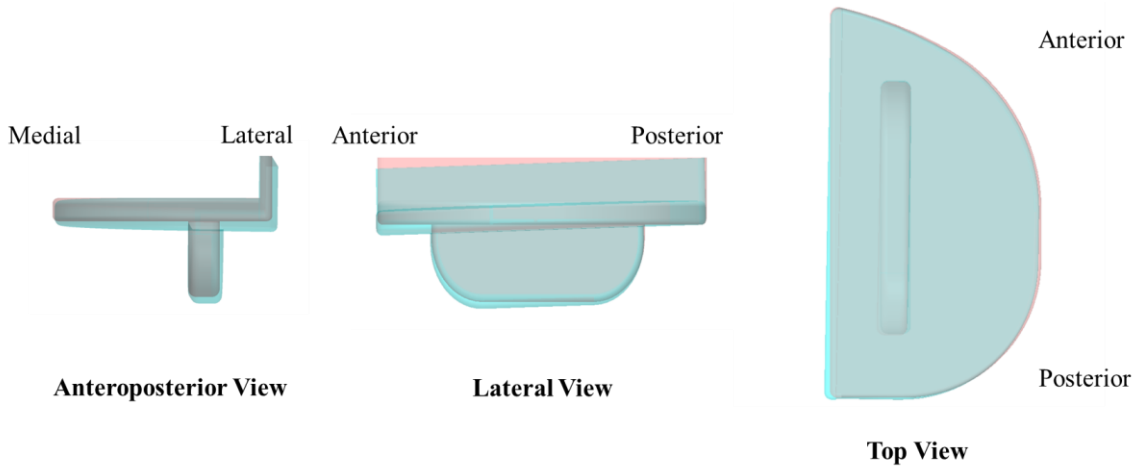

Figure 7.5: Position of the tibial component before (pink) and after (blue) migrations and rotations.

The tibial component was displaced into its final position which represented its position after it subsided under displacement control (the position of the blue component in **Figure 7.5**).

7.3.2.1.3 Contact

The same interference fit contact algorithm with the interference of 0.16 mm used in the FE models in **Chapter 4** and **Chapter 5** was applied in this model [109]. The same COF of 0.99 was applied between the tibial component and the bone [141].

7.3.2.1.4 Material Properties

Two types of tibial bone material properties were tested. In the first simulation, the tibia was again modelled as a heterogeneous linear elastic material as defined in **4.2.1.1.4**. As subsidence happens with the deformation of the bone beneath the component, this process might involve the plastic behaviour of bone. Thus, plasticity was introduced into the model by adapting the Python code from the py_bonemat_abauqs package (**Appendix G**). The yield strain of the bone was 1% [194]. The elastic modulus of the bone dropped to zero until it was plastically strained by 20%, from which point the elastic modulus was regained.

The tibial component was again modelled as rigid due to its high elastic modulus.

7.3.2.2 Bearing Impingement Model

The hypothesis of bearing impingement which was suggested as one of the risk factors of subsidence as summarised in **7.2.2.2** was tested with FEA in ABAQUS/CAE 2020 (Dassault Systèmes, France). The femoral component was displaced laterally relative to the tibial component as suggested by Liddle et al. [87].

The change in pressure distribution in the bone when the femoral component was shifted laterally was monitored.

7.3.2.2.1 Model Setup

To assess the effects that alignment between the tibial and femoral components brought to the supporting bone, a Size medium mobile bearing and a Size medium femoral component were introduced into the proximal tibia model. As only the inferior spherical surface of the femoral component was involved in joint articulation, the geometry of the femoral component was simplified to improve the efficiency of the analysis and for a simpler application of load (**Figure 7.6**). The femoral component was placed directly above the bearing with its inferior spherical surface congruent with the superior spherical surface of the bearing. This represents the standard mediolateral placement of the femoral component. The bearing was placed 1 mm away from the tibial wall and 8 mm posterior to the middle of the tray, which should be the position of the bearing when the femoral component was correctly aligned with the tibial component. This simulated the posterior-most loading position in the AP direction during step-up motion [166]. This posterior loading position tends to occur when the knee is flexed, e.g. ascending stairs and descending stairs. These activities are also associated with high knee joint contact loads [167]. Three other scenarios in which the femoral component was moved laterally by 1 mm, 2 mm and 3 mm

respectively were modelled to simulate the lateral placement of the femoral component relative to the tibial component. When the femoral component was moved laterally, the bearing translated with the femoral component to fulfil the congruency at their contact interface until the bearing hit the tibial wall, i.e. when it was moved by more than 1 mm. When the femoral component was moved by 2 mm, the femoral component overhung lateral to the bearing (**Figure 7.7**).

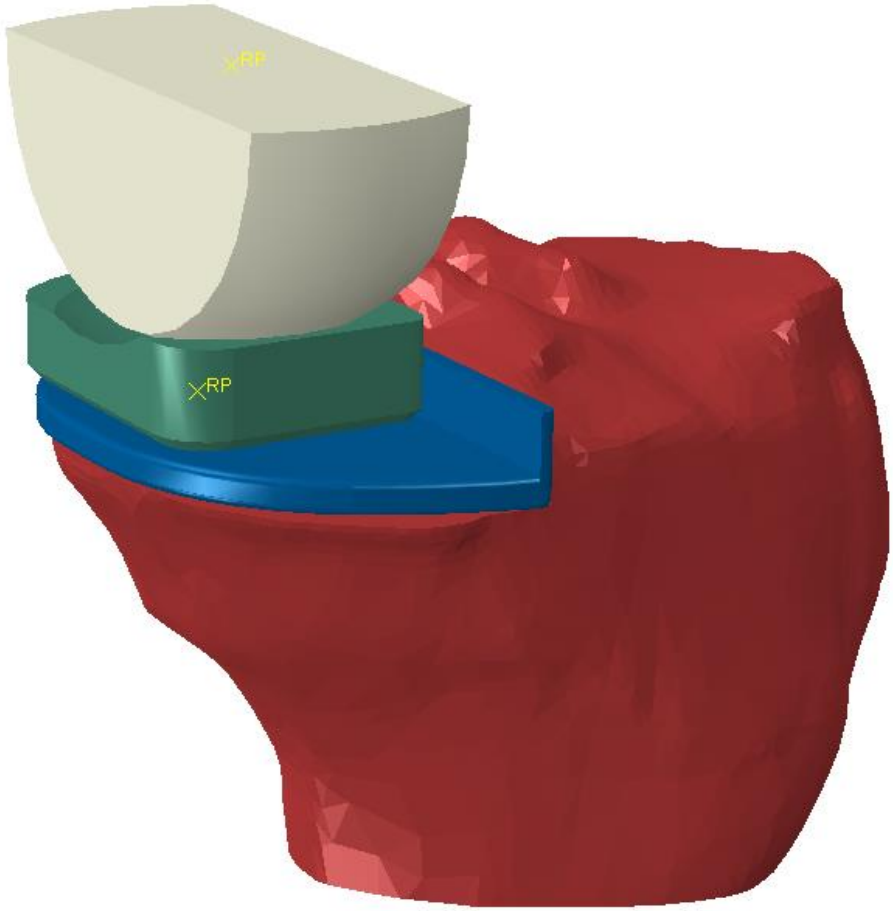

Figure 7.6: Bearing impingement model setup.

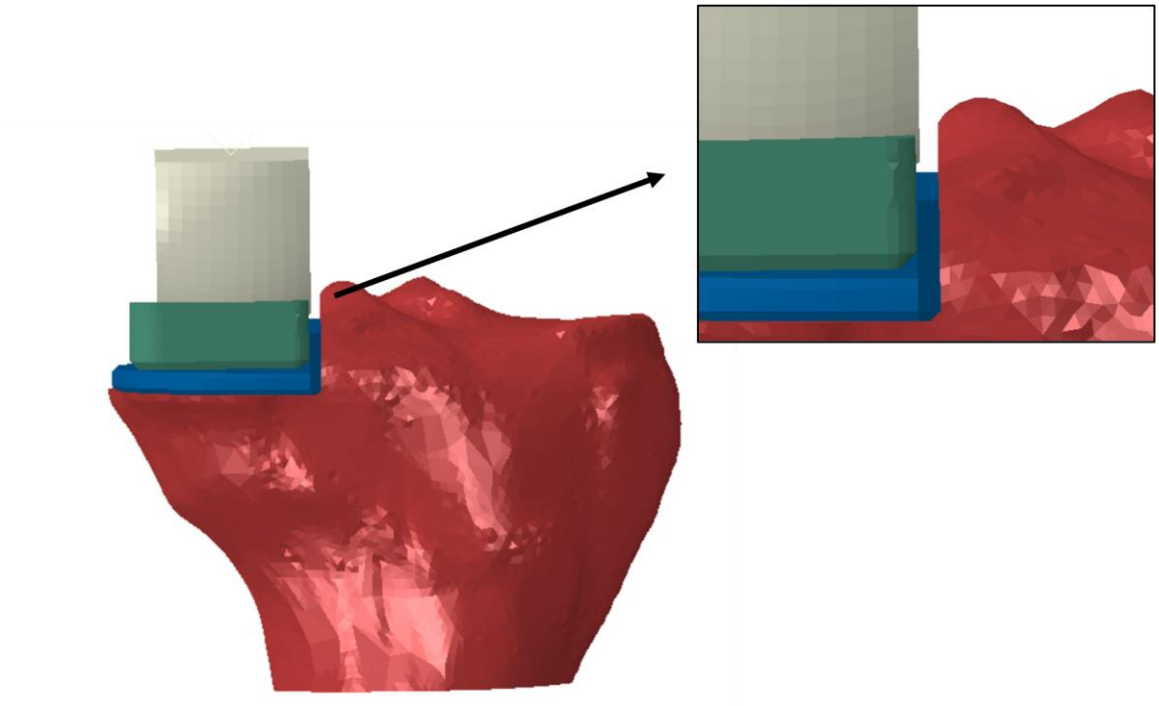

Figure 7.7: When the femoral component was moved further laterally by 2 mm after the bearing hit the wall (overall 3 mm lateral movement), it was overhanging lateral to the bearing.

7.3.2.2.2 Contact

The same interference fit algorithm and the same COF used in the model in **7.3.2.1** were applied in this model. The COF was 0.04 between the bearing and the femoral and tibial components [183].

7.3.2.2.3 Boundary Conditions and Loads

The base of the tibia was fixed in all directions throughout the whole analysis.

For the scenarios in which the femoral component was no longer congruent with the bearing due to its lateral placement (lateral movement larger than 1 mm), before the start of the analysis, the femoral component was moved upwards so it was not touching or penetrating the bearing. Then a vertical displacement in the direction perpendicular to the superior surface of the tibial component was applied to bring the femoral component into

contact with the bearing. This movement was defined as the 'Contact' step. The magnitude of the displacement was determined by first applying an overly large value that would cause the femoral component to deform the bearing. Then the time point at which the femoral component came into contact with the bearing was recorded, from which the appropriate displacement was calculated. Translation or rotation in the other five degrees of freedom was constrained. The tibial component was fixed in this step.

In the 'Loading' step, a 1000 N vertical load was applied to the centre of the femoral component which transferred the load to the bearing through their spherical contact surface [165]. The load was applied perpendicular to the superior surface of the tibial tray, the same as in the FE models in **Chapter 4** and **Chapter 5**. The femoral component was only allowed to move in the vertical direction. The bearing and the tibial component were free to move in this step.

A 5000 N load was also tested in the model. The bearing was moved laterally by 3 mm to simulate an extreme loading case: approximate load transfer through the medial knee compartment of an 80 kg patient running [195].

7.3.2.2.4 Mesh and Material Properties

As the tibial and femoral components are orders of magnitude stiffer than the bearing and the bone, they were modelled as rigid. A reference point was assigned to each rigid component to control their movements. The bearing was meshed with 1.5 mm tetrahedral elements (C3D10). The same element sizes that were used for the tibia in the model in **7.3.2.1.1** were applied in this model: 2.4 mm tetrahedral elements (C3D10M) with a mesh refinement with 0.6 mm elements near the keel slot and the horizontal cut face.

The same linear elastic material properties used in **7.3.2.1.4** for the bone were applied. The elastic modulus and Poisson's Ratio of the meniscal bearing were 700 MPa and 0.3 [108].

7.3.2.3 Posterior Cortex Damage Model

Damage to the posterior cortex during tibial preparation was also listed as one of the risk factors for tibial component subsidence. Thus, this hypothesis was tested with FEA.

Modifications were applied to the FE model described in **7.3.2.2**. Bone was removed from the back of the medial condyle to simulate the damage that might occur to the posterior cortex when removing the resected medial plateau in the surgery (**Figure 7.3**).

Three models with different levels of damage to the posterior cortical bone were made by deliberately creating an extra vertical cut at the back of the tibial resection (**Figure 7.8**). This simulated the removal and 'peeling-off' of the posterior cortex which might occur when the remaining bone from the resection at the back of the medial tibial plateau was knocked off with the chisel.

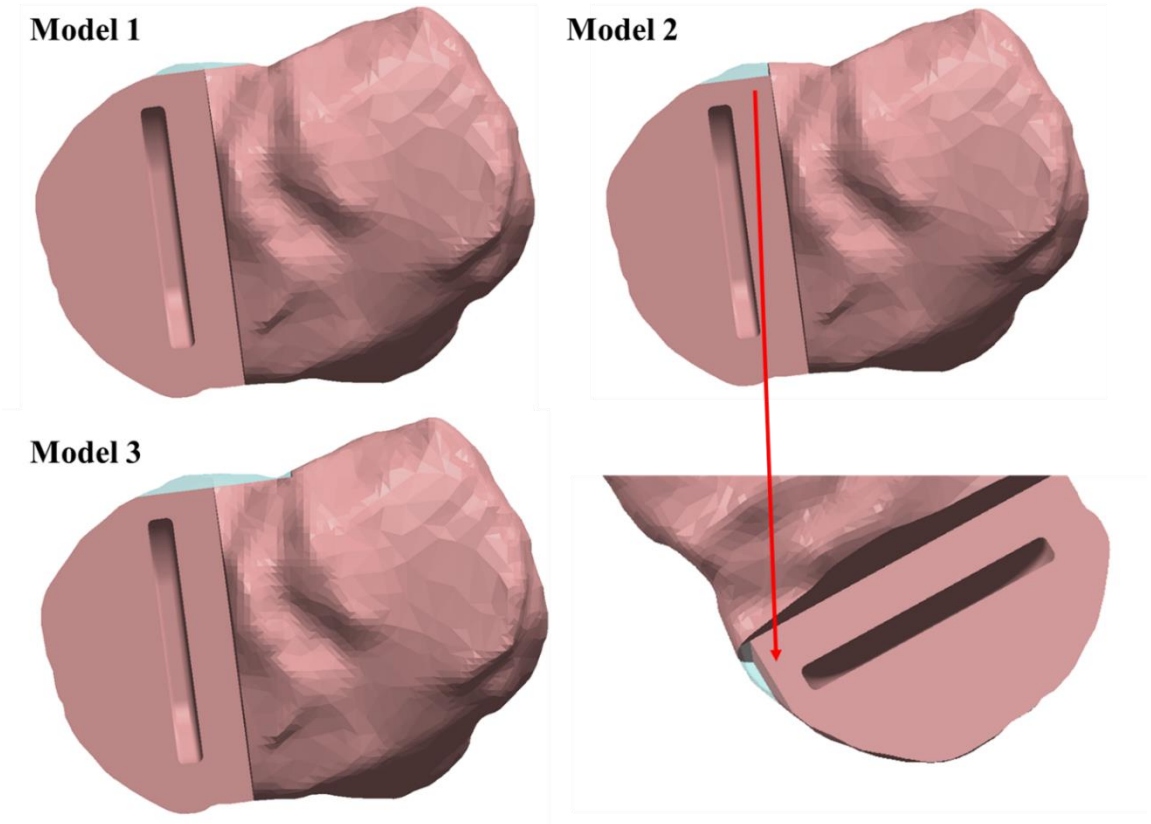

Figure 7.8: Damage to the posterior cortex of three different severity was modelled. Model 1 – Shallow damage to the medial and lateral cortex. Model 2 – Deep damage to the medial cortex only. Model 3 – Deep damage to the medial and lateral cortex. The blue regions represent the excessively removed bone.

The bearing was placed next to the wall and the femoral component was congruent with the bearing. This simulated the extreme case when the bearing hit the wall while not bringing in the effect of the tipping of the bearing. Other settings in the model remain the same as the ones shown in **7.3.2.2**.

7.3.3 Results

7.3.3.1 Forced Subsidence Model

When the bone was modelled as a heterogeneous linear-elastic material, a reaction force of 28,500 N was required to force the component into its subsided position.

After the component was displaced into its subsided position, the bone beneath the posterolateral part of the component experienced concentrated pressure (**Figure 7.9**). All plots of contact pressure presented hereafter are in the unit of MPa.

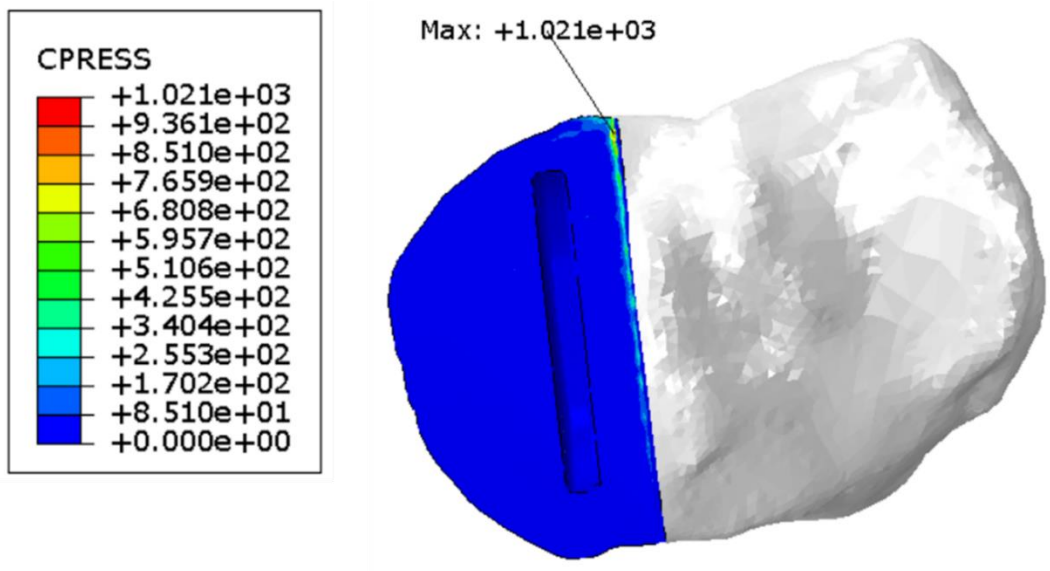

Figure 7.9: Contact pressure (in MPa) in the bone after the tibial component was displaced into its subsided position under displacement control.

When the bone was modelled as a plastic-elastic material as defined in **7.3.2.1.4**, the force required to move the component into its final subsided position was 12,690 N.

7.3.3.2 Bearing Impingement Model

When the centre line of the femoral component was no longer in line with that of the bearing, i.e. when the femoral component was moved further laterally by 1 mm and 2 mm after the bearing hit the wall, the bearing started to tip into valgus when a 1000 N load was applied through the femoral component (**Figure 7.10** and **Figure 7.11**). A small lift-up was also shown under the medial part of the component in these two models.

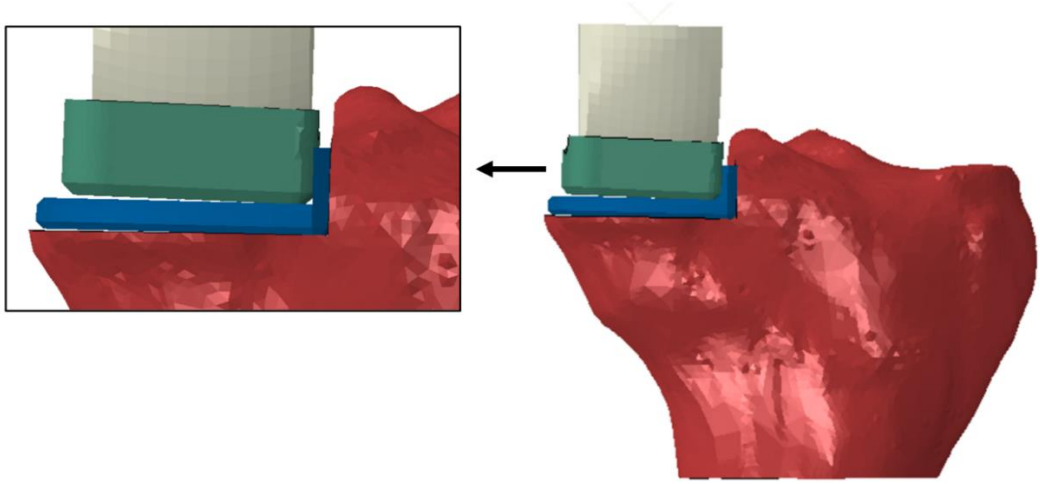

Figure 7.10: The bearing tipped into valgus under a 1000 N load when the femoral component was 1 mm lateral to its centre line.

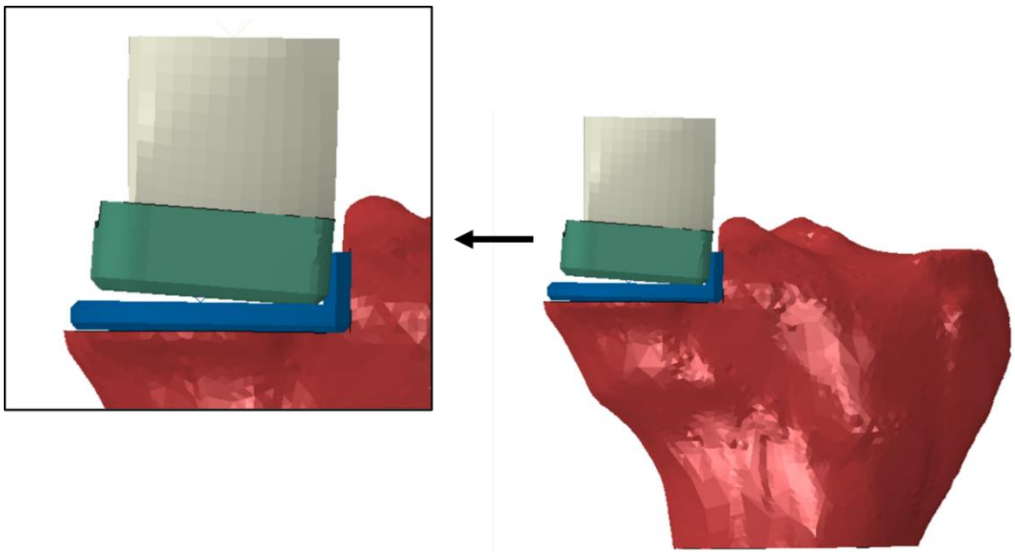

Figure 7.11: The bearing tipped into valgus under a 1000 N load when the femoral component was 2 mm lateral to its centre line.

Figure 7.12 shows the contact pressure in the bone when the femoral component was placed at its standard position, 1 mm lateral (bearing hits wall), 2 mm lateral and 3 mm lateral. High concentrated pressure was shown at the posterolateral corner of the horizontal cut surface when the bearing was lateral to its standard position, and this high pressure extended anteriorly through the AP cut line.

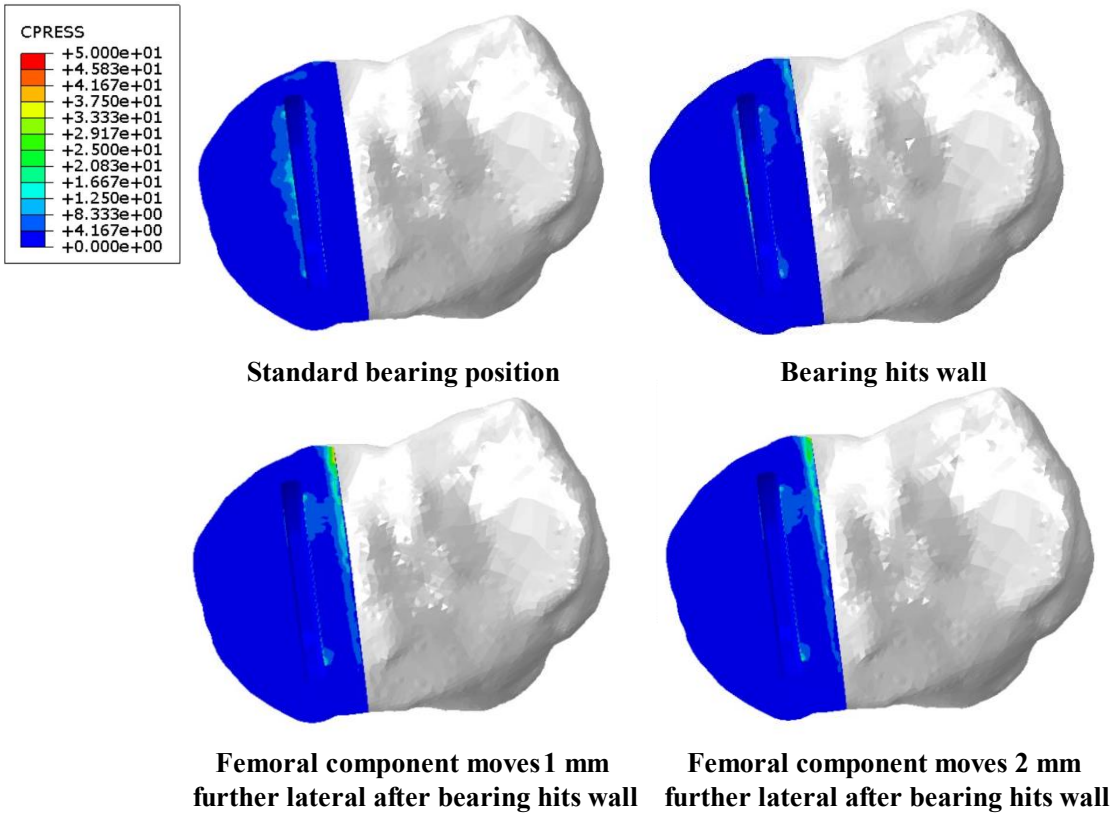

Figure 7.12: Contact pressure under the tibial tray when the femoral component was placed at different mediolateral positions.

Figure 7.13 shows the movements of the tibial components in the proximal-distal direction after the 1000 N load was applied. Negative displacement means movement in the distal direction. When the femoral component was placed at the standard position or 1 mm more lateral, i.e. before the bearing started to tip under load, which is also when the femoral component was still in congruency with the bearing, the tibial component tended to rotate towards the posteromedial corner, into slight varus. After the bearing started to tip under the lateral placement of the femoral component, the component tended to rotate towards the posterolateral corner, into slight valgus, with the posterolateral corner showing the largest negative displacements.

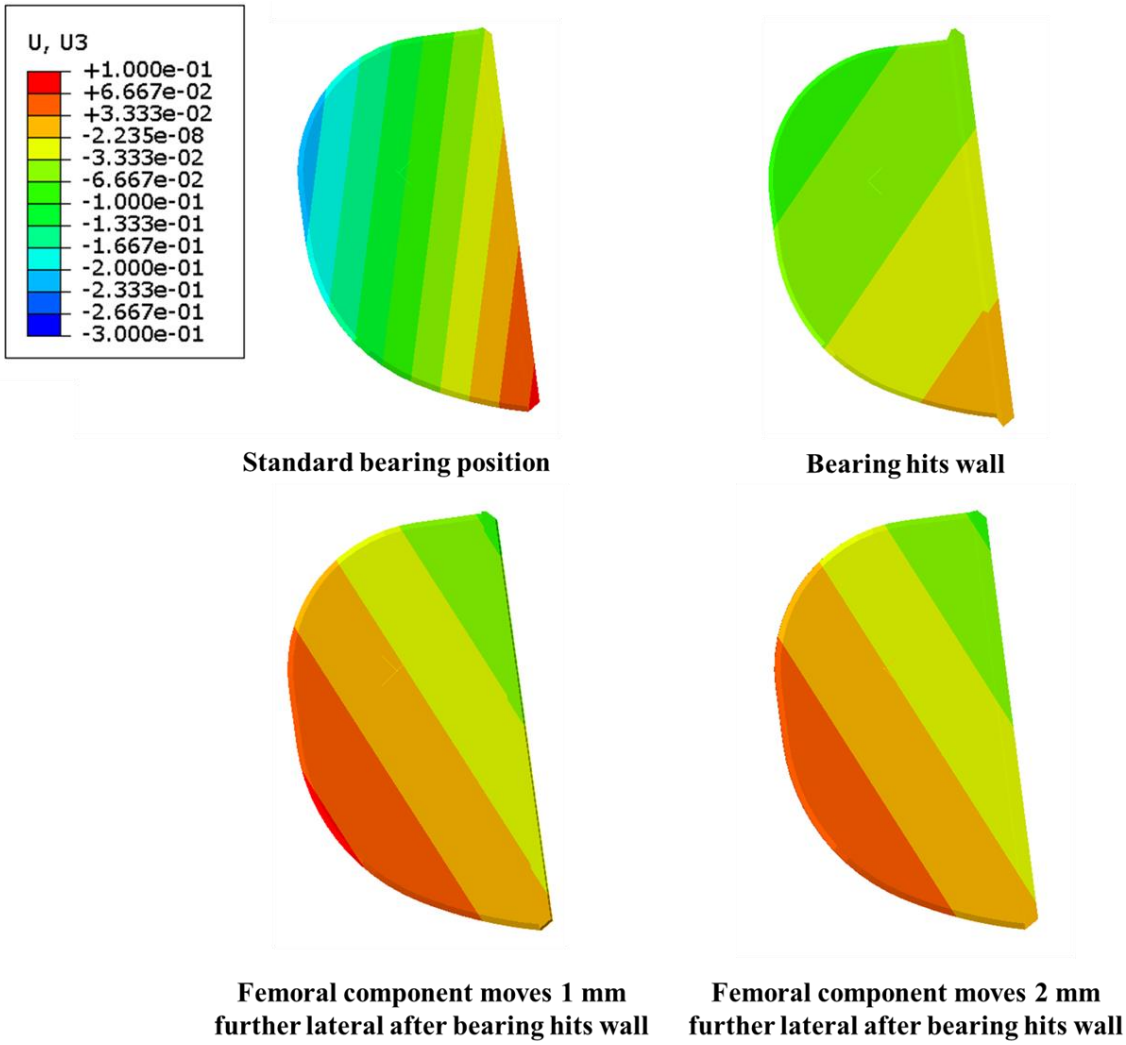

Figure 7.13: Vertical displacement of the tibial component under a 1000 N load when the femoral component was placed at different mediolateral positions. Negative values indicate distal movements (into the page).

When a very high load of 5000 N was applied, the pressure lateral to the keel slot greatly increased (**Figure 7.14**) and the component tilted posteriorly and into valgus (**Figure 7.15**).

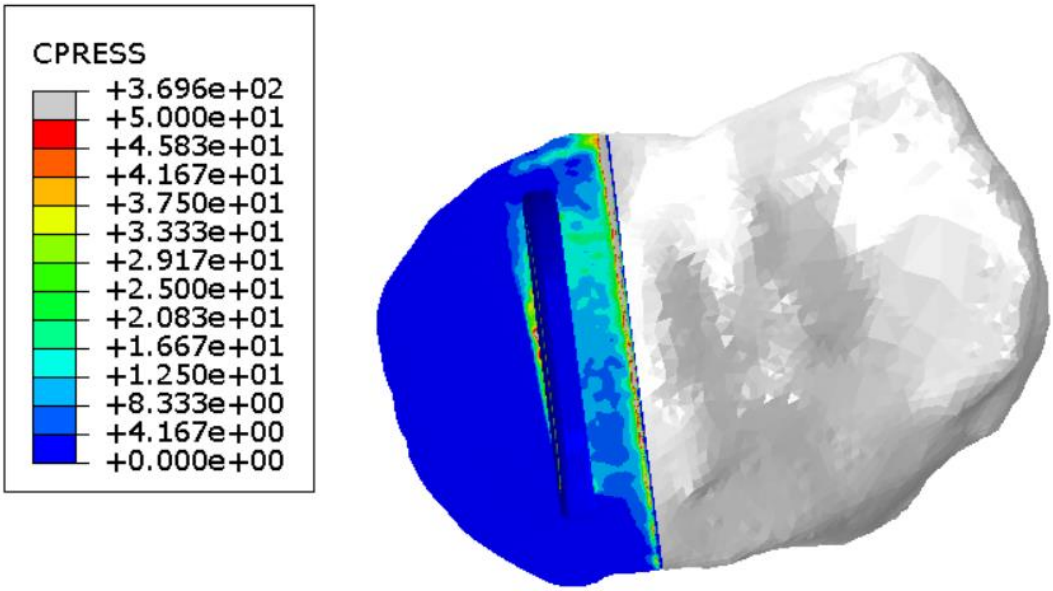

Figure 7.14: Contact pressure in the bone beneath the tibial component when a 5000 N load was applied. The femoral component was 3 mm lateral to its standard position.

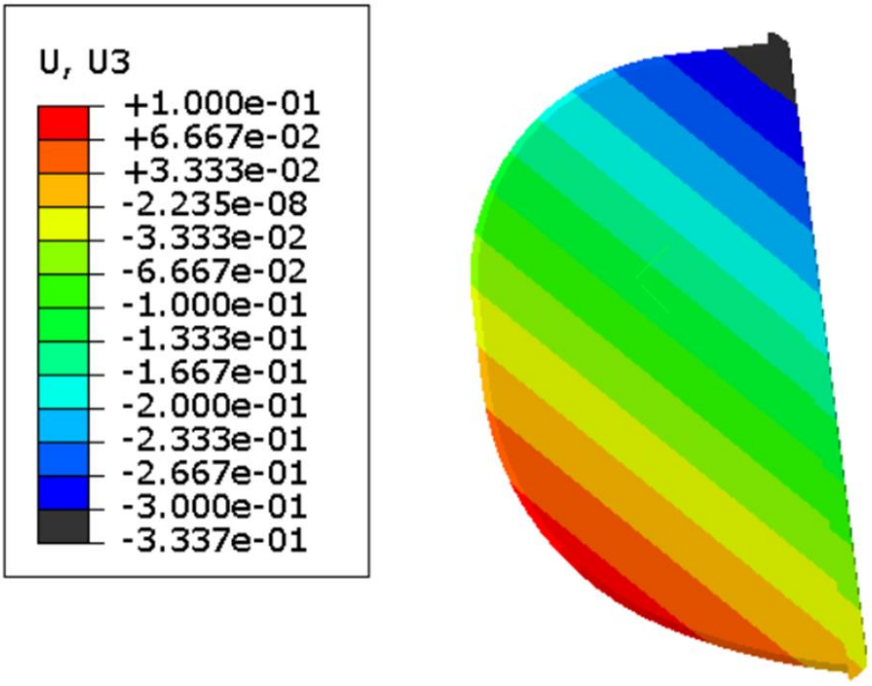

Figure 7.15: Vertical displacement of the tibial component when a 5000 N load was applied. The femoral component was 3 mm lateral to its standard position. Negative values indicate distal movements (into the page).

7.3.3.3 Posterior Cortex Damage Model

Figure 7.16 shows the contact pressure in the bone when different level of damage was made to the posterior cortex. Compared to the situation in which the posterior cortex was intact, the other three models with damaged posterior cortex showed more concentrated pressure at the posterolateral corner of the horizontal cut face.

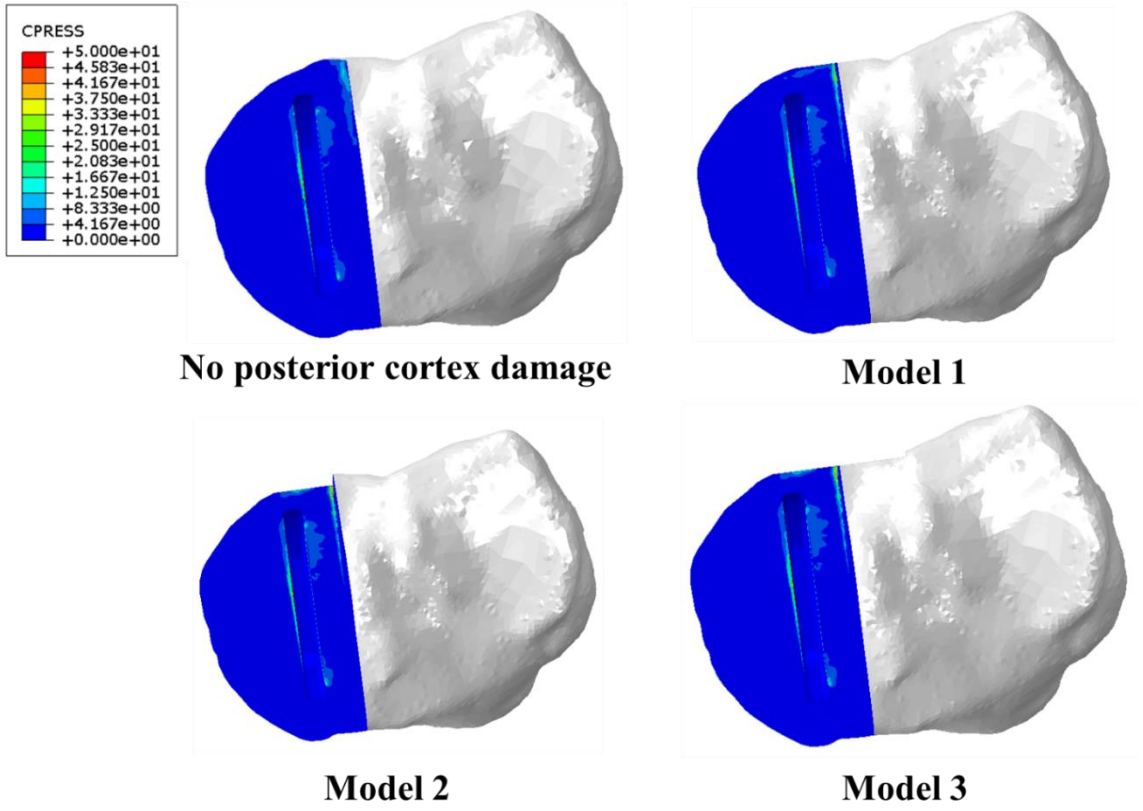

Figure 7.16: Contact pressure in the bone when the posterior cortex was intact and when damage of different severity was made to the cortex. Model 1 – Shallow damage to the medial and lateral cortex. Model 2 – Deep damage to the medial cortex only. Model 3 – Deep damage to the medial and lateral cortex.

Figure 7.17 shows the vertical migration of the tibial components when the posterior cortex of the tibia was damaged. The tibial components moved into varus and tilted posteriorly in all cases.

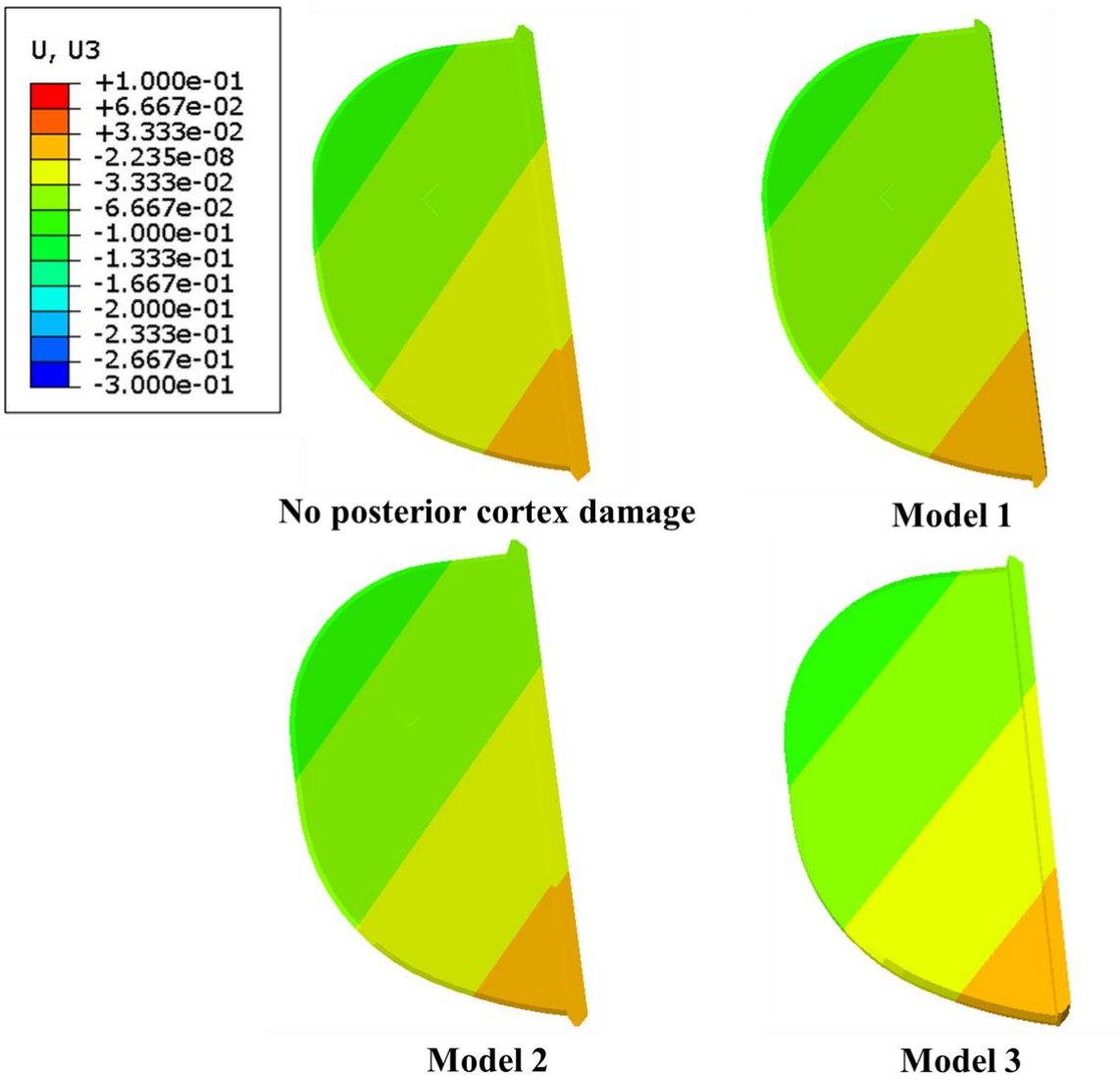

Figure 7.17: Vertical displacement of the tibial component under a 1000 N load when the posterior cortex of the tibias was damaged. Negative values indicate distal movements (into the page). Model 1 – Shallow damage to the medial and lateral cortex. Model 2 – Deep damage to the medial cortex only. Model 3 – Deep damage to the medial and lateral cortex.

7.3.4 Discussion

The results (**7.3.3.1**) suggest that a 28 kN force is needed to displace the tibial component into its subsided position. This is many times the load in the medial compartment of the knee joint during gait [165, 167]. Even when plasticity was considered and with the bone modelled as an elastic-plastic material with a low yield stress, the load required to migrate the component was still large (13 kN). When the femoral component was placed at a position lateral to its standard position and loaded with a 1000 N force, an increase in the contact pressure beneath the lateral part of the tibial tray was seen (**Figure 7.12**). The pressure became higher when the bearing started to tip, i.e. when the mediolateral centre line of the femoral component was no longer in line with that of the bearing. However, these values were still two orders of magnitude smaller than that when the component was forced into its subsided position under displacement control (**Figure 7.9**). The results imply that it is unlikely for subsidence to happen as an instantaneous event as this would require an unrealistically enormous load to cause the component to move into its final position all at once.

When the posterior cortex was damaged which simulated the excess removal of bone during tibial preparation, no large change in pressure distribution was shown. The posterolateral corner of the horizontal cut face showed a concentrated increase in stress in each damage scenario. However, the largest vertical displacement of the tibia tray and deformation in the bone beneath the tibial tray both happened on the posteromedial side of the plateau, which indicates that the component was more likely to move into varus than into valgus when the posterior cortex was damaged.

The results from these FE models imply that subsidence is likely to be a multifactorial problem that involves the continuous biological response of bone to mechanical loading.

Bearing impingement or damage to the posterior cortex alone that changes the mechanical loading environment around the tibial component is not likely to cause the component to subside. Thus, subsidence might be a continuous process that is associated with the biological response of bone during the early healing period. The high concentrated pressure near the posterolateral corner of the medial plateau may cause damage to the bone over time, e.g. small non-displaced fracture of the trabecular bone beneath the tibial component. The component shifts inferiorly as the bone beneath it is crushed under this compressive stress. One hypothesis is that the subsidence of the component could result from the non-union or delayed union of this fracture. Fracture normally heals at around 3-12 weeks post-operation which is after secondary stability takes over, as mentioned in **1.4** (**Figure 1.5**) [196]. However, some fracture patients experience delayed union or non-union of the fracture site after an extended period of recovery time. The exact time point at which subsidence stops is unknown with most studies confirming that the tibial components became well-fixed within one year after the surgeries [87, 88]. Delayed union or non-union has various risk factors which can be patient-related (e.g. advanced age, metabolic disease, genetic disorders) or non-patient-related (e.g. fracture location, fracture pattern) [197]. Subsidence could be a slow or delayed healing of occult and non-displaced fractures under the components alongside bone remodelling. When the femoral component in a patient is placed excessively lateral to the tibial component which causes the bearing to tip and impinge against the tibial wall, the posterolateral corner of the tibial resection surface may experience increased compressive stress, especially under high load during specific activities (e.g. ascending stairs). If this patient is at the meantime at high risk of experiencing non-union or delayed union after fracture due to patient-related risk factors, then there might be a higher chance for this patient to have slow or limited recovery after the bone was fractured under the increased stress caused by the tipping of the bearing.

Another hypothesis is that the cut surface under the tibial tray may not be perfectly flat due to the heterogeneity of trabecular bone structure, or the angle between the vertical and horizontal resections may not be perfectly orthogonal. These features are hard to detect from plain-film radiographs and thus might not have been noticed in radiographic studies. Regions of bone or trabeculae that are protruding from the horizontal cut surface may result in uneven loading and concentrated compressive stress beneath the tray. As bone undergoes continuous resorption and formation process and this remodelling of bone is governed by mechanical loading [198], an abnormal loading environment may alter the structure of the bone supporting the tibial component. This may also explain why some AP radiographs taken at follow-ups show periprosthetic radiolucent lines which indicate bone resorption (**Appendix F**). However, the remodelling of bone, the change in bone structure under mechanical stimulus during recovery, and bone healing are out of the scope of this project. Therefore, these hypotheses are not further investigated in this thesis.

This study should be considered with its limitations. Firstly, the component movement simulated in **7.3.2.1** was not the migration of a tibial component that subsided but rather a component in an RSA study that experienced large displacement and rotation while 'bedding in'. Hence, this might not replicate the actual subsidence movement. However, as no data is available on how the component subsided and this case in the RSA cohort was the only one that had experienced movements in a similar order of magnitude (1 mm and 1°) to the subsidence cases, the motion of this component was used as a reference. Secondly, the material model used for the bone was a simplification of the actual bone properties. When plasticity was considered, it was assumed that both cortical bone and trabecular bone have the same plastic-elastic behaviour and would yield at the same strain. The cortical bone and the trabecular bone were not differentiated into two different sections for plasticity assignment in this model. Thirdly, the bearing impingement hypothesis was based

on the bearing trajectory obtained during passive flexion and extension of the knee when the patients were under anaesthesia [91]. The whole hypothesis was based on the assumption that, when the femoral component was positioned lateral to the tibial component, there would be lateral translations of the bearing over the whole range of flexion-extension motion. When the bearing moved excessively and hit the wall, it would exert a lateral force onto the tibial wall. There is limited knowledge on the 3D kinematics of OUKR knees and therefore, it is unclear if the bearing would behave this way when the patients are performing daily activities. However, simulations here aim to consider the worst loading scenario that could happen which would bring adverse effects to the bone. Hence, it was assumed that the bearing would impinge the wall during flexion-extension movement when the femoral component was placed lateral to the tibial component. Lastly, the tibial geometry used in this study was one of the tibias that were studied for fracture. This patient has a more overhanging tibial plateau compared to the average of the population [156]. This tibial geometry may not be representative of those of the patients who experienced subsidence. However, as no particular morphological characteristic was found in the shape of the tibias that experienced subsidence, and these pre-operative CT scans were the only sets of data we had of patients that received OUKR for OA, these models provided the best estimations that we could make with current knowledge and resources.

7.3.5 Conclusions

FEA of the current hypothesised risk factors for cementless OUKR tibial component subsidence which are lateral placement of the femoral component and damage to the posterior cortex implies that they are unlikely to cause subsidence alone. Further study is needed to identify the cause of this complication while considering the biological response of bone after implantation.

7.4 Chapter Summary

This chapter looked at the incidence and possible risk factors for cementless OUKR tibial component subsidence through a systematic review and exploratory computational simulations of possible mechanisms that might have led to this complication. In total, 28 cases were identified. The incidence was between 0.3% and 5%. Pain was reported by some patients during the early recovery stage. However, this symptom eased off in most patients with modified partial load bearing. Most components stopped subsiding within one-year post-operation and showed good fixation at one-year and later follow-ups without further surgical intervention. Thus, conservative treatments and close monitoring of symptoms and radiographic evidence of further subsidence are recommended to avoid unnecessary surgery.

Hypothesised risk factors of subsidence which are bearing impingement on the tibial wall due to lateral placement of the femoral component and damage of the posterior cortex during tibial preparation are unlikely to be the sole reason for subsidence. Subsidence may be a multifactorial complication that happens under the combination of surgical risk factors that alter the loading mechanism in the knee joint and patient-related risk factors which influence the healing process post-surgery. Further investigations that involve interdisciplinary research are needed.

Chapter 8. Discussion

8.1 Summary of Findings

Cementless OUKR which was first introduced in 2004 to avoid complications associated with the use of bone cement and to prevent unnecessary revisions due to misinterpretation of radiolucent lines, has the potential advantage of improving fixation through bone ingrowth at the porous HA-coated surface [53]. Fixation of cementless components is achieved through press-fit. To facilitate adequate bone ingrowth and osseointegration, which determine the secondary stability of components, primary fixation is required [61]. Primary fixation is the mechanical response of bone immediately after implantation. To assess the primary fixation of press-fit components with computational simulations the mechanical process of insertion needs to be replicated. Previous attempts at modelling cementless component press-fit with computational simulations usually implemented the resolution of initial overclosure with an interference fit contact algorithm [117, 118]. This method, however, does not represent the actual physical process of insertion and the damage in the periprosthetic bone during press-fit. This may provide misleading insight into the primary fixation of cementless components. Thus, an axisymmetric FE model that considers the actual press-fit process was developed in **Chapter 2** with the implementation of element deletion to evaluate primary fixation. A plastic strain-based element deletion mechanism was applied. When an appropriate fracture strain threshold value (0.31, upturn value on the material curve) above which the element would be deleted was defined, the predictions of push-in and pull-out forces for both smooth and porous components were satisfactory. This implies that this method could be applied to assess the primary fixation of new implant designs with different surface morphologies.

To evaluate surface morphologies and roughness of various fixation components, a friction experiment was developed and conducted in **Chapter 3**. This method measured the COF between plastic bone/real bone and the actual implant with a relatively simple setup. As far as the author is aware, this is the first experimental study that investigated the frictional coefficient around OUKR, the most widely used UKR implants in the UK [50]. The COF values found in this chapter were further applied to simulations in other chapters of this thesis.

Tibial periprosthetic fracture (PPF) is a severe complication after cementless OUKR. Complex revision surgeries, e.g. conversion to stemmed TKR, are often required [94]. This greatly affects patients' quality of life and brings extra financial burdens to the healthcare systems. The incidence was relatively low in Caucasian cohorts (less than 1%) [84]. However, a considerably higher incidence has been reported in Asian cohorts (3.8 – 8%) [95-99]. In **Chapter 4**, two tibial PPF cases were analysed with FEA. These two patients experienced PPF in one of their tibias after receiving bilateral OUKR with tibial components of the same size implanted in their left and right knees. No large differences were found in the tibial size or bone properties between the fractured and unfractured tibia in both patients. Large differences were found in the position of the components in the fractured and unfractured tibias. The components in the fractured sides were placed more distally and more medially. They were also more rotated in the transverse plane, more externally in Patient 1 and more internally in Patient 2. These surgical errors caused the keel slot to damage or cut through the cortex and considerably impaired the load-bearing ability of the bone. The highest maximum principal stress values were found at the anteromedial corner of the keel slots. When the tibial resections in the fractured tibias were replicated in the other tibias that did not fracture, i.e. when the components were placed in the unfractured tibias at the same relative position as those in the fractured tibias, the stress

in the bone significantly increased, reaching similar values to those in their fractured counterparts. These simulations excluded the effects of patient-related risk factors and imply that even in the unfractured tibias if the same surgical errors were replicated, fracture was highly likely to occur. Therefore, surgical errors in tibial resection which subsequently caused damage in the cortex were the most determining risk factor in these two cases.

In **Chapter 5**, the effects of surgical errors in the four directional dimensions of the tibial component – mediolateral, proximal-distal, internal-external and varus-valgus – were studied in a parameter study. The results suggest that rotation in the varus-valgus direction while keeping the vertical cut immediately next to the apex of the medial tibial spine had the largest effects on the highest maximum principal stress and slot-cortex distance (SCD). Placing the component in valgus in patients with tibia vara or overhanging tibial plateau would greatly increase the risk of fracture. Placing the component too medial and placing the component too distal were the next two least tolerant errors. These again elevated the highest values of maximum principal stress in the bone which were found at the anteromedial corner of the keel slots. Also, these errors shortened the distance between the keel slot and the cortex which increased the risk of damaging the cortex. Internal or external rotation of the tibial component had the least determining effect on the risk of tibial PPF. However, large rotations should be avoided as they reduce SCD and make the bone less tolerant to surgical errors in other directions. Thus, the tibial component in tibia vara patients with overhanging tibial plateaus who are more prone to tibial PPF should be placed in varus, with the tibial wall abutting the medial tibial spine, with appropriate depth created with a 3 or a 4 G-clamp, and without large internal or external rotation in the horizontal plane.

Five new keel designs that are smaller than the current one in use were tested in **Chapter 5**. The current cementless tibial component has a window in the middle of the keel which

is a remnant from the cemented version that is used for cement filling (**Figure 1.4**). As the keel getting too close to the cortex was found to be a risk factor for tibial PPF, alternations to keel design that could increase SCD were investigated. Three keel designs that have the same surface area as the current keel while having the window removed were tested. These keels are 4 mm shorter and 3 mm shallower than the current design and are aligned to the front margin, middle line, and posterior margin of the original keel, respectively. One of these designs (Design *c*) has been tested in a previous biomechanical experiment and has been proven to provide similar, if not better, primary fixation as the current design [124]. Two other keels which are 4 mm shorter or 3 mm shallower than the current one, respectively, were also tested to assess the effect of each dimension. The results infer that using a smaller keel which is both shorter and shallower, and placing it in the middle of the tray (Design *e*) provides the largest improvement regarding reduction in risk of fracture. As it was previously proven that a keel of this size would not compromise primary fixation [124], this change to the keel design should be considered in the future.

Chapter 6 investigated the risk of lateral progression of OA that might be brought about by the varus placement of the tibial component. The femur has a tendency to slide medially when the tibial component is placed in varus. Large medial subluxation of the femur may cause the femoral intercondylar fossa to impinge the lateral tibial spine. Repetitive contact of these two surfaces and the overloading of these regions may lead to lateral OA. Therefore, though varus placement of the tibial component was recommended based on the findings in **Chapter 5**, large varus should be avoided as this may cause excessively large medial movement of the femur. This medial femur subluxation then may result in an increased risk of developing OA in the lateral compartment.

The systematic review on cementless tibial component subsidence in **Chapter 7** showed that the incidence ranged from 0.3% to 5%. Symptoms in most cases were gone by one-

year post-operation and most components were well-fixed at the subsided position by this time without further surgical intervention. This implies that secondary stability was successfully achieved though the components were not initially well-fixed. Therefore, conservative treatments with close monitoring of pain and radiographic evidence of further tilting of the implants are recommended to avoid unnecessary revision. Bearing impingement caused by the lateral placement of the femoral component and posterior cortex damage during tibial resection were proposed as the possible causes of subsidence [87, 88]. These hypothesised mechanisms were tested in the second part of **Chapter 7** with FEA. The results from these simulations show that these two mechanisms are unlikely to be the sole cause of subsidence. This complication is more likely to be multifactorial and involves the biological response of bone after implantation. Further interdisciplinary research is probably needed to understand the aetiology of tibial component subsidence after cementless OUKR.

8.2 Limitations and Future Works

The limitations of each study are detailed in their respective chapter. However, the thesis should be considered in the context of the following overarching limitations.

Firstly, the method of modelling press-fit developed in **Chapter 2** was not applied in the 3-dimensional FE simulations in **Chapter 4**, **Chapter 5** and **Chapter 7** due to the excessive computational resources required. This method of modelling press-fit with element deletion was designed to assess primary fixation across different component designs. It can be applied to optimise the fixation component's surface morphology. **Chapter 4** and **Chapter 5** assessed the risk of fracture after the component has been seated, and **Chapter 7** assessed the risk of subsidence under specific loading. It was assumed in these simulations that the

level of fixation achieved immediately after implantation was the same across all models. Therefore, the resolution of initial overclosure was adequate for the purpose of these comparative studies. In future studies, if enough computational power is available, the method can be used to study the relationship between the size of interference and the primary fixation of 3D press-fit components.

Secondly, though a previous experiment done in Sawbones blocks showed that using a smaller keel would not compromise the primary fixation of the cementless OUKR tibial component, it was not tested computationally or in real bone. To introduce this new small keel design, further justification that proves that adequate stability can be secured is required. The method introduced in **Chapter 2** can potentially be adapted and developed to look at pull-out forces and micromotions of the tibial component with a small keel. This can give an estimation of the level of primary fixation that the small keel can provide.

Lastly, little is known about the kinematics of tibia vara knees. In **Chapter 6**, it was assumed that the load in the leg would go through the direction of the mechanical axis of the lower limb. However, as the shape of a tibia vara tibia is notably different to that of a typical tibia, this deformity may alter the direction in which the load is transferred. Future studies could incorporate musculoskeletal modelling with 3D gait data of tibia vara patients from motion capture. This will provide a clearer idea of how tibia vara deformity affects the direction and magnitude of joint contact force in the knee. Musculoskeletal modelling of knees with OUKR components implanted can also be investigated to understand how knee kinematics changes before and after the knee is replaced. The effects of the varus-valgus orientation of the tibial component on the lateral compartment can also be further examined with musculoskeletal modelling.

Despite the aforementioned future studies that are proposed above to address the limitations of the thesis, future research can build on the following aspects of this work.

The distribution of bone density may be different in tibial component subsidence patients. A particular region of bone could be stiffer or less stiff than that in non-subsidence patients. For example, these patients may have bone cysts in the tibial plateau which are hard to identify on radiographs. These voids filled with fluid cannot resist compressive load and may cause the tibial component to sink. A small-scale radiographic study was conducted to investigate if there was any difference in the bone density distribution in subsidence and non-subsidence patients (**Appendix H**). Bone density at the tibial plateau of five subsidence patients and five non-subsidence patients who have undergone cementless medial OUKR were compared radiographically with ImageJ (National Institutes of Health, Bethesda, Maryland, USA). No significant conclusion could be drawn, partly because the sample size was small. Future studies can increase the number of samples to evaluate if subsidence patients show notably different local bone properties or irregular bone density distribution. Future studies can also assess subsidence patients' bone density from their pre-operative CT scans or MRI scans if available.

Another study on unilateral subsidence in bilateral OUKR patients was conducted to identify if component positioning had an impact on the risk of subsidence (**Appendix I**). However, as the direction of internal-external rotation was not identifiable from a plain film radiograph which is a compressed 2D image of a 3D object, no useful conclusion could be drawn from this study. If post-operative CT scans are available in future studies, the component position could be reconstructed. Then the effects of component rotation in the horizontal plane which may lead to different loading in the bone as the bearing slides with the flexion and extension of the knee can be investigated. Bone density distribution can also be assessed with these CT images.

Lastly, the FE method which applies element deletion developed in **Chapter 2** can be further enhanced to study the primary fixation of other axisymmetric implants, for example, dental implants (straight or tapered peg, screws) and acetabular cups in hip replacements. Together with the FEA workflow and Python code used to generate FE models of proximal tibias developed in **Chapter 4** for assessment of the risk of fracture, models that evaluate the effects of size of press-fit interference or implant surface morphology on the risk of post-operative periprosthetic fracture can be developed and used for hip, knee and dental implant design optimisation.

8.3 Thesis Conclusions

This thesis aimed to understand the effects of surgical factors on two poorly understood complications of the cementless medial OUKR: tibial periprosthetic fracture (PPF) and tibial component subsidence. Both complications are related to the stability of the tibial component.

Tibial PPF, which is more common in Asian populations who generally have smaller tibias and more overhanging tibial plateaus is likely to be caused by the damage in the peripheral cortical bone due to inappropriate component positioning. Placing the tibial component too medial or too distal reduces the volume of bony support and shortens the SCD. This impairs the load-bearing ability of the bone and makes it more prone to PPF. The angle of internal or external rotation of the component in the transverse plane is more tolerant. However, large rotations should be avoided as they shorten the distance from the keel slot to the cortex and this subsequently makes the tibia more prone to surgical errors in other directions and orientations. Placing the tibial component in valgus relative to the standard position in these patients reduces the distance between the keel slot and the cortex and

increases the highest maximum principal stress in the bone. Oppositely, placing the component in varus reduces the stress and therefore, lowers the risk of PPF. However, the femur has a tendency to subluxate medially when the tibial component is placed in varus. Therefore, large varus of the tibial component should be avoided to prevent the femur from sliding medially excessively which may increase the risk of lateral progression of OA in the long-term. Further musculoskeletal modelling that can look into how load transfers in tibia vara knees should be considered to find the optimal range of angle of varus in these patients.

Regarding changes in component design, making the keel shallower and shorter at both the front and the back proves to provide the largest improvement regarding the reduction in risk of PPF. If future studies can further justify that using a smaller keel will not compromise the primary fixation of the component, then this change in keel design should be considered and implemented. This will greatly reduce the risk of PPF and benefit cementless medial OUKR patients with tibia vara, small tibias and/or overhanging tibial plateaus, commonly seen in Asian cohorts.

Tibial component subsidence, which has an incidence of 0.3% to 5%, is recommended to be treated conservatively. Most subsided components were well-fixed at one-year follow-up without surgical interventions. Therefore, close monitoring of symptoms and further migration after the first discovery of subsidence is suggested to avoid unnecessary revisions. The aetiology of subsidence is still unclear, and this complication is likely to be multifactorial. Further interdisciplinary research that involves the analysis of the biological response of bone is required.

Chapter 9. References

1. Jones, O. *The Knee Joint*. 2023; Available from: https://teachmeanatomy.info/lower-limb/joints/knee-joint/.

2. D'Lima, D.D., et al., *Knee joint forces: prediction, measurement, and significance.* Proc Inst Mech Eng H, 2012. **226**(2): p. 95-102.

3. Knarr, B.A., J.S. Higginson, and J.A. Zeni, *Change in knee contact force with simulated change in body weight.* Comput Methods Biomech Biomed Engin, 2016. **19**(3): p. 320-323.

4. Abulhasan, J. and M. Grey, *Anatomy and Physiology of Knee Stability.* Journal of Functional Morphology and Kinesiology, 2017. **2**(4).

5. Cleveland Clinic. *Knee Joint*. 2023; Available from: https://my.clevelandclinic.org/health/body/24777-knee-joint#anatomy.

6. Loeser, R.F., et al., *Osteoarthritis: a disease of the joint as an organ.* Arthritis Rheum, 2012. **64**(6): p. 1697-707.

7. Krause, W.R., et al., *Mechanical changes in the knee after meniscectomy.* J. Bone Jt. Surg., 1976. **58**(5).

8. McDermott, I.D. and A.A. Amis, *The consequences of meniscectomy.* J Bone Joint Surg Br, 2006. **88**(12): p. 1549-56.

9. Chahla, J., et al., *Meniscal Pathology*, in *Evidence-Based Management of Complex Knee Injuries*, R.F. LaPrade and J. Chahla, Editors. 2022. p. 157-175.

10. Bartels, D.W., R. Kyle Martin, and B.A. Levy, *Meniscus Biomechanics*, in *Evidence-Based Management of Complex Knee Injuries*, R.F. LaPrade and J. Chahla, Editors. 2022. p. 176-184.

11. Goodfellow, J., et al., *Unicompartmental arthroplasty with the oxford knee*. 2nd edition. ed. 2015, Oxford: Goodfellow Publishers Lim.

12. Mameri, E.S., et al., *Review of Meniscus Anatomy and Biomechanics.* Curr Rev Musculoskelet Med, 2022. **15**(5): p. 323-335.

13. Physiopedia. *Knee*. 2024; Available from: https://www.physio-pedia.com/Knee.

14. Comprehensive Orthopaedics. *Anatomy of the Knee*. 2016; Available from: https://comportho.com/anatomy/anatomy-of-the-knee/.

15. Ombregt, L., *Applied anatomy of the knee*, in *A System of Orthopaedic Medicine*. 2013. p. e262-e269.

16. Kreder, H.J. and G.A. Hawker, *6 - THE KNEE*, in *Fam's Musculoskeletal Examination and Joint Injection Techniques (Second Edition)*, G.V. Lawry, et al., Editors. 2010, Mosby: Philadelphia. p. 65-88.

17. Kesson, M. and E. Atkins, *Chapter 11 - The knee*, in *Orthopaedic Medicine (Second Edition)*, M. Kesson and E. Atkins, Editors. 2005, Butterworth-Heinemann: Edinburgh. p. 403-452.

18. Gollehon, D.L., P.A. Torzilli, and R.F. Warren, *The role of the posterolateral and cruciate ligaments in the stability of the human knee. A biomechanical study.* J Bone Joint Surg Am, 1987. **69**(2): p. 233-42.

19. Gupton, M., et al., *Anatomy, Bony Pelvis and Lower Limb, Knee*. 2023, StatPearls [Internet]: Treasure Island (FL): StatPearls Publishing.

20. Cox, C.F., et al., *Anatomy, Bony Pelvis and Lower Limb, Knee Patella*. 2023, StatPearls [Internet]: Treasure Island (FL): StatPearls Publishing.

21. Cleveland Clinic. *Femur*. 2022; Available from: https://my.clevelandclinic.org/health/body/22503-femur.

22. Cleveland Clinic. *Tibia*. 2022; Available from: https://my.clevelandclinic.org/health/body/24777-knee-joint#anatomy.

23. Creamer, P., *Chapter 2 - Osteoarthritis*, in *Handbook of Pain Management*, R. Melzack and P.D. Wall, Editors. 2003, Churchill Livingstone: Philadelphia. p. 31-38.

24. Wolff, D., *Osteoarthritis*, in *xPharm: The Comprehensive Pharmacology Reference*, S.J. Enna and D.B. Bylund, Editors. 2007, Elsevier: New York. p. 1-12.

25. Cucchiarini, M., et al., *Basic science of osteoarthritis.* J Exp Orthop, 2016. **3**(1): p. 22.

26. Martel-Pelletier, J., et al., *Osteoarthritis.* Nat Rev Dis Primers, 2016. **2**: p. 16072.

27. Hunter, D.J. and S. Bierma-Zeinstra, *Osteoarthritis.* Lancet, 2019. **393**(10182): p. 1745-1759.

28. Carr, A.J., et al., *Knee replacement.* Lancet, 2012. **379**(9823): p. 1331-40.

29. Public Health England, *Musculoskeletal Health: A 5 year strategic framework for prevention across the lifecourse*. 2019.

30. Nelson, A.E. and J.M. Jordan, *Clinical Features of Osteoarthritis*, in *Kelley's Textbook of Rheumatology*. 2013. p. 1636-1645.

31. Blaustein, D.M. and E.M. Phillips, *Knee Osteoarthritis*, in *Essentials of Physical Medicine and Rehabilitation*. 2020. p. 391-398.

32. Zimmer Biomet, *Oxford Partial Knee Microplasty Instrumentation Surgical Technique*. 2019, Zimmer Biomet.

33. Physiopedia. *Knee Osteoarthritis*. 2024; Available from: https://www.physiopedia.com/Knee_Osteoarthritis.

34. Richard, M.J., J.B. Driban, and T.E. McAlindon, *Pharmaceutical treatment of osteoarthritis.* Osteoarthritis Cartilage, 2023. **31**(4): p. 458-466.

35. van der List, J.P., et al., *Outcomes of cementless unicompartmental and total knee arthroplasty: A systematic review.* Knee, 2017. **24**(3): p. 497-507.

36. Brown, N.M., et al., *Total knee arthroplasty has higher postoperative morbidity than unicompartmental knee arthroplasty: a multicenter analysis.* J Arthroplasty, 2012. **27**(8 Suppl): p. 86-90.

37. Liddle, A.D., et al., *Patient-reported outcomes after total and unicompartmental knee arthroplasty: a study of 14,076 matched patients from the National Joint Registry for England and Wales.* Bone Joint J, 2015. **97-B**(6): p. 793-801.

38. Newman, J., R.V. Pydisetty, and C. Ackroyd, *Unicompartmental or total knee replacement: the 15-year results of a prospective randomised controlled trial.* J Bone Joint Surg Br, 2009. **91**(1): p. 52-7.

39. Liddle, A.D., et al., *Adverse outcomes after total and unicompartmental knee replacement in 101,330 matched patients: a study of data from the National Joint Registry for England and Wales.* Lancet, 2014. **384**(9952): p. 1437-45.

40. Mohammad, H.R., A. Judge, and D.W. Murray, *A matched comparison of cementless unicompartmental and total knee replacement outcomes based on the National Joint Registry for England, Wales, Northern Ireland and the Isle of Man.* Acta Orthopaedica, 2022. **93**: p. 478-487.

41. Lombardi, A.V., Jr., et al., *Is recovery faster for mobile-bearing unicompartmental than total knee arthroplasty?* Clin Orthop Relat Res, 2009. **467**(6): p. 1450-7.

42. Sheth, N.P. and J.R.H. Foran. *Total Knee Replacement*. 2024; Available from: https://orthoinfo.aaos.org/en/treatment/total-knee-replacement/.

43. Willis-Owen, C.A., et al., *Unicondylar knee arthroplasty in the UK National Health Service: an analysis of candidacy, outcome and cost efficacy.* Knee, 2009. **16**(6): p. 473-8.

44. Martin, B., et al., *Comparison of five-year clinical outcomes of 524 cemented and cementless medial unicompartmental knee replacements.* Knee, 2022. **34**: p. 89-97.

45. Dalury, D.F., *Cementless total knee arthroplasty: current concepts review.* Bone Joint J, 2016. **98-B**(7): p. 867-73.

46. Dan, M.J., et al., *Cementless fixation techniques and problems*, in *Joint Replacement Technology*. 2021. p. 185-211.

47. Helvie, P.F., E.R. Deckard, and R.M. Meneghini, *Cementless Total Knee Arthroplasty Over the Past Decade: Excellent Survivorship in Contemporary Designs.* J Arthroplasty, 2023. **38**(6S): p. S145-S150.

48. Prasad, A.K., et al., *Cemented vs. cementless fixation in primary total knee arthroplasty: a systematic review and meta-analysis.* EFORT Open Rev, 2020. **5**(11): p. 793-798.

49. Matassi, F., et al., *Cemented versus cementless fixation in total knee arthroplasty.* Joints, 2013. **1**(3): p. 121-5.

50. *NJR 20th Annual Report 2023*. 2023, National Joint Registry.

51. Mohammad, H.R., A. Judge, and D.W. Murray, *A Matched Comparison of the Long-Term Outcomes of Cemented and Cementless Total Knee Replacements: An Analysis from the National Joint Registry of England, Wales, Northern Ireland and the Isle of Man.* J Bone Joint Surg Am, 2021. **103**(24): p. 2270-2280.

52. American Joint Replacement Registry, *AJRR 2023 Annual Report*. 2023, American Academy of Orthopaedic Surgeons.

53. Puri, S., et al., *Cementless Versus Cemented Total Knee Arthroplasty of the Same Design: Shorter Operative Times and Minimal Differences in Early Outcomes.* HSS J, 2023.

54. Asokan, A., et al., *Cementless knee arthroplasty: a review of recent performance.* Bone Jt Open, 2021. **2**(1): p. 48-57.

55. Matthias, J., M.P. Bostrom, and J.M. Lane, *A Comparison of Risks and Benefits Regarding Hip Arthroplasty Fixation.* J Am Acad Orthop Surg Glob Res Rev, 2021. **5**(11).

56. Mohammad, H.R., et al., *Ten-year clinical and radiographic results of 1000 cementless Oxford unicompartmental knee replacements.* Knee Surg Sports Traumatol Arthrosc, 2020. **28**(5): p. 1479-1487.

57. Trisi, P., et al., *Validation of value of actual micromotion as a direct measure of implant micromobility after healing (secondary implant stability). An in vivo histologic and biomechanical study.* Clin Oral Implants Res, 2016. **27**(11): p. 1423-1430.

58. Andersen, O.Z., et al., *Determining primary stability for adhesively stabilized dental implants.* Clin Oral Investig, 2023. **27**(7): p. 3741-3748.

59. O'Sullivan, D., et al., *A comparison of two methods of enhancing implant primary stability.* Clin Implant Dent Relat Res, 2004. **6**(1): p. 48-57.

60. Cross, M.J. and J. Spycher, *Cementless fixation techniques in joint replacement*, in *Joint Replacement Technology*. 2008. p. 190-211.

61. Sennerby, L., P. Thomsen, and L.E. Ericson, *A morphometric and biomechanic comparison of titanium implants inserted in rabbit cortical and cancellous bone.* Int J Oral Maxillofac Implants, 1992. **7**(1): p. 62-71.

62. Sennerby, L. and N. Meredith, *Implant stability measurements using resonance frequency analysis: biological and biomechanical aspects and clinical implications.* Periodontol 2000, 2008. **47**: p. 51-66.

63. Kohli, N., J.C. Stoddart, and R.J. van Arkel, *The limit of tolerable micromotion for implant osseointegration: a systematic review.* Sci Rep, 2021. **11**(1): p. 10797.

64. Shigeto, K., et al., *Changes in Bone Metabolisim Around Osseointegrated Implants Under Loading*, in *Implant Dentistry*, T. Ilser, Editor. 2011, IntechOpen: Rijeka. p. Ch. 9.

65. O'Sullivan, D., L. Sennerby, and N. Meredith, *Influence of implant taper on the primary and secondary stability of osseointegrated titanium implants.* Clin Oral Implants Res, 2004. **15**(4): p. 474-80.

66. Rues, S., et al., *Effect of bone quality and quantity on the primary stability of dental implants in a simulated bicortical placement.* Clin Oral Investig, 2021. **25**(3): p. 1265-1272.

67. Turkyilmaz, I. and E.A. McGlumphy, *Influence of bone density on implant stability parameters and implant success: a retrospective clinical study.* BMC Oral Health, 2008. **8**: p. 32.

68. Bartolomeu, F., et al., *Implant surface design for improved implant stability – A study on Ti6Al4V dense and cellular structures produced by Selective Laser Melting.* Tribology International, 2019. **129**: p. 272-282.

69. Langer, B., et al., *The wide fixture: a solution for special bone situations and a rescue for the compromised implant. Part 1.* Int J Oral Maxillofac Implants, 1993. **8**(4): p. 400-8.

70. Swami, V., V. Vijayaraghavan, and V. Swami, *Current trends to measure implant stability.* J Indian Prosthodont Soc, 2016. **16**(2): p. 124-30.

71. Elias, C.N., et al., *Influence of implant shape, surface morphology, surgical technique and bone quality on the primary stability of dental implants.* J Mech Behav Biomed Mater, 2012. **16**: p. 169-80.

72. Campi, S., et al., *Optimal interference of the tibial component of the cementless Oxford Unicompartmental Knee Replacement.* Bone Joint Res, 2018. **7**(3): p. 226-231.

73. Javed, F., et al., *Role of primary stability for successful osseointegration of dental implants: Factors of influence and evaluation.* Interv Med Appl Sci, 2013. **5**(4): p. 162-7.

74. Lin, T.H., et al., *NF-kappaB as a Therapeutic Target in Inflammatory-Associated Bone Diseases.* Adv Protein Chem Struct Biol, 2017. **107**: p. 117-154.

75. Crockett, J.C., et al., *Bone remodelling at a glance.* J Cell Sci, 2011. **124**(Pt 7): p. 991-8.

76. Yamada, H., et al., *Cementless total hip replacement: past, present, and future.* J Orthop Sci, 2009. **14**(2): p. 228-41.

77. Biemond, J.E., et al., *Frictional and bone ingrowth properties of engineered surface topographies produced by electron beam technology.* Arch Orthop Trauma Surg, 2011. **131**(5): p. 711-8.

78. Karageorgiou, V. and D. Kaplan, *Porosity of 3D biomaterial scaffolds and osteogenesis.* Biomaterials, 2005. **26**(27): p. 5474-91.

79. Gibson, I.R., *Synthetic hydroxyapatite for bone-healing applications*, in *Hydroxyapatite (Hap) for Biomedical Applications*. 2015. p. 269-287.

80. Otsuki, B., et al., *Pore throat size and connectivity determine bone and tissue ingrowth into porous implants: three-dimensional micro-CT based structural analyses of porous bioactive titanium implants.* Biomaterials, 2006. **27**(35): p. 5892-900.

81. Kamenaga, T., et al., *CLINICAL OUTCOMES AFTER UNICOMPARTMENTAL KNEE ARTHROPLASTY FOR OSTEONECROSIS OF THE KNEE.* Acta Ortop Bras, 2021. **29**(1): p. 12-16.

82. Kozinn, S.C. and R. Scott, *Unicondylar knee arthroplasty.* JBJS, 1989. **71**(1).

83. Gulati, A., et al., *The incidence of physiological radiolucency following Oxford unicompartmental knee replacement and its relationship to outcome.* Journal of Bone and Joint Surgery - Series B, 2009. **91**(7): p. 896-902.

84. Mohammad, H.R., et al., *Comparison of the 10-year outcomes of cemented and cementless unicompartmental knee replacements: data from the National Joint Registry for England, Wales, Northern Ireland and the Isle of Man.* Acta Orthop, 2020. **91**(1): p. 76-81.

85. Widari, N., et al. *Fifteen year results of cementless medial Oxford Unicompartmental Knee Replacement*. in *21st European Society of Sports Traumatology, Knee Surgery and Arthroscopy (ESSKA) Congress*. 2024. Milan.

86. Liddle, A.D., et al., *Cementless fixation in Oxford unicompartmental knee replacement: a multicentre study of 1000 knees.* Bone Joint J, 2013. **95-B**(2): p. 181-7.

87. Liddle, A.D., et al., *Valgus subsidence of the tibial component in cementless Oxford unicompartmental knee replacement.* Bone Joint J, 2014. **96-b**(3): p. 345-9.

88. Kamenaga, T., et al., *Valgus Subsidence of the Tibial Component Caused by Tibial Component Malpositioning in Cementless Oxford Mobile-Bearing Unicompartmental Knee Arthroplasty.* J Arthroplasty, 2019. **34**(12): p. 3054-3060.

89. Hefny, M.H., N.A. Smith, and J. Waite, *Cementless medial Oxford unicompartmental knee replacement. Five-year results from an independent series.* Knee, 2020. **27**(4): p. 1219-1227.

90. Panzram, B., et al., *Cementless oxford medial unicompartmental knee replacement—clinical and radiological results of 228 knees with a minimum 2-year follow-up.* Journal of Clinical Medicine, 2020. **9**(5).

91. Kamenaga, T., et al., *Adequate Positioning of the Tibial Component Is Key to Avoiding Bearing Impingement in Oxford Unicompartmental Knee Arthroplasty.* Journal of Arthroplasty, 2019. **34**(11): p. 2606-2613.

92. Burger, J.A., et al., *Comparable incidence of periprosthetic tibial fractures in cementless and cemented unicompartmental knee arthroplasty: a systematic review and meta-analysis.* Knee Surg Sports Traumatol Arthrosc, 2022. **30**(3): p. 852-874.

93. Keppler, L., et al., *Impact of keel saw blade design and thickness on the incidence of tibial plateau fracture and tibial implant-loosening in cementless medial UKR.* BMC Musculoskelet Disord, 2022. **23**(1): p. 597.

94. Pandit, H., et al., *Medial tibial plateau fracture and the Oxford unicompartmental knee.* Orthopedics, 2007. **30**(5 Suppl): p. 28-31.

95. Yoshikawa, R., et al., *The Medial Eminence Line for Predicting Tibial Fracture Risk after Unicompartmental Knee Arthroplasty.* Clin Orthop Surg, 2020. **12**(2): p. 166-170.

96. Kamenaga, T., et al., *Short distance from the keel to the posterior tibial cortex is associated with fracture after cementless Oxford UKA in Asian patients.* Knee Surg Sports Traumatol Arthrosc, 2021.

97. Akan, B., et al., *Cemented versus Uncemented Oxford Unicompartmental Knee Arthroplasty: Is There a Difference?* Adv Orthop, 2013. **2013**: p. 245915.

98. Campi, S., et al., *Ten-year survival and seven-year functional results of cementless Oxford unicompartmental knee replacement: A prospective consecutive series of our first 1000 cases.* Knee, 2018. **25**(6): p. 1231-1237.

99. Hiranaka, T., et al., *Tibial shape and size predicts the risk of tibial plateau fracture after cementless unicompartmental knee arthroplasty in Japanese patients.* Bone Joint J, 2020. **102-B**(7): p. 861-867.

100. Nagamine, R., et al., *Anatomic variations should be considered in total knee arthroplasty.* J Orthop Sci, 2000. **5**(3): p. 232-7.

101. Yau, W.P., et al., *Coronal bowing of the femur and tibia in Chinese: its incidence and effects on total knee arthroplasty planning.* J Orthop Surg (Hong Kong), 2007. **15**(1): p. 32-6.

102. Wang, F.X., et al., *Prosthesis size distribution in Oxford phase III unicompartmental knee arthroplasty - Based on more than 1900 Chinese patients.* J Orthop, 2021. **25**: p. 230-236.

103. Brekelmans, W.A.M., H.W. Poort, and T.J.J.H. Slooff, *A New Method to Analyse the Mechanical Behaviour of Skeletal Parts.* Acta Orthopaedica Scandinavica, 1972. **43**(5): p. 301-317.

104. Prendergast, P.J., *Finite element models in tissue mechanics and orthopaedic implant design.* Clinical Biomechanics, 1997. **12**(6): p. 343-366.

105. Imada, T., et al., *Enhancing the Unicompartmental Knee Arthroplasty Safety via Finite Element Analysis of Coronary Plane Alignment: A Case Report.* Cureus, 2024. **16**(6): p. e61765.

106. Yang, Y., et al., *Finite element analysis of sagittal angles of unicompartmental knee arthroplasty.* Clin Biomech (Bristol, Avon), 2024. **114**: p. 106232.

107. Koh, Y.G., et al., *Finite element analysis of the influence of the posterior tibial slope on mobile-bearing unicompartmental knee arthroplasty.* Knee, 2021. **29**: p. 116-125.

108. Dai, X., et al., *How does the inclination of the tibial component matter? A three-dimensional finite element analysis of medial mobile-bearing unicompartmental arthroplasty.* Knee, 2018. **25**(3): p. 434-444.

109. MacAulay, A., et al., *A finite element model for investigating the influence of keel design and position on unicompartmental knee replacement cementless tibial component fixation.* Med Eng Phys, 2024. **125**: p. 104119.

110. Pegg, E.C., et al., *Minimising tibial fracture after unicompartmental knee replacement: A probabilistic finite element study.* Clin Biomech (Bristol, Avon), 2020. **73**: p. 46-54.

111. Pegg, E.C., et al., *Evaluation of factors affecting tibial bone strain after unicompartmental knee replacement.* J Orthop Res, 2013. **31**(5): p. 821-8.

112. Pfeiffer, F.M., *The Use of Finite Element Analysis to Enhance Research and Clinical Practice in Orthopedics.* J Knee Surg, 2016. **29**(2): p. 149-58.

113. Zhang, Z.H., et al., *Application strategy of finite element analysis in artificial knee arthroplasty.* Front Bioeng Biotechnol, 2023. **11**: p. 1127289.

114. Kazemi, M., Y. Dabiri, and L.P. Li, *Recent advances in computational mechanics of the human knee joint.* Comput Math Methods Med, 2013. **2013**: p. 718423.

115. Meredith, N., *Assessment of Implant Stability as a Prognostic Determinant.* INT J PROSTHODONT, 1998. **11**(5): p. 491-501.

116. De Vries, E., et al., *Predicting friction at the bone - Implant interface in cementless total knee arthroplasty.* J Mech Behav Biomed Mater, 2022. **128**: p. 105103.

117. Janssen, D., et al., *Computational assessment of press-fit acetabular implant fixation: The effect of implant design, interference fit, bone quality, and frictional properties.* P I MECH ENG H, 2010. **224**(1): p. 67-75.

118. Post, C.E., et al., *A FE study on the effect of interference fit and coefficient of friction on the micromotions and interface gaps of a cementless PEEK femoral component.* J Biomech, 2022. **137**: p. 111057.

119. Keaveny, T.M., et al., *Differences between the tensile and compressive strengths of bovine tibial trabecular bone depend on modulus.* J. Biomech., 1994. **27**(9): p. 1137-1146.

120. Morgan, E.F., G.U. Unnikrisnan, and A.I. Hussein, *Bone Mechanical Properties in Healthy and Diseased States.* Annu Rev Biomed Eng, 2018. **20**: p. 119-143.

121. Kelly, N. and J.P. McGarry, *Experimental and numerical characterisation of the elasto-plastic properties of bovine trabecular bone and a trabecular bone analogue.* J Mech Behav Biomed Mater, 2012. **9**: p. 184-97.

122. Petrini, M., et al., *Fixture Length and Primary Stability: An In Vitro Study on Polyurethane Foam.* Applied Sciences, 2022. **12**(5).

123. Ovesy, M., M. Aeschlimann, and P.K. Zysset, *Explicit finite element analysis can predict the mechanical response of conical implant press-fit in homogenized trabecular bone.* J Biomech, 2020. **107**: p. 109844.

124. Rahman, A., *Assessing and Improving Clinical Outcomes of the Cementless Oxford Unicompartmental Knee Replacement Tibial Component*. 2022, University of Oxford.

125. *M2 Series 5 Titanium CpTi*. 2023: AP&C.

126. MatWeb. *Sawbones Solid Rigid Polyurethane Foam 20 pcf Density*. 2024.

127. Min, X., et al., *Finite element modelling of press-fit implant insertion*, in *18th International Symposium on Computer Methods in Biomechanics and Biomedical Engineering*. 2023: Paris, France.

128. Bishop, N.E., et al., *The influence of bone damage on press-fit mechanics.* J Biomech, 2014. **47**(6): p. 1472-8.

129. Rapagna, S., et al., *Quantification of human bone microarchitecture damage in press-fit femoral knee implantation using HR-pQCT and digital volume correlation.* J Mech Behav Biomed Mater, 2019. **97**: p. 278-287.

130. Silva-Henao, J.D., et al., *Post-yield mechanical properties of bovine trabecular bone – Relationships with bone volume fraction and strain rate.* Engineering Fracture Mechanics, 2020. **233**.

131. Ovesy, M., et al., *Non-linear explicit micro-FE models accurately predict axial pull-out force of cortical screws in human tibial cortical bone.* J Mech Behav Biomed Mater, 2022. **126**: p. 105002.

132. Harrison, N., et al., *Micromotion and friction evaluation of a novel surface architecture for improved primary fixation of cementless orthopaedic implants.* J Mech Behav Biomed Mater, 2013. **21**: p. 37-46.

133. Berahmani, S., D. Janssen, and N. Verdonschot, *Experimental and computational analysis of micromotions of an uncemented femoral knee implant using elastic and plastic bone material models.* J Biomech, 2017. **61**: p. 137-143.

134. Al-Dirini, R.M.A., et al., *Influence of collars on the primary stability of cementless femoral stems: A finite element study using a diverse patient cohort.* J Orthop Res, 2018. **36**(4): p. 1185-1195.

135. Kanaizumi, A., et al., *Patient-specific three-dimensional evaluation of interface micromotion in two different short stem designs in cementless total hip arthroplasty: a finite element analysis.* J Orthop Surg Res, 2022. **17**(1): p. 437.

136. Nandi, S., et al., *Short single-wedge stems have higher risk of periprosthetic fracture than other cementless stem designs in Dorr type A femurs: a finite element analysis.* Hip Int, 2022. **32**(3): p. 298-303.

137. Tissakht, M., H. Eskandari, and A.M. Ahmed, *Micromotion analysis of the fixation of total knee tibial component.* Computers & Structures, 1995. **56**(2): p. 365-375.

138. Ovesy, M., M. Indermaur, and P.K. Zysset, *Prediction of insertion torque and stiffness of a dental implant in bovine trabecular bone using explicit micro-finite element analysis.* J Mech Behav Biomed Mater, 2019. **98**: p. 301-310.

139. Grant, J.A., et al., *Artificial composite bone as a model of human trabecular bone: the implant-bone interface.* J Biomech, 2007. **40**(5): p. 1158-64.

140. Purcell, R.L., et al., *Bone Ongrowth of Contemporary Cementless Tibial Components: A Retrieval Analysis.* Arthroplast Today, 2022. **13**: p. 149-153.

141. Min, X., et al. *Experimental characterisation of coefficient of friction at bone-implant interface*. in *ORS 2024 Annual Meeting*. 2024. Long Beach, California.

142. Damm, N.B., M.M. Morlock, and N.E. Bishop, *Friction coefficient and effective interference at the implant-bone interface.* J Biomech, 2015. **48**(12): p. 3517-21.

143. Hashemi, A., A. Shirazi-Adl, and M. Dammak, *Bidirectional friction study of cancellous bone-porous coated metal interface.* J Biomed Mater Res, 1996. **33**(4): p. 257-267.

144. Dammak, M., et al., *Friction properties at the bone-metal interface: Comparison of four different porous metal surfaces.* J Biomed Mater Res, 1997. **35**(3): p. 329-336.

145. Rancourt, D., et al., *Friction properties of the interface between porous-surfaced metals and tibial cancellous bone.* J Biomed Mater Res, 1990. **24**(11): p. 1503-19.

146. Shirazi-Adl, A., M. Dammak, and G. Paiement, *Experimental determination of friction characteristics at the trabecular bone/porous-coated metal interface in cementless implants.* J Biomed Mater Res, 1993. **27**(2): p. 167-75.

147. Thoreau, L., D. Morcillo Marfil, and E. Thienpont, *Periprosthetic fractures after medial unicompartmental knee arthroplasty: a narrative review.* Archives of Orthopaedic and Trauma Surgery, 2021.

148. Nandra, R., et al., *Regional five-year clinical outcomes of 289 consecutive cementless oxford uni-compartmental knee replacements at a non-inventor centre.* J Clin Orthop Trauma, 2021. **17**: p. 176-181.

149. Yue, B., et al., *Differences of knee anthropometry between Chinese and white men and women.* J Arthroplasty, 2011. **26**(1): p. 124-30.

150. Moreland, J.R., L.W. Bassett, and G.J. Hanker, *Radiographic analysis of the axial alignment of the lower extremity.* J Bone Joint Surg Am, 1987. **69**(5): p. 745-9.

151. Tang, W.M., Y.H. Zhu, and K.Y. Chiu, *Axial alignment of the lower extremity in Chinese adults.* J Bone Joint Surg Am, 2000. **82**(11): p. 1603-8.

152. Lasam, M.P.G., et al., *Femoral lateral bowing and varus condylar orientation are prevalent and affect axial alignment of TKA in Koreans knee.* Clinical Orthopaedics and Related Research, 2013. **471**(5): p. 1472-1483.

153. Nayak, M., et al., *A radiographic analysis of alignment in 966 lower extremities with knee pain and its association with osteoarthritis in Indian population: Alignment of lower limb with knee pain.* Journal of Orthopaedics, 2020. **20**: p. 207-212.

154. Ruangsomboon, P., et al., *The factors influencing the component sizes in Oxford Phase 3 unicompartmental knee arthroplasty.* Jt Dis Relat Surg, 2022. **33**(3): p. 505-512.

155. Mullaji, A. and G. Shetty, *EFFECT OF EXTRA-ARTICULAR DEFORMITIES ON LIMB ALIGNMENT AFTER MOBILE-BEARING UNICOMPARTMENTAL KNEE ARTHROPLASTY.* Orthopaedic Proceedings, 2019. **101-B**(SUPP_4): p. 83-83.

156. Erlichman, R.E., et al., *Impact of Proximal Tibial Varus Anatomy on Survivorship After Medial Unicondylar Knee Arthroplasty.* J Arthroplasty, 2023.

157. Houskamp, D.J., T. Tompane, and B.T. Barlow, *What Is the Critical Tibial Resection Depth During Unicompartmental Knee Arthroplasty? A Biomechanical Study of Fracture Risk.* J Arthroplasty, 2020. **35**(8): p. 2244-2248.

158. Kamenaga, T., et al., *Varus placement of the tibial component reduces the potential risk of fracture with adequate bony coverage in the Oxford unicompartmental knee arthroplasty.* Sci Rep, 2024. **14**(1): p. 1274.

159. Riviere, C., et al., *Kinematic alignment of medial UKA is safe: a systematic review.* Knee Surgery Sports Traumatology Arthroscopy, 2022. **30**(3): p. 1082-1094.

160. Cobb, J.P., et al., *The anatomical tibial axis: reliable rotational orientation in knee replacement.* J Bone Joint Surg Br, 2008. **90**(8): p. 1032-8.

161. Simpson, D.J., et al., *Elevated proximal tibial strains following unicompartmental knee replacement--a possible cause of pain.* Med Eng Phys, 2009. **31**(7): p. 752-7.

162. Bessho, M., et al., *Prediction of strength and strain of the proximal femur by a CT-based finite element method.* J Biomech, 2007. **40**(8): p. 1745-53.

163. Moss, D.R. and M. Basic, *1 - General Topics*, in *Pressure Vessel Design Manual (Fourth Edition)*, D.R. Moss and M. Basic, Editors. 2013, Butterworth-Heinemann: Oxford. p. 1-36.

164. Maeda, K., et al., *Cortical thickness of the tibial diaphysis reveals age- and sex-related characteristics between non-obese healthy young and elderly subjects depending on the tibial regions.* J Exp Orthop, 2020. **7**(1): p. 78.

165. Armillotta, N., E. Bori, and B. Innocenti, *Finite element analysis of malposition in bi-unicompartmental knee arthroplasty.* Arch Orthop Trauma Surg, 2023. **143**(6): p. 3447-3455.

166. Pegg, E.C., et al., *Sagittal kinematics of mobile unicompartmental knee replacement in anterior cruciate ligament deficient knees.* Clin Biomech (Bristol, Avon), 2016. **31**: p. 33-9.

167. Kutzner, I., et al., *Loading of the knee joint during activities of daily living measured in vivo in five subjects.* J Biomech, 2010. **43**(11): p. 2164-73.

168. Pegg, E.C. and H.S. Gill, *An open source software tool to assign the material properties of bone for ABAQUS finite element simulations.* J Biomech, 2016. **49**(13): p. 3116-3121.

169. Arthur, L., *Instrumentation Optimisation for Unicompartmental Knee Replacement*. 2024, University of Oxford.

170. *Sawbones general catalog*. Sawbones.

171. Ghouse, S., et al., *The Design and In Vivo Testing of a Locally Stiffness-Matched Porous Scaffold.* Appl Mater Today, 2019. **15**: p. 377-388.

172. Keaveny, T.M., E.F. Morgan, and O.C. Yeh, *BONE MECHANICS*, in *Standard Handbook of Biomedical Engineering & Design*. 2003, McGraw-Hill Education: New York.

173. Lee, S.Y., et al., *Tibial component rotation during the unicompartmental knee arthroplasty: is the anterior superior iliac spine an appropriate landmark?* Knee Surg Sports Traumatol Arthrosc, 2017. **25**(12): p. 3723-3732.

174. Gao, G., et al., *Effect of vertical cut on coronal coverage and rotation of tibial component in Oxford unicompartmental knee arthroplasty.* J Int Med Res, 2020. **48**(5): p. 300060520922426.

175. Akagi, M., et al., *Variability of extraarticular tibial rotation references for total knee arthroplasty.* Clin Orthop Relat Res, 2005(436): p. 172-6.

176. Kamenaga, T., et al., *Influence of tibial component rotation on short-term clinical outcomes in Oxford mobile-bearing unicompartmental knee arthroplasty.* Knee, 2018. **25**(6): p. 1222-1230.

177. Chau, R., et al., *Tibial component overhang following unicompartmental knee replacement-Does it matter?* Knee, 2009. **16**(5): p. 310-313.

178. Bellemans, J., et al., *The Chitranjan Ranawat award: is neutral mechanical alignment normal for all patients? The concept of constitutional varus.* Clin Orthop Relat Res, 2012. **470**(1): p. 45-53.

179. Readioff, R., et al., *Image-based parametric finite element modelling for studying contact mechanics in human knee joints.* bioRxiv, 2023: p. 2023.09.07.556747.

180. Papaioannou, G., et al., *Patient-specific knee joint finite element model validation with high-accuracy kinematics from biplane dynamic Roentgen stereogrammetric analysis.* J Biomech, 2008. **41**(12): p. 2633-8.

181. Agustoni, G., et al., *High Resolution Micro-Computed Tomography Reveals a Network of Collagen Channels in the Body Region of the Knee Meniscus.* Ann Biomed Eng, 2021. **49**(9): p. 2273-2281.

182. Navarro, M., et al., *Biomaterials in orthopaedics.* J R Soc Interface, 2008. **5**(27): p. 1137-58.

183. Godest, A.C., et al., *Simulation of a knee joint replacement during a gait cycle using explicit finite element analysis.* Journal of Biomechanics, 2002. **35**(2): p. 267-275.

184. Kang, K.-T., et al., *In vivo evaluation of the subject-specific finite element model for knee joint cartilage contact area.* International Journal of Precision Engineering and Manufacturing, 2015. **16**(6): p. 1171-1177.

185. Murray, D.W., J.W. Goodfellow, and J.J. O'Connor, *The Oxford medial unicompartmental arthroplasty.* The Journal of Bone & Joint Surgery British Volume, 1998. **80-B**(6): p. 983-989.

186. Pandit, H., et al., *Aetiology of lateral progression of arthritis following Oxford medial unicompartmental knee replacement: a case–control study.* Musculoskeletal Surgery, 2016. **100**(2): p. 97-102.

187. Pandit, H., et al., *Improved fixation in cementless unicompartmental knee replacement: five-year results of a randomized controlled trial.* J Bone Joint Surg Am, 2013. **95**(15): p. 1365-72.

188. Campi, S., et al., *Five-year results of a randomised controlled trial comparing cemented and cementless Oxford unicompartmental knee replacement using radiostereometric analysis.* The Knee, 2021. **28**: p. 383-390.

189. Aspinall, G.R. and M.J. Dunbar, *CHAPTER 4 - Assessing Clinical Results and Outcome Measures*, in *Surgical Treatment of Hip Arthritis*, W.J. Hozack, J. Parvizi, and B. Bender, Editors. 2009, W.B. Saunders: Philadelphia. p. 30-36.

190. Arthur, L., et al. *EARLY TIBIAL SUBSIDENCE OF THE CEMENTLESS OXFORD UNICOMPARTMENTAL KNEE ARTHROPLASTY*. in *Orthopaedic Proceedings*. 2023. London.

191. Hefny, M., et al., *EVALUATION OF RADIOLUCENCY AND SUBSIDENCE OF THE CEMENTLESS OXFORD MEDIAL UNICOMPARTMENTAL KNEE REPLACEMENT.* Ain Shams Medical Journal, 2020. **71**(2): p. 327-337.

192. Liddle, A.D., *Failure of Unicompartmental Knee Replacement*. 2013, University of Oxford.

193. Arthur, L.W., et al., *Polyethylene bearing wear is comparable for cemented and cementless Oxford unicompartmental knee replacements: Ten-year results of a randomized controlled trial.* Knee Surg Sports Traumatol Arthrosc, 2024. **32**(2): p. 405-417.

194. Kopperdahl, D.L. and T.M. Keaveny, *Yield strain behavior of trabecular bone.* J Biomech, 1998. **31**(7): p. 601-8.

195. Miller, R.H., et al., *Why don't most runners get knee osteoarthritis? A case for per-unit-distance loads.* Med Sci Sports Exerc, 2014. **46**(3): p. 572-9.

196. Nicholson, J.A., et al., *Monitoring of fracture healing. Update on current and future imaging modalities to predict union.* Injury, 2021. **52 Suppl 2**: p. S29-S34.

197. Hak, D.J., et al., *Delayed union and nonunions: epidemiology, clinical issues, and financial aspects.* Injury, 2014. **45 Suppl 2**: p. S3-7.

198. Mellon, S.J. and K.E. Tanner, *Bone and its adaptation to mechanical loading: a review.* International Materials Reviews, 2012. **57**(5): p. 235-255.

199. Ryd, L., et al., *Migration of the tibial component in successful unicompartmental knee arthroplasty. A clinical, radiographic and roentgen stereophotogrammetric study.* Acta Orthop Scand, 1983. **54**(3): p. 408-16.

200. Ryd, L., *Micromotion in knee arthroplasty. A roentgen stereophotogrammetric analysis of tibial component fixation.* Acta Orthopaedica Scandinavica (Supplement), 1986. **220**: p. 1-80.

201. Ryd, L. and L. Linder, *On the correlation between micromotion and histology of the bone-cement interface. Report of three cases of knee arthroplasty followed by roentgen stereophotogrammetric analysis.* Journal of Arthroplasty, 1989. **4**(4): p. 303-9.

202. Ryd, L., et al., *The influence of metal backing in unicompartmental tibial component fixation. An in vivo roentgen stereophotogrammetric analysis of micromotion.* Archives of Orthopaedic & Trauma Surgery, 1992. **111**(3): p. 148-54.

203. Miskovsky, C., L.A. Whiteside, and S.E. White, *The cemented unicondylar knee arthroplasty. An in vitro comparison of three cement techniques.* Clinical Orthopaedics & Related Research, 1992(284): p. 215-20.

204. Buechel, F.F., et al., *Low contact stress meniscal bearing unicompartmental knee replacement: Long-term evaluation of cemented and cementless results.* Journal of Orthopaedic Rheumatology, 1994. **7**(1): p. 31-41.

205. RYD, L. and N. EGUND, *Subsidence of Tibial Components in Knee Arthroplasty: A Comparison Between Conventional Radiography and Roentgen Stereophotogrammetry.* Investigative Radiology, 1995. **30**(7): p. 396-400.

206. Squire, M.W., et al., *Unicompartmental knee replacement. A minimum 15 year followup study.* Clinical Orthopaedics & Related Research, 1999(367): p. 61-72.

207. Lindstrand, A., et al., *The introduction period of unicompartmental knee arthroplasty is critical: a clinical, clinical multicentered, and radiostereometric study of 251 Duracon unicompartmental knee arthroplasties.* Journal of Arthroplasty, 2000. **15**(5): p. 608-16.

208. Soavi, R., et al., *A roentgen stereophotogrammetric analysis of unicompartmental knee arthroplasty.* Journal of Arthroplasty, 2002. **17**(5): p. 556-61.

209. Bragonzoni, L., et al., *The stress-inducible displacement detected through RSA in non-migrating UKR.* Knee, 2005. **12**(4): p. 301-306.

210. Carlsson, L.V., B.E. Albrektsson, and L.R. Regner, *Minimally invasive surgery vs conventional exposure using the Miller-Galante unicompartmental knee arthroplasty: a randomized radiostereometric study.* Journal of Arthroplasty, 2006. **21**(2): p. 151-6.

211. Gillies, R.M., et al., *Adaptive bone remodelling of all polyethylene unicompartmental tibial bearings.* ANZ Journal of Surgery, 2007. **77**(1-2): p. 69-72.

212. Saenz, C.L., et al., *Early failure of a unicompartmental knee arthroplasty design with an all-polyethylene tibial component.* Knee, 2010. **17**(1): p. 53-56.

213. Small, S.R., et al., *Metal backing significantly decreases tibial strains in a medial unicompartmental knee arthroplasty model.* Journal of Arthroplasty, 2011. **26**(5): p. 777-82.

214. Bruni, D., et al., *Is unicompartmental arthroplasty an acceptable option for spontaneous osteonecrosis of the knee?* Clinical Orthopaedics & Related Research, 2012. **470**(5): p. 1442-51.

215. Clement, N.D., et al., *Medium-term results of Oxford phase-3 medial unicompartmental knee arthroplasty.* J Orthop Surg (Hong Kong), 2012. **20**(2): p. 157-61.

216. Small, S.R., et al., *Tibial loading after UKA: Evaluation of tibial slope, resection depth, medial shift and component rotation.* Journal of Arthroplasty, 2013. **28**(9 SUPPL): p. 179-183.

217. Ensini, A., et al., *Early migration of the cemented tibial component of unicompartmental knee arthroplasty: a radiostereometry study.* Knee Surgery, Sports Traumatology, Arthroscopy, 2013. **21**(11): p. 2474-9.

218. O'Donnell, T.M.P., O. Abouazza, and M.J. Neil, *Revision of Minimal Resection Resurfacing Unicondylar Knee Arthroplasty to Total Knee Arthroplasty: Results Compared With Primary Total Knee Arthroplasty.* Journal of Arthroplasty, 2013. **28**(1): p. 33-39.

219. Barbadoro, P., et al., *Tibial component alignment and risk of loosening in unicompartmental knee arthroplasty: a radiographic and radiostereometric study.* Knee Surgery, Sports Traumatology, Arthroscopy, 2014. **22**(12): p. 3157-3162.

220. Engh, G.A. and D.J. Ammeen, *Unicondylar arthroplasty in knees with deficient anterior cruciate ligaments knee.* Clinical Orthopaedics and Related Research, 2014. **472**(1): p. 73-77.

221. Bruni, D., et al., *Roentgen stereophotogrammetric analysis: an effective tool to predict implant survival after an all-poly unicompartmental knee arthroplasty—a 10 year follow-up study.* Knee Surgery, Sports Traumatology, Arthroscopy, 2015. **23**(11): p. 3273-3280.

222. Hooper, N., et al., *The five-year radiological results of the uncemented Oxford medial compartment knee arthroplasty.* Bone Joint J, 2015. **97-b**(10): p. 1358-63.

223. Koppens, D., et al., *Low implant migration of the SIGMA® medial unicompartmental knee arthroplasty.* Knee Surgery, Sports Traumatology, Arthroscopy, 2018. **26**(6): p. 1776-1785.

224. Scott, C.E.H., et al., *Ten-year survival and patient-reported outcomes of a medial unicompartmental knee arthroplasty incorporating an all-polyethylene tibial component.* Archives of Orthopaedic and Trauma Surgery, 2018. **138**(5): p. 719-729.

225. Scott, C.E.H., et al., *Revision of Unicompartmental to Total Knee Arthroplasty: Does the Unicompartmental Implant (Metal-Backed vs All-Polyethylene) Impact the Total Knee Arthroplasty?* The Journal of Arthroplasty, 2018. **33**(7): p. 2203-2209.

226. Zsakai, Z., et al., *Medial unicompartmental knee arthroplasty: Correlation between components' malalignment and long-term outcome in obese patients.* Trauma Monthly, 2018. **23**(3).

Appendices

Appendix A: Python Script for Generating Model of Patient 1 Left Tibia

Python scripts used to generate the FE models of Patient 1 right tibia and Patient 2 left and right tibias are of the same structure as the following one but with different inputs of points' coordinates used to define datum point/axis/plane positions. Therefore, those scripts are not included here.

```
# File:  Case_2_LeftLeg_complete_neutral_Static.py
# Date:  2023
# Created by: Elise Pegg, University of Oxford
# Edited by: Xiaoyi Min, University of Oxford
# Purpose: Replicate the cut in the left tibia of case 2 (Patient 1) (did not fracture)
# Comments:
#         - Model assumes vertical cut is always perpendicular to the horizontal cut
#         - in the unit of mm
# Version: 1
# ----------------------------INITIALISING PROGRAM-------------------------------
# -------------------------------------------------------------------------------
### Import Modules
# -------------------------------------------------------------------------------
from abaqus import *
from abaqusConstants import *
from math import *
import mesh
import regionToolset
import os
from numpy import diff, matrix, array, tan, sin, mean, arange, arctan

# -------------------------------------------------------------------------------
modelName = 'Case_2_LeftLeg_CTPos_01'
# -------------------------------------------------------------------------------
```

```
### Define parameters
# ----------------------------------------------------------------------------
# filenames
os.chdir('C:\Xiaoyi_DPhil\Abaqus\Python\Create_Interference_Models\Case2LeftLeg')
# The OS module in Python provides functions for interacting with the operating system


# os.getcwd(): get current working directory
tibCAD = os.getcwd().split('.')[0] +
'/JapaneseTibiaCase2LeftNoFracture/CASE2_LEFT_Wrapped_Smoothed_shorter.SAT'
# adds tibia geometry
trayCAD = os.getcwd().split('.')[0] +
'/JapaneseTibiaCase2LeftNoFracture/SimpleTibialComponentLeftMedial_SizeC.sat'
# tray geometry
keelCAD = os.getcwd().split('.')[0] + \
'/JapaneseTibiaCase2LeftNoFracture/SimpleTibialComponentLeftMedial_SizeC_KeelforSlot.sat'

# model parameters
angleBetweenCuts = 90  # between horizontal and vertical cuts
totalMeshSize = 2.4
fineMeshSize = totalMeshSize / 6
interference = 0.16
keelOffset = 6.7 + interference / 2
# distance from the lateral face of the keel to the lateral face of the wall
# points on tibial tray to define axis for corner and plane of tray base # local to tray
pt1 = (-15.67 - interference / 2, 0, -28.28)
pt2 = (-15.67 - interference / 2, 0, 21.32)
# pt1 and pt2 are on the lateral-most bottom edge of the tray
pt3 = (-26.01, 0, 5.32)  # pt3 is on the bottom face of the tray

fieldOutputRequests = ['S', 'PE', 'NE', 'U', 'RT']
historyOutputRequests = ('ALLAE', 'ALLCD', 'ALLDMD', 'ALLFD', 'ALLIE', 'ALLKE',
'ALLPD', 'ALLSE', 'ALLVD', 'ALLWK', 'ETOTAL', 'DT', 'DMASS')
```

```
# ----------------------------CREATING GEOMETRY--------------------------------
# -----------------------------------------------------------------------------
### Create model
# -----------------------------------------------------------------------------
# create new model
myModel = mdb.Model(name=modelName)
# remove redundant models if exist
if 'Model-1' in mdb.models.keys():
   del mdb.models['Model-1']
# -----------------------------------------------------------------------------

### Load geometry components (Tibia, Tray and KeelCuttingBlock)
# -----------------------------------------------------------------------------
mdb.openAcis(fileName=tibCAD)
myModel.PartFromGeometryFile(combine=False, dimensionality=THREE_D,
geometryFile=mdb.acis, name='TibiaTmp', scale=1.0, type=DEFORMABLE_BODY)
myPart2 = myModel.parts['TibiaTmp']

mdb.openAcis(fileName=trayCAD)
myModel.PartFromGeometryFile(combine=False, dimensionality=THREE_D,
geometryFile=mdb.acis, name='Tray', scale=1.0, type=DEFORMABLE_BODY)

mdb.openAcis(fileName=keelCAD)
myModel.PartFromGeometryFile(combine=False, dimensionality=
THREE_D, geometryFile=mdb.acis, name='Keel', scale=1.0,
type=DEFORMABLE_BODY)

# -----------------------------------------------------------------------------
# create assembly
myAssembly = myModel.rootAssembly
myInstance1 = myAssembly.Instance(name='Tibia-0', part=myPart2, dependent=OFF)
myPart1 = myModel.parts['TibiaTmp']
# this reassigns the new tibia as the new myPart1, which is a solid
```

```
horizontal_cutPlanept1 = (88.3025, -17.62943, 975.67308)
horizontal_cutPlanept2 = (81.93936, 31.7332, 975.05373)
horizontal_cutPlanept3 = (56.56268, 7.11242, 976.13084)
# these three pts define the horizontal cut plane
myPart1.DatumPlaneByThreePoints(point1=horizontal_cutPlanept1,
                        point2=horizontal_cutPlanept2,
                        point3=horizontal_cutPlanept3)  # myPart1.datums.keys()[0]

AP_cutAxispt1 = (88.3025, -17.62943, 975.67308)
AP_cutAxispt2 = (81.93936, 31.7332, 975.05373)
myPart1.DatumAxisByTwoPoint(point1=AP_cutAxispt1, point2=AP_cutAxispt2)
# myPart1.datums.keys()[1]

myPart1.DatumPlaneByRotation(plane=myPart1.datums[myPart1.datums.keys()[0]],
                        axis=myPart1.datums[myPart1.datums.keys()[1]], angle=90)
# myPart1.datums.keys()[2]

# myPart1.datums = {12: 'DatumPlane object', 13: 'DatumPlane object', 14: 'DatumPlane
# object', 15: 'DatumAxis object', 16: 'DatumPlane object', 17: 'DatumAxis object', 18:
# 'DatumPlane object'}

# ----------------------------------------------------------------------------
### Create surgical cuts
# ----------------------------------------------------------------------------
# create sketch for cutting block
# myPart1.datums.keys()[5] is a datumAxis
axisPoint = myPart1.datums[myPart1.datums.keys()[1]].pointOn
# A tuple of Floats specifying the X-, Y-, and Z-coordinates of a point located on the
# datum - for this one, this is a point on the AP cut axis
axisDirection = myPart1.datums[myPart1.datums.keys()[1]].direction
# A tuple of Floats specifying a sequence of three Floats specifying the direction of the
axis - AP cut axis.
mySketch2 = myModel.ConstrainedSketch(name='CuttingBlock', sheetSize=200.0,
                            transform=myPart1.MakeSketchTransform(
```

```
                                sketchPlane=myPart1.datums[myPart1.datums.keys()[0]],
# posterior slope
                                sketchPlaneSide=SIDE2,
                                sketchUpEdge=myPart1.datums[myPart1.datums.keys()[1]],
                                sketchOrientation=RIGHT, origin=axisPoint))
mySketch2.rectangle(point1=(0, -200), point2=(100, 200))
mySketch2.ConstructionLine(point1=(0, 100), point2=(0, -100))
# cut tibia using block
myPart1.CutRevolve(sketch=mySketch2, sketchOrientation=RIGHT, angle=90,
flipRevolveDirection=OFF,
        sketchPlane=myPart1.datums[myPart1.datums.keys()[0]],
sketchPlaneSide=SIDE2,
        sketchUpEdge=myPart1.datums[myPart1.datums.keys()[1]])
# angle: angle to be revolved
# ----------------------------------------------------------------------------

### Analyse keel cutting block part to get parameters
# ----------------------------------------------------------------------------
# Create a datum axis and plane on the keel part
myPart3 = myModel.parts['Keel']
myPart3.DatumAxisByTwoPoint(point1=pt1, point2=pt2)
# myPart3.datums.keys()[0] - AP axis of the lateral side of the
# lateral wall
myPart3.DatumPlaneByThreePoints(point1=pt1, point2=pt2, point3=pt3)
# myPart3.datums.keys()[1] - bottom face of the tibial component/top of keel
myPart3.DatumPlaneByPrincipalPlane(principalPlane=XYPLANE, offset=0)
# myPart3.datums.keys()[2] - the offset of -x moves the keel slot forward by x mm in the
direction of the keel slot; -ve means anterior


### Create assembly with keel cutting block to create keel slot
# ----------------------------------------------------------------------------
# load in tibia and keel cutting block
myInstance1 = myAssembly.Instance(name='Tibia-0', part=myPart1, dependent=OFF)
```

```
myInstance3 = myAssembly.Instance(name='Keel-0', part=myPart3, dependent=OFF)
# find the centre of the medial plateau for positioning the keel
XYZ = [85, -18, 976]
# XYZ  = [3mm medial to the vertical cut, the anterior edge of the plateau in the AP
direction, the anterior edge of the plateau in the vertical direction]

f = myInstance1.faces.getClosest(((XYZ[0], XYZ[1], XYZ[2]),), )[0][0]
# this selects the horizontal cut surface
TibCentroid = f.getCentroid()[0]  # this picks the centroid of the horizontal cut face

f = myInstance1.faces.getClosest(((XYZ[0], XYZ[1], XYZ[2] + 5),), )[0][0]
# this selects the vertical cut surface

p1 = myPart1.DatumPlaneByOffset(plane=myPart1.datums[myPart1.datums.keys()[2]],
point=TibCentroid)
# myPart1.datums[myPart1.datums.keys()[2]] is the vertical cut plane


a1 = myPart1.DatumAxisByNormalToPlane(plane=myPart1.datums[p1.id],
                                      point=TibCentroid)
# this creates an axis normal to p1 while passing centroid
a2 =
myPart1.DatumAxisByNormalToPlane(plane=myPart1.datums[myPart1.datums.keys()[0
]],
                                      point=TibCentroid)
# an axis normal to horizontal cut while passing centroid

p2 = myPart1.DatumPlaneByRotation(plane=myPart1.datums[p1.id],
axis=myPart1.datums[a2.id], angle=90)
# this forms a datum plane that is perpendicular to p1. it is also perpendicular to the
vertical cut
# position keel cutting block
myAssembly.EdgeToEdge(fixedAxis=myInstance1.datums[myPart1.datums.keys()[1]],
# horizontal cut axis
```

```
                movableAxis=myInstance3.datums[myPart3.datums.keys()[0]],
                # lateral wall ap axis
                flip=OFF)
myAssembly.FaceToFace(clearance=0.0,
fixedPlane=myInstance1.datums[myPart1.datums.keys()[0]],
                # horizontal cut plane
                flip=ON, movablePlane=myInstance3.datums[myPart3.datums.keys()[1]])
# bottom of the tray
myAssembly.FaceToFace(movablePlane=myInstance3.datums[myInstance3.datums.keys
()[-1]],
                # vertical to the horizontal cut
                fixedPlane=myInstance1.datums[myInstance1.datums.keys()[-1]],
                # plane parallel to the XZ plane
                flip=OFF, clearance=3.91)
# this moves the keel slot backwards by 3.91mm
# perform a boolean operation
myAssembly.InstanceFromBooleanCut(name='Tibia', instanceToBeCut=myInstance1,
                        cuttingInstances=(myInstance3,),
                        originalInstances=DELETE)
# remove redundant parts
del myModel.parts['Keel']
del myAssembly.instances['Tibia-1']
myPart1 = myModel.parts['Tibia']
myPart2 = myModel.parts['Tray']
myPart3 = myModel.parts['TibiaTmp']


###-----------------------------DEFINING MODEL---------------------------------
###----------------------------------------------------------------------------
##### Define surfaces on parts
###----------------------------------------------------------------------------
def createSurface(PART, XYZ, NAME):
   f = PART.faces.getClosest(((XYZ[0], XYZ[1], XYZ[2]),), )[0][0]
   PART.Surface(side1Faces=(PART.faces[f.index:f.index + 1],), name=NAME)
```

```
# Tray surfaces
# create contact surfaces
createSurface(myPart2, [-15, 5, 20], 'Tray_WallInt')
createSurface(myPart2, [-10, 3, 0], 'Tray_BearingInt')  # top of the tray
f = myPart2.faces.getByBoundingBox(xMax=-4, xMin=-9)
myPart2.Surface(side1Faces=f, name='Tray_TibiaInt')
f = myPart2.faces.getByBoundingBox(yMax=pt1[1] + .1, yMin=pt1[1] - .1)
myPart2.Surface(side1Faces=f, name='Tray_Tibiabottom')

createSurface(myPart3, [axisPoint[0] - 5, axisPoint[1], axisPoint[2]],
            'Tibia_TrayIntUpper')  # axisPoint is on the AP cut
# Tibia surfaces

# create surfaces for boundary conditions
createSurface(myPart1, [100, 0, 900], 'BaseTib')  # bottom face (base) of the tibia

f = myPart1.faces.getClosest(((XYZ[0] + 4, XYZ[1] - 10, XYZ[2] + 5),), )[0][0]
# lateral wall of the cut
# create surface where tibia keel slot has been cut
facesToIgnore = [myPart3.surfaces[s].faces[0] for s in myPart3.surfaces.keys()]
# this is the horizontal cut face
part3faces = [f for f in myPart3.faces if f not in facesToIgnore]
# this excludes the horizontal cut face
part1faces = myPart1.faces  # myPart1 is 'Tibia'
f1 = [part1faces.findAt(f.pointOn)[0] for f in part3faces]
  this excludes the horizontal cut face
# this goes through every face in myPart3-'TibiaTmp2'. part1faces.findAt(f.pointOn)[0]
gives all the corresponding faces in Tibia, which also excludes the horizontal cut face


indx = [part1faces.index(f) for f in f1]
indx2 = [i for i in range(len(myPart1.faces)) if i not in indx]
```

```
# this includes all the faces in the keel slot and the horizontal cut surface
f = [myPart1.faces[i] for i in indx2]
for n in indx2:
   createSurface(myPart1, part1faces[n].pointOn[0], 'tmp' + repr(n))
# the repr() function returns a printable representation of the given object-this creates
each face as a surface

keelSurfaces = [myPart1.surfaces[s] for s in myPart1.surfaces.keys() if 'tmp' in s]
# myPart1.surfaces.keys() prints the list of names of all the surfaces
myPart1.SurfaceByBoolean(name='Tibia_TrayInt', surfaces=keelSurfaces)
for s in myPart1.surfaces.keys():
   if 'tmp' in s:
      del myPart1.surfaces[s]  # deletes all the temporary surfaces
# create contact surfaces

createSurface(myPart1, [axisPoint[0], axisPoint[1], axisPoint[2] + 2], 'Tibia_WallInt')
createSurface(myPart1, [axisPoint[0] - 5, axisPoint[1], axisPoint[2]],
'Tibia_TrayIntUpper')

myPart1.SurfaceByBoolean(name='KeelCut',
surfaces=(myPart1.surfaces['Tibia_TrayInt'],  # horizontal face and slot
                                    myPart1.surfaces['Tibia_TrayIntUpper']),  # horizontal
face
                  operation=DIFFERENCE)
# this selects only the faces inside the keel slot
del myPart1.surfaces['Tibia_TrayInt']
myPart1.SurfaceByBoolean(name='Tibia_TrayInt',
surfaces=(myPart1.surfaces['KeelCut'],
                                       myPart1.surfaces['Tibia_TrayIntUpper']))

del myModel.parts['TibiaTmp']

### Material creation
BoneMaterial = myModel.Material(name='Bone')
```

```
myModel.materials['Bone'].Density(table=((320.0E-12,),))
myModel.materials['Bone'].Elastic(table=((250.0, 0.3),))


### Assemble Components
# ------------------------------------------------------------------------
# instance components
myInstance1 = myAssembly.Instance(name='Tibia-1', part=myPart1, dependent=ON)
myInstance2 = myAssembly.Instance(name='Tray-1', part=myPart2, dependent=ON)
# define datum planes for keel positioning
# p1, a1, a2 and p2 are the same as the ones defined above. Need to redefine datum
planes first
myPart1.DatumPlaneByThreePoints(point1=horizontal_cutPlanept1,
                        point2=horizontal_cutPlanept2,
                        point3=horizontal_cutPlanept3)
# myPart1.datums.keys()[0]

myPart1.DatumAxisByTwoPoint(point1=AP_cutAxispt1, point2=AP_cutAxispt2)
# myPart1.datums.keys()[1]

myPart1.DatumPlaneByRotation(plane=myPart1.datums[myPart1.datums.keys()[0]],
                    axis=myPart1.datums[myPart1.datums.keys()[1]], angle=90)
# myPart1.datums.keys()[2]

p1 = myPart1.DatumPlaneByOffset(plane=myPart1.datums[myPart1.datums.keys()[2]],
point=TibCentroid)
# myPart1.datums[myPart1.datums.keys()[2]] is the vertical cut plane

a1 = myPart1.DatumAxisByNormalToPlane(plane=myPart1.datums[p1.id],
                            point=TibCentroid)
# this creates an axis normal to p1 while passing centroid
a2 =
myPart1.DatumAxisByNormalToPlane(plane=myPart1.datums[myPart1.datums.keys()[0
]], point=TibCentroid)
```

```
# an axis normal to horizontal cut while passing centroid

p2 = myPart1.DatumPlaneByRotation(plane=myPart1.datums[p1.id],
axis=myPart1.datums[a2.id], angle=90)
# this forms a datum plane that is perpendicular to p1. it is also perpendicular to the
vertical cut

# the keel of the tray is along the z-axis. z-value of front of keel = -19.68; z value of back
of keel = 13.86. Therefore, the middle of the keel is at z = (-19.68 + 13.86) / 2 = -2.91
p3 = myPart2.DatumPlaneByPrincipalPlane(principalPlane=XYPLANE, offset=-2.91)  #
halfway across the keel length

# position tray
myAssembly.FaceToFace(movablePlane=myAssembly.allSurfaces['Tray-
1.Tray_Tibiabottom'].faces[0],  # tibia tray bottom
                fixedPlane=myInstance1.datums[myPart1.datums.keys()[0]],  # tibia hori
cut face
                flip=ON, clearance=0)  # depth of keel = 9.65
myAssembly.FaceToFace(movablePlane=myAssembly.allSurfaces['Tray-
1.Tray_WallInt'].faces[0],  # tray lateral wall
                fixedPlane=myAssembly.allSurfaces['Tibia-1.Tibia_WallInt'].faces[0],  #
tibia vertical cut face
                flip=ON, clearance=0)
myAssembly.FaceToFace(movablePlane=myInstance2.datums[myInstance2.datums.keys
()[-1]],  # coronal plane of the tray-p3
                fixedPlane=myInstance1.datums[myInstance1.datums.keys()[-1]],
# coronal plane of the tibia-p2
                flip=OFF, clearance=1)
# change the clearance to move the component in the AP direction.
# 1 moves the tibial component back by 1
# myAssembly.instances['Tray-1'].translate(vector=(0, 2, 0))  # this fails
# record positioning parameters
```

```
# create a new coordinate system in the assembly's coordinate
AsCoord = myAssembly.DatumCsysByTwoLines(coordSysType=CARTESIAN,
                                line1=myInstance1.datums[a1.id],
                                line2=myInstance1.datums[myPart1.datums.keys()[1]],
                                name='Assembly coordinate')
# x = medial; y = posterior; z = proximal

# create a partition surface for load patch
a3 = myPart2.DatumAxisByPrincipalAxis(principalAxis=ZAXIS)

mySketch1 = myModel.ConstrainedSketch(name='LoadPatch', sheetSize=200.0,
                               transform=myPart2.MakeSketchTransform(
                                  sketchPlane=myPart2.allSurfaces['Tray_BearingInt'].faces[0],
                                  sketchUpEdge=myPart2.datums[a3.id],
                                  origin=(-14.12, 2.95, -3.48)))  # top face

mySketch1.CircleByCenterPerimeter(center=(13, -8), point1=(13, -3))
# positive x-direction is pointing from medial to lateral
# positive y-direction is pointing from posterior to anterior
myPart2.PartitionFaceBySketch(faces=myPart2.allSurfaces['Tray_BearingInt'].faces[0],
sketch=mySketch1)
createSurface(myPart2, [-1.12, 2.95, 4.52], 'LoadPatch')
# Area_LoadPatch = pi * 5 ^ 2

### Make tibial tray rigid
# ----------------------------------------------------------------------------
myPart2.RemoveCells(cellList=myPart2.cells)  # turned into a shell
myPart2.setValues(space=THREE_D, type=DISCRETE_RIGID_SURFACE)
myPart2.ReferencePoint(point=(-1.12, 2.95, 4.52))
trayRef = myPart2.referencePoints[myPart2.referencePoints.keys()[0]]
# myPart2.engineeringFeatures.PointMassInertia(name='TrayMass',
#                                 region=(trayRef,),
#                                 mass=trayMass)
```

```
# partition the tibia before meshing and create cells for analysis; myPart1 is 'Tibia'
myPart2 is 'Tray'

# first partition the tibia into top and bottom two parts
myPart1.DatumPlaneByOffset(plane=myPart1.datums[myPart1.datums.keys()[0]],
flip=SIDE2, offset=25)
# 25 mm distal to the horizontal plane
myPart1.PartitionCellByDatumPlane(cells=myPart1.cells,
datumPlane=myPart1.datums[myPart1.datums.keys()[-1]])
topcell = myPart1.cells.findAt((AP_cutAxispt1[0], AP_cutAxispt1[1],
AP_cutAxispt1[2]))

# then partition the top part next to the wall
myPart1.DatumPlaneByOffset(plane=myPart1.datums[myPart1.datums.keys()[2]],
flip=SIDE1, offset=0)
# 0.3 mm medial to the wall
myPart1.PartitionCellByDatumPlane(cells=topcell,
datumPlane=myPart1.datums[myPart1.datums.keys()[-1]])
underCut = myPart1.cells.findAt((TibCentroid[0], TibCentroid[1], TibCentroid[2]))

# then partition the part under the tibial component into anterior and posterior parts
myPart1.PartitionCellByDatumPlane(cells=underCut,
datumPlane=myPart1.datums[p2.id])

# then partition the part under the tibial component right next to the keel slot
myPart1.DatumPlaneByOffset(plane=myPart1.datums[p1.id], flip=SIDE1, offset=-2)  # 2
mm medial to the tibcentroid plane
nearCortex_Anterior = myPart1.cells.findAt((TibCentroid[0], TibCentroid[1] - 5,
TibCentroid[2]))
myPart1.PartitionCellByDatumPlane(cells=nearCortex_Anterior,
datumPlane=myPart1.datums[myPart1.datums.keys()[-1]])
nearCortex_Posterior = myPart1.cells.findAt((TibCentroid[0], TibCentroid[1] + 5,
TibCentroid[2] - 5))
```

```
myPart1.PartitionCellByDatumPlane(cells=nearCortex_Posterior,
datumPlane=myPart1.datums[myPart1.datums.keys()[-1]])



### Use virtual topography and geometry edit to ensure no small faces prior to meshing
# ----------------------------------------------------------------------------
# remove small faces
myPart1.createVirtualTopology(applyBlendControls=True, blendRadiusTolerance=1.3,
                    blendSubtendedAngleTolerance=60.0, cornerAngleTolerance=30.0,
                    faceAspectRatioThreshold=5.0, ignoreRedundantEntities=True,
                    mergeShortEdges=True, mergeSliverFaces=True,
mergeSmallAngleFaces=True,
                    mergeSmallFaces=True, mergeThinStairFaces=True,
shortEdgeThreshold=2.4,
                    smallFaceAreaThreshold=5, smallFaceCornerAngleThreshold=10.0,
                    thinStairFaceThreshold=0.05)

myPart1.createVirtualTopology(applyBlendControls=True, blendRadiusTolerance=1.3,
                    blendSubtendedAngleTolerance=60.0, cornerAngleTolerance=30.0,
                    faceAspectRatioThreshold=5.0, ignoreRedundantEntities=True,
                    mergeShortEdges=True, mergeSliverFaces=True,
mergeSmallAngleFaces=True,
                    mergeSmallFaces=True, mergeThinStairFaces=True,
shortEdgeThreshold=2.4,
                    smallFaceAreaThreshold=5, smallFaceCornerAngleThreshold=10.0,
                    thinStairFaceThreshold=0.05)

myPart1.checkGeometry()
# convert to an analytical part
myPart1.ConvertToAnalytical()  # When you convert a part to its analytical
representation,
# ABAQUS/CAE tries to change the internal definition of edges, faces, and cells into a
simpler form that can be
```

```
# represented analytically

### Mesh parts
# ----------------------------------------------------------------------------
# mesh tibia
# assign mesh controls
elemType = mesh.ElemType(elemCode=C3D10M, elemLibrary=STANDARD)  # 10-node quad tetrahedral element
# C3D10M should be used if there is contact. Otherwise, the model won't run
myPart1.setMeshControls(regions=myPart1.cells, elemShape=TET, technique=FREE, allowMapped=False)
myPart1.setElementType(regions=(myPart1.cells,), elemTypes=(elemType,))


def meshEdge(surfaceName, part, meshSize):  # a function called meshEdge with 3 inputs
    e = [f.getEdges() for f in part.surfaces[surfaceName].faces]
    e = [item for sublist in e for item in sublist]  # this lists out all the components in e, which are all the edges
    mesh = [part.seedEdgeBySize(edges=(part.edges[n],), size=meshSize) for n in e]
    # create fine mesh seed


meshEdge('KeelCut', myPart1, fineMeshSize)

myPart1.seedPart(size=totalMeshSize)  # myPart1 = tibia. This creates a global mesh
# create mesh
myPart1.generateMesh()
# mesh tray
# assign mesh controls
elemType2 = mesh.ElemType(elemCode=R3D4, elemLibrary=STANDARD)  # rigid element, 3d, 4 nodes
myPart2.setMeshControls(regions=myPart2.faces, elemShape=QUAD, technique=FREE)
myPart2.setElementType(regions=(myPart2.faces,), elemTypes=(elemType2,))
```

```
# create Fine mesh seed
meshEdge('Tray_BearingInt', myPart2, 2.4)
meshEdge('Tray_TibiaInt', myPart2, 0.8)
# seed parts with coarse seeds
myPart2.seedPart(size=totalMeshSize)
# create mesh
myPart2.generateMesh()

# face set for base tib for fixation
myPart1.Set(faces=myPart1.surfaces['BaseTib'].faces, name='BaseTib')
myPart2.Set(faces=myPart2.surfaces['Tray_BearingInt'].faces, name='TrayTop')
myPart1.Set(faces=myPart1.surfaces['Tibia_TrayIntUpper'].faces, name='TibiaCutTop')
myPart1.Set(faces=myPart1.surfaces['Tibia_WallInt'].faces, name='WallSet')
myPart2.Set(nodes=myPart2.surfaces['LoadPatch'].nodes, name='LoadPatch')

ROI3 = myPart1.cells.findAt((AP_cutAxispt1[0], AP_cutAxispt1[1], AP_cutAxispt1[2]))
ROI2 = myPart1.cells.findAt((AP_cutAxispt2[0] - 3, AP_cutAxispt2[1] - 5,
AP_cutAxispt2[2]))
ROI1 = myPart1.cells.findAt((AP_cutAxispt1[0] + 5, AP_cutAxispt1[1] + 10,
AP_cutAxispt1[2]))
ROI4 = myPart1.cells.findAt((TibCentroid[0] - 5, TibCentroid[1] + 5, TibCentroid[2]))
ROI5 = myPart1.cells.findAt((TibCentroid[0] - 5, TibCentroid[1] - 5, TibCentroid[2]))

myPart1.Set(elements=myPart1.cells[ROI1.index].getElements(), name='ROI1')
myPart1.Set(elements=myPart1.cells[ROI2.index].getElements(), name='ROI2')
myPart1.Set(elements=myPart1.cells[ROI3.index].getElements(), name='ROI3')
myPart1.Set(elements=myPart1.cells[ROI4.index].getElements(), name='ROI4')
myPart1.Set(elements=myPart1.cells[ROI5.index].getElements(), name='ROI5')


### Section creation and assignment
myModel.HomogeneousSolidSection(material='Bone', name='TibiaSection',
thickness=None)
myPart1.Set(cells=myPart1.cells, name='WholeTibia')
```

```
myPart1.SectionAssignment(offset=0.0, offsetField='', offsetType=MIDDLE_SURFACE,
region=myPart1.sets['WholeTibia'],
                    sectionName='TibiaSection', thicknessAssignment=FROM_SECTION)
# ---------------------------------------------------------------------------

# medial
myAssembly.regenerate()
loadSurfNodeCoords = [n.coordinates for n in
myInstance2.surfaces['Tray_BearingInt'].nodes]

# # ---------------------------------------------------------------------------

# -------------------------DEFINE BOUNDARY CONDITIONS--------------------------
# ---------------------------------------------------------------------------
### Define fixation
# ---------------------------------------------------------------------------
myModel.EncastreBC(createStepName='Initial',
                name='BaseFix',
                region=myInstance1.sets['BaseTib'])
TrayRP = myAssembly.Set(name='RP',
referencePoints=(myInstance2.referencePoints[11],))
myAssembly.Set(faces=myInstance2.faces, name='WholeTray')
myModel.RigidBody(bodyRegion=myAssembly.sets['WholeTray'], name='TraytoRP',
refPointRegion=myAssembly.sets['RP'])
myModel.DisplacementBC(amplitude=UNSET, createStepName='Initial',
distributionType=UNIFORM, fieldName='',
                localCsys=myAssembly.datums[myAssembly.datums.keys()[0]],
name='TrayNoRotation',
                region=TrayRP, u1=SET, u2=SET, u3=SET, ur1=SET, ur2=SET,
ur3=SET, )

### Create steps
# ---------------------------------------------------------------------------
```

```
myModel.StaticStep(name='InterferenceFitStep',
                previous='Initial',
                description='Apply interference fit',
                nlgeom=ON,
                initialInc=0.1,
                maxNumInc=1000)

myModel.StaticStep(name='LoadingStep',
                previous='InterferenceFitStep',
                description='Vertical load is applied in this step',
                nlgeom=ON,
                initialInc=0.01,
                maxNumInc=1000)

myModel.boundaryConditions['TrayNoRotation'].deactivate(stepName='LoadingStep')

### Define interactions
# ----------------------------------------------------------------------------
myModel.ContactProperty('Frictionless')
myModel.interactionProperties['Frictionless'].TangentialBehavior(formulation=FRICTIO
NLESS)
myModel.interactionProperties['Frictionless'].NormalBehavior(
   allowSeparation=ON, constraintEnforcementMethod=DEFAULT,
   pressureOverclosure=HARD)

myModel.ContactProperty('Friction')
myModel.interactionProperties['Friction'].TangentialBehavior(
   absoluteDistance=0.2, dependencies=0, directionality=ISOTROPIC,
   elasticSlipStiffness=None, formulation=PENALTY, maximumElasticSlip=
   ABSOLUTE_DISTANCE, pressureDependency=OFF, shearStressLimit=None,
   slipRateDependency=OFF, table=((0.99,),), temperatureDependency=OFF)
myModel.interactionProperties['Friction'].NormalBehavior(
   allowSeparation=ON, constraintEnforcementMethod=DEFAULT,
   pressureOverclosure=HARD)
```

```
myModel.SurfaceToSurfaceContactStd(name='TrayBottomContact',
                        createStepName='Initial',
                        interactionProperty='Frictionless',
                        master=myInstance2.surfaces['Tray_Tibiabottom'],
                        slave=myInstance1.surfaces['Tibia_TrayIntUpper'],
                        sliding=FINITE)  # implicit surface to surface contact

myModel.interactions['TrayBottomContact'].setValuesInStep(stepName='LoadingStep',
interactionProperty='Friction')

myModel.SurfaceToSurfaceContactStd(name='KeelContact',
                        createStepName='Initial',
                        interactionProperty='Frictionless',
                        enforcement=NODE_TO_SURFACE,
                        master=myInstance2.surfaces['Tray_TibiaInt'],
                        slave=myInstance1.surfaces['KeelCut'],
                        sliding=FINITE)  # implicit surface to surface contact

myModel.interactions['KeelContact'].setValuesInStep(interferenceType=SHRINK_FIT,
stepName='InterferenceFitStep')
myModel.interactions['KeelContact'].setValuesInStep(stepName='LoadingStep',
interactionProperty='Friction')

myModel.SurfaceToSurfaceContactStd(name='WallContact',
                        createStepName='Initial',
                        interactionProperty='Frictionless',
                        master=myInstance2.surfaces['Tray_WallInt'],
                        slave=myInstance1.surfaces['Tibia_WallInt'],
                        sliding=FINITE)  # implicit surface to surface contact

# ----------------------------------------------------------------------

### Create field output requests
```

```
if 'F-Output-1' in myModel.fieldOutputRequests.keys():
   del myModel.fieldOutputRequests['F-Output-1']

myModel.FieldOutputRequest(name='F-Output-General',
createStepName='InterferenceFitStep',
                    variables=['S', 'E', 'NE', 'LE', 'U', 'RT', 'CSTRESS', 'CFORCE',
'CSTATUS'], numIntervals=20)

### Define loads
# ----------------------------------------------------------------------------

# code below to apply load

# apply load to load patch #
myModel.Pressure(name='VerticalLoad', createStepName='LoadingStep',
             region=myAssembly.allSurfaces['Tray-1.LoadPatch'], magnitude=1000.0,
             distributionType=TOTAL_FORCE)  # load of 1000N perpendicular to the
surface

## Export input file for bone material assignment
# ----------------------------------------------------------------------------
# myJob = mdb.Job(name=modelName, model=modelName, description='')
myJob = mdb.Job(activateLoadBalancing=False, atTime=None, contactPrint=OFF,
             description='', echoPrint=OFF,
             historyPrint=OFF, memory=90, memoryUnits=PERCENTAGE,
model=modelName,
             modelPrint=OFF, multiprocessingMode=DEFAULT, name=modelName,
             nodalOutputPrecision=FULL, numCpus=3, numDomains=3,
             queue=None, resultsFormat=ODB,
             scratch='', type=ANALYSIS, userSubroutine='', waitHours=0, waitMinutes=0)
# myJob.writeInput()
```

Appendix B: Python Script for Generating Models of Patient 1 Left Tibia with Modified Vertical and Horizontal Cuts

The following script is the Python code used to generate the model in which the fractured cuts in Patient 1 were replicated in the unfractured tibia. This Python script was also adapted in Chapter 5 to make models with the tibial component placed at various mediolateral positions, proximal-distal positions, varus-valgus orientations and internal-external directions by changing how far the horizontal and vertical cut planes move from their original positions.

Python scripts used to generate model of Patient 2 with modified cuts has the same structure with different inputs of points' coordinates used to define datum point/axis/plane positions. Therefore, those scripts are not included here.

```
# -*- coding: utf-8 -*-with
"""

@author: sholtof
"""

# !/usr/bin/python
# -*- coding: utf-8 -*-
# ----------------------------------------------------------------------------
# File:  Case_2_LeftLeg_FracturedCutinLeftLeg_SizeC_Static.py
# Date:  2023
# Created by: Elise Pegg, University of Oxford
# Edited by: Xiaoyi Min, University of Oxford
# Purpose: move the cuts in the left tibia of Patient 1 into the same relative position as the cuts in the right (fractured) tibia
```

```
# Comments:
#         - Model assumes vertical cut it always parallel with the mechanical axis
#         - in the unit of mm
# Version: 1
# ----------------------------INITIALISING PROGRAM-----------------------------
# -----------------------------------------------------------------------------
### Import Modules
# -----------------------------------------------------------------------------
from abaqus import *
from abaqusConstants import *
from math import *
import mesh
import regionToolset
import os
from numpy import diff, matrix, array, tan, sin, mean, arange, arctan

varusAngle = -1.73  # this defines the varus valgus orientation of the component relative
to its original position

# -----------------------------------------------------------------------------
modelName = 'Case_2_LeftLeg_FracturedCutinLeftLeg_SizeC'
# -----------------------------------------------------------------------------
### Define parameters
# -----------------------------------------------------------------------------
# filenames
os.chdir('C:\Xiaoyi_DPhil\Abaqus\Python\Create_Interference_Models\Case2LeftLeg')
# The OS module in Python provides functions for interacting with the operating system


# os.getcwd(): get current working directory
tibCAD = os.getcwd().split('.')[0] +
'/JapaneseTibiaCase2LeftNoFracture/CASE2_LEFT_Wrapped_Smoothed_shorter.SAT'
# adds tibia geometry
```

```
trayCAD = os.getcwd().split('.')[0] +
'/JapaneseTibiaCase2LeftNoFracture/SimpleTibialComponentLeftMedial_SizeC.sat'
# tray geometry
keelCAD = os.getcwd().split('.')[0] + \

'/JapaneseTibiaCase2LeftNoFracture/SimpleTibialComponentLeftMedial_SizeC_KeelforSlot_0_20mmInterference.sat'

# model parameters
angleBetweenCuts = 90  # between horizontal and vertical cuts
totalMeshSize = 2.4
fineMeshSize = totalMeshSize / 6
interference = 0.20
KeelWallDistance = 6.7
keelOffset = 6.7 + interference / 2  # distance from lateral face of the keel to the lateral face of the wall
# tibial tray points to define axis for corner and plane of tray base # local to tray
pt1 = (-15.67 - interference / 2, 0, -28.28)
pt2 = (-15.67 - interference / 2, 0, 21.32)
# pt1 and pt2 are on the lateral-most bottom edge of the tray
pt3 = (-26.01, 0, 5.32)
# pt3 is on the bottom face of the tray

fieldOutputRequests = ['S', 'PE', 'NE', 'U', 'RT']
historyOutputRequests = ('ALLAE', 'ALLCD', 'ALLDMD', 'ALLFD', 'ALLIE', 'ALLKE', 'ALLPD', 'ALLSE', 'ALLVD', 'ALLWK', 'ETOTAL', 'DT', 'DMASS')
# ----------------------------CREATING GEOMETRY--------------------------------
# -----------------------------------------------------------------------------
### Create model
# -----------------------------------------------------------------------------
# create new model
myModel = mdb.Model(name=modelName)
# remove redundant models if exist
if 'Model-1' in mdb.models.keys():
```

```
    del mdb.models['Model-1']
# -------------------------------------------------------------------------

### Load geometry components (Tibia, Tray and KeelCuttingBlock)
# -------------------------------------------------------------------------
mdb.openAcis(fileName=tibCAD)
myModel.PartFromGeometryFile(combine=False, dimensionality=
THREE_D, geometryFile=mdb.acis, name='TibiaTmp', scale=1.0, type=
                        DEFORMABLE_BODY)
myPart2 = myModel.parts['TibiaTmp']
mdb.openAcis(fileName=trayCAD)
myModel.PartFromGeometryFile(combine=False, dimensionality=
THREE_D, geometryFile=mdb.acis, name='Tray', scale=1.0, type=
                        DEFORMABLE_BODY)

mdb.openAcis(fileName=keelCAD)
myModel.PartFromGeometryFile(combine=False, dimensionality=
THREE_D, geometryFile=mdb.acis, name='Keel', scale=1.0, type=
                        DEFORMABLE_BODY)

# -------------------------------------------------------------------------
# create assembly
myAssembly = myModel.rootAssembly
myInstance1 = myAssembly.Instance(name='Tibia-0', part=myPart2, dependent=OFF)
myPart1 = myModel.parts['TibiaTmp']  # this reassigns the new tibia as the new myPart1,
which is a solid

horizontal_cutPlanept1 = (88.3025, -17.62943, 975.67308)
horizontal_cutPlanept2 = (81.93936, 31.7332, 975.05373)
horizontal_cutPlanept3 = (56.56268, 7.11242, 976.13084)
myPart1.DatumPlaneByThreePoints(point1=horizontal_cutPlanept1,
                            point2=horizontal_cutPlanept2,
                            point3=horizontal_cutPlanept3)
# myPart1.datums.keys()[0] Original hori plane
```

```
AP_cutAxisMidPt = ((horizontal_cutPlanept1[0] + horizontal_cutPlanept2[0]) / 2,
                   (horizontal_cutPlanept1[1] + horizontal_cutPlanept2[1]) / 2,
                   (horizontal_cutPlanept1[2] + horizontal_cutPlanept2[2]) / 2)
# midpoint of the original AP cut

AP_cutAxispt1 = (88.3025, -17.62943, 975.67308)
AP_cutAxispt2 = (81.93936, 31.7332, 975.05373)

myPart1.DatumAxisByTwoPoint(point1=AP_cutAxispt1, point2=AP_cutAxispt2)
# myPart1.datums.keys()[1] - original AP cut

myPart1.DatumPlaneByRotation(plane=myPart1.datums[myPart1.datums.keys()[0]],
                             axis=myPart1.datums[myPart1.datums.keys()[1]], angle=90)
# myPart1.datums.keys()[2] - original vertical plane

myPart1.DatumAxisByNormalToPlane(plane=myPart1.datums[myPart1.datums.keys()[0
]], point=AP_cutAxisMidPt)
# myPart1.datums.keys()[3] - axis of rotation for the vertical cut

myPart1.DatumPlaneByRotation(plane=myPart1.datums[myPart1.datums.keys()[2]],
                             axis=myPart1.datums[myPart1.datums.keys()[3]], angle=18.83)
# myPart1.datums.keys()[4] - new plane of vertical cut after internal rotation (for the
surgeon) of 18.83 degrees

myPart1.DatumPlaneByOffset(plane=myPart1.datums[myPart1.datums.keys()[4]],
flip=SIDE1, offset=-2)
# myPart1.datums.keys()[5] - moved vertical cut medially by 2mm

myPart1.DatumPlaneByOffset(plane=myPart1.datums[myPart1.datums.keys()[0]],
offset=-2.44)
# myPart1.datums.keys()[6] -# new hori plane

RotAxis_pt1 = (73.357374,12.167159,973.156803)
```

```
RotAxis_pt2 = (80.651379,-2.677617,973.198291)
# the line connecting these 2 points is the lateral edge of the
# keel slot when the tibial component is placed at the neutral position. The components in varus and valgus will rotate around this axis

myPart1.DatumAxisByTwoPoint(point1=RotAxis_pt1, point2=RotAxis_pt2)
# myPart1.datums.keys()[7]

myPart1.DatumPlaneByRotation(plane=myPart1.datums[myPart1.datums.keys()[6]],
                    axis=myPart1.datums[myPart1.datums.keys()[7]],
                    angle=varusAngle)
# myPart1.datums.keys()[8]  # this is the final horizontal cut plane after varus angle is added. This plane is rotated about the lateral edge of the original neutral keel slot.

myPart1.DatumPlaneByRotation(plane=myPart1.datums[myPart1.datums.keys()[8]],
                    axis=myPart1.datums[myPart1.datums.keys()[7]], angle=90)
# myPart1.datums.keys()[9], a plane vertical to the horizontal cut and passes through the medial edge of the keel slot

myPart1.DatumPlaneByOffset(plane=myPart1.datums[myPart1.datums.keys()[9]],
flip=SIDE2, offset=KeelWallDistance)
# myPart1.datums.keys()[10] - final vertical cut plane
myPart1.DatumAxisByTwoPlane(plane1=myPart1.datums[myPart1.datums.keys()[8]],
# horizontal cut plane
                    plane2=myPart1.datums[myPart1.datums.keys()[10]])
# vertical cut plane
# myPart1.datums.keys()[11] - new AP axis

# ----------------------------------------------------------------------------
### Create surgical cuts
# ----------------------------------------------------------------------------
# create sketch for cutting block
# myPart1.datums.keys()[5] is a datumAxis
axisPoint = myPart1.datums[myPart1.datums.keys()[11]].pointOn
```

```
# A tuple of Floats specifying the X-, Y-, and Z-coordinates of a point located on the
datum - for this one, this is a point on the AP cut axis
axisDirection = myPart1.datums[myPart1.datums.keys()[11]].direction  # A tuple of
Floats specifying a sequence of
# three Floats specifying the direction of the axis -  AP cut axis.
mySketch2 = myModel.ConstrainedSketch(name='CuttingBlock', sheetSize=200.0,
                                transform=myPart1.MakeSketchTransform(
                                   sketchPlane=myPart1.datums[myPart1.datums.keys()[8]],
# posterior slope
                                   sketchPlaneSide=SIDE2,
                                   sketchUpEdge=myPart1.datums[myPart1.datums.keys()[11]],
                                   sketchOrientation=RIGHT, origin=axisPoint))
mySketch2.rectangle(point1=(0, -500), point2=(100, 500))
mySketch2.ConstructionLine(point1=(0, 100), point2=(0, -100))
# cut tibia using block
myPart1.CutRevolve(sketch=mySketch2, sketchOrientation=LEFT, angle=90,
flipRevolveDirection=OFF,
                sketchPlane=myPart1.datums[myPart1.datums.keys()[8]],
sketchPlaneSide=SIDE2,
                sketchUpEdge=myPart1.datums[myPart1.datums.keys()[11]])
# angle: angle to be revolved
# ----------------------------------------------------------------------------

### Analyse keel cutting block part to get parameters
# ----------------------------------------------------------------------------
# Create datum axis and plane on keel part
myPart3 = myModel.parts['Keel']
myPart3.DatumAxisByTwoPoint(point1=pt1, point2=pt2)
# myPart3.datums.keys()[0] - AP axis of the lateral side of the
# lateral wall
myPart3.DatumPlaneByThreePoints(point1=pt1, point2=pt2, point3=pt3)
# myPart3.datums.keys()[1] - bottom face of the
# tibial component/top of keel
myPart3.DatumPlaneByPrincipalPlane(principalPlane=XYPLANE, offset=0)
```

```
# myPart3.datums.keys()[2] - the offset of -x moves the keel slot forward by x mm in the direction of the keel slot; -ve means anterior


### Create assembly with keel cutting block to create keel slot
# ----------------------------------------------------------------------------
# load in tibia and keel cutting block
myInstance1 = myAssembly.Instance(name='Tibia-0', part=myPart1, dependent=OFF)
myInstance3 = myAssembly.Instance(name='Keel-0', part=myPart3, dependent=OFF)
# find the centre of the medial plateau for positioning the keel
XYZ = [85, -18, 976]
# XYZ  = [3mm medial to the vertical cut, the anterior edge of the plateau in the AP direction,
# the anterior edge of the plateau in the vertical direction]

f = myInstance1.faces.getClosest(((XYZ[0], XYZ[1], XYZ[2]),), )[0][0]  # this selects the horizontal cut surface
TibCentroid = f.getCentroid()[0]  # this picks the centroid of the horizontal cut face

f = myInstance1.faces.getClosest(((XYZ[0], XYZ[1], XYZ[2] + 10),), )[0][0]  # this selects the vertical cut surface

p1 = myPart1.DatumPlaneByOffset(plane=myPart1.datums[myPart1.datums.keys()[10]], point=TibCentroid) #myPart1.datums.keys()[12]
# myPart1.datums[myPart1.datums.keys()[10]] is the vertical cut plane


a1 = myPart1.DatumAxisByNormalToPlane(plane=myPart1.datums[p1.id],
                                      point=TibCentroid)  # this creates an axis normal to p1 while passing centroid
# myPart1.datums.keys()[13]
a2 =
myPart1.DatumAxisByNormalToPlane(plane=myPart1.datums[myPart1.datums.keys()[8
]],
```

```
                    point=TibCentroid)  # an axis normal to horizontal cut while
passing centroid
# myPart1.datums.keys()[14]
p2 = myPart1.DatumPlaneByRotation(plane=myPart1.datums[p1.id],
axis=myPart1.datums[a2.id], angle=90)
# this forms a datum plane that is perpendicular to p1. it is also perpendicular to the
vertical cut
# position keel cutting block
myAssembly.EdgeToEdge(fixedAxis=myInstance1.datums[myPart1.datums.keys()[11]],
# horizontal cut axis
        movableAxis=myInstance3.datums[myPart3.datums.keys()[0]],
# lateral wall ap axis
        flip=OFF)
myAssembly.FaceToFace(clearance=0.0,
fixedPlane=myInstance1.datums[myPart1.datums.keys()[8]],
        # horizontal cut plane
        flip=ON, movablePlane=myInstance3.datums[myPart3.datums.keys()[1]])
# bottom of the tray
myAssembly.FaceToFace(movablePlane=myInstance3.datums[myInstance3.datums.keys
()[-1]],
        # vertical to the horizontal cut
        fixedPlane=myInstance1.datums[myInstance1.datums.keys()[-1]],
        # plane parallel to the XZ plane
        flip=OFF, clearance=1.91)
# this moves the keel slot backward by 3.91mm
# perform boolean operation
myAssembly.InstanceFromBooleanCut(name='Tibia', instanceToBeCut=myInstance1,
            cuttingInstances=(myInstance3,),
            originalInstances=DELETE)
# remove redundant parts
del myModel.parts['Keel']
del myAssembly.instances['Tibia-1']
myPart1 = myModel.parts['Tibia']
myPart2 = myModel.parts['Tray']
```

```
myPart3 = myModel.parts['TibiaTmp']


###------------------------------DEFINING MODEL---------------------------------
###-----------------------------------------------------------------------------
##### Define surfaces on parts
###-----------------------------------------------------------------------------
def createSurface(PART, XYZ, NAME):
    f = PART.faces.getClosest(((XYZ[0], XYZ[1], XYZ[2]),), )[0][0]
    PART.Surface(side1Faces=(PART.faces[f.index:f.index + 1],), name=NAME)



# Tray surfaces
# create contact surfaces
createSurface(myPart2, [-15, 5, 20], 'Tray_WallInt')
createSurface(myPart2, [-10, 3, 0], 'Tray_BearingInt')  # top of the tray
f = myPart2.faces.getByBoundingBox(xMax=-4, xMin=-9)
myPart2.Surface(side1Faces=f, name='Tray_TibiaInt')
f = myPart2.faces.getByBoundingBox(yMax=pt1[1] + .1, yMin=pt1[1] - .1)
myPart2.Surface(side1Faces=f, name='Tray_Tibiabottom')

createSurface(myPart3, [AP_cutAxisMidPt[0] - 5, AP_cutAxisMidPt[1],
AP_cutAxisMidPt[2]-3],
            'Tibia_TrayIntUpper')  # axisPoint is on the AP cut
# Tibia surfaces

# create surfaces for boundary conditions
createSurface(myPart1, [100, 0, 900], 'BaseTib')  # bottom face (base) of the tibia

f = myPart1.faces.getClosest(((XYZ[0] + 4, XYZ[1] - 10, XYZ[2] + 5),), )[0][0]
# lateral wall of the cut
# create surface where tibia keel slot has been cut
facesToIgnore = [myPart3.surfaces[s].faces[0] for s in myPart3.surfaces.keys()]
# this is the horizontal cut face
```

```
part3faces = [f for f in myPart3.faces if f not in facesToIgnore]
# this excludes the horizontal cut face
part1faces = myPart1.faces  # myPart1 is 'Tibia'
f1 = [part1faces.findAt(f.pointOn)[0] for f in part3faces]
# this excludes the horizontal cut face
# this goes through every face in myPart3-'TibiaTmp2'. part1faces.findAt(f.pointOn)[0]
gives all the corresponding
# faces in Tibia, which also excludes the horizontal cut face


indx = [part1faces.index(f) for f in f1]
indx2 = [i for i in range(len(myPart1.faces)) if i not in indx]
# this includes all the faces in the keel slot and
# the horizontal cut surface
f = [myPart1.faces[i] for i in indx2]
for n in indx2:
    createSurface(myPart1, part1faces[n].pointOn[0], 'tmp' + repr(n))
    # the repr() function returns a printable representation of the given object-this creates
each face as a surface

keelSurfaces = [myPart1.surfaces[s] for s in myPart1.surfaces.keys() if 'tmp' in s]
# myPart1.surfaces.keys() prints the list of names of all the surfaces
myPart1.SurfaceByBoolean(name='Tibia_TrayInt', surfaces=keelSurfaces)
for s in myPart1.surfaces.keys():
    if 'tmp' in s:
        del myPart1.surfaces[s]  # deletes all the temporary surfaces
    # create contact surfaces

createSurface(myPart1, [AP_cutAxisMidPt[0] + 5, AP_cutAxisMidPt[1],
AP_cutAxisMidPt[2]], 'Tibia_WallInt')
createSurface(myPart1, [AP_cutAxisMidPt[0] - 10, AP_cutAxisMidPt[1],
AP_cutAxisMidPt[2]], 'Tibia_TrayIntUpper')
```

```
myPart1.SurfaceByBoolean(name='KeelCut',
surfaces=(myPart1.surfaces['Tibia_TrayInt'],  # horizontal face and slot
                                    myPart1.surfaces['Tibia_TrayIntUpper']),  # horizontal
face
                  operation=DIFFERENCE)  # this selects only the faces inside the keel
slot
del myPart1.surfaces['Tibia_TrayInt']
myPart1.SurfaceByBoolean(name='Tibia_TrayInt',
surfaces=(myPart1.surfaces['KeelCut'],
                                        myPart1.surfaces['Tibia_TrayIntUpper']))

del myModel.parts['TibiaTmp']

### Material creation - this is the material properties for element deletion
BoneMaterial = myModel.Material(name='Bone')
myModel.materials['Bone'].Density(table=((320.0E-12,),))
myModel.materials['Bone'].Elastic(table=((250.0, 0.3),))



### Assemble Components
# ----------------------------------------------------------------------------
# instance components
myInstance1 = myAssembly.Instance(name='Tibia-1', part=myPart1, dependent=ON)
myInstance2 = myAssembly.Instance(name='Tray-1', part=myPart2, dependent=ON)
# define datum planes for keel positioning
# p1, a1, a2 and p2 are the same as the ones defined above. Need to redefine datum
planes first
myPart1.DatumPlaneByThreePoints(point1=horizontal_cutPlanept1,
                        point2=horizontal_cutPlanept2,
                        point3=horizontal_cutPlanept3)  # myPart1.datums.keys()[0]

myPart1.DatumAxisByTwoPoint(point1=AP_cutAxispt1, point2=AP_cutAxispt2)
# myPart1.datums.keys()[1]
```

```
myPart1.DatumPlaneByRotation(plane=myPart1.datums[myPart1.datums.keys()[0]],
                    axis=myPart1.datums[myPart1.datums.keys()[1]], angle=90)  #
myPart1.datums.keys()[2]
myPart1.DatumAxisByNormalToPlane(plane=myPart1.datums[myPart1.datums.keys()[0
]], point=AP_cutAxisMidPt)
# myPart1.datums.keys()[3] - axis of rotation for the vertical cut

myPart1.DatumPlaneByRotation(plane=myPart1.datums[myPart1.datums.keys()[2]],
                    axis=myPart1.datums[myPart1.datums.keys()[3]], angle=18.83)
# myPart1.datums.keys()[4] - new plane of vertical cut after internal rotation (for the
surgeon) of 15 degrees

myPart1.DatumPlaneByOffset(plane=myPart1.datums[myPart1.datums.keys()[4]],
flip=SIDE1, offset=-2)
# myPart1.datums.keys()[5] - moved vertical cut medially by 0.74mm

myPart1.DatumPlaneByOffset(plane=myPart1.datums[myPart1.datums.keys()[0]],
offset=-2.44)  # myPart1.datums.keys()[6] - new hori plane

RotAxis_pt1 = (73.357374,12.167159,973.156803)
RotAxis_pt2 = (80.651379,-2.677617,973.198291)
# the line connecting these 2 points is the lateral edge of the
# keel slot when the tibial component is placed at the neutral position. The components in
varus and valgus will
# rotate around this axis

myPart1.DatumAxisByTwoPoint(point1=RotAxis_pt1, point2=RotAxis_pt2)  #
myPart1.datums.keys()[7]

myPart1.DatumPlaneByRotation(plane=myPart1.datums[myPart1.datums.keys()[6]],
                    axis=myPart1.datums[myPart1.datums.keys()[7]],
                    angle=varusAngle)  # myPart1.datums.keys()[8]
# this is the final horizontal cut plane
```

```
# after varus angle is added. This plane is rotated about the medial edge of the original neutral keel slot.

myPart1.DatumPlaneByRotation(plane=myPart1.datums[myPart1.datums.keys()[8]],
                        axis=myPart1.datums[myPart1.datums.keys()[7]], angle=90)  # myPart1.datums.keys()[9]
# a plane vertical to the horizontal cut and passes through the medial edge of the keel slot

myPart1.DatumPlaneByOffset(plane=myPart1.datums[myPart1.datums.keys()[9]], flip=SIDE2, offset=KeelWallDistance)
# myPart1.datums.keys()[10] - final vertical cut plane
myPart1.DatumAxisByTwoPlane(plane1=myPart1.datums[myPart1.datums.keys()[8]], # horizontal cut plane
                        plane2=myPart1.datums[myPart1.datums.keys()[10]])
# vertical cut plane. myPart1.datums.keys()[11] - new AP axis


p1 = myPart1.DatumPlaneByOffset(plane=myPart1.datums[myPart1.datums.keys()[10]], point=TibCentroid)
# myPart1.datums[myPart1.datums.keys()[2]] is the vertical cut plane

a1 = myPart1.DatumAxisByNormalToPlane(plane=myPart1.datums[p1.id],
                                point=TibCentroid)
# this creates an axis normal to p1 while passing centroid
a2 = myPart1.DatumAxisByNormalToPlane(plane=myPart1.datums[myPart1.datums.keys()[8]],
                                point=TibCentroid)
# an axis normal to horizontal cut while passing centroid

p2 = myPart1.DatumPlaneByRotation(plane=myPart1.datums[p1.id], axis=myPart1.datums[a2.id], angle=90)
# this forms a datum plane that is perpendicular to p1. it is also perpendicular to the vertical cut
```

```
# keel of the tray is along the z-axis. z-value of front of keel = -19.68; z value of back of keel = 13.86. Therefore, the middle of the keel is at z = (-19.68 + 13.86) / 2 = -2.91

p3 = myPart2.DatumPlaneByPrincipalPlane(principalPlane=XYPLANE, offset=-2.91)
# halfway across the keel length

# position tray
myAssembly.FaceToFace(movablePlane=myAssembly.allSurfaces['Tray-
1.Tray_Tibiabottom'].faces[0],  # tibia tray bottom
                fixedPlane=myInstance1.datums[myPart1.datums.keys()[8]],
# tibia hori cut face
                flip=ON, clearance=0)  # depth of keel = 9.65
myAssembly.FaceToFace(movablePlane=myAssembly.allSurfaces['Tray-
1.Tray_WallInt'].faces[0],  # tray lateral wall
                fixedPlane=myAssembly.allSurfaces['Tibia-1.Tibia_WallInt'].faces[0],
# tibia vertical cut face
                flip=ON, clearance=0)
myAssembly.FaceToFace(movablePlane=myInstance2.datums[myInstance2.datums.keys
()[-1]],  # coronal plane of the tray-p3
                fixedPlane=myInstance1.datums[myInstance1.datums.keys()[-1]],
# coronal plane of the tibia-p2
                flip=OFF, clearance=-1)
# change the clearance to move the component in the AP direction.
# 1 moves the tibial component back by 1


# create a new coordinate system in the assembly's coordinate
AsCoord = myAssembly.DatumCsysByTwoLines(coordSysType=CARTESIAN,
                        line1=myInstance1.datums[a1.id],
                        line2=myInstance1.datums[myPart1.datums.keys()[11]],
                        name='Assembly coordinate')
# x = medial; y = posterior; z = proximal
```

```
# create a partition surface for load patch
a3 = myPart2.DatumAxisByPrincipalAxis(principalAxis=ZAXIS)

mySketch1 = myModel.ConstrainedSketch(name='LoadPatch', sheetSize=200.0,
                                transform=myPart2.MakeSketchTransform(
                                   sketchPlane=myPart2.allSurfaces['Tray_BearingInt'].faces[0],
                                   sketchUpEdge=myPart2.datums[a3.id],
                                   origin=(-14.12, 2.95, -3.48)))  # top face

mySketch1.CircleByCenterPerimeter(center=(13, -8), point1=(13, -3))
# positive x-direction is pointing from medial to lateral
# positive y-direction is pointing from posterior to anterior
myPart2.PartitionFaceBySketch(faces=myPart2.allSurfaces['Tray_BearingInt'].faces[0],
sketch=mySketch1)
createSurface(myPart2, [-1.12, 2.95, 4.52], 'LoadPatch')
# Area_LoadPatch = pi * 5 ^ 2

### Make tibial tray rigid
# ----------------------------------------------------------------------------
myPart2.RemoveCells(cellList=myPart2.cells)  # turned into a shell
myPart2.setValues(space=THREE_D, type=DISCRETE_RIGID_SURFACE)
myPart2.ReferencePoint(point=(-1.12, 2.95, 4.52))
trayRef = myPart2.referencePoints[myPart2.referencePoints.keys()[0]]



# partition the tibia before meshing and create cells for analysis; myPart1 is 'Tibia'
myPart2 is 'Tray'
# first partition the tibia into top and bottom two parts
myPart1.DatumPlaneByOffset(plane=myPart1.datums[myPart1.datums.keys()[8]],
flip=SIDE2, offset=25)
# 25 mm distal to the horizontal plane
myPart1.PartitionCellByDatumPlane(cells=myPart1.cells,
datumPlane=myPart1.datums[myPart1.datums.keys()[-1]])
```

```
topcell = myPart1.cells.findAt((AP_cutAxispt2[0], AP_cutAxispt2[1], AP_cutAxispt2[2]-
4))

# then partition the top part next to the wall
myPart1.DatumPlaneByOffset(plane=myPart1.datums[myPart1.datums.keys()[10]],
flip=SIDE1, offset=0)
# 0 mm medial to the wall
myPart1.PartitionCellByDatumPlane(cells=topcell,
datumPlane=myPart1.datums[myPart1.datums.keys()[-1]])
underCut = myPart1.cells.findAt((TibCentroid[0]+5, TibCentroid[1], TibCentroid[2]-2))

# then partition the part under the tibial component into anterior and posterior parts
myPart1.PartitionCellByDatumPlane(cells=underCut,
datumPlane=myPart1.datums[p2.id])

# then partition the part under the tibial component right next to the keel slot
myPart1.DatumPlaneByOffset(plane=myPart1.datums[p1.id], flip=SIDE1, offset=-2)
# 2 mm medial to the tibcentroid plane
nearCortex_Anterior = myPart1.cells.findAt((TibCentroid[0], TibCentroid[1]-5,
TibCentroid[2]))
myPart1.PartitionCellByDatumPlane(cells=nearCortex_Anterior,
datumPlane=myPart1.datums[myPart1.datums.keys()[-1]])
nearCortex_Posterior = myPart1.cells.findAt((TibCentroid[0]+5, TibCentroid[1]+5,
TibCentroid[2]-1))
myPart1.PartitionCellByDatumPlane(cells=nearCortex_Posterior,
datumPlane=myPart1.datums[myPart1.datums.keys()[-1]])



### Use virtual topography and geometry edit to ensure no small faces prior to meshing
# ----------------------------------------------------------------------------

# remove small faces
myPart1.createVirtualTopology(applyBlendControls=True, blendRadiusTolerance=1.3,
```

```
                    blendSubtendedAngleTolerance=60.0, cornerAngleTolerance=30.0,
                    faceAspectRatioThreshold=5.0, ignoreRedundantEntities=True,
                    mergeShortEdges=True, mergeSliverFaces=True,
mergeSmallAngleFaces=True,
                    mergeSmallFaces=True, mergeThinStairFaces=True,
shortEdgeThreshold=2.4,
                    smallFaceAreaThreshold=2.4, smallFaceCornerAngleThreshold=10.0,
                    thinStairFaceThreshold=0.05)

myPart1.createVirtualTopology(applyBlendControls=True, blendRadiusTolerance=1.3,
                    blendSubtendedAngleTolerance=60.0, cornerAngleTolerance=30.0,
                    faceAspectRatioThreshold=5.0, ignoreRedundantEntities=True,
                    mergeShortEdges=True, mergeSliverFaces=True,
mergeSmallAngleFaces=True,
                    mergeSmallFaces=True, mergeThinStairFaces=True,
shortEdgeThreshold=2.4,
                    smallFaceAreaThreshold=2.4, smallFaceCornerAngleThreshold=10.0,
                    thinStairFaceThreshold=0.05)


myPart1.checkGeometry()
# convert to analytical part
myPart1.ConvertToAnalytical()  # When you convert a part to its analytical
representation,
# ABAQUS/CAE tries to change the internal definition of edges, faces, and cells into a
simpler form that can be
# represented analytically

### Mesh parts
# ----------------------------------------------------------------------------
# mesh tibia
# assign mesh controls
elemType = mesh.ElemType(elemCode=C3D10M, elemLibrary=STANDARD)  # 10-
node quad tetrahedral element
```

```
# C3D10M should be used if there is contact. Otherwise, the model won't run
myPart1.setMeshControls(regions=myPart1.cells, elemShape=TET, technique=FREE,
allowMapped=False)
myPart1.setElementType(regions=(myPart1.cells,), elemTypes=(elemType,))



def meshEdge(surfaceName, part, meshSize):  # a function called meshEdge with 3
inputs
    e = [f.getEdges() for f in part.surfaces[surfaceName].faces]
    e = [item for sublist in e for item in sublist]  # this lists out all the components in e,
which are all the edges
    mesh = [part.seedEdgeBySize(edges=(part.edges[n],), size=meshSize) for n in e]
    # create fine mesh seed


meshEdge('KeelCut', myPart1, fineMeshSize)

myPart1.seedPart(size=totalMeshSize)  # myPart1 = tibia. This creates a global mesh
# create mesh
myPart1.generateMesh()
# mesh tray
# assign mesh controls
elemType2 = mesh.ElemType(elemCode=R3D4, elemLibrary=STANDARD)  # rigid
element, 3d, 4 nodes
myPart2.setMeshControls(regions=myPart2.faces, elemShape=QUAD, technique=FREE)
myPart2.setElementType(regions=(myPart2.faces,), elemTypes=(elemType2,))
# create Fine mesh seed
meshEdge('Tray_BearingInt', myPart2, 2.4)
meshEdge('Tray_TibiaInt', myPart2, 0.8)
# seed parts with coarse seeds
myPart2.seedPart(size=totalMeshSize)
# create mesh
myPart2.generateMesh()
```

```
# face set for base tib for fixation
myPart1.Set(faces=myPart1.surfaces['BaseTib'].faces, name='BaseTib')
myPart2.Set(faces=myPart2.surfaces['Tray_BearingInt'].faces, name='TrayTop')
myPart1.Set(faces=myPart1.surfaces['Tibia_TrayIntUpper'].faces, name='TibiaCutTop')
myPart1.Set(faces=myPart1.surfaces['Tibia_WallInt'].faces, name='WallSet')
myPart2.Set(nodes=myPart2.surfaces['LoadPatch'].nodes, name='LoadPatch')

ROI1 = myPart1.cells.findAt((AP_cutAxispt2[0] - 3, AP_cutAxispt2[1] - 5,
AP_cutAxispt2[2] - 3))
ROI2 = myPart1.cells.findAt((AP_cutAxispt2[0] - 10, AP_cutAxispt2[1] - 10,
AP_cutAxispt2[2] - 3))
ROI3 = myPart1.cells.findAt((TibCentroid[0], TibCentroid[1] - 5, TibCentroid[2]))
ROI4 = myPart1.cells.findAt((TibCentroid[0] - 5, TibCentroid[1] + 5, TibCentroid[2]))
ROI5 = myPart1.cells.findAt((TibCentroid[0] - 5, TibCentroid[1] - 5, TibCentroid[2]))

myPart1.Set(elements=myPart1.cells[ROI1.index].getElements(), name='ROI1')
myPart1.Set(elements=myPart1.cells[ROI2.index].getElements(), name='ROI2')
myPart1.Set(elements=myPart1.cells[ROI3.index].getElements(), name='ROI3')
myPart1.Set(elements=myPart1.cells[ROI4.index].getElements(), name='ROI4')
myPart1.Set(elements=myPart1.cells[ROI5.index].getElements(), name='ROI5')


### Section creation and assignment
myModel.HomogeneousSolidSection(material='Bone', name='TibiaSection',
thickness=None)
myPart1.Set(cells=myPart1.cells, name='WholeTibia')

myPart1.SectionAssignment(offset=0.0, offsetField='', offsetType=MIDDLE_SURFACE,
region=myPart1.sets['WholeTibia'],
                    sectionName='TibiaSection', thicknessAssignment=FROM_SECTION)
# ------------------------------------------------------------------------

# medial
```

```
myAssembly.regenerate()
loadSurfNodeCoords = [n.coordinates for n in
myInstance2.surfaces['Tray_BearingInt'].nodes]

# # ----------------------------------------------------------------------------

# -------------------------DEFINE BOUNDARY CONDITIONS--------------------------
# ----------------------------------------------------------------------------
### Define fixation
# ----------------------------------------------------------------------------
myModel.EncastreBC(createStepName='Initial',
                   name='BaseFix',
                   region=myInstance1.sets['BaseTib'])
TrayRP = myAssembly.Set(name='RP',
referencePoints=(myInstance2.referencePoints[11],))
myAssembly.Set(faces=myInstance2.faces, name='WholeTray')
myModel.RigidBody(bodyRegion=myAssembly.sets['WholeTray'], name='TraytoRP',
refPointRegion=myAssembly.sets['RP'])
myModel.DisplacementBC(amplitude=UNSET, createStepName='Initial',
distributionType=UNIFORM, fieldName='',
                     localCsys=myAssembly.datums[myAssembly.datums.keys()[0]],
name='TrayNoRotation',
                     region=TrayRP, u1=SET, u2=SET, u3=SET, ur1=SET, ur2=SET,
ur3=SET, )

### Create steps
# ----------------------------------------------------------------------------
myModel.StaticStep(name='InterferenceFitStep',
                   previous='Initial',
                   description='Apply interference fit',
                   nlgeom=ON,
                   initialInc=0.1,
                   maxNumInc=1000)
```

```
myModel.StaticStep(name='LoadingStep',
                   previous='InterferenceFitStep',
                   description='Vertical load is applied in this step',
                   nlgeom=ON,
                   initialInc=0.01,
                   maxNumInc=1000)

myModel.boundaryConditions['TrayNoRotation'].deactivate(stepName='LoadingStep')

### Define interactions
# ----------------------------------------------------------------------------
myModel.ContactProperty('Frictionless')
myModel.interactionProperties['Frictionless'].TangentialBehavior(formulation=FRICTIO
NLESS)
myModel.interactionProperties['Frictionless'].NormalBehavior(
   allowSeparation=ON, constraintEnforcementMethod=DEFAULT,
   pressureOverclosure=HARD)

myModel.ContactProperty('Friction')
myModel.interactionProperties['Friction'].TangentialBehavior(
   absoluteDistance=0.2, dependencies=0, directionality=ISOTROPIC,
   elasticSlipStiffness=None, formulation=PENALTY, maximumElasticSlip=
   ABSOLUTE_DISTANCE, pressureDependency=OFF, shearStressLimit=None,
   slipRateDependency=OFF, table=((0.99,),), temperatureDependency=OFF)
myModel.interactionProperties['Friction'].NormalBehavior(
   allowSeparation=ON, constraintEnforcementMethod=DEFAULT,
   pressureOverclosure=HARD)

myModel.SurfaceToSurfaceContactStd(name='TrayBottomContact',
                                   createStepName='Initial',
                                   interactionProperty='Frictionless',
                                   master=myInstance2.surfaces['Tray_Tibiabottom'],
                                   slave=myInstance1.surfaces['Tibia_TrayIntUpper'],
                                   sliding=FINITE)  # implicit surface to surface contact
```

```
myModel.interactions['TrayBottomContact'].setValuesInStep(stepName='LoadingStep',
interactionProperty='Friction')

myModel.SurfaceToSurfaceContactStd(name='KeelContact',
                        createStepName='Initial',
                        interactionProperty='Frictionless',
                        enforcement=NODE_TO_SURFACE,
                        master=myInstance2.surfaces['Tray_TibiaInt'],
                        slave=myInstance1.surfaces['KeelCut'],
                        sliding=FINITE)  # implicit surface to surface contact

myModel.interactions['KeelContact'].setValuesInStep(interferenceType=SHRINK_FIT,
stepName='InterferenceFitStep')
myModel.interactions['KeelContact'].setValuesInStep(stepName='LoadingStep',
interactionProperty='Friction')

myModel.SurfaceToSurfaceContactStd(name='WallContact',
                        createStepName='Initial',
                        interactionProperty='Frictionless',
                        master=myInstance2.surfaces['Tray_WallInt'],
                        slave=myInstance1.surfaces['Tibia_WallInt'],
                        sliding=FINITE)  # implicit surface to surface contact

# ----------------------------------------------------------------------------

### Create field output requests
if 'F-Output-1' in myModel.fieldOutputRequests.keys():
   del myModel.fieldOutputRequests['F-Output-1']

myModel.FieldOutputRequest(name='F-Output-General',
createStepName='InterferenceFitStep',
                    variables=['S', 'E', 'NE', 'LE', 'U', 'RT', 'CSTRESS', 'CFORCE',
'CSTATUS'], numIntervals=20)
```

```
### Define loads
# ----------------------------------------------------------------------------

# code below to apply load

# apply load to load patch #
myModel.Pressure(name='VerticalLoad', createStepName='LoadingStep',
                 region=myAssembly.allSurfaces['Tray-1.LoadPatch'], magnitude=1000.0,
                 distributionType=TOTAL_FORCE)  # load of 1000N perpendicular to the
surface

## Export input file for bone material assignment
# ----------------------------------------------------------------------------
# myJob = mdb.Job(name=modelName, model=modelName, description='')
myJob = mdb.Job(activateLoadBalancing=False, atTime=None, contactPrint=OFF,
                 description='', echoPrint=OFF,
                 historyPrint=OFF, memory=90, memoryUnits=PERCENTAGE,
model=modelName,
                 modelPrint=OFF, multiprocessingMode=DEFAULT, name=modelName,
                 nodalOutputPrecision=FULL, numCpus=3, numDomains=3,
                 queue=None, resultsFormat=ODB,
                 scratch='', type=ANALYSIS, userSubroutine='', waitHours=0, waitMinutes=0)
# myJob.writeInput()
```

Appendix C: Change in Loading Position when Tibial Component was Rotated Internally/Externally

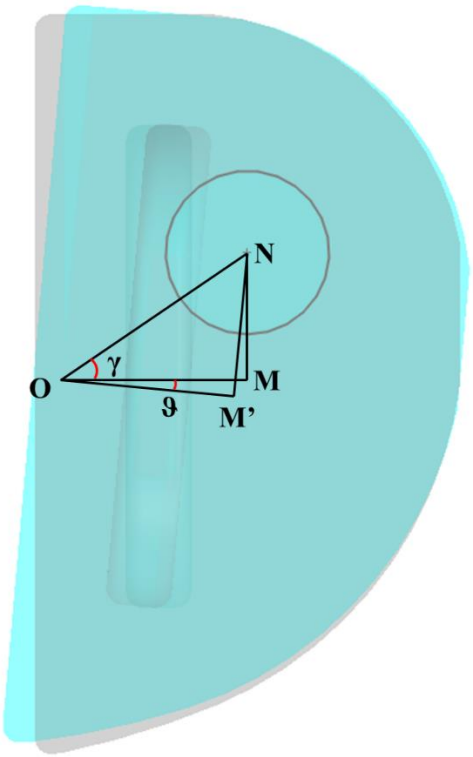

Appendix Figure 1: Change in loading position as the component is rotated. Grey: Original implant position. Blue: Implant position after rotation.

θ is the angle of rotation. θ is positive for external rotations and negative for internal rotations.

$$\gamma = \tan^{-1}\left(\frac{MN}{MO}\right) = \tan^{-1}\left(\frac{8}{bearing\ width + 1}\right)$$

$$ON = \sqrt{OM^2 + MN^2}$$

$$OM' = ON * \cos(\gamma + \theta)$$

$$M'N = ON * \sin(\gamma + \theta)$$

After the component was rotated, the loading position relative to the new component position was OM' away from the wall and M'N posterior to the centre line.

Appendix D: Search Strings Used in Systematic Review

Embase/Medline

1 Arthroplasty, Replacement, Knee/

2 Knee Prosthesis/

3 1 or 2

4 (Unicompartment* or Uni-compartment*).ti,ab.

5 (Unicondyl* or Uni-condyl*).ti,ab.

6 partial.ti,ab.

7 (UKA or UKR or PKA or PKR or UCA or UCR).ti,ab.

8 4 or 5 or 6 or 7

9 3 and 8

10 migrat*.mp.

11 subsid*.mp.

12 (RSA or Radiostereo* or "roentgen stereo*").mp.

13 ("primary fixation*" or "secondary fixation*" or "primary stability" or "secondary stability").mp.

14 10 or 11 or 12 or 13

15 9 and 14

Web of Science

(TS=(Knee$) AND (TS=(Uni$compartment*) OR TS=(Uni$condyl*) OR TS=(partial) OR TS=(UKA or UKR or PKA or PKR or UCA or UCR))) AND (TS=(migrat*) OR TS=(subsid*) OR TS=(RSA or Radiostereo* or "roentgen stereo*") OR TS=("primary fixation*" or "secondary fixation*" or "primary stability" or "secondary stability"))
Search strings in other databases were adapted accordingly.

Search strings in other databases were adapted accordingly.

Appendix E: Excluded Studies in Systematic Review with Reasons

The following results were excluded during the abstract screening:

- Book or book chapter
- Comment
- Conference abstracts
- Non-English
- Animal study
- Cadaveric study
- Other reviews

Appendix Table 1: Excluded studies with reasons.

First Author	Year of Publication	Reason for Exclusion
Ryd [199]	1983	Fixed bearing – Marmor Knee
Ryd [200]	1986	Fixed bearing – Marmor Knee
Ryd [201]	1989	Fixed bearing – Marmor Knee
Ryd [202]	1992	Fixed bearing – Marmor Knee
Miskovsky [203]	1992	Fixed bearing - Ortholoc II Unicondylar
Buechel [204]	1994	Mobile bearing New Jersey LCS Knee System – the bearing moved in a fixed track, thus, not fully mobile. No cases of subsidence or migration identified
Ryd [205]	1995	Total knee replacement or tri-compartmental knee replacement
Squire [206]	1999	Fixed bearing – Marmor Knee
Lindstrand [207]	2000	Fixed bearing – Duracon Unicompartmental Knee Replacement
Soavi [208]	2002	Fixed bearing – Duracon Unicompartmental Knee Replacement
Bragonzoni [209]	2005	Fixed bearing – Duracon Unicompartmental Knee Replacement
Carlsson [210]	2006	Fixed bearing – Miller-Galante Unicompartmental Knee Arthroplasty

Gillies [211]	2007	Fixed bearing - St George Sled Link and EIUS
Chau [177]	2009	No cases of subsidence or migration identified
Saenz [212]	2010	Fixed bearing – EIUS Unicompartmental Knee Replacement
Small [213]	2011	No cases of subsidence or migration identified
Bruni [214]	2012	Fixed bearing – Preservation® Unicompartmental Knee Replacement
Clement [215]	2012	No cases of migration of subsidence identified
Small [216]	2013	No cases of subsidence or migration identified
Ensini [217]	2013	Fixed bearing – OptetrakÒ Unicompartmental Knee Replacement
O'Donnell [218]	2013	Fixed bearing – Repicci and Active Unicompartmental Knee Replacement
Barbadoro [219]	2014	Fixed bearing – OptetrakÒ Unicompartmental Knee Replacement
Engh [220]	2014	Fixed bearing – Preservation® Unicompartmental Knee Replacement
Bruni [221]	2015	Fixed bearing – Duracon Unicompartmental Knee Replacement
Hooper [222]	2015	No cases of tibial component subsidence or migration mentioned
Koppens [223]	2018	Fixed bearing – Sigma medial Unicompartmental Knee Replacement
Scott [224]	2018	Fixed bearing – Preservation® Unicompartmental Knee Replacement
Scott [225]	2018	No cases of migration or subsidence identified
Zsakai [226]	2018	Fixed bearing – Metrimed Unicompartmental Cemented Knee System

Appendix F: Radiographs of Cementless OUKR Tibial Component Subsidence Cases and Supplementary Details

F: female / M: male

[86]:

Case 1 (61-year-old/F/Valgus):

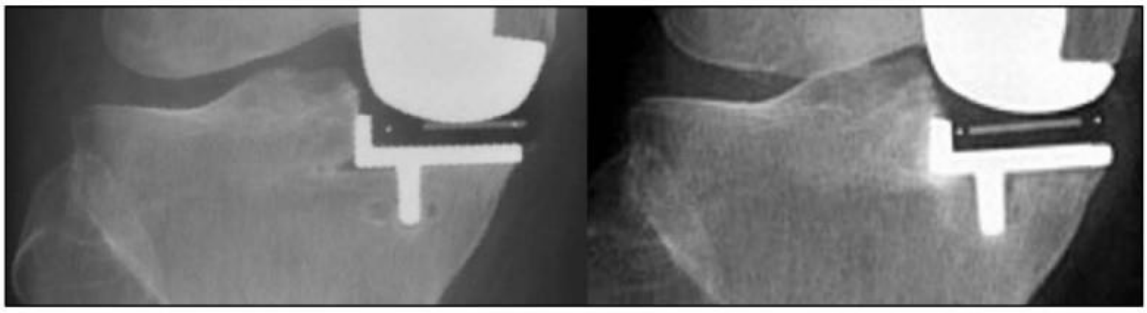

Postoperative One year

Lateral unavailable

Case 2 (Valgus): Not available

Case 3 (Valgus): Not available

Case 4 (64-year-old/M/Varus):

Immediate post-operative radiographs showed that the tibial component had not been seated properly. The suggested cause of subsidence was that the keel had not been cleared completely before the tibial component was implanted. One-year post-operative radiographs showed varus subsidence and incomplete fixation.

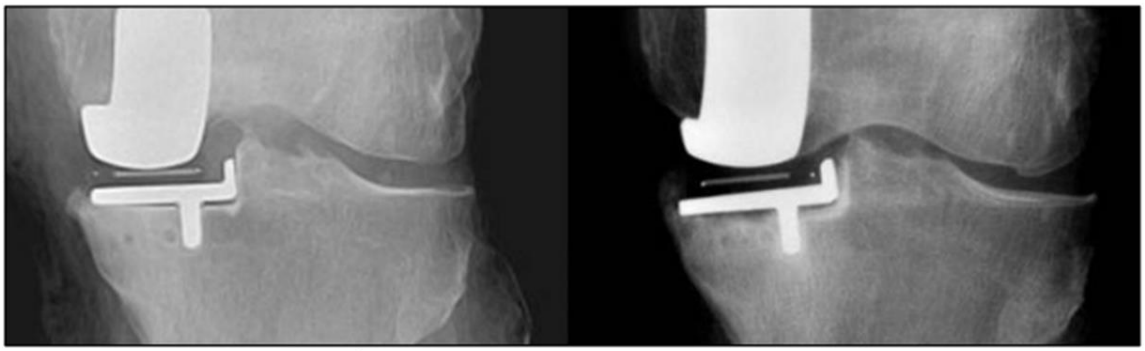

Postoperative One year

Lateral not available

[87]:

Case 5 (79-year-old/M/Valgus):

79-year-old male. ACL-deficient. At 6 weeks post-operation, there was an effusion with 5 to 10 degrees of flexion deformity but no discomfort or loss of mobility. At 4 months post-operatively, full knee flexion was regained but pain was reported. Radiographs showed that the tibial component had subsided from 4 degrees varus into 8 degrees valgus relative to the mechanical axis. The tibial component also loosened.

However, the pain improved without revision surgery and subsidence stopped. By the end of year 3, the implant was well fixed, and the OKS was 39/48. At 5 years post-operatively, no further subsidence was noted.

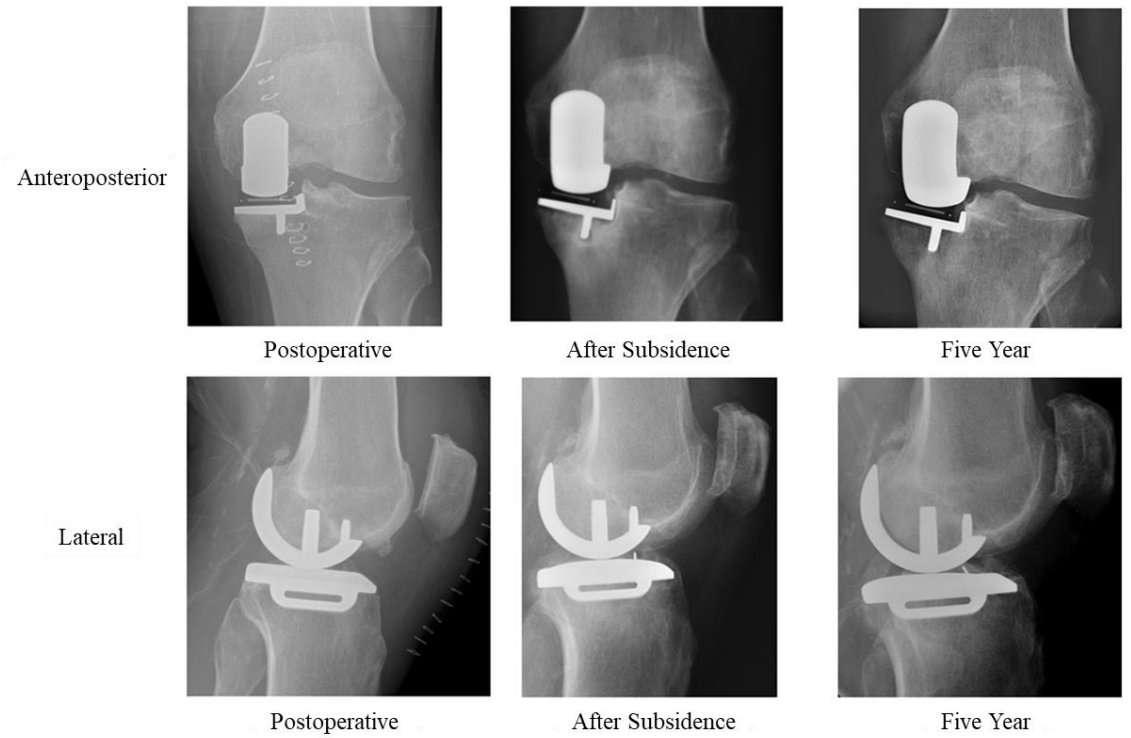

Case 6 (66-year-old/M/Valgus):

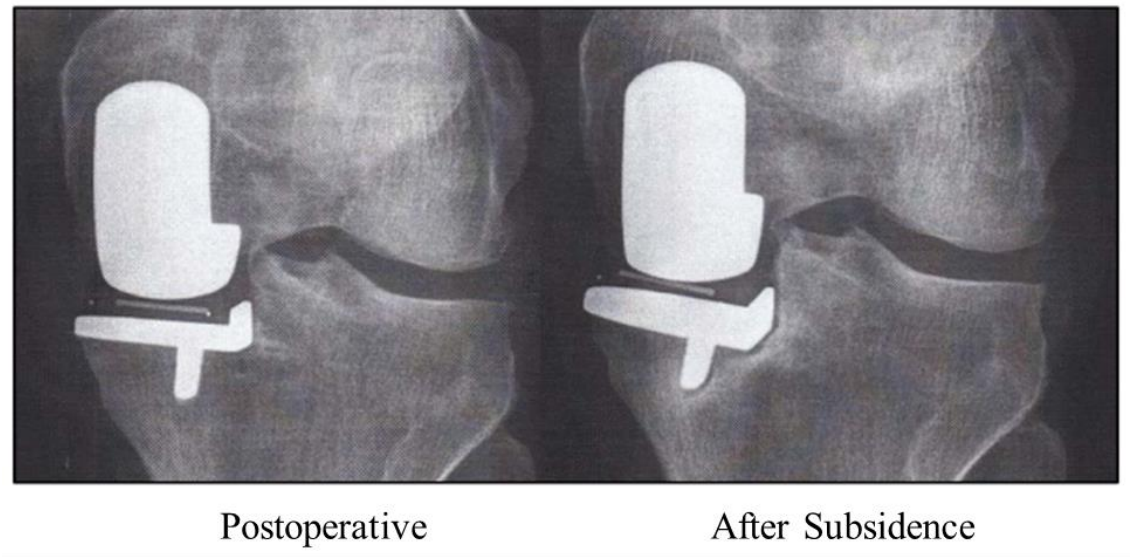

Lateral not available

The radiographs showed a valgus subsidence of the tibial component and radiolucency formed around the keel.

Case 7 (66-year-old/M/Valgus): Not available

Case 8 (65-year-old/M/Valgus and Posterior):

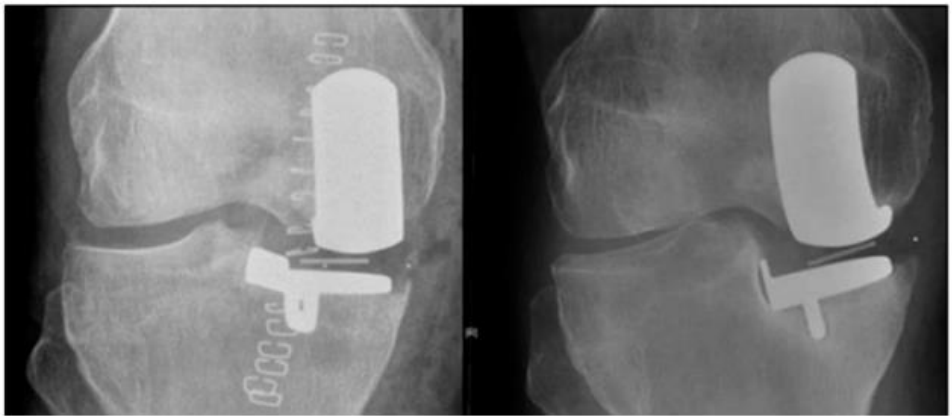

Postoperative Pre-revision

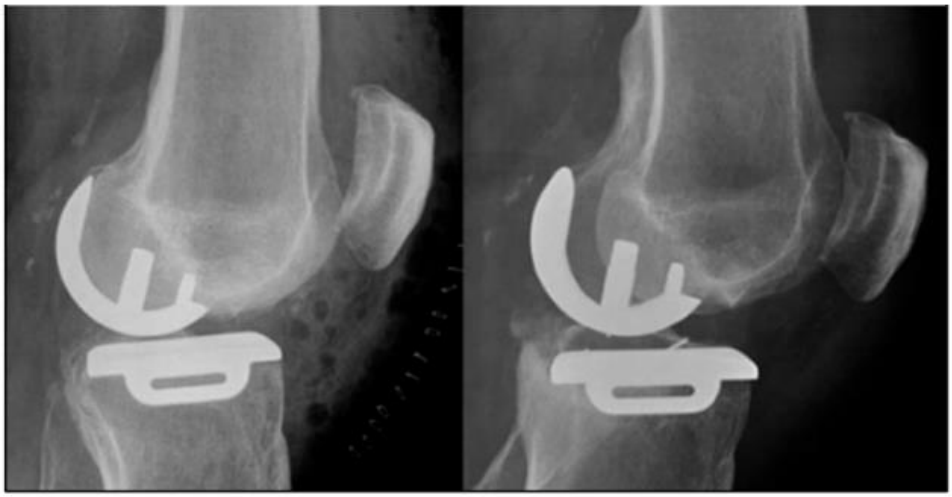

Postoperative Pre-revision

Case 9 (62-year-old/F/Valgus): Not available

Case 10 (76-year-old/M/Valgus and Posterior):

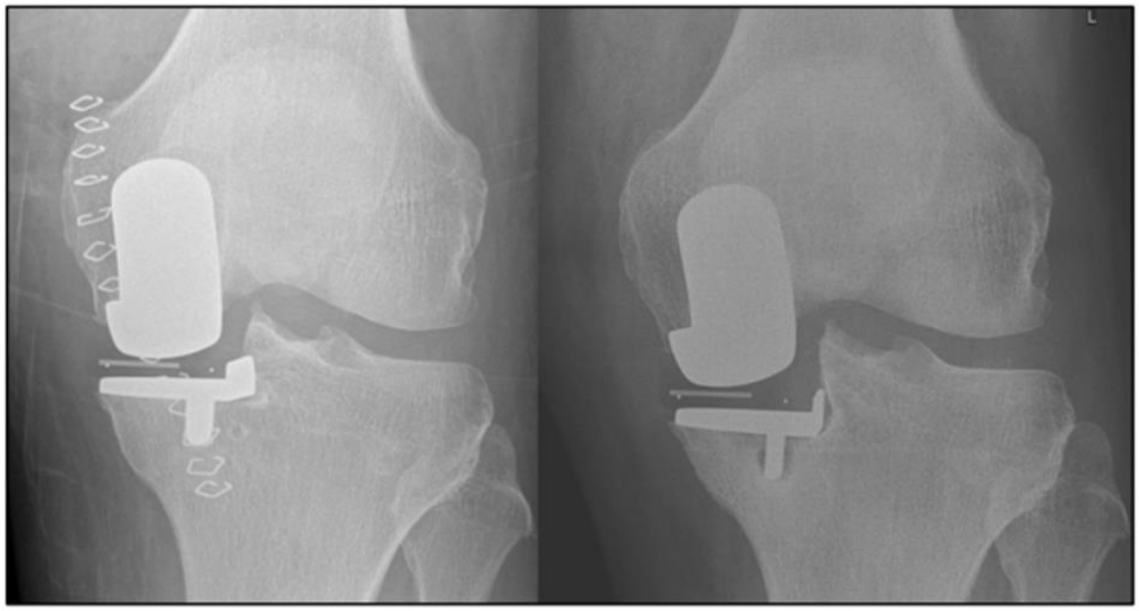

Postoperative Three Months

Lateral not available

[88]: No cases developed posterior-only subsidence

Case 11 (Valgus):

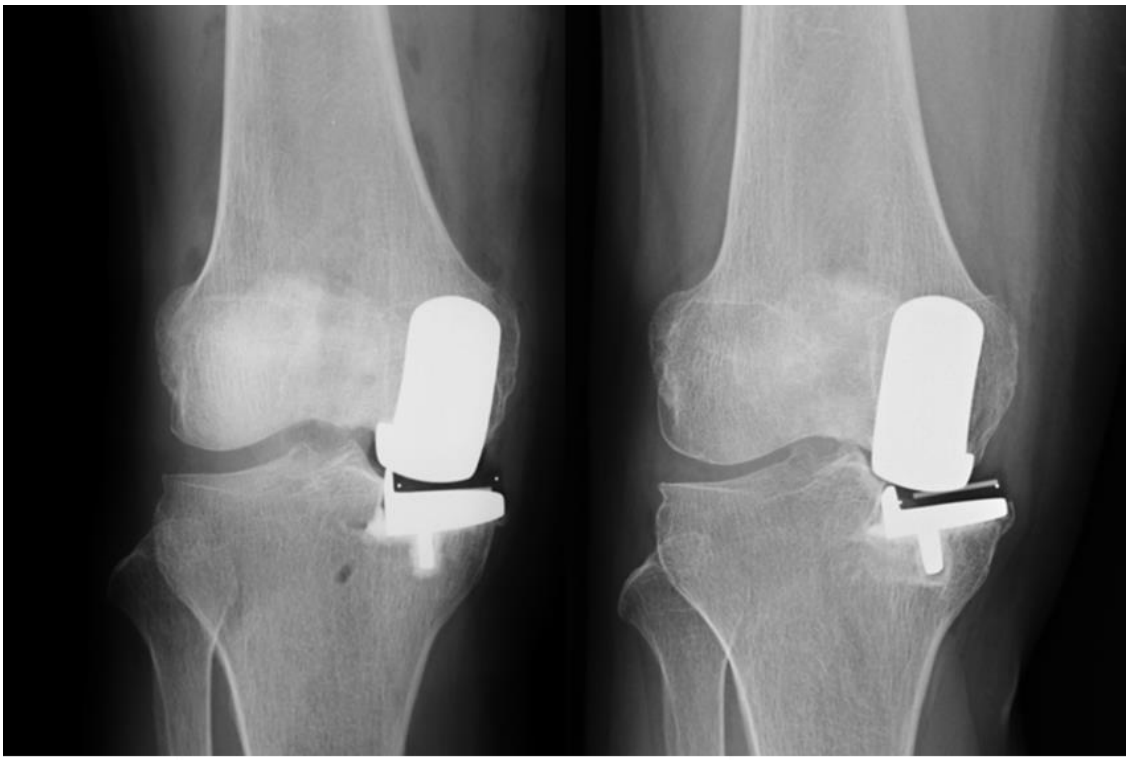

One Month Two Years

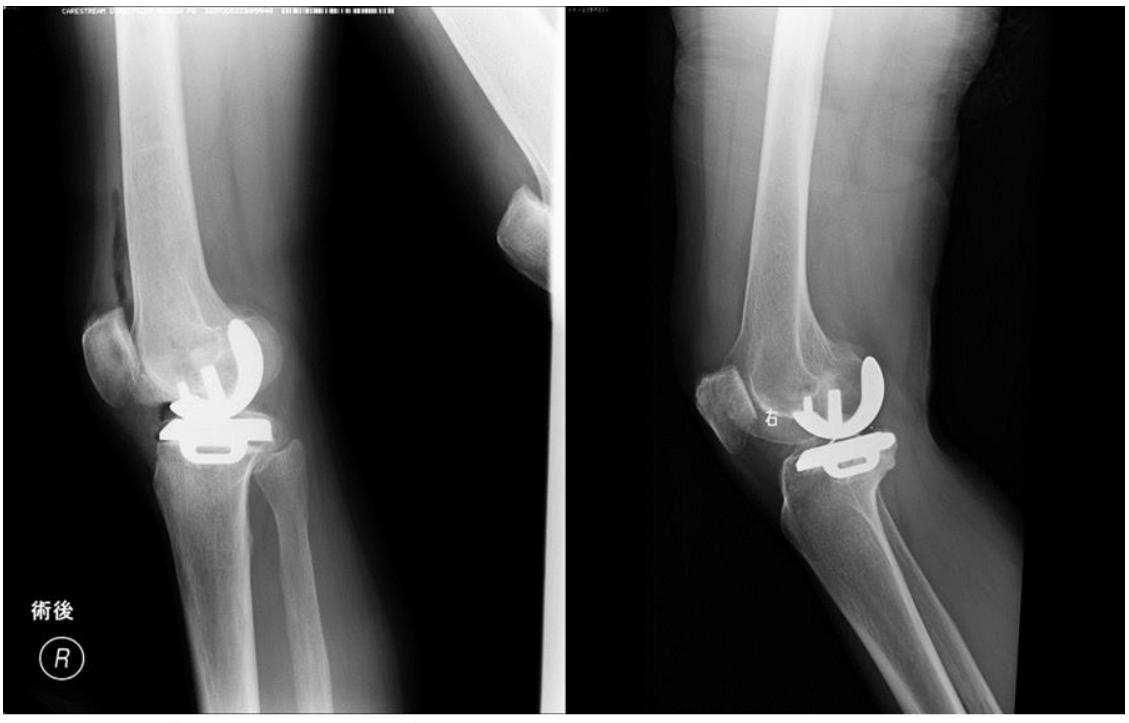

One Month Two Years

Case 12 (Valgus):

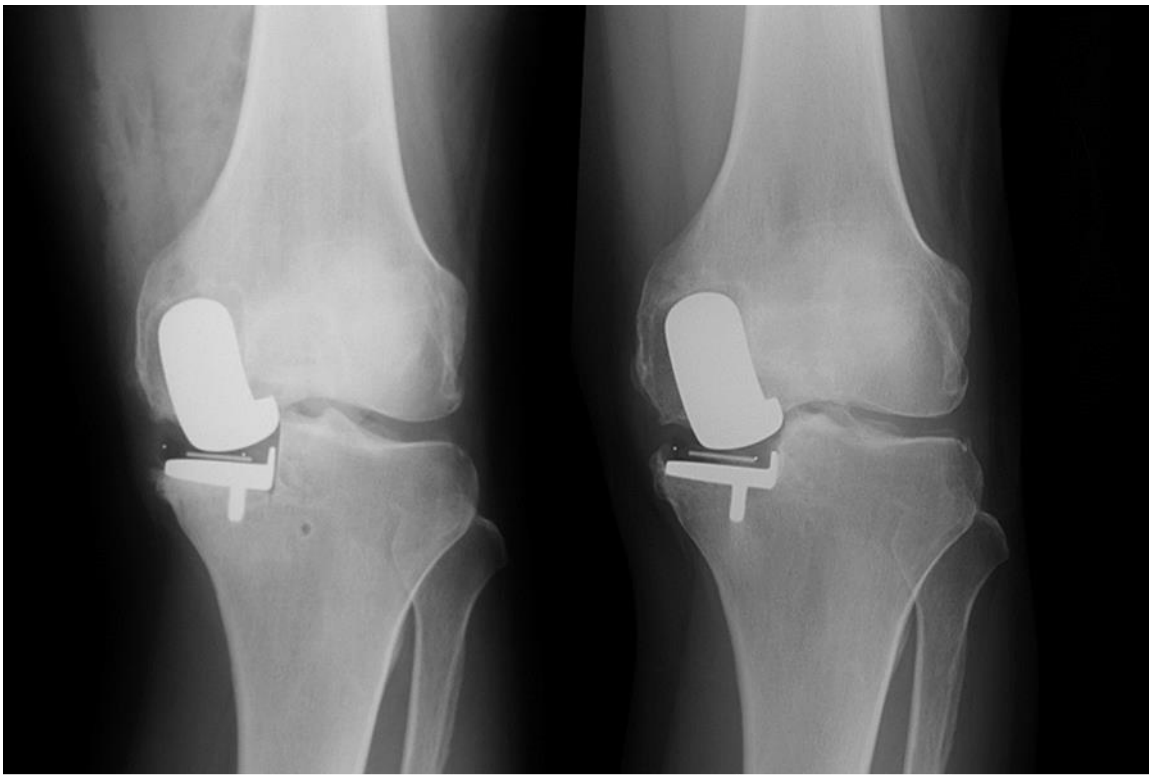

One Month Two Years



One Month Two Years

Case 13 (Valgus):

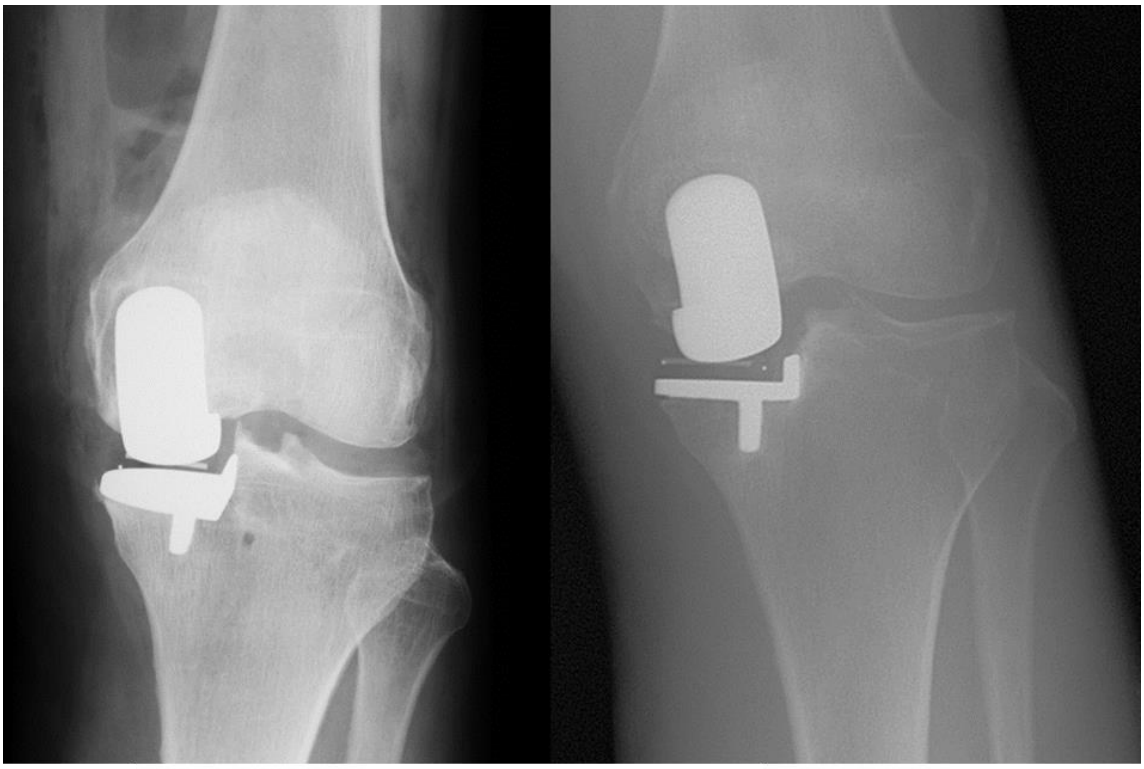

One Month One Year

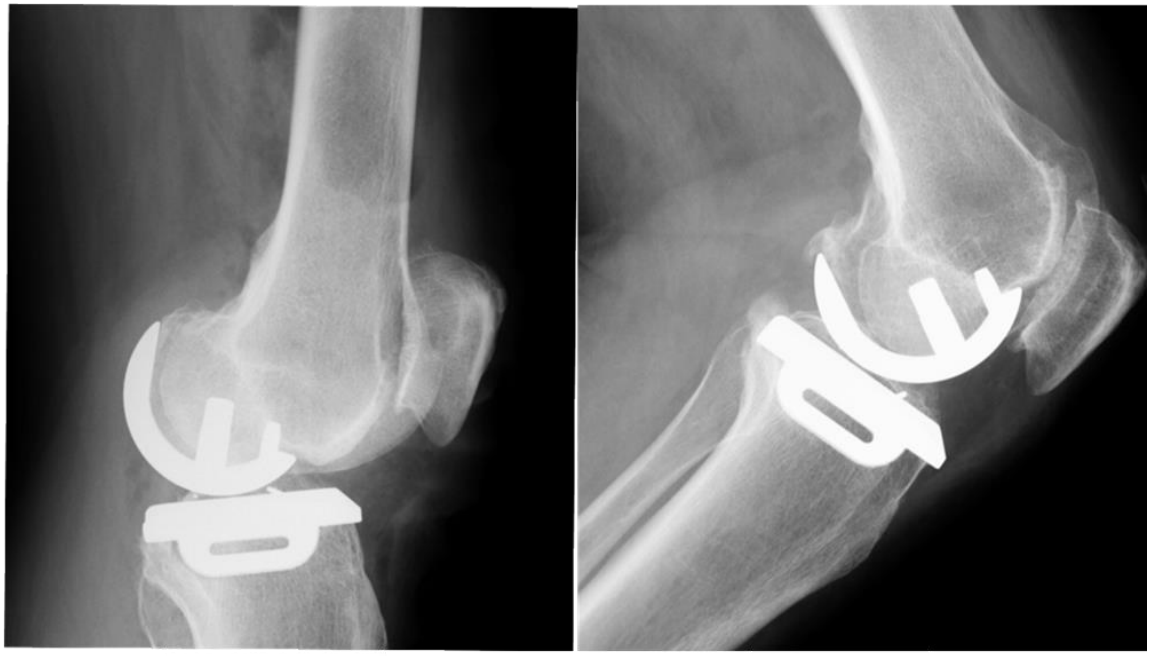

One Month One Year

Case 14 (Valgus):

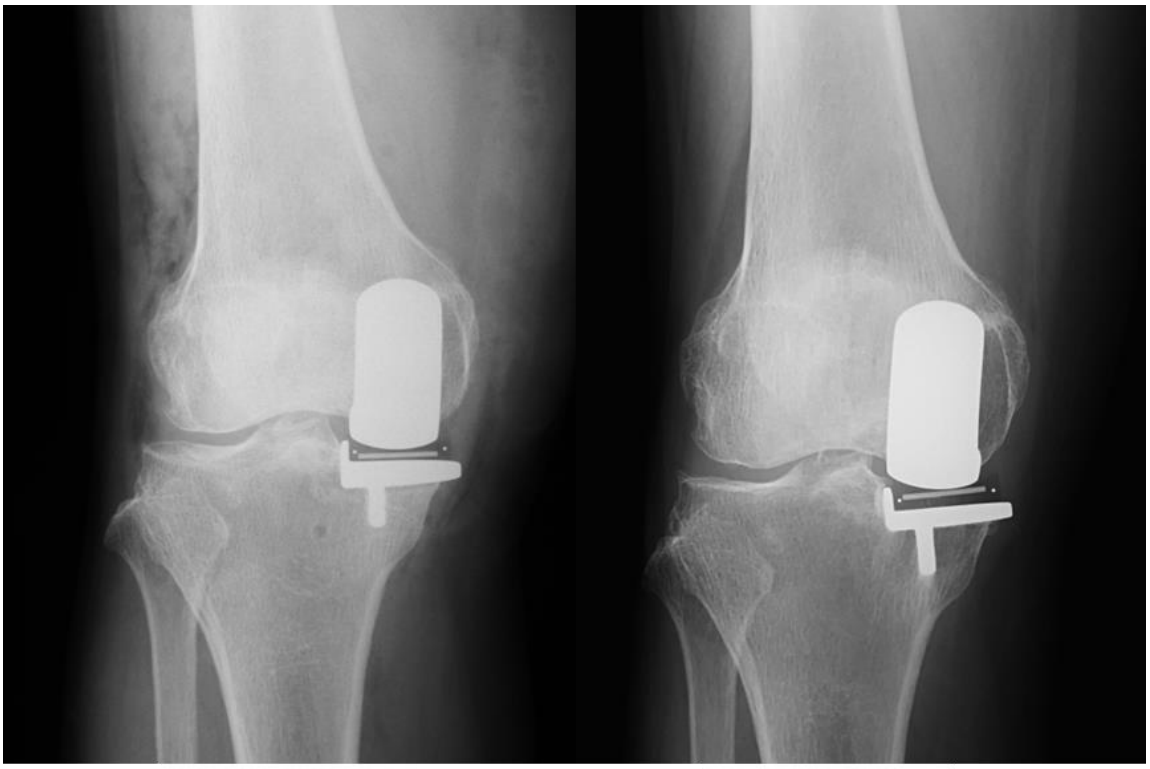

One Month Three Years

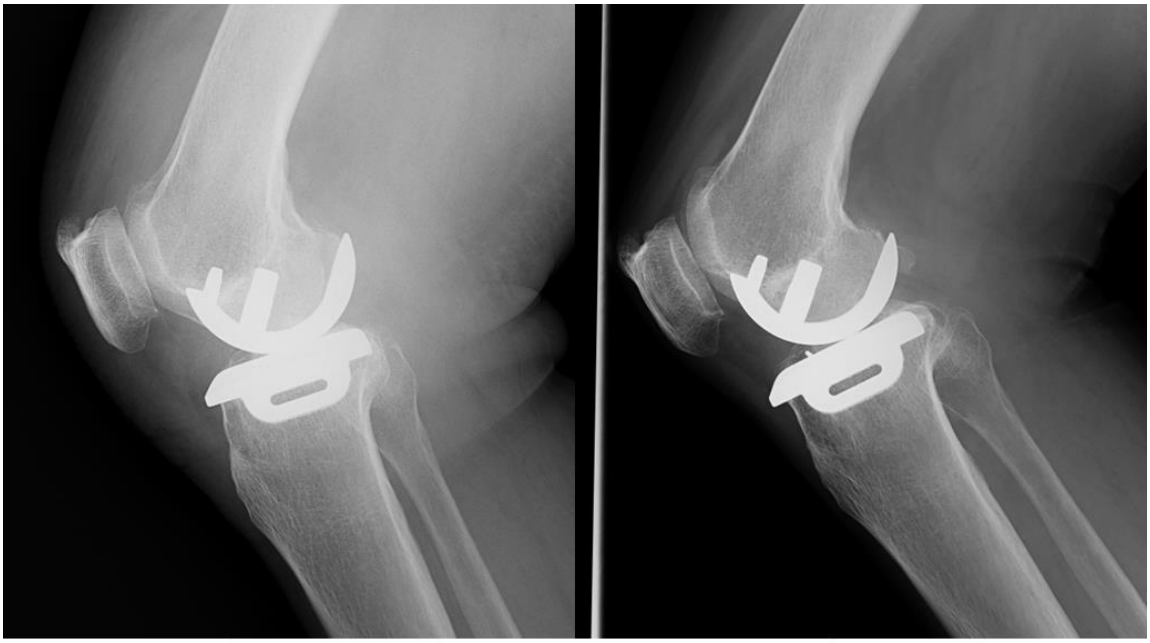

One Month Three Years

Case 15 (Valgus):

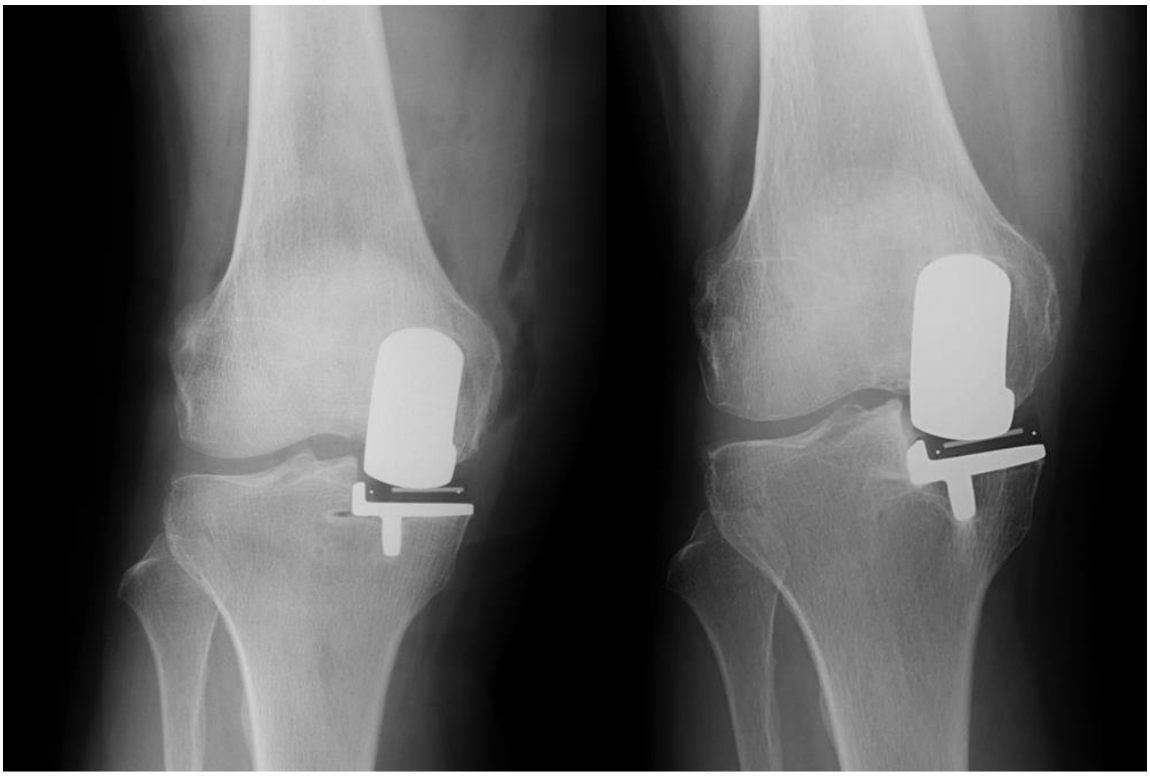

One Month Four Years

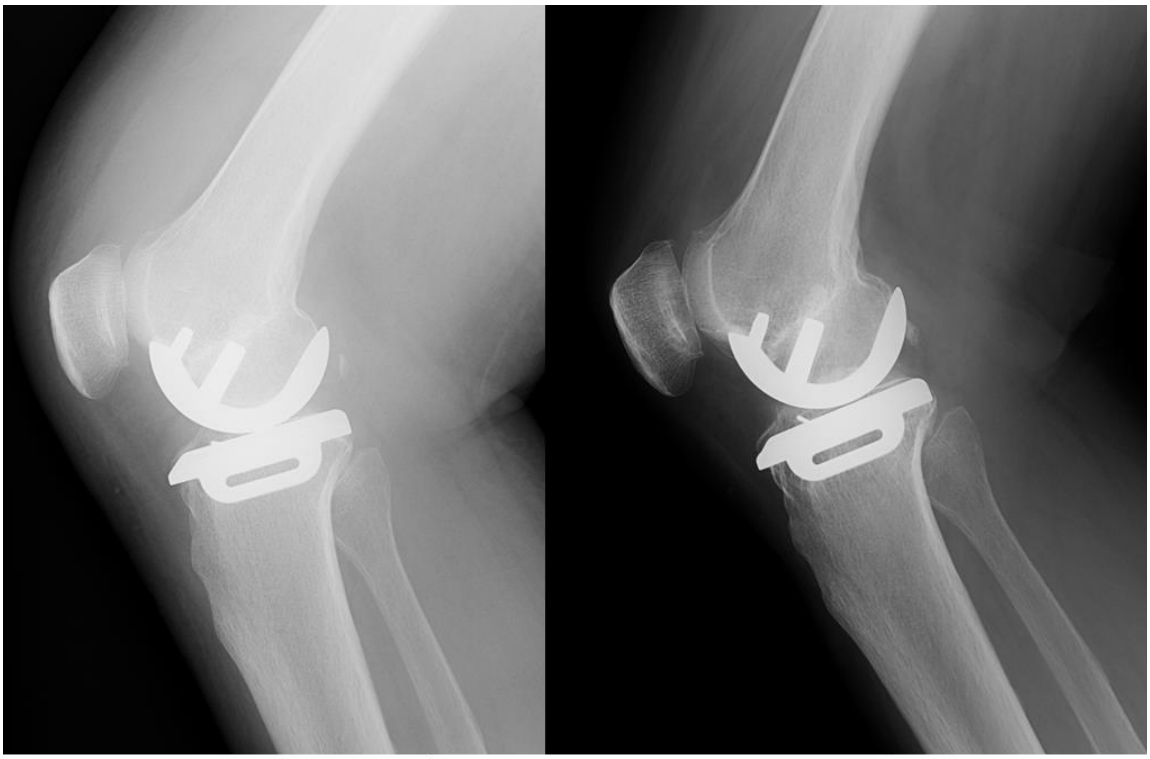

One Month Four Years

Case 16 (Valgus):

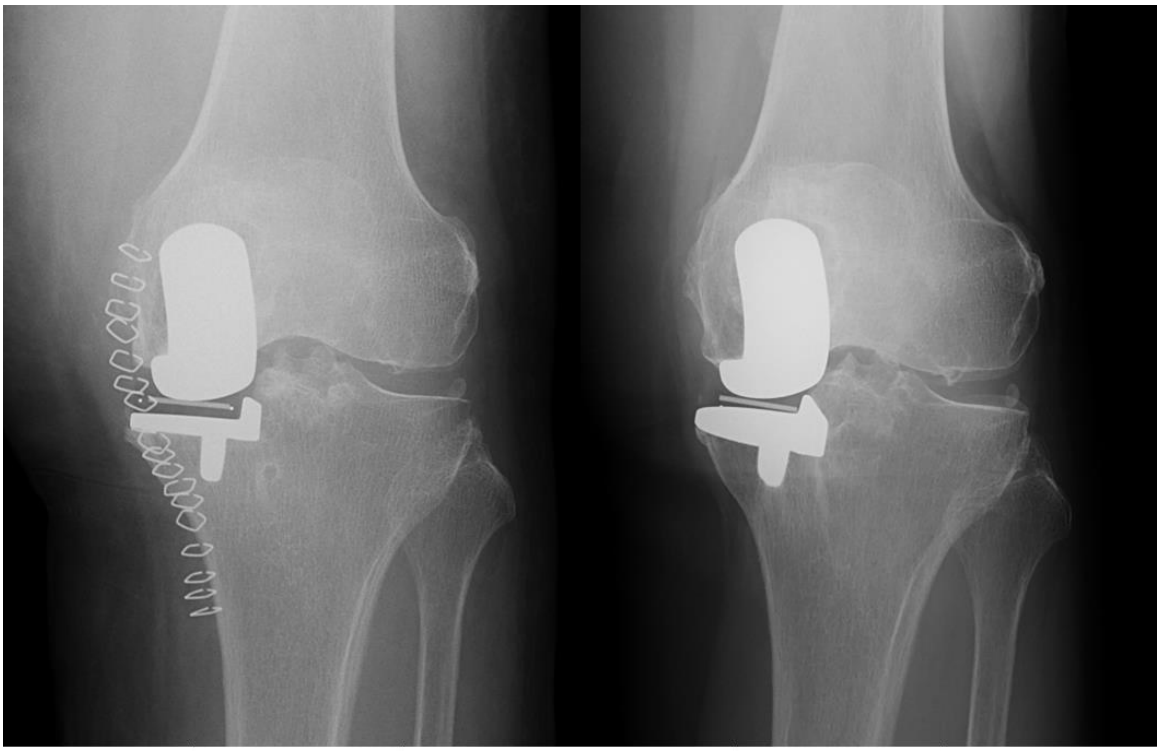

One Month Three Years

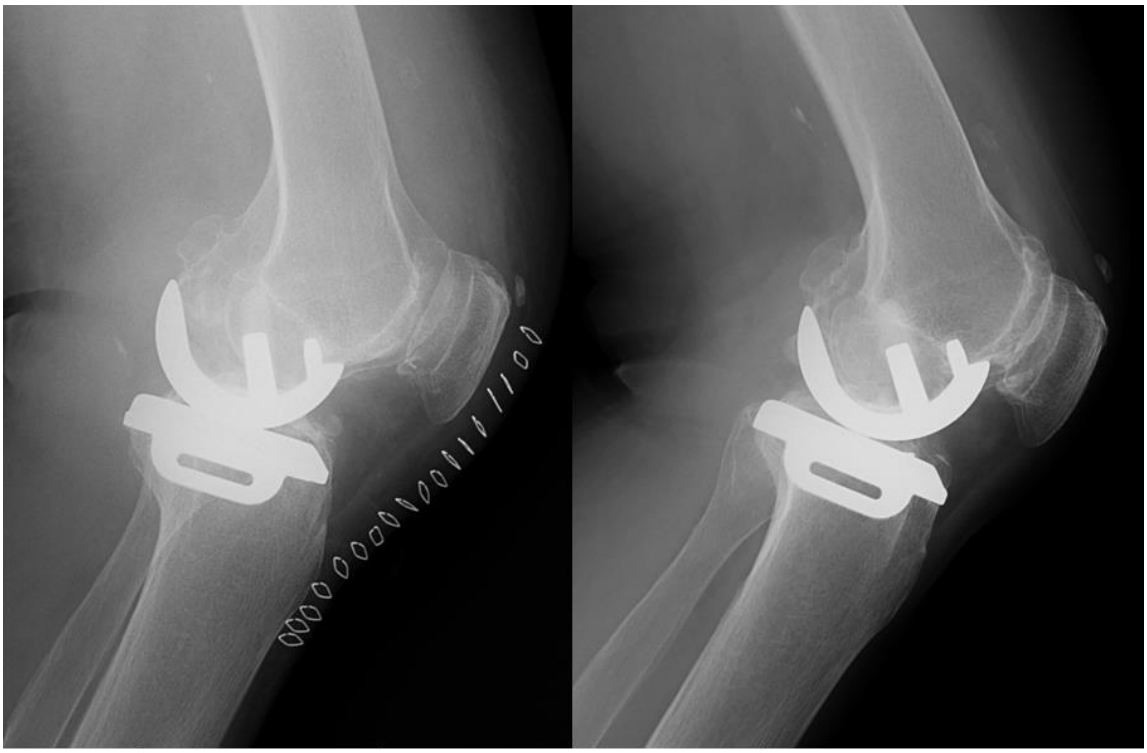

One Month Three Years

[89]:

Case 17 (Valgus and Posterior): Not available

Case 18 (Valgus and Posterior): Not available

Case 19 (Valgus and Posterior): Not available

Case 20 (Posterior):

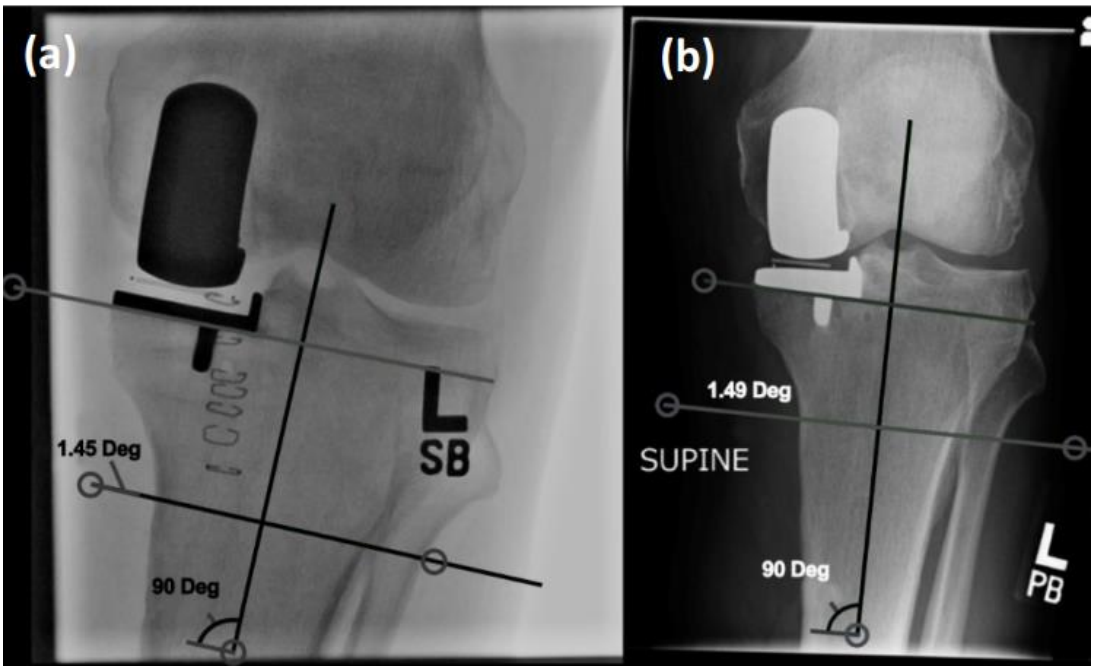

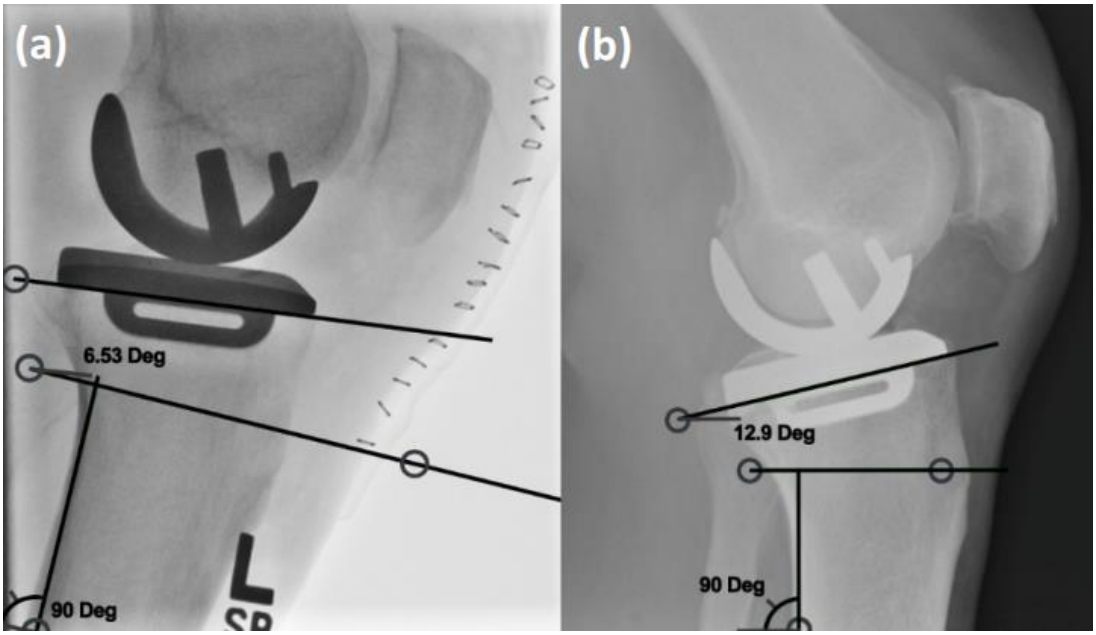

[90]:

Case 22 (Valgus and Posterior): Not available

Case 23 (Valgus and Posterior): Not available

[191]:

Case 24 (Valgus): Not available

[190]:

Case 24 (71-year-old/M/Valgus and Posterior)

5-yr OKS:26; 2.7-degree valgus subsidence; 6.0-degree posterior subsidence

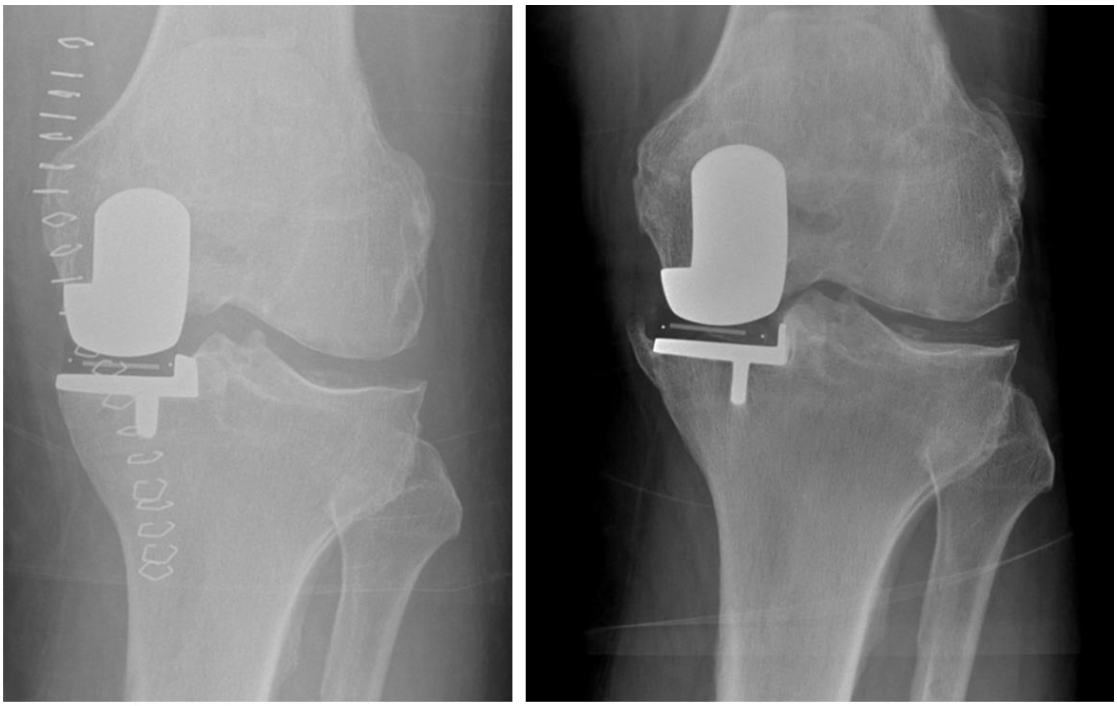

Postoperative Five Years

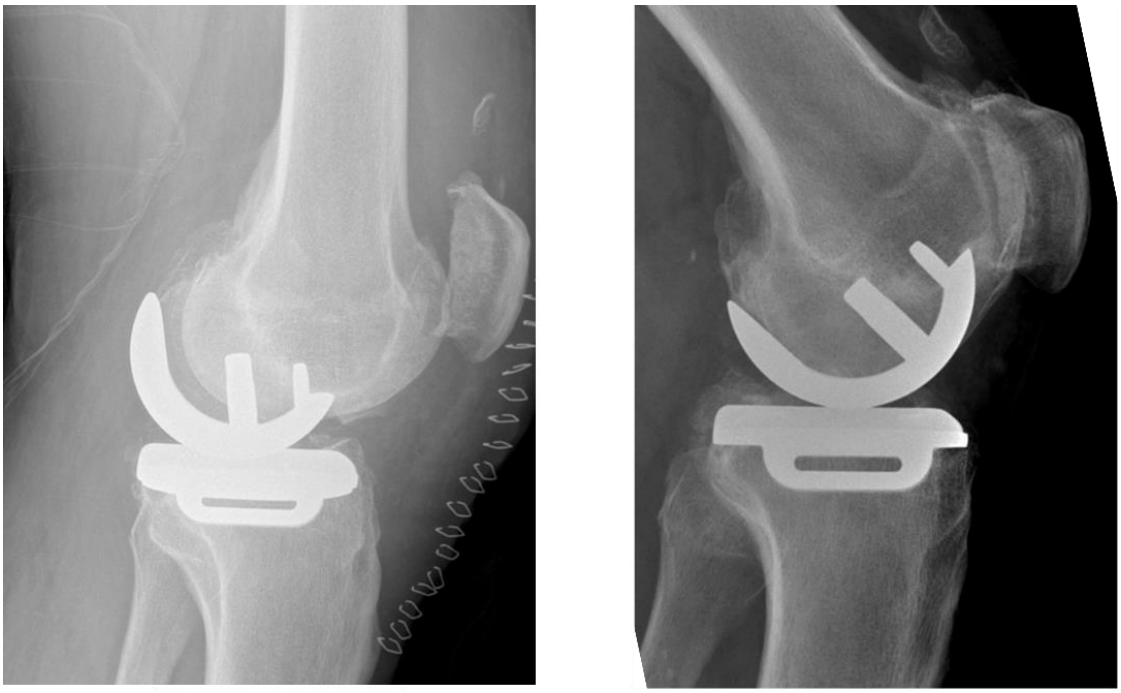

Postoperative Five Years

Case 25 (65/M/Valgus and Posterior):

2-yr OKS: 48; 2.8-degree valgus subsidence; 1.6-degree posterior subsidence

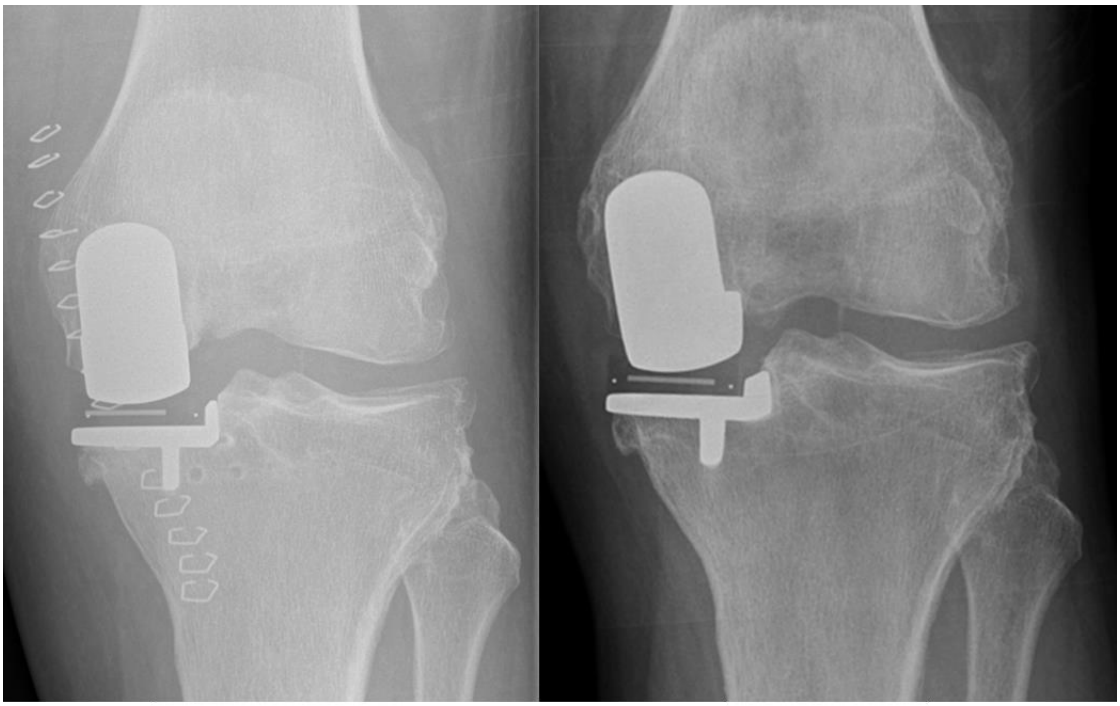

Postoperative Two Years

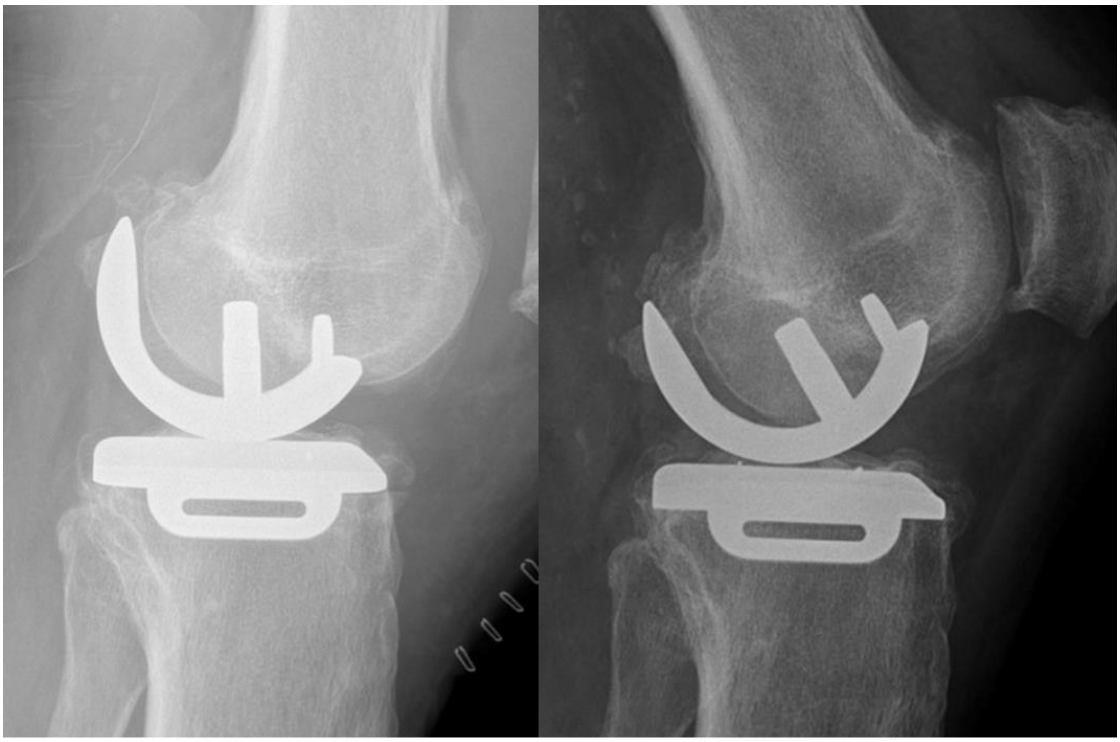

Postoperative Two Years

Case 26 (74/F/Valgus and Posterior):

5-yr OKS:31; 2.4-degree valgus subsidence; 2.7-degree posterior subsidence

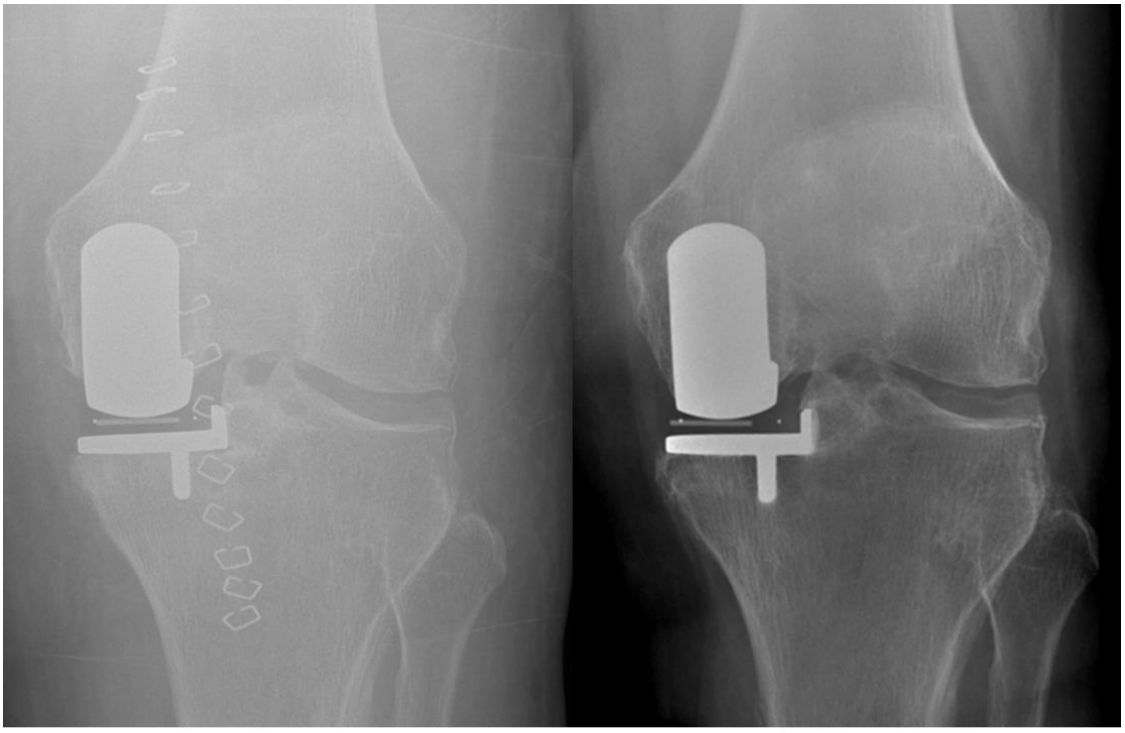

Postoperative Five Years

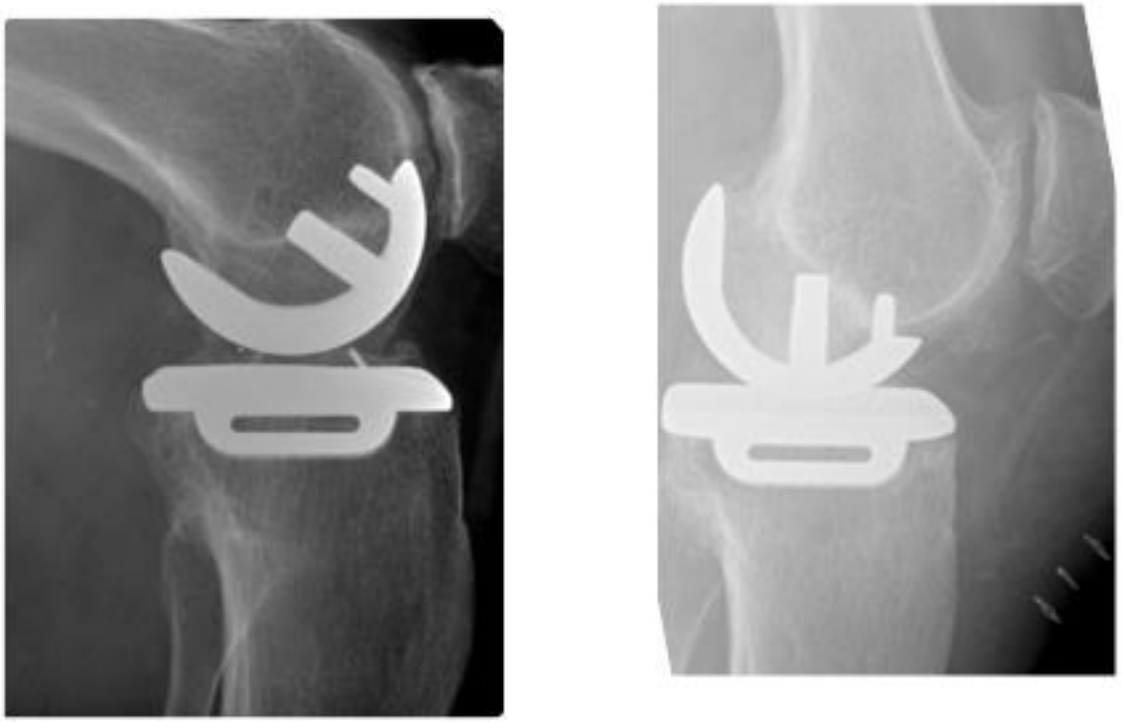

Postoperative Five Years

Case 27: (69/M/Valgus and Posterior)

5-yr OKS: 48; 4.9-degree valgus subsidence; 1.0-degree posterior subsidence



Postoperative



Five Years



Postoperative



Five Years

Case 28 (57/F /Varus and Posterior):

5-yr OKS: 45; 1.6-degree varus subsidence; 3.8-degree posterior subsidence



Postoperative



Five Years



Postoperative



Five Years

Appendix G: Modifications to the py_bonemat_abaqus Python Package to Apply Elastic-plastic Material Properties

Appendix G – 1: Update to code run.py

```
#!/usr/bin/python
#
# py_bonemat_abaqus - run
# ===========================
#
# Created by Elise Pegg, University of Bath
# Edited by Xiaoyi Min, University of Oxford

__all__ = ['run']

#--------------------------------------------------------------------------
# Import modules
#--------------------------------------------------------------------------
import sys, os
from py_bonemat_abaqus_plastic import general, data_import, calc, data_output
from py_bonemat_abaqus_plastic.version import __version__

#--------------------------------------------------------------------------
# Define run program
#--------------------------------------------------------------------------
def run(argv0, argv1, argv2):
   print("""
   ************** PY_BONEMAT ABAQUS Plastic""" + __version__ + """
************
   ** Elise Pegg,  University of Oxford,  Aug 2015 **
   ** XiaoyiM, University of Oxford, edited Dec 2023 **
   ************************************************
   """)
```

```
#--------------------------------------------------------------------------
# check input arguments
#--------------------------------------------------------------------------
argv = [argv0, argv1, argv2]
if general.check_argv(argv) == False:
    sys.exit(1)
param_file = argv[0]
ct_data = argv[1]
mesh_file = argv[2]

#--------------------------------------------------------------------------
# Import parameters
#--------------------------------------------------------------------------
param = data_import.import_parameters(param_file)

#--------------------------------------------------------------------------
# Import Abaqus input file data
#--------------------------------------------------------------------------
print("    Importing mesh file: " + mesh_file)
parts = data_import.import_mesh(mesh_file, param)

#--------------------------------------------------------------------------
# Import CT data
#--------------------------------------------------------------------------
print("    Importing CT data: " + ct_data)
vtk_data = data_import.import_ct_data(ct_data)

#--------------------------------------------------------------------------
# Determine material properties for elements within each part
#--------------------------------------------------------------------------
print("    Calculating material properties")
parts = calc.calc_mat_props(parts, param, vtk_data)
```

```
    #--------------------------------------------------------------------------
    # Write data to new abaqus input file
    #--------------------------------------------------------------------------
    print("    Writing material data to new abaqus input file:")
    print("\t" + mesh_file[:-4] + "PlasticMAT.inp")
    data_output.output_abq_inp(parts, mesh_file, param['poisson'])

    #--------------------------------------------------------------------------
    # End
    #--------------------------------------------------------------------------
    print("""    **    !!!  Bone  material  assignment  complete  !!!
********************************************************** """)
    os._exit(0)
```

Appendix G – 2: Update to code data_output.py (edits in bold)

The first part of the codes was the same as the original version.

```
#--------------------------------------------------------------------------
# Functions to create sections of output file
#--------------------------------------------------------------------------
def _create_header(fle):
    """ Text header for abaqus input file """

    header1 = "*Heading\n** Job name: " + os.path.split(fle)[-1][:-4] + " Model name: " +
os.path.split(fle)[-1][:-4] + "\n"
    header2 = "** Generated by: py_bonemat_abaqus\n"
    header3 = "*Preprint, echo=NO, model=NO, history=NO, contact=NO\n"
    header4 = "**\n** PARTS\n**\n"

    return header1 + header2 + header3 + header4

def _create_node_lines(part):
```

```
    """ Node text for abaqus input file """

    node_data = _get_node_data(part)
    node1 = "*Part, name=" + part.name +"\n*Node\n"
    node2 = _get_node_text(node_data)

    return node1 + node2

def _create_element_lines(part):
    """ Element text for abaqus input file """

    ele_data = _get_ele_data(part)
    ele1 = "*Element, type=" + part.ele_name + "\n"
    ele2 = _get_ele_text(ele_data)

    return ele1 + ele2

def _create_materials(parts, poisson):
    """ Text to define materials """

    materials = '**\n** MATERIALS\n**\n'
    moduli = _get_all_modulus_values(parts)
    materials_data = sorted(list(set(moduli)))
    for m in range(len(materials_data)-1):
        materials = materials + '*Material, name=BoneMat_' + repr(m + 1) + '\n'
        materials = materials + '*Elastic\n' + repr(materials_data[m]) + ', ' + repr(poisson) +
'\n'
        ## ----------MY EDIT 18th Dec 2023----------
--------Start--##
        ## this part adds plasticity to the bone
        x = materials_data[m] * 0.01
        y = materials_data[m] * 0.01
        z = y + materials_data[m] * (0.5-0.2)
        materials = materials + '*Plastic\n' + repr(x) + ', ' + repr(0) + '\n'
```

materials = materials + repr(y) + ', ' + repr(0.2) + '\n'

materials = materials + repr(z) + ', ' + repr(0.5) + '\n'

----------MY EDIT 18th Dec 2023----------Finish--##

materials = materials + '*Material, name=BoneMat_' + repr(len(materials_data)) + '\n'

materials = materials + '*Elastic\n' + repr(materials_data[len(materials_data)-1]) + ', ' + repr(poisson)+ '\n'

----------MY EDIT 18th Dec 2023----------Start--##

materials = materials + '*Plastic\n' + repr(materials_data[len(materials_data)-1] * 0.01) + ', ' + repr(0) + '\n'

materials = materials + repr(materials_data[len(materials_data)-1] * 0.01) + ', ' + repr(0.2) + '\n'

materials = materials + repr(materials_data[len(materials_data)-1] * (0.01 + (0.5-0.2))) + ', ' + repr(0.5) + '\n'

----------MY EDIT 18th Dec 2023----------Finish--##

return materials, materials_data

…….

The rest of the codes were the same as the original version.

Appendix H: Radiographic Study of Difference in Bone Density in Subsidence and Non-Subsidence Patients

Introduction

The local bone density distribution at the tibial plateau may be different in OUKR tibial component subsidence patients and this may cause the tibial component to migrate differently when compared to that in the non-subsidence patients. Cyst, which is a lesional spot in bone filled with fluid, in the tibial plateau was one suspected cause of subsidence. The brightness on radiographs can give an indication of the relative density of a specific part of a bone. A radiographic study was conducted to investigate if there were any differences in the bone density in the tibial plateau in the subsidence and non-subsidence cohorts.

Methods

Five patients who experienced tibial component subsidence and five patients who did not experience subsidence with matched age and gender after OUKR were selected from a radiographic study done by Nisrina Widari.

Their pre-operative and immediate post-operative AP radiographs were overlayed in PowerPoints to identify the position of the tibial component on the pre-operative radiographs (**Appendix Figure 2**). Lines were drawn around the margin of the tibial component and around the keel on the pre-operative radiographs referring to the immediate post-operative radiographs (**Appendix Figure 3** and **Appendix Figure 4**).



Appendix Figure 2: Example of overlaying the pre-operative and immediate post-operative AP radiographs. Yellow – pre-operative radiograph. Black/white – immediate post-operative radiograph.



Appendix Figure 3: Lines were drawn around the margin of the tibial component.



Appendix Figure 4: The post-operative radiograph was hidden with the position of the tibial component showing on the pre-operative radiograph.

Their pre-operative AP radiographs with the position of the tibial component marked out were imported into ImageJ (National Institutes of Health, Bethesda, Maryland, USA). Regions of interest (ROIs) that were of the same dimension as the tibial keel were marked out next to the tibial keel (**Appendix Figure 5**). The keel was always in ROI3 for consistency.

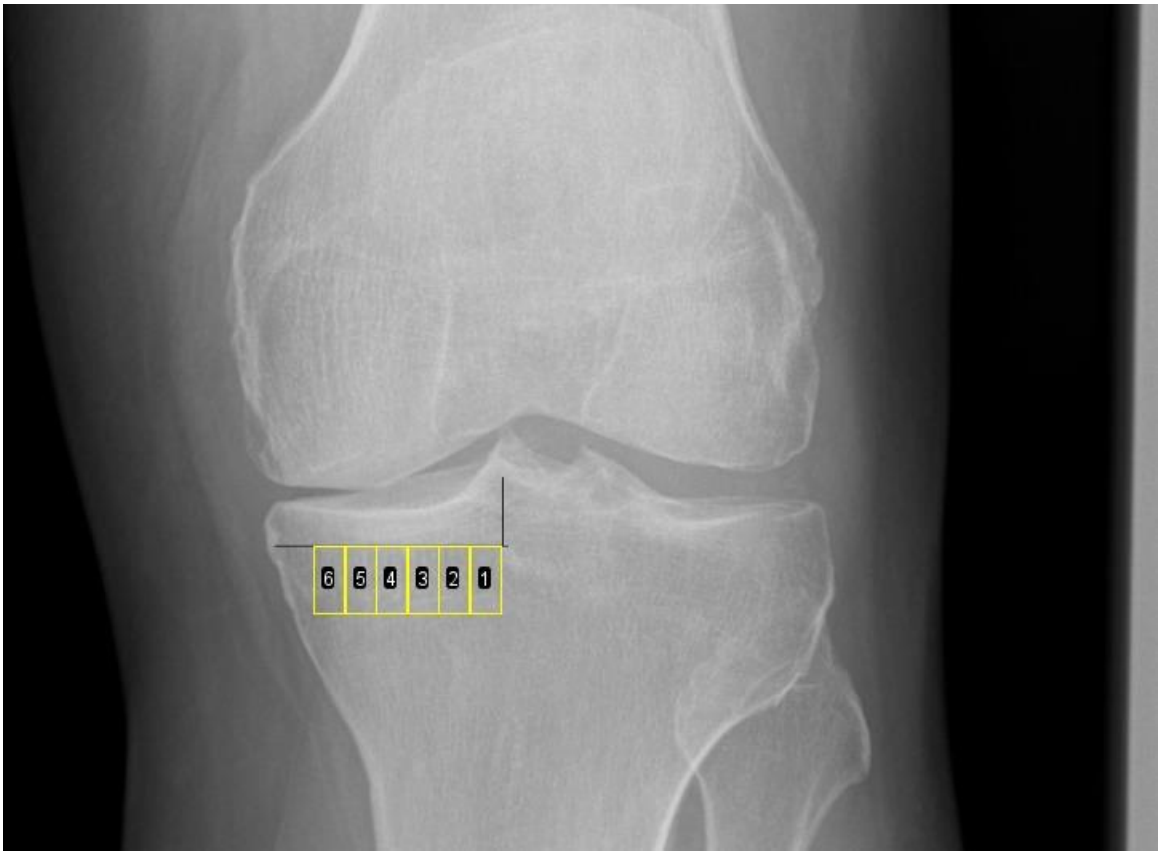

Appendix Figure 5: Regions of interest that were of the same size as the cross-section of the keel were marked out next to the position of the keel.

The average brightness of each ROI was computed with ImageJ (National Institutes of Health, Bethesda, Maryland, USA) on a scale from 0-256 (0: darkest, 256: brightest).

The brightness of each ROI was standardized by assigning them a number on a scale from 0 to 1, with 0 being the darkest ROI and 1 being the brightest ROI. This minimized the effects brought by the difference in overall brightness between radiographs due to variable machine settings and the difference in the time at which they were taken.

Results

Appendix Figure 6 gives the mean standardised grey value at each ROI for the subsidence and non-subsidence groups with a 95% confidence interval.

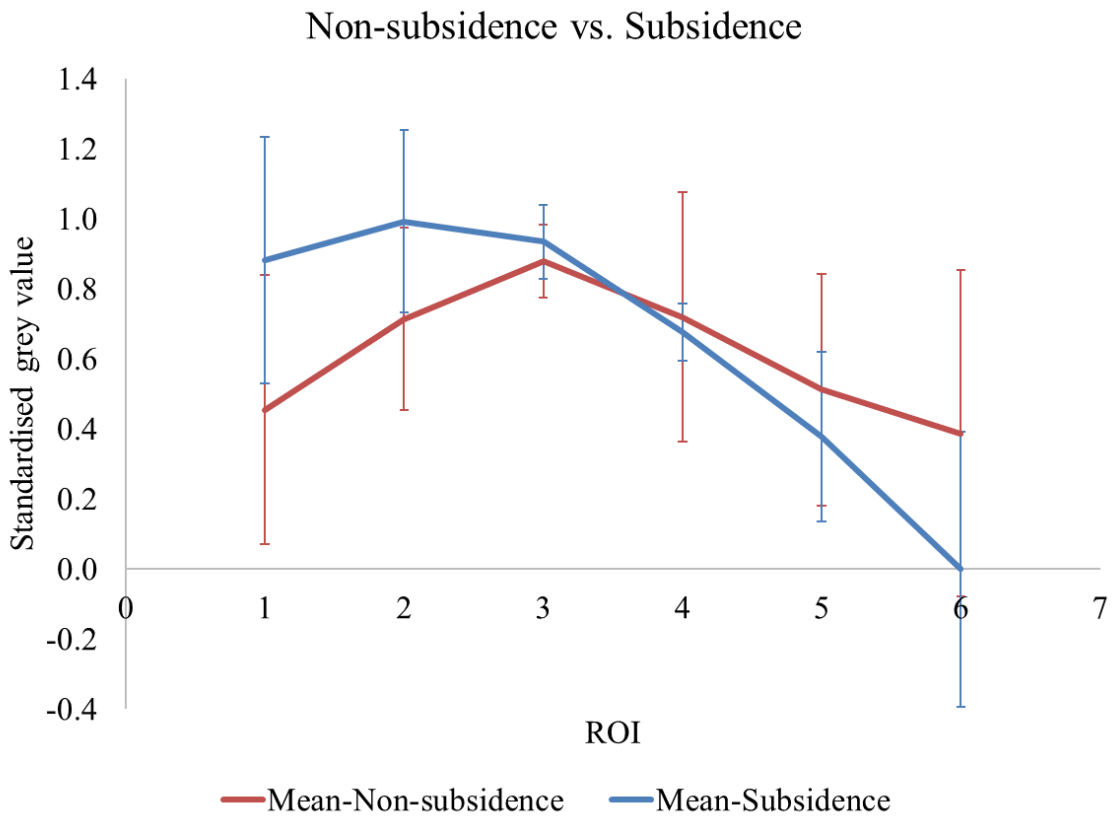

Appendix Figure 6: Mean standardised grey value at each ROI with a 95% confidence interval. ROI3 is the position of the keel.

Discussion

The confidence interval was very large at each ROI suggesting the sample size was too small for any meaningful conclusion to be drawn. If the bone density distribution is to be studied with plain film radiographs, a larger sample size is needed.

Appendix I: Study of Unilateral Subsidence in Bilateral OUKR Patients

Introduction

Patients who have received bilateral cementless OUKR, but experienced valgus and/or posterior subsidence in one knee were shortlisted from a radiographic study on identifying tibial component subsidence conducted by Nisrina Widari (**Appendix Table 2**). This study aimed to find out if the subsided components were more rotated in the horizontal plane as larger external rotations were found in valgus subsidence patients than the non-subsidence patients in a previous study [88]. It was investigated if the internal/external rotation of the subsided component relative to that of the non-subsided one could be identified from the immediate post-operative AP radiographs.

Appendix Table 2: Details of bilateral Oxford Unicompartmental Knee Replacement who experienced subsidence in one of their knees.

Patient no.	Varus/Valgus	Posterior
1 – left	Y	N
1 – right	Y	Y
2 – left	N	N
2 – right	N	Y
3 – left	Y	N
3 – right	N	N
4 – left	N	N
4 – right	(Excluded)	Y

Methods

A few dimensions of the tibial component were defined as below:

Fixed values in all sizes

- wt: wall thickness
- tt: tray thickness
- kt: keel thickness
- ewh: external wall height

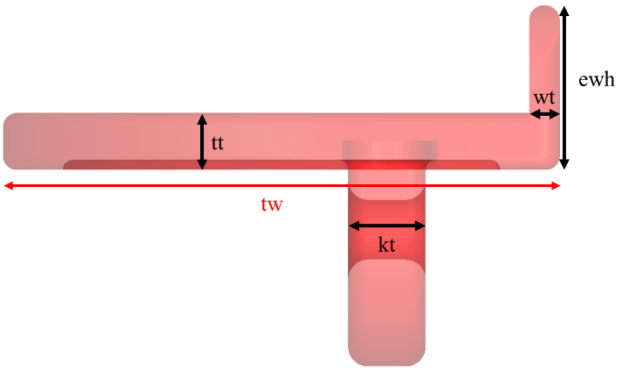

Different values based on sizes

- tw: tray width
- tl: tray length

There are in total 8 positions that the tibial component could be at relative to the x-ray beam:

- Internally rotated
- Externally rotated
- Anteriorly tilted
- Posteriorly tilted
- Internally rotated + anteriorly tilted
- Internally rotated + posteriorly tilted
- Externally rotated + anteriorly tilted
- Externally rotated + posteriorly tilted

Landmarks that could possibly be seen on AP radiographs to identify component's rotation were searched for using a 3-dimensional CAD model of a tibial component.

Results

The following sections summarize the characteristics of the frontal projection of tibial component when it was at each position, which could possibly be used to identify landmarks on radiographs.

Scenario 1: Internally rotated

- Exterior wall and bottom line perpendicular to each other
- Small angle between internal wall and exterior wall, i.e. angle between internal wall and superior edge of tray > 90 deg (almost unnoticeable at small rotation)
- Medial-most edge and lateral-most edge are always parallel for internal rotation

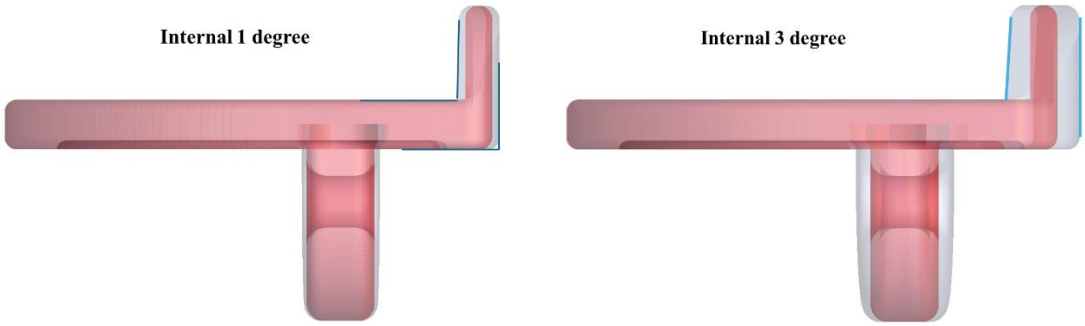

Scenario 2: Internally rotated

- Exterior wall not straight - top part slightly bending in (almost unnoticeable at small rotation)
- Bottom of the interior wall always perpendicular to the superior face of the tray

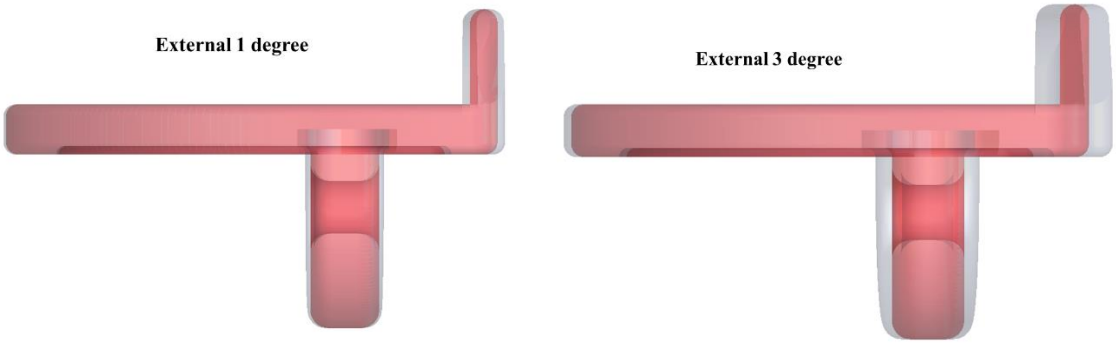

Scenario 3: Anteriorly tilted

- Tray thickness larger at the lateral end
- wt/tw constant
- kt/tw constant
- Interior and exterior wall surface perfectly parallel

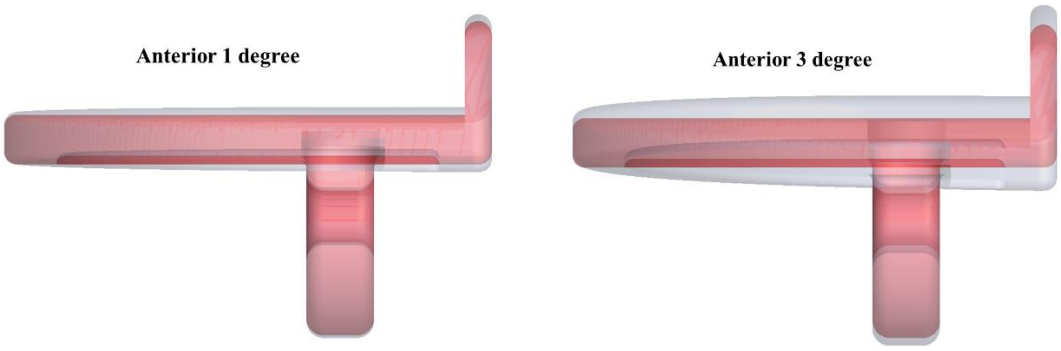

Scenario 4: Posteriorly tilted

- Tray thickness larger at the lateral end
- wt/tw constant
- kt/tw constant
- Interior and exterior wall surface perfectly parallel

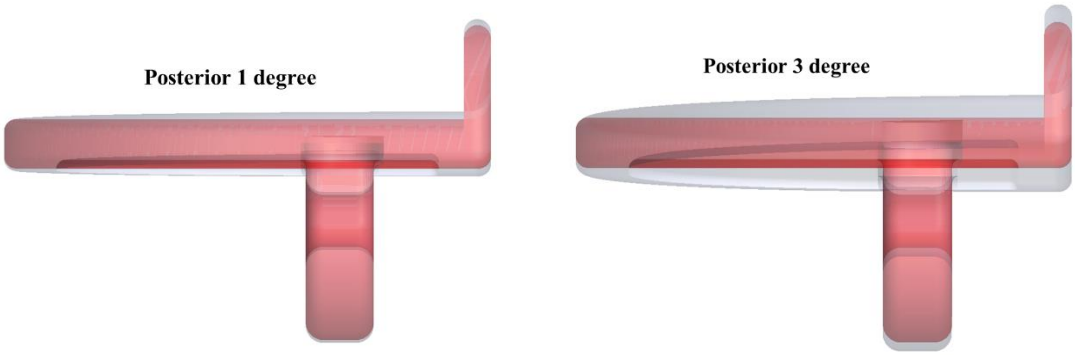

Scenario 5: Internally rotated + anteriorly tilted

- Tray thickness larger at the lateral end
- Sloped edge at the top and bottom of the wall (ascending from medial to lateral)
- Radius smaller at the medial corner or the keel – lateral corner more like a straight line for larger rotation
- Medial-most edge and lateral-most edge are always parallel for internal rotation

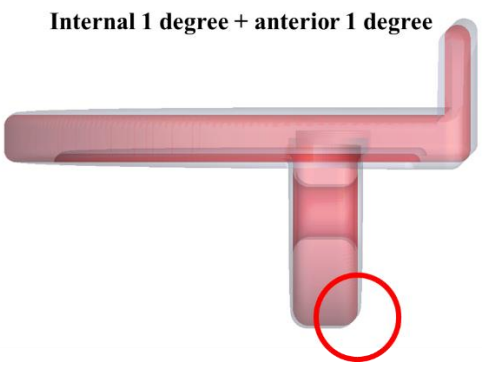

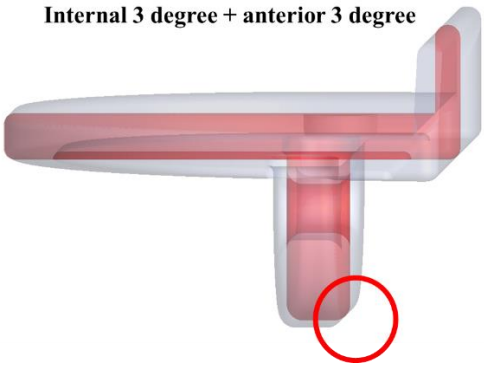

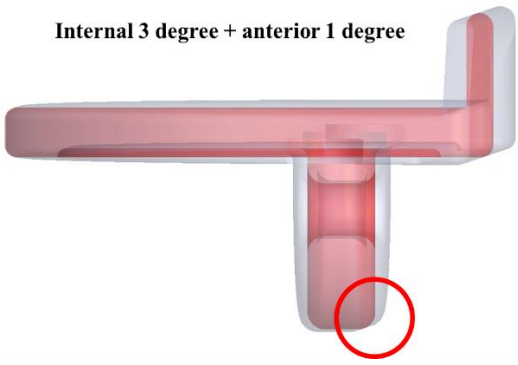

Scenario 6: Internally rotated + posteriorly tilted

- Tray thickness larger at the lateral end
- Slope at the top of the wall only (descending from medial to lateral)
- Radius smaller at the lateral corner or the keel – medial corner more like a straight line for larger rotation

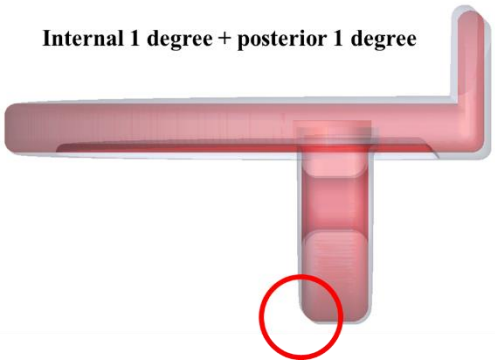

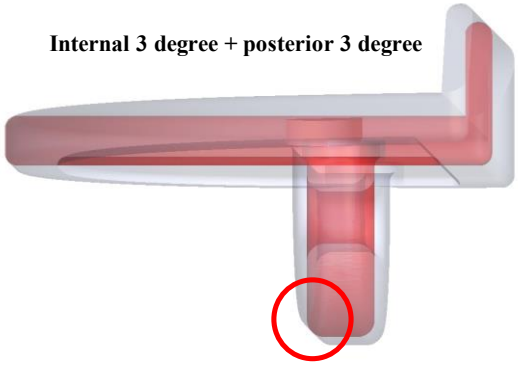

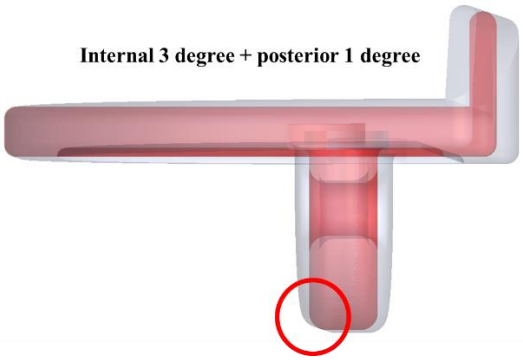

Scenario 7: Externally rotated + anteriorly tilted

- Tray thickness larger at the lateral end
- Slope at the top of the wall only (descending from medial to lateral)
- Radius smaller at the lateral corner or the keel – medial corner more like a straight line for larger rotation

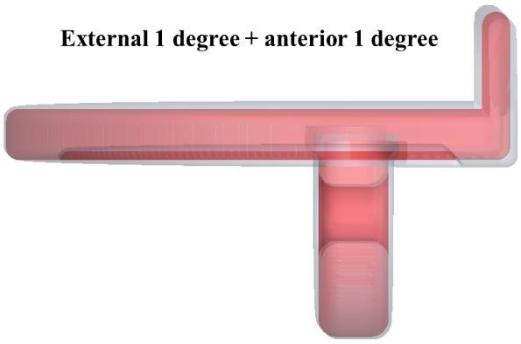

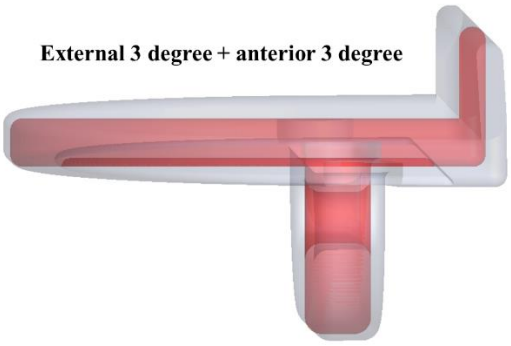

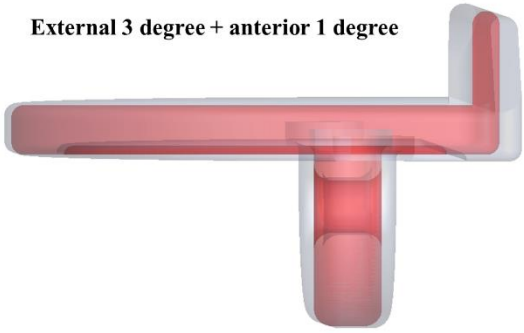

Scenario 8: Externally rotated + posteriorly tilted

- Tray thickness larger at the lateral end
- Slope at the top of the wall only (ascending from medial to lateral)
- Radius smaller at the medial corner or the keel – lateral corner more like a straight line for larger rotation
- For larger external rotation, the lateral-most edge is not straight (unnoticeable at small angle)

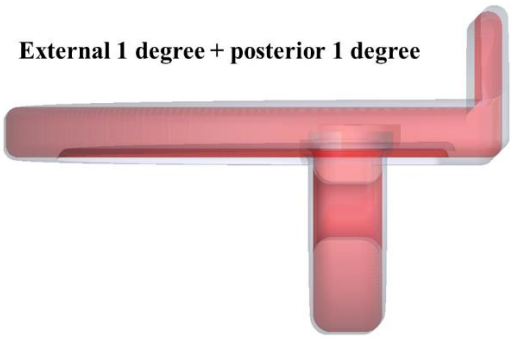

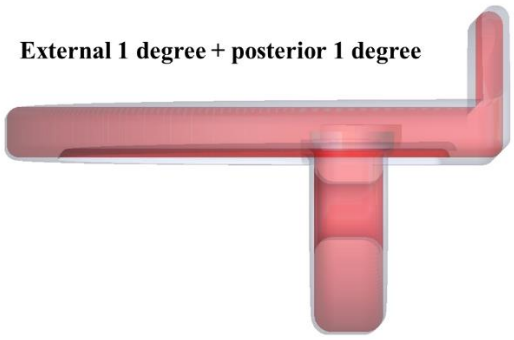

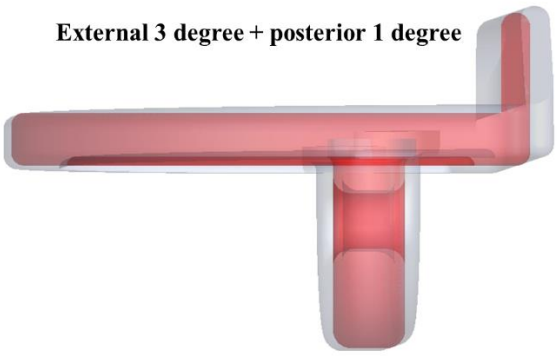

Based on the above figures, it could be seen that when the angle of rotation is small, an internally rotated + posteriorly tilted component looks similar to one that is externally rotated + anteriorly tilted. Also, it is almost impossible to distinguish between an internally rotated + anteriorly tilted component and an externally rotated + posteriorly tilted component. Therefore, it is not feasible to identify if there are any differences in tibial components' internal-external rotation from plain film AP radiographs of these bilateral patients who experienced subsidence in one of their tibias.